Controlling the Au/Iron Oxide Interface to Optimise Plasmonic Resonance for Magneto-Optic Diagnostics

Date: 07/05/2021

Josh Davies-Jones

Abstract

Sepsis is one of the biggest causes of child mortality across the globe accounting for 1 in 5 deaths. Often these deaths could have been prevented with faster diagnosis. This can be achieved by developing point of care diagnostics which can be carried out in a pharmacy or general practitioners office. One way to develop portable diagnostics such as this is the use of the unique magnetic and optical properties possessed by anisotropic nanoparticles. A possible method to identify sepsis is through the presence of bacterial endotoxins. These can be detected magneto-optically by monitoring the rotational dynamics of anisotropic nanoparticles in an external magnetic field.

Nanoparticles of hematite and cerium phosphate were synthesised and evaluated for their use as sensors in magneto-optical diagnosis. The sensitivity of such a probe depends upon a combination of magnetic and plasmonic properties. These are affected by morphology, magnetic susceptibility, and surface plasmon resonance.

The hydrothermal growth mechanisms of hematite nanorods were examined and the relationship between directing agent concentration, reaction temperature and time was examined. The effect of 1,2 propanediamine and alkali metal phosphates acting as directing agents were evaluated on hematite, resulting in the formation of tuneable nanorods with aspect ratios between 3-10 and 1-7 respectively. The rotational dynamics of these hematite particles was assessed in glycerol solution and shown to be sensitive to changes in viscosity at different frequencies of rotation.

Cerium phosphate nanorods were prepared with a tuneable length from 78 nm to 432 nm and aspect ratios of 3-27. The magnetic susceptibility of these rods was changed through the addition of W, Fe, Ni and Mn ions. The addition of Co ions had only a minimum effect n the magnetic susceptibility. The particles were rotated in external magnetic fields and were shown to be sensitive to changes in the viscosity of a solution based on changes in phase shift.

Hematite and cerium phosphate core shell particles were produced. The cores were coated in gold through the seed-mediated method and the morphology of the Au shell was shown to depend heavily upon the number of gold seeds pre-deposited on the

surface as well as the concentration of the gold growth solution. Using this understanding of the growth mechanism, nanorods with smooth gold surfaces which would produce strong plasmonic signals were synthesised.

Acknowledgements

I would not have been able to finish this PhD without the support of so many people around me and it is very hard to acknowledge everyone. Thank you to Phil Davies & Sankar, the best and most supportive supervisors across my entire academic career from undergraduate until now. I appreciate every late evening meeting or last-minute feedback I forced you into.

Thank you to Lisa Allen and Sarah King for being amazing masters students and friends this work is built on the concepts and ideas we explored together.

Everyone in the CCI and Chemistry department who helped me learn a technique or took the time to explain where I was going wrong. I especially thank Lee Edwards, Dave Morgan, Beth Bowden for their help with XPS and for lightening up the long days spent with the AFM.

Alice without your constant support through the hard days of my PhD I would have never finished this. I am lucky to have someone who loves me irrespective of how stressed I am.

Contents

Chapter 1 Introduction

1.1 Background

1.1.1 Point of Care Diagnostics

It is well known that early detection is one of the most important factors contributing to positive outcomes in patients suffering from time-critical diseases. Often issues lie in the time taken for diagnostic tests to be carried out with the most accurate and reliable tests being carried out in centralised labs by experts and requiring damaging amounts of time. This is an inherent problem with the current diagnostic system. A typical test requires to be taken by a medical professional, sent to the lab, the test is carried out by another medical professional and then finally the result is relayed to the patient. Some tests can take days to return results and each day can be integral to a patient with a time-critical disease.

Point of care diagnostics (POC) are tests that can be carried out at a doctor's office or pharmacy by the patient's primary care physician giving results immediately. The potential of such technology to reduce needless deaths is huge. One area of research subject driving these POC diagnostics forward is nanotechnology. Nanoparticles have a huge potential of increasing the accuracy, speed, and ease of diagnostic tests.

This study will examine the combined effects of magnetic, optical, and size properties of nanoparticles on their ability to act as sensors and potential diagnostics.

1.1.2 Optical Properties of Nanoparticles

Nanoparticles are of interest due to their unique characteristics in comparison to bulk materials. Gold is an excellent example; it is inert in the bulk form but shows significant catalytic activity and optical properties on the nanoscale. These characteristics have led to a multitude of significant developments in areas such as drug delivery, energy storage and photonics[1,2].

The use of the unique optical properties found in nanoparticles dates back to the Romans where they would impregnate their glass with noble metals. One such example is the Lycurgus cup, an ornate glass cup with gold and silver alloy particles with a diameter of 70 nm. The cup is known for its ability to change colour from green under reflection to blood red when light is transmitted through the glass, a property that relies upon the surface plasmon resonance of the noble metal nanoparticles[3].

Surface plasmon resonance (SPR) is the result of polarity and electron oscillations formed when light interacts with the surface of a metal nanoparticle. This oscillation of the electron cloud propagates along the surface of the particle until it is released as a new wavelength of light. SPR is highly dependent upon the shape and morphology of the nanoparticles[4], and therefore subtle changes in the surface composition will result in measurable and quantifiable differences in the emission spectra of materials that have SPR.

One example of SPR being used as a sensor is surface-enhanced Raman spectroscopy or SERS. SERS uses SPR to enhance Raman scattering in the study of molecules adsorbed onto rough surfaces. This allows for these materials to be used for molecular detection, drug monitoring and the studying of biomolecule structures. This was first demonstrated by Fleischmann et al. in 1974[5] who noted that scattering from adsorbed pyridine upon a silver electrode was enhanced by a factor of 6 when the surface was rough. The effect has been explained by two mechanisms[6]:

1. An enhancement of the electromagnetic field.
2. Increased charge transfer.

On a rough surface, the multiple interfaces caused by the heterogeneous surface allow the plasmons to become localised to small sections of the particle. These localised plasmons can oscillate both parallel and perpendicular to the surface. This enhances the electromagnetic field and allows absorbates to be more successfully covered by it leading to the excitement of the absorbate molecules. In addition, when a compound is bonded to the surface electrons can travel between the plasmonically active metal and the compound resulting in a charge transfer that enhances Raman activity[7].

SERS based systems are of great interest as sensors in large areas of chemistry[8–11] . In the field of water purification, the detection limits of SERS outperform conventional methods. For example, when detecting cyanide in water, which is limited to 1 ppm by the environmental protection agency. Lee et al. were able to detect cyanide levels between 0-500 ppm with detection sensitivity several orders of magnitude higher than those found in alternative methods[12].

Not all SERS experiments are carried out upon simple surfaces but instead rely upon gold or silver nanoparticles. Gold nanospheres possess a plasmon peak in the range of 500-600 nm

however this peak can be greatly shifted by small changes in diameter or dimension of a particle. These particles have been used for medical purposes such as biosensors. While spherical particles do have their uses, anisotropic particles are of interest[13,14].

The SPR of an anisotropic nanoparticle consists of two main components, the longitudinal and the transverse axis. This means as nanorods become larger the longitudinal component becomes the more prevalent resonance band while shifting wavelength up.

In nanorods, this relationship can be explained mathematically using the Mie-Gans theory which explains the dependence of absorption upon a nanoparticle's aspect ratio. This relationship can be simplified to shows the linear relationship between aspect ratio (R) and the maximum adsorption of an anisotropic nanoparticle[15].

Equation 1-1 $$\lambda_{max} = 95R + 420$$

Other morphologies of anisotropic nanoparticles also possess optical properties such as octahedrons and bipyramids. These systems show similar oscillations to those of nanorods but are significantly more complex to quantify.

Cubic silver nanoparticles also show a spectrum that is very sensitive to morphology. There are 9 possible plasmon peaks for a simple cube, however, 6 of them account for a significant portion of the spectrum. When these cubic structures are truncated towards a spherical morphology the plasmon bands combine to form one strong signal becoming blue shifted[16].

The optical anisotropy described by the Mie-Gans theory has been used to explain why the SPR of nanoparticles results in them being much more optically active than traditional absorbing or fluorescent dyes. With simple spherical particles having absorption cross-sections 5 times higher than that of a dye and more complex morphologies being more active still. For example, in core-shell gold structures their optical response depends upon their size and the thickness of their nanoshell with scattering increasing significantly with core: shell ratio[17].

This work has been used in the development of two-photon luminescence imaging of cancer cells, utilising gold nanorods with aspect ratios of 3.42. The method allowed for the non-invasive imaging 75 microns deep into epithelial tissue with 3 orders of magnitude higher

brightness than untreated cells. These gold nanorods have higher extinction coefficients compared to those of conventional dyes[18,19].

Gold nanostars have also been examined for their plasmon resonance. The overall plasmon resonance was a function of the central core of the particle and that of the elliptical tips of the star. When the particles were modelled as identical and symmetrical. Each tip acted like an independent elliptical particle. Essentially increasing the 'longitudinal' 730 nm Plasmon peak component of the spectra. However, with a more complex system, it is evident that each tip is not symmetrical and identical so behave differently than modelled. Nordlander et al. developed a more complex model. Modelling a nano star with 5 distinct tips. When analysing experimental and computational data they identified 5 distinct peaks, each corresponding to a tip. The longer tips of the star corresponded to the highest wavelenght[15,20].

1.1.3 Magneto-Optical Properties of Anisotropic Particles

A magneto-optic effect is any situation where the polarisation or transmittance of light is changed by exposure or interaction with a magnetic field. The effects can vary depending upon the orientation of the magnetic field. For example, when light is propagating parallel to a magnetic field the Faraday effect is observed whilst light propagating perpendicular to the magnetic field results in the Cotton Mouton effect. These phenomena are often simply referred to as examples of magnetically induced birefringence.

One of the first cases of magnetically induced birefringence was observed by John Kerr in 1901. Kerr wrote about 'Brush Grating' present in a colloidal suspension of Fe_2O_3 particles in water if the iron particles aligned in magnetic field lines to cause an optical effect. This effect was renamed the Cotton-Mouton effect in 1905 when Cotton and Mouton illustrated magnetic birefringence in pure liquids.

The relationship between the magnetic field and the magnitude of the Cotton Mouton effect is quadratic and be shown using the equation below:

Equation 1-2 $$C_m = \frac{2nV_m\mu^2}{3(n^2+2)^2}\left(\frac{n_{||}-n_{\perp}}{B^2}\right)_{B=0}$$

Where C_m is the molar Cotton-Mouton constant, n is the refractive index, V_m the molar volume, μ and B are the magnetic permeability and field strength, respectively. The $n_{||}-n_{\perp}$

term is simply the difference between the refractive index of parallel and perpendicular light and can be thought of as Δn.

Birefringence is defined as a material having a differing refractive index depending upon the polarization or propagation direction of light. This can be thought of as occurring around an axis within a material, where the light will pass through with varying speeds dependent upon its orientation about this axis. Uniaxial birefringence crystals are the most common sort and only contain one optical axis. In this case, the degree of birefringence within a crystal can be described as the difference between the refractive index parallel and perpendicular to this axis. i.e.

Equation 1-3 $$\Delta n = n_{||} - n_{\perp}$$

Figure 1 and can be used to visualise how birefringence can be induced under a magnetic field. In the case of the Cotton-Mouton effect, the medium can be imagined as a uniaxial crystal where the optical axis is the direction in which the magnetic field is applied.

The light passed through a birefringent material is often distorted in its path, transmittance, or polarisation. In this study polarisation is the main effect of which one must be aware. In magneto-optics optical rotation is often observed. It can be described by a simple rotation in the plane of polarised light after travelling through an optically active medium, Figure 1-1;

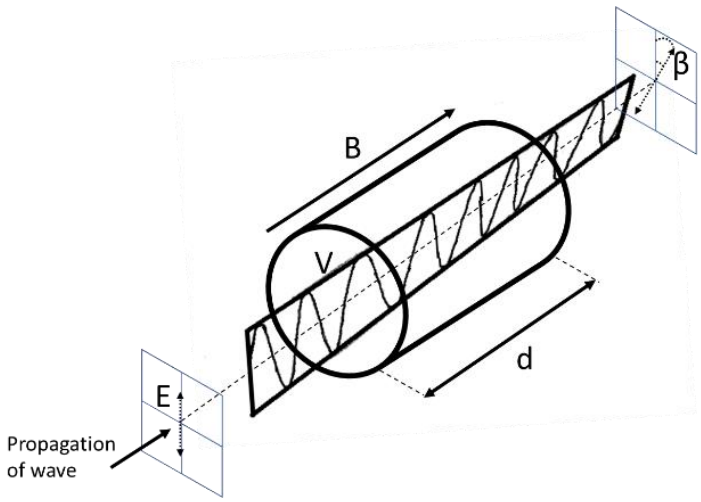

Figure 1-1: Illustration optical rotation observed in the Faraday effect where V is the verdet constant, B is the magnetic field strength, d is the length of material, β is the angle of optical rotation.

To understand why optical rotation occurs it is helpful to split light into vectors based upon the crystal axis or refractive index of the medium shown in Figure 1-2. In this example, it is imagined that a polarised beam of light is passing at 45° to both refractive indices, as $n_1 >$

n_2 the magnitude of light propagating through n_1 decreases. This results in a small amount of light flipping polarisation and thus rotating the beam.

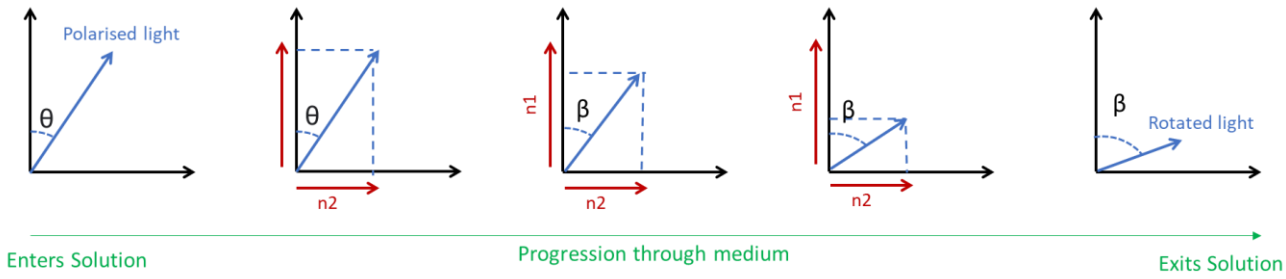

Figure 1-2: Vector illustration of rotation of polarised light where β is optical rotation, n is the refractive index. The blue line is the vector of polarised light which is a function of the refractive index.

Another effect often observed in magneto-optics is circular dichroism. This can be explained by thinking of unpolarised light consisting of both left-handed and right-handed rotations of light which interfere with each other to eliminate rotation. However, in some optically active media, there can be a difference in the rate at which the left hand and right-hand waves propagate, giving rise to circular dichroism. Materials causing circular dichroism possess a different refractive index for the left and right-handed waves of light thus we can state that:

(9) $$n_L \neq n_R.$$

Circularly polarised light can be thought of as containing two sine waves where the peak of the perpendicular waves is at 90 degrees to each other. The effect of this wave alignment is a superposition, where circularly polarised light does not differ in magnitude but the orientation of the wave vector. Elliptically polarised light can be thought of as an intermediate between linear and circular polarised light in which there is less than a complete 90 ° phase shift between the two waves. There is a small amount of retardation resulting in a wave that has both a differing magnitude and is rotated as shown in Figure 1-3:

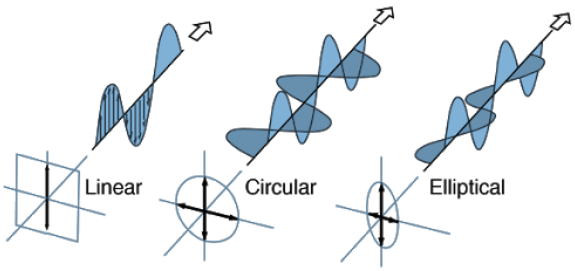

Figure 1-3 The wave profile of different forms of polarised light: linear, elliptical, and circular light.

The Cotton Mouton effect is like the faraday effect shown in Figure 1-1. However, the Cotton Mouton effect occurs when light is transmitted through a medium, perpendicular to an applied magnetic field. This results in the formation of elliptically polarised light and optical rotation.

Equation 1-4 $\beta = VBd$

Where β is the angle of optical rotation, B is the magnetic field strength, D is the length of medium light is propagating through, and V is the verdet constant that describes the strength of the Faraday effect in a particular medium.

1.1.4 Magneto-optical Diagnosis

Point of care diagnostics are tools that can be used at the time or place of medical care. These tests are of particular significance in the cases of diagnosing time-critical diseases such as sepsis, where currently, medical tests carried out in a lab are often needed, with a wait of days.

One modern example of point of care diagnostics is the magneto-optical diagnosis of malaria. This mechanism depends upon a waste product of the malaria parasite itself, called hemozoin which is formed from the digestion of the haemoglobin within the parasite's body. These hemozoin are of nanorod morphology and formed from iron oxide. As a result, the particles are paramagnetic and are therefore influenced by a magnetic field[21].

The method works by the application of a magnetic field which results in the orientation of all the nanoparticles in one uniform direction. Due to the anisotropic nature of the particles, this results in the formation of a temporary birefringence liquid so that transmittance of light is different depending on the magnetic field orientation. This unique property of the

liquid can be used as a positive test for the presence of the malaria parasite in blood samples suspected of malaria infection.

1.1.3 Multiplex Sensing

Combining the SPR and magneto-optical properties of nanoparticles in a system like that mentioned above could lead to highly responsive sensors which can detect complex diseases. These systems would consist of multiple nanorods each absorbing in different areas of the spectrum. With each particle being designed to absorb a given analyte. Such a technology would be called a multiplex system. This is a case where there are multiple signatures to a disease such as antigens which must be positively identified to confirm the presence of a disease. This could be achieved by tuning several different properties to create a combination of nanoparticles with different optical properties. Such a combination could be:

- A mixture of magnetic nanorods where each is coated with a plasmonic metal and is acting as a sensor for a different antigen. Each batch of nanorods has a different aspect ratio or morphology. Based on Mie-Gans theory, each sensor would transmit light in a different area of the spectrum.
- Nanorods of the same morphology, size and shape but coated in different plasmonic metals. Each plasmonic metal will transmit light in a different region of the spectrum. For example, copper, silver, and gold.

When making these tests, it is ideal to have the greatest difference between the analyte spectral regions, so using both methods combined would be ideal. This however requires a significant understanding of the surface chemistry and growth of the anisotropic magnetic core and the growth mechanism of the plasmonic metal coat.

1.1.3 Thesis Aims

This thesis aims to develop anisotropic nanoparticles which have tuneable magnetic, optical, and size properties. These particles will be used to adapt the magneto-optical detection of sepsis by developing by mimicking the morphology, magnetic and optical properties of hemozoin. The nanoparticles devised will act as a proof of concept for magneto-optical detection using the Cotton Mouton effect. This project has been carried out in collaboration with Cotton Mouton Diagnostics (CMD) and successful rods are measured by their appropriateness introduction into CMDs industrial applications. Consequently, rods must be

formed by a simple one-pot hydrothermal process that produces paramagnetic rod-like nanoparticles which can be coated in a smooth layer of gold.

This will be achieved by examining the synthesis of nanorods with three main objectives:

1. Anisotropic with a method to tune morphology or aspect ratio.
2. Uniformly smooth gold coatings to develop consistent SPR peaks.
3. Magnetic so they can be orientated in an external magnetic field.

1.2 Literature Review

1.2.1 Growth and Morphological Control of Anisotropic Nanoparticles

Nanoscience and nanoparticles have been a subject of scientific interest since Faraday's time, an interest that was only intensified by Feynman's lecture 'There's plenty of room at the bottom'. With recent developments in electron and force microscopy, the study of nanoparticles has never been easier. A plethora of nanoparticle preparations have been reported in literature, a significant proportion of which focuses on the formation and characterisation of nanoparticles. When forming anisotropic nanoparticles key similarities can be seen between almost all methods, whether they are metal or metal oxide. Often simple precursor compounds such as phosphates or chlorides are paired with directing agents which are expected to preferentially bind to certain crystal surfaces of a nanoparticle. This results in an asymmetric growth along one preferred crystal lattice.

1.2.2 Anisotropic Metal Nanoparticles

Pure metal nanorods can be synthesised by several main mechanisms summarised below:

Seed-mediated: This method requires the preparation of isotropic seeds before being added to the growth solution in multiple steps. In this case, the seed particle type and reducing agent plays a role in the aspect ratio of the nanoparticles formed.

Photochemical method: relies upon UV light to reduce the metal ions in the presence of a growth solution containing capping agents to control the morphology of the nanorods. Take for example the photochemical reduction of silver nanoparticles carried out by Scaiano et al.[22], by irradiating gold seeds with wavelengths varying between 400 and 720 nm, 5 unique morphologies were formed ranging from decahedral nanoparticles to nanorods.

Polyol method: this is one of the most versatile methods and is used to prepare both metal and metal oxide nanoparticles. The method involves polyol compounds such as ethylene glycol (EG) being used as both the reaction solution and the reducing agent.

Electrochemical method: uses a metal and a platinum plate as electrodes suspended in a growth solution consisting of two capping agents, cetyl trimethyl ammonium bromide (CTAB) and tetra octyl ammonium bromide (TCAB). When metal ions move from the anode to the cathode become reduced to the simple metal state. These particles are then encapsulated with other metal ions with the TCAB directing the growth and the CTAB acting as a mediator to prevent aggregation. The aspect ratio of the nanorods formed can be changed by controlling the ratio between CTAB and TCAB.

The importance of anisotropic morphology was best observed in the work of Ye et al. who examined the effects of different organic additives upon the aspect ratios of gold nanorods formed. They were also able to predict the aspect ratios of nanoparticles entirely based upon their plasmon peaks. This fingerprint-like UV-VIS spectra of anisotropic nanoparticles and their surface sensitivity are what makes them so ideal for sensors[23]. The effect of aspect ratio upon plasmon peaks is illustrated in Table 1-1.

Aspect ratio	Calculated plasmon peak (nm)	Experimental plasmon peak (nm)
2.36	630	627
2.57	651	653
3.64	753	754
3.32	722	723
3.5	735	734
3.83	777	757
4.9	886	904
4.4	828	844
4.38	723	705

Table 1-1: Summary of data obtained by Ye et al., showing the dependence of plasmon frequencies on the shape of gold nanoparticles. [23]

1.2.3 Gold Nanoparticles

The seed-mediated method was first reported in 2001 and involves the synthesis of isotropic seed gold nanoparticles first. These are then sequentially exposed to multiple growth steps to facilitate a weak reducing agent such as ascorbic acid and a stabilising surfactant CTAB.

In both cases, the growth mechanism is similar and relies upon several factors. However, it can be reduced to the fact that CTAB and Ag ions act as capping agents bonding preferentially to crystal facets. These facets depend upon the exact shape and morphology of gold seeds used in the method[24,25].

One such example, nanoparticles are synthesised by the seed-mediated method with the addition of small amounts of silver nitrate, which when the concentration increases, so does the aspect ratio. This relationship is more complex than first thought and relies upon several states. The ratio of [$HauCl_4$]:[$AgNO_3$] where the proportion of silver nitrate to gold seeds will

result in higher aspect ratios. However, this also depends upon the size of the isotropic gold seeds formed if they do not fall within a 4-6 nm range the symmetry of the nanoparticles will result in the formation of other gold morphologies. This is since gold nanorods grow along the [110] crystal facet with capping along the [111] facet. The CTA-Br-Ag^{+} species act as a capping agent and Ag ions show a preference to the [110] crystal surface. This can be explained in terms of nearest neighbours for the silver adatoms. Where on the [111] surface silver would have 3 neighbours on the [100] 4 and on [110] 5. Therefore it is more favourable and stable for The CTA-Br-Ag+ species to bond to the [110] surface, facilitating preferential growth on the [111] surface[24,26,27].

Preparation Method	**Growth solution**	**Aspect ratio**	**Ref**
CTAB Seed-Mediated	CTAB, $HAuCl_4$, H_2SO_4, $AgNO_3$	1.82-5.04	[28]
Citrate Seed-Mediated	CTAB, $HAuCl_4$, Ascorbic Acid	4.6-20	[29]
CTAB Seed-Mediated	CTAB, $HAuCl_4$, NaOH, HNO_3	20-25	[30]
Seedless	CTAB, $HAuCl_4$, HCl, $AgNO_3$, Paradoxybenzene	6.7 – 20.6	[31]
Seedless	CTAB, $HAuCl_4$, HCl, $AgNO_3$, $NaBH_4$	3.7-5	[32]

Table 1-2: Summary of different anisotropic nanoparticles with a seed-mediated or seedless growth from literature.

This original seed-mediated method used citrate as a stabilising agent for the initial metal seed particles. However, this was modified with the use of CTAB. This method drastically improved on the previous seed-mediated method. Where a yield of only 5% of the particles would display rod morphology compared to 95% in the latter method. However, with these huge changes in yield came a significant change in aspect ratio where the citric acid method would result in aspect ratios between 6-20 while CTAB- Ag particle would have maximum aspect ratios of 5[33]

When removing Ag+ Ions from the growth solution and replacing it with nitric acid, highly reproducible particles with high aspect ratios can be reached. Where the pH of the solution can vary the aspect ratio between 20-25.

Seed-mediated methods are a way to successfully form nanorods, however, they rely upon seed particles being consistent, growth times and even small changes in the growth solution. Table 1-2 details the different aspect ratios that can be obtained from different seed-mediated methods compared to seedless methods. The aspect ratio in most cases is limited to 5 and only a small proportion of the gold solution is used in the reaction[34]. Therefore, a seedless one-pot synthesis would be a preferable system. This was achieved for gold nanoparticles originally using $NaBH_4$ as a reducing agent which resulted in the formation of small nanoparticles with diameters of up to 3 nm. However, the aspect ratio of these particles was small. For optical applications, high aspect ratio rods are preferable because of their plasmonic behaviour.

Xu et al.[35] improved upon this method with the use of paradoxybenzene which resulted in large gold nanorods with aspect ratios varying between 6 and 20. These particles were formed with a yield of over 90%. It was theorised that the hydrophobic nature of paradoxybenzene compared to other reducing agents resulted in higher aspect ratios.

1.2.3 Silver Nanorods.

Anisotropic silver nanoparticles have been of wide interest since their first wet synthesis in 2001 by Murphy et al. by a two-step seed-mediated system. This involved the formation of silver seeds from their $AgNO_3$ precursor paired with a strong reducing agent such as $NaBH_4$ followed by addition to growth solutions of CTAB and ascorbic acid. This resulted in a range of aspect ratios of 2.5 to 15 for silver nanorods and silver nanowires of aspect ratios up to 350[36]. The aspect ratio was controllable by the ratio of metal salt to metal seeds of the solution. While the formation of silver nanowires was achieved by reducing the pH. While this method was successful in forming nanorods, a size distribution was variable and lower aspect ratio particles would destabilise and revert to spherical morphology. pH controls the growth of silver nanorods as it acts as a control of the reduction potential of the ascorbic acid which is increased at higher pH values resulting in a quicker rate of silver reduction and nucleation which outcompetes the rate of CTAB absorption and thus has less control and results in smaller particles. However, in the presence of lower pH, the AA has a lower reduction potential, and the opposite is true. This is seen throughout the preparation of

silver nanoparticles, when reducing growth rate, higher aspect ratios can be obtained[37,38]. Table 1-3 shows a selection of different methods to prepare silver nanorods.

Preparation Method	Growth solution	Aspect ratio	Ref
CTAB Seed-Mediated	CTAB, NaOH, $AgNO_3$	4-17.5	[39]
Citrate Seed-Mediated	CTAB, NaOH, $AgNO_3$, Ascorbic Acid	1.8 - 3	[40]
Citrate Seed-mediated	CTAB, NaOH, $AgNO_3$, Ascorbic Acid	9-19	[41]
Photochemical 600-750 nm	CTAB, NaOH, $AgNO_3$, Ascorbic Acid	5.5-20	[42]
CTAB Seed-mediated	CTAC, AgDS, $NaBH_4$	5-20	[43]
CTAB Seed-mediated	CTAB, NaOH, $AgNO_3$, Ascorbic Acid	2.5-15	[36]

Table 1-3: Summary of different silver anisotropic nanoparticles prepared with seed-mediated, seedless, photochemical and their aspect ratios.

The exact growth mechanism of silver nanorods is not entirely understood, however, it is expected to be similar across the preparation methods. Take, for example, a comparison between growth in the seed-mediated method and the polyol method. In both cases, the initial growth seeds possess a multiply twinned nanoparticle with a decahedral morphology having ten [111] crystal facets. In both cases, the capping agent adsorbs to the more open [100] crystal surface leaving the [111] surface at the face of the particle for nucleation of silver ions. In the case of Kaler et al.[43] the surfactant is cetyltrimethylammonium tosylate (CTAT) and for Xia et al. PVP (poly(vinylpolypyrrolidone))[44].

However, this growth mechanism holds the answer to why silver nanoparticles are not often formed with high yields or low particle size distributions. Monk et al. predicted the energetic effects of the multitwinned crystal structure based on the aspect ratio of a silver nanoparticle. It was found that at lower aspect ratios the twinned structure is favoured over the bulk FCC silver crystal. However, as the aspect ratio increases, this decahedral structure becomes less favourable. The exact relationship depends upon length and diameter.[45] Where A_{cs} is the cross-sectional area and L is the critical length of a nanoparticle.

Equation 1-5 $$L = 3.38 \times A_{cs}^{\frac{1}{2}}$$

If the critical length (L) is exceeded the nanorods begin to decompose. This happens upon the weaker [111] twinned interfaces resulting in the formation of pits along the

nanoparticles length. These pits are essentially reducing the diameter. This results in the dissolution of silver ions which will either nucleate on other rods, into FCC spheres or into smaller decahedral structures which satisfy this rule.[41]

By using the photochemical method with light wavelengths varying between 600-750 nm Mirkin et al. were able to tune the aspect ratio from 5.5-20 with a high yield of anisotropic particles with the twinned crystal structure seen in other methods. However, these particles had large particle size distributions especially at wavelengths below 600 nm. Like the effects seen in other synthesises, conditions that control reaction rate result in changes to aspect ratio. In this case, using longer wavelengths result in a slower reduction of Ag^{+} to Ag^{o} which favours the growth of nanorods for reasons explained above[42].

1.2.3 Cobalt Nanorods

Most plasmonic metals are not ferromagnetic and this gives cobalt nanorods a distinct advantage over other elemental nanorods. However, preparing these particles can be more difficult than other elemental nanorods like gold or silver. The two main preparation routes for cobalt nanoparticles are the Polyol preparation and the organometallic method. Table 1-4 shows several prevalent methods of preparing cobalt nanorods.

The organometallic method gets its name from the use of unstable organometallic precursors to the nanorods. This method was first used to prepare cobalt rods in 2002 by Zurcher et al. [46] which involved the use of [Coη^3-C_8H_{13})(η^4-C_8H_{12})] at 150^{o}C under H_2 gas acting as the reducing agent in the presence of long-chain amines such as hexadecylamine and oleylamine. Aspect ratios between 1.7 and 22 were obtainable and controlled by the length of carbon chains attached to amines. It is theorised that these amines act like other capping agents and coordinate with the cobalt to control growth. This method was improved upon by changing the precursor Co[N($SiMe_3$)$_2$] in the presence of lauric acid and hexamethylenediamine. This gave greater control over the aspect ratio by changing the lauric acid amine ratio[47–49].

Preparation Method	Growth solution	Aspect ratio	Ref
Polyol	1,2-butanediol, RuCL3, NaOH, $Co(C_{11}H_{23}COO)_2$	5-10	[50]
Organometallic	$[Co\eta^3\text{-}C_8H_{13})(\eta^4\text{-}C_8H_{12})]$, Hexadecylamine, H_2	1.7-22	[46]
Organometallic	$Co[N(SiMe_3)_2]$, Hexadecylamine, H_2, $C_{11}H_{23}COOH$	3-21	[51]
Solvatothermal	$Co(C_{11}H_{23}COO)_2$, 1,2-butanediol, RuCL3	3-14	[52,53]
Polyol	1,2-butanediol IrCL3, NaOH, $Co(C_{11}H_{23}COO)_2$	6.5-10	[52]

Table 1-4: Summary of different cobalt anisotropic nanoparticles prepared with a different method and their aspect ratios.

The polyol preparations of cobalt nanorods rely upon much of the same as the previous methods mentioned before this. With one exception where a small amount of another metal such as Ruthenium or Iridium is used as a seed particle for the nucleation of the cobalt ions. The cobalt carboxylate precursor length plays a key role in the morphology of the nanorod where carbon chain lengths below and would result in a mixture of particles but when greater than this number monodispersed rods were obtained. For this reason, most methods use cobalt laurite as their metal precursor[50]. The ratio of is the reduction is facilitated by the presence of ethylene glycol or 1,2 butanediol. The asymmetric growth is achieved by the carboxylate chains adsorbing preferentially to certain crystal facets.

Following the polyol preparation method, a solvothermal preparation was prepared where the nanorods formed do not have the signature dumbbell morphology[51,52,54] often obtained when creating cobalt rods from Ru or Ir seeds. This method formed smooth rods where the aspect ratio and particle size distribution could be controlled by varying stirring speed in the growth stages[52].

1.2.3 Anisotropic Metal Oxide Nanoparticles

Transition metal oxide nanoparticles are of interest because of their incredible chemical versatility with their variety of oxidation states and electronic character due to the unfilled d orbitals they can be tailored to many uses including gas sensing, catalysis, energy conversion or storage and medicine[55,56]. Their magnetic properties are of particular interest showing

the full spectrum of ferri, ferro and antiferromagnetic behaviour which can be influenced by doping and particle size[57].

Metal oxide nanoparticles can be formed in exotic shapes from several different methods however, this section will be focused on wet chemical synthesis. Most metal oxide nanoparticles are formed from many preparation routes, for example, co-precipitation which involves the mixing of two solutions where both contain metal ions of desired within the final particle. This method is an easy way to develop bimetallic or doped nanoparticles simply by mixing the precursors of two different metal compounds. Hydrothermal is another method that relies upon the thermal decomposition of a metal precursor in the presence of a capping agent to direct anisotropic growth. Other methods rely upon the use of either soft or hard templates where the nanoparticles are forced to grow within the confines of a solid structure which is removed following synthesis.

1.2.3 Iron Oxides

Iron oxide nanoparticles are of particular interest because of their magnetic behaviour and their low toxicity. The three main iron oxide forms are hematite, maghemite and magnetite, each considered to be relatively biologically inert. Magnetite has been of particular interest because of its composition, containing both Fe(II) and Fe(III) ions which allow for electrons to transfer between the two states.

Magnetite is often formed from the co-precipitation of Fe(II) and Fe(III) in the presence of a base such as NaOH or NH_3OH. This is well illustrated by Zhao et al.[58] who were able to produce anisotropic nanoparticles varying in morphology from nanocubes to nanostars by co-precipitating $FeSO_4$ and $Fe_2(SO_4)_3$ in the presence of sodium dodecyl sulfate (SDS) and NaOH. It was found that the morphology of the nanoparticles depended heavily upon the quantity of SDS added to the reaction solution. They also showed that the magnetic character of the nanoparticles varied with morphology through a mixture of the size-dependent magnetic effects based on the surface spin disorder and crystal nature of the particles. The nanorods formed were of lower crystallinity than the nanocubes whose larger crystal domains present also gave a higher magnetic response.

Similar hydrothermal methods using $FeCl_3$ and $FeSO_4$ in the presence of ethylenediamine were studied by Wang et al. and Deng et al. [59,60] using benzene to create an oil membrane

separating oxygen from the iron cations. This resulted in single-crystal nanorods however the product contained a mixture of different morphologies. It was found that the diamine was vital to the reaction acting as a surfactant to direct growth[59,60]. In the absence of benzene, the reaction resulted in the formation of hematite. Sun et al., eliminated the need for benzene by increasing the concentration of the diamine. However, this ultimately resulted in the formation of less morphologically consistent batches with lower aspect ratios[61] Furthermore, in both of these cases, the magnetic behaviour of the nanoparticles was less than is observed in the bulk which has a magnetic saturation of 92.5 emu g^{-1} while these methods formed particles with 72.94 and 71.3 emu g^{-1} respectively.

Other methods have been used to form magnetite nanorods and succeeded in approaching their bulk magnetisation while forming an anisotropic nanoparticle, see Table 1-5.

Preparation Method	**Growth solution**	**Aspect ratio**	**Magnetic saturation (emu g^{-1})**	**Ref**
Hydrothermal	$FeCl_3$, $FeSO_4$, ethylenediamine, Benzene	10-20	72.94	59
Hydrothermal	$FeCl_3$, $FeSO_4$, ethylenediamine,	8	71.3	61
Coprecipitation	$FeCl_3$, $FeCl_2$, PVP NaOH	17	28	62
Co-precipitation	$FeSO_4$ and $Fe_2(SO_4)_3$ SDS, NaOH	9	94.2	58
Hydrothermal	$FeSO_4$, KNO_3, NAOH, NH_4	15-20	76	61
Two step (FeOOH)	$FeCl_3$, NaOH, CTAB, N_2H_4	6-9	81.7	62

Table 1-5: Summary of different Iron anisotropic nanoparticles prepared with a different method with their aspect ratios and magnetic saturation.

1.2.4 Modifying Nanorod Magnetic or Plasmonic Characteristics

Obtaining magnetic and optically active rods has been achieved using two main preparation methods. The first involves the preparation of a plasmonic metal nanoparticle which is doped with some degree of a magnetic metal. The dopant can only make only small differences to the plasmon peaks and still result in a consistent nanoparticle morphology

with a small size distribution. The alternative method is the development of a core-shell structure, and this approach is explored in more detail in the following sections.

1.2.3 Coatings and Core-shell Particles

Core-shell particles have a centre coated in a different material. Bimetallic core-shell structures have been the focus of numerous studies due to their rare combination of electronic and plasmonic properties which differ from single-component materials. They have applications across science varying from catalysis to diagnostics due to the range of magnetic and optical characteristics that can be obtained by different compositions of bimetallic core-shell structures[63]. An added benefit to the use of these nanomaterials is the protection offered by an outer shell can increase the stability of the core nanoparticle[64].

In general, the formation of core-shell nanoparticles is achieved by the reduction of a precursor compound in the presence of the core particles, resulting in the deposition of the shell onto the surface of the core. One such example is the formation of SiO_2/Au nanostructures, where core silica nanoparticles are coated in gold by the reduction of $HAuCl_4$ by formaldehyde. The plasmonic behaviour of the nanostructures could be influenced by changing the core: shell ratio, with thinner cores of 5 nm exhibiting plasmon peaks above 1000 nm. While thicker coatings between 10-20 nm show plasmon bands between 850-700 nm[65].

1.2.3 Coating Growth

The nucleation of ions upon inorganic surfaces follows the basic rules of surface-adatom interactions and coat growth[66] and the main factor which controls the growth mechanism is the Gibbs free energy change(ΔG_s) of the surface. Take for example a system where a core particle, (component 1) is exposed to a colloid which will nucleate upon its surface, (component 2). The thermodynamics of the growth of the coat formed can be described by:[67,68]

Equation 1-6 $$\Delta G_s = \gamma_1 - \gamma_2 + \gamma_{1,2}$$

Where $\gamma_1$and γ_2 are the solid/solution interfacial energies of the two materials where γ_1 can be influenced and controlled by the addition of surfactants. $\gamma_{1,2}$ is the solid/solid interfacial energy which is dependent upon the strength of the surface adatom interactions and their crystallographic compatibility. Depending on the systems and surfactants present three growth mechanisms are expected to occur:

1. Volmer-Weber occurs when $\gamma_1<\gamma_2$ and adatom-adatom interactions are stronger than surface-adatom interactions or the crystal lattices of the two mediums are too dissimilar resulting in a high $\gamma_{1,2}$ value i.e ($\Delta G_s < 0$). This results in which results in the formation of 3D islands upon the surface of the core particle as the adatoms attempt to reduce overall contact with the surface.
2. Frank-van der Merwe growth occurs when $\gamma_1>\gamma_2$ and adatom-adatom interactions are weaker than surface-adatom interactions and the crystal lattices of the two mediums are well-matched resulting in a low $\gamma_{1,2}$ value i.e ($\Delta G_s > 0$). when the metal-surface interaction is stronger than the metal-metal interactions. This results in layer-by-layer growth which results in a homogenous coat across the surface.
3. Stranksi-Krastanov is the intermediate of these two extremes, where growth consists of two stages. The growth of multiple layers results in surface-adatom interactions weakening until the point at which ΔG_s of the reaction switches from $\Delta G_s > 0$ to $\Delta G_s < 0$ resulting in the formation of islands upon the already smooth surface.

An example of these different growth modes can be seen in the work of Yang et al. who prepared[66] Pd/Pt core-shell nanostructures for electrocatalytic oxidation of methanol. Pd core nanoparticles were synthesised and exposed to a platinum precursor H_2PtCl_6. Normally, when Pt is deposited upon a Pd surface, islands form due to the more favourable Pt-Pt

interactions (γ_1<γ_2, Volmer-Web growth). However, in the presence of olyemine, the surface energy of the Pt is reduced by the surfactant and this allows the formation of hexapod and octopod morphologies through a two-step Stranski-Krastanov growth mechanism. In the first step, Pt deposited in a layer-by-layer process resulting in a fully homogenous coating. However, in the corner of each nanostructure, local strain results in preferential growth forming the octopod or hexapod morphology. [66].

1.2.3 Stöber Method

Silica is an ideal coating for plasmonic metals due to its transparency to wavelengths between 400 and 1000 nm, biocompatibility and ability to stabilise metal nanoparticles from degradation[69]. There are multiple ways to deposit silica onto the surface of nanoparticles[70] but of all of them, the Stöber method is by far the most common.

The Stöber method was originally devised in 1968[71] to form monodispersed spherical nanoparticles between 10-500 nm in size. This was achieved by a sol-gel method where silicon alkoxides are catalytically reduced by ammonia and its concentration could control particle size. The method has been modified for the coating of both anisotropic and isotropic nanoparticles and is used in much the same way as when the method was first designed involving tetra ethylorthosilicate (TEOS) being reduced by tetramethylammonium hydroxide, (TMAH) in an alcoholic solution such as ethanol.

The first coating of gold nanoparticles by the Stöber method was carried out by Mulvaney et al. [72] in 1996 using 50 nm citrate capped gold nanoparticles. Gold is not the ideal substrate for the Stöber method due to a lack of chemical or electrostatic affinity with the silica and so the surface of the gold is often first functionalised with amino silanes which allow for the NH^+ to adsorb to the surface of the metal and act as a foundation for the formation of the silica coat. By controlling the silica coating thickness, the plasmon peaks of the gold particles can be tuned in with thicker coats of over 70 nm showing overall higher absorbance but the lower resolution of the peaks. Coats thinner than 60 nm have little effect on the plasmon peak.

Similar effects are seen in (poly(ethylene glycol) PEG-gold nanorods where coating thickness can have little effect upon the overall plasmonic behaviour of the particle when the coat is thin. Gold nanoseeds were formed through a seed-mediated CTAB controlled method. The

CTAB was then replaced by methoxypoly(ethylene glycol) to form a silane coupling agent. The presence of a silica coat made only small changes to the plasmon peaks of the nanorods, and thin coatings of 6 nm resulted in plasmon peaks like those of uncoated PEG-Nanorods. When the silica coating thickness was increased to 20 nm the longitudinal plasmon resonance peak shift to 800 nm[73]. Shell thickness is easily controllable as a function of the silicon precursor volume, where increased volumes of TEOS results in the formation of thicker silica coatings.

The Stöber method has been used successfully to combat the lack of biocompatibility of some nanoparticles and the tendency to aggregate seen in magnetic nanoparticles such as iron oxides. Silica deposited upon the surface also acts as a barrier between the metal ions and the environment, so for example reducing the extent of oxidation of iron (II) to form iron(III), which can result in a significant loss in magnetism[74–76]. However, coating with silica does affect the magnetic behaviour of the core[77,78] reducing magnetic saturation and coercivity. This results from the significant contribution of 'surface spin effects' to the magnetic behaviour of nanoparticles since the low symmetry of surface atoms can result in the development of local magnetic anisotropy upon the surface increasing magnetic disorder[79]. This effect of increasing surface anisotropy is increased with shell thickness resulting in less magnetically responsive nanoparticles as shell width increased[80].

1.2.3 Magnetisation of Metal Nanorods

Plasmonic metal rods such as gold and silver are more difficult to dope with magnetic nuclei so more creative solutions are needed. Most of these involve either embedding magnetic metal nuclei within the bulk of the metal rod. Gold nanorods can be magnetised by the addition of cobalt for example, which results in only slight changes in the UV spectrum of the nanorods in a small dose. However, when exceeding 100 µg of cobalt seeds in an aqueous ($1x10^{-3}$ M) gold growth solution the aspect ratios and UV spectrum change drastically, in fact only spherical particles are formed. Rao et al. showed[81] that smaller concentrations of cobalt seed particles form larger aspect ratio particles, thus a compromise between strongly magnetic particles and aspect ratio must be found.

However, not all coatings reduce magnetic behaviour, core-shell particles can take the form of a magnetic coat formed upon a magnetic particle[82], or there can be more complex

combinations involving a sandwich structure of several layers with polymer intermediates between the coat and the rod[81].

One method to introduce magnetic behaviour to plasmonic rods such as gold is to support prepared nanoparticles such as magnetite or cobalt upon the surface of a functionalised plasmonic rod. While these particles exhibit magnetic behaviour, this process cannot be called a 'coating' since the second component is present only as islands. In one such example, gold nanorods functionalised with poly(sodium 4-styrenesulfonate) were exposed to Fe_3O_4 nanoparticles in the presence of poly(diallyldimethylammonium chloride)[83]. This formed magnetic composite structures where there was little change to the UV-VIS spectrum but a significant increase in magnetism. The same study also showed that coatings can be formed *in situ* by the reduction of iron salts onto the surface of a gold rod. However, the resulting rods while fully coated were less magnetic and expressed less plasmonic activity.

1.2.5 Photoinduced Force Microscopy (PiFM)

Infra-Red spectroscopy studies the vibration transitions of molecules through their interactions with IR radiation. Typical infra-Red Spectroscopy measures these vibrations by monitoring the fraction of light absorbed by a sample at a specific wavelength[84]. Since this depends on the interaction of light on a sample, such techniques are limited by abbe 'diffraction limit of light'[85]. This means that the maximum spatial resolution of IR spectroscopy is limited to the micrometre range[86]. Consequently, typical IR spectroscopy such as FTIR is not capable of carrying out nanoscale measurements.

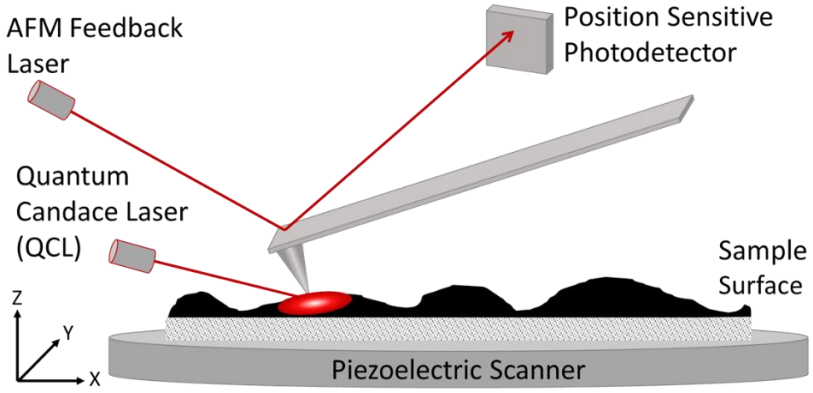

Figure 1-1 simple illustration of a PiFM measuring a surface. A QCL laser is pulsed at the interface of the AFM tip exciting the surface which is detected by the position-sensitive photodetector.

Photoinduced Force Microscopy (PiFM) is a combination of AFM and IR spectroscopy[87], it relies on the vibrations induced by dipole-dipole interactions between the tip and the surface in the presence of a laser. Subsequently, PiFM is not limited by the diffraction limit and has nanometre resolutions[86]. A pulsing laser with variable wavelengths 750-1850cm^{-1} is directed at the interface between the tip and the surface, see Figure 1-1. As the name suggests this technique depends upon a force induced by the IR radiation. Essentially when a laser is shined upon a surface a dipole is induced, a reflection of this dipole is also found in the tip. The interaction between these two dipoles pulls the tip closer to the surface, the extend of this force is a function of how polarised the surface is. A surface becomes more polarised at the vibrational frequencies of a bond. The produces a local force is which is exacted on the cantilever of the AFM which is detected by a position sensitive photo detect and the PiFM signal is generated[88].

PiFM can combine topographical and spectral imagining into one map across a sample

surface. This allows for the study of morpholgy[89,90], plasmonics[91,92] and magnetic behaviour[93]. The technology has two imagining modes:

- Wide analysis - IR-spectrum can be taken at each position the AFM tip measures allowing for spectra to be obtained for specific topographical regions of a sample source.
- Targeted Analysis - A scan across a surface at a specific wavelength that can be targeted at specific molecules to study their binding or morphology.

The applications of PiFM are wide and span from typical material science to biomedical. Several such examples have been summarised in Table 1-6:

Application	Purpose of PiFM	Ref
Polymer solar cells	Study the effect of preparation conditions on surface morphology	94
Nanogeochemistry	Measure distribution of carbon species in nanopores of geological samples	95
Surface-enhanced Raman scattering (SERS)	Examine local near-field forces at the interface between Ag particles.	96
Protein cage development	Confirm the presence of and map protein distribution across cage structure	97
Photocatalytic hydrolysation	Measure local electric field enhancement by graphene nanopetals	98

Table 1-6: Summary of PiFM studies carried out across multiple disciples with a brief explanation of the possible application of the study and the purpose of PiFM.

1.2.3 Measuring Photoinduced Force

The best model of this interaction assumes that the AFM tip is sharp, with a single spherical atom at its apex and that there is a single atom. When this interface is illuminated with a light field E_0 is linearly polarised along the x-direction, shown in Figure 1-5

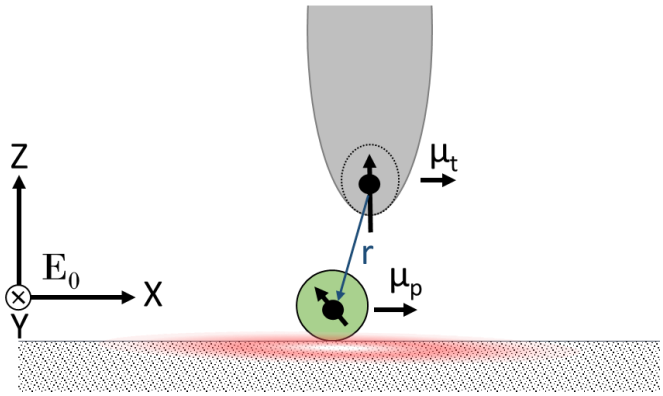

Figure 1-2 illustration of a tip-surface interface while being illuminated with a Laser with electric field E0. The distance between the surface atom and tip is shown as r and the dipole moments of the tip/surface atom are showed as μt and μp respectively.

Both the tip and the surface atom have a dipole moment denoted as μ_t and μ_p respectively. As the cantilever measures through deviations in the Z axis, only the forces along this axis are significant. The photoinduced force exerted in this situation can be expressed as[99]:

Equation 1-7 $$\langle F \rangle \propto \langle \sum_i Re\{p_i(r) \nabla E_{0i}(r)\} \rangle$$

Where $p_i(r)$ is the optically induced polarisation along the axis i (x,y,z). The $\langle F \rangle$ term can be rewritten as a combination of F_g and F_{sc} which are the gradient force and scattering force, respectively.

Equation 1-8 $$\langle F \rangle = F_g + F_{sc}$$

The gradient force is caused by differences along the axis of electric field E_{0i}. This inhomogeneity of the electric field is caused by the polarisation of the tip α_t and the particle α_p. This polarisation is a complex function made of real and imaginary components but can be illustrated in Equation 1-9.

Equation 1-9 $$\alpha_{(t,p)} = \alpha'_{(t,p)} + i\alpha''_{(t,p)}$$

The force caused by scattering is proportional to the polarisation of the tip and the electronic field along the x axis.

Equation 1-10 $$F_g \propto \frac{1}{z^4} \alpha'_p \alpha'_t |E_{0z}|^2$$

Equation 1-11 $$F_{sc} \propto \alpha''_t |E_{0x}|^2$$

F_{sc} is constant across the sample surface and has no contribution from the surface, therefore it can be discounted when measuring the surface tip interaction[100]. The gradient force, F_g depends upon the polarisation of the particle α'_p this force is a measure of degree of polarisation caused by the incident laser. Furthermore, as the gradient force is inversely

proportional to the distance between the tip and surface as shown by $\frac{1}{z^4}$. This means that the gradient force is incredibly dependent on small distances between the particle and the tip. This produces a local force which can be measured with a nanometre resolution depending on the thickness of an AFM tip[88,99,100].

1.3 Summary

This thesis aims to produce paramagnetic plasmonically active nanorods which can be used as magneto-optical sensors. These rods need to possess long term stability in water and air to be useful as diagnostics[101]. Pure metal rods such as cobalt and Iron have low stability and need complex preparation methods[102,103] to increase their longevity. While they are a promising route, this increased complexity causes them to be unideal for the industrial applications of this project. A similar issue can be observed in gold nanorods. While their plasmonic behaviour and preparation are subject to much research. Introducing magnetism to gold nanoparticles is a difficult prospect[104] and often results in rough surfaces[105,106] so could compromise their plasmonic response. Metal oxide core-shell nanoparticles have the potential to fulfil all aims of this project, allowing for a tuneable morphology, coating, and magnetism. Such particles can be prepared with simple hydrothermal methods while allowing for suitable morphological control through varying basic parameters[107]. To be optimal magneto-optic nanoprobes the metal oxide core must be paramagnetic to respond to an external magnetic field. Metal Oxide cores are promising as they can be doped and their magnetic response varied[108], which is essential for the optimisation of the process. Therefore, this project will focus on the optimisation of metal oxide nanorods for the use of magneto-optical diagnosis. The optimisation process will focus on tuning particle morphology, coatings, and magnetic response.

1.4 References

1 S. Zeng, D. Baillargeat, H.-P. Ho and K.-T. Yong, *Chem. Soc. Rev.*, 2014, **43**, 3426–52.

2 I. Rosenberger, A. Strauss, S. Dobiasch, C. Weis, S. Szanyi, L. Gil-Iceta, E. Alonso, M. González Esparza, V. Gómez-Vallejo, B. Szczupak, S. Plaza-García, S. Mirzaei, L. L. Israel, S. Bianchessi, E. Scanziani, J.-P. Lellouche, P. Knoll, J. Werner, K. Felix, L. Grenacher, T. Reese, J. Kreuter and M. Jiménez-González, *J. Control. Release*, 2015, **214**, 76–84.

3 I. Freestone, N. Meeks, M. Sax and C. Higgitt, *Gold Bull.*, 2007, **40**, 270–277.

4 A. J. Tudos and R. B. M. Schasfoort, *Introduction to Surface Plasmon Resonance*, 1968.

5 M. Fleischmann, P. J. Hendra and A. J. McQuillan, *Chem. Phys. Lett.*, 1974, **26**, 163–166.

6 Y. T. Chen, L. Pan, A. Horneber, M. Van Den Berg, P. Miao, P. Xu, P. M. Adam, A. J. Meixner and D. Zhang, *Nanophotonics*, 2019, **8**, 1533–1546.

7 A. Wei, in *Nanoparticles: Building Blocks for Nanotechnology*, 2012, pp. 1–28.

8 X. López-Lozano, H. Barron, C. Mottet and H.-C. Weissker, *Phys. Chem. Chem. Phys.*, 2014, **16**, 1820–1823.

9 M. H. Shin, W. Hong, Y. Sa, L. Chen, Y.-J. Jung, X. Wang, B. Zhao and Y. M. Jung, *Vib. Spectrosc.*, 2014, **72**, 44–49.

10 W. Lu, A. K. Singh, S. A. Khan, D. Senapati, H. Yu and P. C. Ray, *J. Am. Chem. Soc.*, 2010, **132**, 18103–18114.

11 T. Y. Jeon, D. J. Kim, S.-G. Park, S.-H. Kim and D.-H. Kim, *Nano Converg.*, 2016, **3**, 18.

12 K. H. Yea, S. Lee, J. B. Kyong, J. Choo, E. K. Lee, S. W. Joo and S. Lee, *Analyst*, 2005, **130**, 1009–1011.

13 H. Raether, *Surface Plasmons on Smooth and Rough Surfaces and on Gratings*, Springer-Verlag, Berlin Heidelberg, 1988.

14 Q. Wei and A. Wei, *Supramol. Chem. Org. Hybrid Mater.*, 2010, 319–349.

15 B. Yan, Y. Yang and Y. Wang, *J. Phys. Chem. B*, 2003, 107, 9159.

16 L. J. Sherry, S. H. Chang, G. C. Schatz, R. P. Van Duyne, B. J. Wiley and Y. Xia, *Nano Lett.*, 2005, **5**, 2034–2038.

17 P. K. Jain, K. S. Lee, I. H. El-Sayed and M. A. El-Sayed, *J. Phys. Chem. B*, 2006, **110**, 7238–7248.

18 L. Tong, Q. Wei, A. Wei and J. X. Cheng, *Photochem. Photobiol.*, 2009, 85, 21–32.

19 O. B. Knights, S. Ye, N. Ingram, S. Freear and J. R. McLaughlan, *Nanoscale Adv.*, 2019, **1**, 1472–1481.

20 F. Hao, C. L. Nehl, J. H. Hafner and P. Nordlander, *Nano Lett.*, 2007, **7**, 729–732.

21 P. F. Mens, R. J. Matelon, B. Y. M. Nour, D. M. Newman and H. D. F. H. Schallig, *Malar. J.*, 2010, **9**, 207.

22 K. G. Stamplecoskie and J. C. Scaiano, 2010, **132**, 14.

23 X. Ye, L. Jin, H. Caglayan, J. Chen, G. Xing, C. Zheng, V. Doan-Nguyen, Y. Kang, N. Engheta, C. R. Kagan and C. B. Murray, *ACS Nano*, 2012, **6**, 2804–2817.

24 M. Grzelczak, J. Pérez-Juste, P. Mulvaney and L. M. Liz-Marzán, *Chem. Soc. Rev.*, 2008, **37**,

1783–1791.

25 T. Placido, R. Comparelli, F. Giannici, P. Davide Cozzoli, G. Capitani, M. Striccoli, A. Agostiano and M. Lucia Curri, *Chem. Mater.*, 2009, **21**, 4192–4202.

26 W. Tong, M. J. Walsh, P. Mulvaney, J. Etheridge and A. M. Funston, *J. Phys. Chem. C*, 2017, **13**, 55.

27 C. J. Johnson, E. Dujardin, S. A. Davis, C. J. Murphy and S. Mann, *J. Mater. Chem.*, 2002, **12**, 1765–1770.

28 L. Feng, Z. Xuan, J. Ma, J. Chen, D. Cui, C. Su, J. Guo and Y. Zhang, *J. Exp. Nanosci.*, 2015, **10**, 258–267.

29 N. R. Jana, L. Gearheart and C. J. Murphy, *J. Phys. Chem. B*, 2001, 105, 4065–4067.

30 W. M. Park, Y. S. Huh and W. H. Hong, *Curr. Appl. Phys.*, 2009, **9**, e140–e143.

31 X. Xu, Y. Zhao, X. Xue, S. Huo, F. Chen, G. Zou and X.-J. Liang, *J. Mater. Chem. A*, 2014, **2**, 3528.

32 M. R. K. Ali, B. Snyder and M. A. El-Sayed, *Langmuir*, 2012, **28**, 9807–9815.

33 S. E. Lohse and C. J. Murphy, *Chem. Mater.*, 2013, 25, 1250–1261.

34 C. J. Ward, R. Tronndorf, A. S. Eustes, M. L. Auad and E. W. Davis, *J. Nanomater.*

35 X. Wen, C. Li and F. Meng, *J. Wuhan Univ. Technol. Mater. Sci. Ed.*, 2014, **29**, 229–232.

36 N. R. Jana, L. Gearheart and C. J. Murphy, *Chem. Commun.*, 2001, 617–618.

37 G. J. Lee, S. Il Shin, Y. C. Kim and S. G. Oh, *Mater. Chem. Phys.*, 2004, **84**, 197–204.

38 Q. Zhang and Y. Yin, *Chem. Commun.*, 2013, **49**, 215–217.

39 C. R. Rekha, V. U. Nayar and K. G. Gopchandran, *J. Sci. Adv. Mater. Devices*, 2018, **3**, 196–205.

40 A. K. Ojha, S. Forster, S. Kumar, S. Vats, S. Negi and I. Fischer, *J. Nanobiotechnology*.

41 C. Damm, D. Segets, G. Yang, B. F. Vieweg, E. Spiecker and W. Peukert, *Small*, 2011, **7**, 147–156.

42 J. Zhang, M. R. Langille and C. A. Mirkin, *Nano Lett.*, 2011, **11**, 2495–2498.

43 C. Ni, P. A. Hassan and E. W. Kaler, *Langmuir*, 2005, **21**, 3334–3337.

44 Y. Sun, B. Mayers, T. Herricks and Y. Xia, *Nano Lett.*, 2003, **3**, 955–960.

45 J. Monk, J. J. Hoyt and D. Farkas, *Phys. Rev. B - Condens. Matter Mater. Phys.*, 2008, **78**, 024112.

46 F. Dumestre, B. Chaudret, C. Amiens, M. Fromen, M. Casanove, P. Renaud and P. Zurcher, *Angew. Chemie*, 2002, **114**, 4462–4465.

47 M. Vázquez, *Magnetic Nano- and Microwires: Design, Synthesis, Properties and Applications*, 2015.

48 N. Liakakos, B. Cormary, X. Li, P. Lecante, M. Respaud, L. Maron, A. Falqui, A. Genovese, L. Vendier, S. Koïnis, B. Chaudret and K. Soulantica, *J. Am. Chem. Soc.*, 2012, **134**, 17922–17931.

49 B. Cormary, T. Li, N. Liakakos, L. Peres, P. F. Fazzini, T. Blon, M. Respaud, A. J. Kropf, B. Chaudret, J. T. Miller, E. A. Mader and K. Soulantica, *J. Am. Chem. Soc.*, 2016, **138**, 8422–8431.

50 M. Pousthomis, E. Anagnostopoulou, I. Panagiotopoulos, R. Boubekri, W. Fang, F. Ott, K. A. Atmane, J. Y. Piquemal, L. M. Lacroix and G. Viau, *Nano Res.*, 2015, **8**, 2231–2241.

51 F. Wetz, K. Soulantica, M. Respaud, A. Falqui and B. Chaudret, *Mater. Sci. Eng. C*, 2007, **27**, 1162–1166.

52 C. Li, Q. Wu, M. Yue, H. Xu, S. Palaka, K. Elkins and J. P. Liu, *AIP Adv.*, 2017, **7**, 56229.

53 H. Xu, Q. Wu, M. Yue, C. Li, H. Li and S. Palaka, *AIP Adv.*, 2018, **8**, 56422.

54 A. Viola, M. Peboscq, J. Peron, M. Giraud, L. Sicard, R. K. Ramamoorthy, B. Azeredo, S. Nowak, P. Decorse, G. Viau and J. Y. Piquemal, *Catal. Today*, 2019, **333**, 97–104.

55 A. V. Nikam, B. L. V. Prasad and A. A. Kulkarni, *CrystEngComm*, 2018, **20**, 5091–5107.

56 M. S. Chavali and M. P. Nikolova, *SN Appl. Sci.*, 2019, **1**, 1–30.

57 D. Lisjak and A. Mertelj, *Prog. Mater. Sci.*, 2018, 95, 286–328.

58 L. Shen, Y. Qiao, Y. Guo, S. Meng, G. Yang, M. Wu and J. Zhao, *Ceram. Int.*, 2014, **40**, 1519–1524.

59 J. Wan, X. Chen, Z. Wang, X. Yang and Y. Qian, *J. Cryst. Growth*, 2005, **276**, 571–576.

60 Z. X. Deng, L. Li and Y. Li, *Inorg. Chem.*, 2003, **42**, 2331–2341.

61 Y. Ding, F. Liu, Q. Jiang, B. Du and H. Sun, *J. Inorg. Organomet. Polym. Mater.*, 2013, **23**, 379–384.

62 L. Feng, L. Jiang, Z. Mai and D. Zhu, *J. Colloid Interface Sci.*, 2004, **278**, 372–375.

63 R. G. Chaudhuri and S. Paria, *Chem. Rev.*, 2011, **112**, 2373–2433.

64 F. Neville and R. Moreno-Atanasio, *Front. Chem.*, 2018, **0**, 201.

65 C. Loo, A. Lin, L. Hirsch, M. H. Lee, J. Barton, N. Halas, J. West and R. Drezek, *Technol. Cancer Res. Treat.*, 2004, **3**, 33–40.

66 X. Li and G. Yang, *Nanotechnology*, 2014, **25**, 435605.

67 J. Yang, *Noble metal-based nanocomposites: Preparation and applications*, Wiley, 2019.

68 L. E. Norena and J.-A. Wang, *Advanced Catalytic Materials - Photocatalysis and Other Current Trends*, InTech, 2016.

69 M. Rothe, Y. Zhao, G. Kewes, Z. Kochovski, W. Sigle, P. A. van Aken, C. Koch, M. Ballauff, Y. Lu and O. Benson, *Sci. Rep.*, 2019, **9**, 1–12.

70 S. Liu and M.-Y. Han, *Chem. - Asian J.*, 2009, **5**, 36–42.

71 W. Stöber, A. Fink and E. Bohn, *J. Colloid Interface Sci.*, 1968, **26**, 62–69.

72 L. M. Liz-Marzá, M. Giersig and P. Mulvaney, *Langmuir*, 1996, **12**, 4329–4335.

73 Z. Wu, Q. Zeng and H. Wang, *J. Mater. Chem. C*, 2016, **4**, 2614–2620.

74 J. Wallyn, N. Anton and T. F. Vandamme, *Pharmaceutics*, 2019, 11.

75 R. L. Rebodos and P. J. Vikesland, *Langmuir*, 2010, **26**, 16745–16753.

76 M. Faraji, Y. Yamini and M. Rezaee, *J. Iran. Chem. Soc.*, 2010, **7**, 1–37.

77 S. Larumbe, C. Gómez-Polo, J. I. Pérez-Landazábal and J. M. Pastor, *J. Phys. Condens. Matter*, 2012, **24**, 266007.

78 F. Zeb, K. Nadeem, S. K. A. Shah, M. Kamran, I. H. Gul and L. Ali, *J. Magn. Magn. Mater.*, 2017, **429**, 270–275.

79 M. Darbandi, F. Stromberg, J. Landers, N. Reckers, B. Sanyal, W. Keune and H. Wende, *J. Phys. D. Appl. Phys.*, 2012, **45**, 195001.

80 A. G. Kolhatkar, A. C. Jamison, D. Litvinov, R. C. Willson and T. R. Lee, *Int. J. Mol. Sci.*, 2013, 14, 15977–16009.

81 A. N. Emam, M. B. Mohamed, E. Girgis and K. V. Rao, *RSC Adv.*, 2015, **5**, 34696–34703.

82 Y. Li, J. Zhao, W. You, D. Cheng and W. Ni, *Nanoscale*, 2017, **9**, 3925–3933.

83 A. Gole, J. W. Stone, W. R. Gemmill, H. C. Zur Loye and C. J. Murphy, *Langmuir*, 2008, **24**, 6232–6237.

84 R. C. Gore, *Anal. Chem.*, 1954, **26**, 11–19.

85 E. Abbe, *Arch. für mikroskopische Anat.*, 1873, **9**, 413–418.

86 A. Centrone, *Annu. Rev. Anal. Chem.*, 2015, **8**, 101–126.

87 L. M. Otter, M. W. Förster, E. Belousova, P. O'Reilly, D. Nowak, S. Park, S. Clark, S. F. Foley and D. E. Jacob, *Geostand. Geoanalytical Res.*, 2021, **45**, 5–27.

88 J. Jahng, E. O. Potma and E. S. Lee, *Proc. Natl. Acad. Sci. U. S. A.*, 2019, **116**, 26359–26366.

89 Z. Chen, X. Chen, B. Qiu, G. Zhou, Z. Jia, W. Tao, Y. Li, Y. M. Yang and H. Zhu, *J. Phys. Chem. Lett.*, 2020, **11**, 3226–3233.

90 F. Wan, W. Wang, Z. Zou, H. Xie, H. Ping and Z. Fu, *J. Mater. Sci. Technol.*, 2021, **72**, 61–68.

91 T. U. Tumkur, X. Yang, B. Cerjan, N. J. Halas, P. Nordlander and I. Thomann, *Nano Lett.*, 2016, **16**, 7942–7949.

92 J. Jahng, F. T. Ladani, R. M. Khan, X. Li, E. S. Lee and E. O. Potma, *Opt. Lett.*, 2015, **40**, 5058.

93 Y. Martin and H. K. Wickramasinghe, *Appl. Phys. Lett.*, 1987, **50**, 1455–1457.

94 C. Sun, F. Pan, H. Bin, J. Zhang, L. Xue, B. Qiu, Z. Wei, Z. G. Zhang and Y. Li, *Nat. Commun.*, 2018, **9**, 1–10.

95 J. Nan, H. E. King, G. Delen, F. Meirer, B. M. Weckhuysen, Z. Guo, X. Peng and O. Plümper, *Geology*, 2021, **49**, 330–334.

96 J. Yun, H. Lee, C. Mun, J. Jahng, W. A. Morrison, D. B. Nowak, J. H. Song, D. K. Lim, T. S. Bae, H. M. Kim, N. H. Kim, S. H. Nam, J. Kim, M. K. Seo, D. H. Kim, S. G. Park and Y. D. Suh, *RSC Adv.*, 2018, **8**, 6444–6451.

97 A. S. Cristie-David, J. Chen, D. B. Nowak, A. L. Bondy, K. Sun, S. I. Park, M. M. Banaszak Holl, M. Su and E. N. G. Marsh, *J. Am. Chem. Soc.*, 2019, **141**, 9207–9216.

98 C. Xu, Z. Bo, S. Wu, Z. Wen, J. Chen, T. Luo, E. Lee, G. Xiong, R. Amal, A. T. S. Wee, J. Yan, K. Cen, T. S. Fisher and K. (Ken) Ostrikov, *Sol. Energy*, 2020, **208**, 379–387.

99 J. Jahng, D. A. Fishman, S. Park, D. B. Nowak, W. A. Morrison, H. K. Wickramasinghe and E. O. Potma, *Acc. Chem. Res.*, 2015, **48**, 2671–2679.

100 J. Jahng, J. Brocious, D. A. Fishman, F. Huang, X. Li, V. A. Tamma, H. K. Wickramasinghe and E. O. Potma, *Phys. Rev. B - Condens. Matter Mater. Phys.*, 2014, **90**, 155417.

101 A. Ramzannezhad, P. Gill and A. Bahari, *BioNanoMaterials*, 2017, 18.

102 S. Lentijo-Mozo, R. P. Tan, C. Garcia-Marcelot, T. Altantzis, P.-F. Fazzini, T. Hungria, B. Cormary, J. R. Gallagher, J. T. Miller, H. Martinez, S. Schrittwieser, J. Schotter, M. Respaud, S. Bals, G. Van Tendeloo, C. Gatel and K. Soulantica, *ACS Nano*, 2015, **9**, 2792–2804.

103 M. Ibrahim, C. Marcelot-Garcia, K. A. Atmane, E. Berrichi, L.-M. Lacroix, A. Zwick, B. Warot-Fonrose, S. Lachaize, P. Decorse, J.-Y. Piquemal and G. Viau, *J. Phys. Chem. C*, 2013, **117**, 15808–15816.

104 E. Redolfi Riva, I. Pastoriza-Santos, A. Lak, T. Pellegrino, J. Pérez-Juste and V. Mattoli, *J. Colloid Interface Sci.*, 2017, **502**, 201–209.

105 B. S. Chapman, W.-C. Wu, Q. Li, N. Holten-Andersen and J. B. Tracy, *Chem. Mater.*, 2017, **29**, 10362–10368.

106 L. León Félix, B. Sanz, V. Sebastián, T. E. Torres, M. H. Sousa, J. A. H. Coaquira, M. R. Ibarra and G. F. Goya, *Sci. Reports 2019 91*, 2019, **9**, 1–11.

107 Y. X. Gan, A. H. Jayatissa, Z. Yu, X. Chen and M. Li, *J. Nanomater.*, 2020, 2020.

108 J. Mohapatra, A. Mitra, H. Tyagi, D. Bahadur and M. Aslam, *Nanoscale*, 2015, **7**, 9174–9184.

Chapter 2 Growth and Morphological Control of Iron Oxide Magnetic Nanoparticles

2.1 Introduction

With potential applications in analytical chemistry, catalysis, magnetic resonance imaging, and nanomedicine, the synthesis of magnetic nanoparticles and identifying strategies to control their size and morphologies have been the subject of a great deal of fundamental research[1–4] . Magnetic properties facilitate both physical manipulation of particles as well as the ability to selectively heat them by magnetic hysteresis energy loss. However, the physical properties of the nanoparticles such as size, shape, and degree of crystallinity are important parameters that need to be optimized in many potential applications. To influence these properties additional "structure-directing" components are often added to the synthesis procedure. Understanding the role of such additives is important if nanoparticles with improved aspect ratios and crystallinity are to be achieved. In many cases, very different additives result in similar particle growth, but it is not clear whether the mechanisms by which they control growth are similar.

The precipitation of paramagnetic hematite nanorods from ferric chloride solutions is a case in point, two contrasting structure-directing additives, phosphate [5] and 1,2 propanediamine [6], lead to hematite "nanorods" as the final product but since the 1,2 propanediamine - directed rods achieve higher crystallinities and larger aspect ratios, the two processes may involve different mechanisms. There has been considerable discussion of the mechanisms involved[7–10], but the picture is complicated by the range of conditions under which nanorod synthesis is performed, phosphate-directed nanorods have been synthesized at temperatures ranging from ~100 °C[11] to 210 °C [7]for example whilst the $FeCl_3$:PO_4− ratio ranges from 6:1 to 40:1. This diverse system can also be further tuned with the addition of redox steps to form more magnetic magnetite and maghemite.

Studying the formation mechanism of such nanoparticles is also hindered by the difficulty of identifying individual components and phases at the nanoscale; transmission electron microscopy (TEM) is extremely informative but is only effective in areas of good structural order leading to the potential to neglect amorphous regions.

This study aims to explore some of the factors that influence the synthesis of hematite nanorods, the concentration of phosphate ions, and to compare results using two different

structural promoters. A variety of bulk and surface analysis techniques were used to assess the growth effects of the different structural promoters.

2.1.1 Phosphate Hematite Growth

Hematite nanorice were prepared by precipitation from 50 mL of 40 mM iron(III) chloride solution ($FeCl_3$) with 10 ml of potassium dihydrogen phosphate (H_2KPO_4) varying concentration from 0 to 70 mM with an additional 40 mL of deionised water before being sealed and heated in an oil bath for up to 72 hours at 110 ^oC Following this, the hematite particles are carefully washed in a centrifuge using ethanol and water to remove impurities and narrow particle size distribution through separating smaller particles into the supernatant.

2.1.2 Magnetite and Maghemite Preparation

Magnetite and maghemite rods were prepared by freeze-drying hematite solution and placing the resulting solid in a furnace. To form magnetite, the solid was left for 6 hours at 350 ^oC while being exposed to $H_2(g)$. The resulting dark brown solid is then placed in the furnace for a further 1 hour at 280 ^oC in air to form maghemite.

2.1.3 Reactant Flow Control Study

Two syringe pump injectors were filled with 10 mL of $FeCl_3$ and H_2KPO_4 and injected into a 50 mL round bottom flask fitted with a bung and a gas balloon, see Figure 2-1. The solution was injected at a rate of 0.397 mL per hour until all the solutions had been introduced. The solution was then left for 48 hours at 100 ^oC. The experiment aimed to control the phosphate concentration during the reaction and ensure a constant supply.

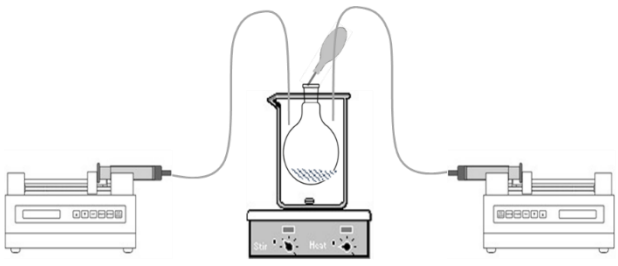

Figure 2-1: illustration of flow control experiment. Each syringe contains 10 mL of either $FeCl_3$ or H_2KPO_4 injected at a rate of 0.4 mL per hour.

2.1.3 1,2 Propanediamine Hematite

7 mL of 0.86 M $FeCl_3$ were added to a glass pressure reactor and stirred in an ice bath. 7 mL of 1,2 propanediamine was added slowly to the flask and allowed to stir in the ice bath for

15 minutes. The flask was then sealed and heated at 180 °C for 16 hours. After cooling, the nanoparticles were separated by centrifugation and washed thoroughly with ethanol and water before freeze-drying.

2.1.3 Characterisation

Magnetite and maghemite particles were analysed with a combination of XPS and magnetic measurements, with electron microscopy used to confirm their morphology.

For mechanistic studies of the growth of the nanoparticles using XRD, XAFS and Raman, the nanorods were extracted from solution by centrifugation and deposited on silica surfaces without further washing. For XPS, TEM and PiFM, the nanoparticles were isolated with a series of washing/ centrifugation steps and vacuum dried. TEM Samples were supported on copper support grids and analysed on a JEOL JEM-2100.

For XPS the dried nanorods were pressed onto conductive tape and analysed with a Kratos Axis Ultra-DLD photoelectron spectrometer with a monochromatic al. Kα x-ray source in the "hybrid spectroscopy" mode. The analysis area was approximately 700 × 300 µm. A pass-energy of 40 eV was used for high-resolution scans and 60 eV for survey scans. CasaXPS [12]was used to analyse the spectra. Binding energies are referenced to the largest C(1 s) peak at 284.7 eV with an uncertainty of ~ 0.2 eV. Since intensities for powder samples are dependent on the surface area analysed, which can be poorly reproducible between different powder samples, XP spectra in the figures are normalized to the point of maximum intensity.

Powder X-ray diffraction (XRD) was performed using a PANalytical X'Pert Pro diffractometer with a monochromatic Cu Kα source (λ = 0.154 nm) operated at 40 kV and 40 mA. The scans were recorded over the 2θ 10–80°

Magnetic susceptibility measurements were taken using a Gouy balance on all samples following washing and drying.

X-ray absorption spectroscopy (XAS) measurements were performed on beamline B18 at Diamond Light Source[13]. Calibration of the monochromator was conducted using an iron metal foil before the measurements. Pellets of the different samples were collected in transmission mode at the Fe K-edge (7111 eV) simultaneously with the foil. The data was analysed using the Athena software[14].

For the measurements with PiFM, the washed nanoparticles were deposited onto a mica sheet and allowed to dry before submitting for analysis. The measurements were made in the Molecular Vista laboratories by Dr. O'Reilly.

2.2 Results

2.2.1 Morphological Tuning

The nanorods generated using the two different structure-directing molecules: phosphate and 1,2 propanediamine, were examined with a range of techniques and are discussed below. The results are classified in terms of shape and crystallography and subsequently, their spectroscopic properties.

2.2.2 Shape and Crystallography

2.2.3 Transmission Electron Microscopy (TEM)

2.2.2.1.1 Phosphate Directed Nanorods

TEM images of the phosphate directed nanorods synthesised at a phosphate concentration of 4 mmol are shown in Figure 2-2. The ellipsoid shape and uneven surface of the nanorods is visible in (a) and a relatively well-defined mean aspect ratio (length/width) of 5.91 was calculated from a sample of ~ 200 particles, (b). A higher magnification TEM micrograph of a particle in (c) shows few signs of long-range structure with only occasional examples in the TEM images of distinct lattice fringes. We were unable to determine any direction of growth along any crystal planes. Where lattice fringing was identified, fast Fourier transform (FFT) indicates two d spacings at 0.27 nm, consistent with the [104] plane of hematite and in agreement with the most intense peak of the XRD spectrum, and 0.376 nm, consistent with the hematite [012] plane.

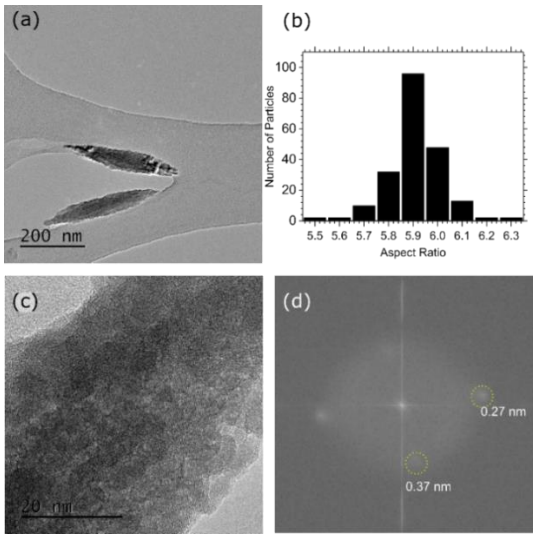

Figure 2-2: (a) TEM micrographs of hematite nanorods Distribution of aspect ratios amongst ~ 200 hematite nanorods synthesised in the presence of 4 mM phosphate capping agent at 110 °C; (b) & (c) TEM micrographs of hematite nanorods with lattice fringing indicated and the crystal plane identified and (d) the fast Fourier transform of the lattice fringe showing the d-spacing of the hematite nanorod sample.

2.2.3 Effect of Phosphate Concentration on Aspect Ratio

Previous work by Ma et al. [8] has shown that different quantities of the phosphate directing agent affect the final morphologies of the nanoparticles, however, their study did not include a detailed determination of the extent to which the aspect ratio could be controlled.

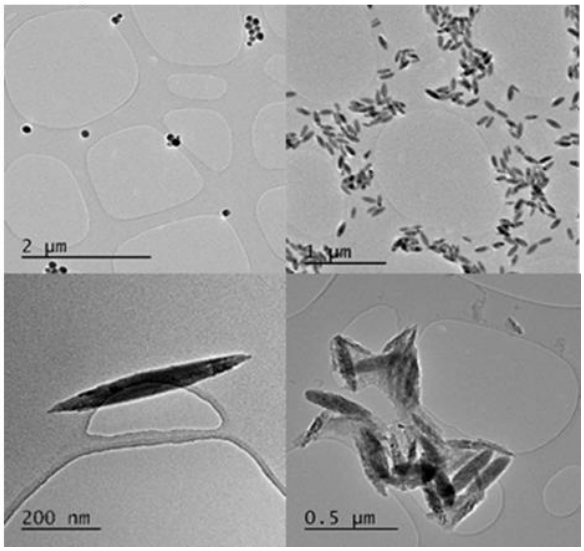

Figure 2-3 . TEM micrographs taken at 0, 3, 5.75 and 6 mM phosphate concentrations.

Using sodium or potassium phosphate concentrations between 0 and 8 mM, Figure 2-4 and Figure 2-3 shows an elongation of the nanoparticles as the phosphate concentration is increased until ~6 mmol. This can be accounted for by the increased extent of adsorption of

phosphates upon the growth axis. However, above a concentration of ~5.75 mM there is a sharp inflection point and morphological control are lost. From this point onwards, particles tend towards a spherical morphology.

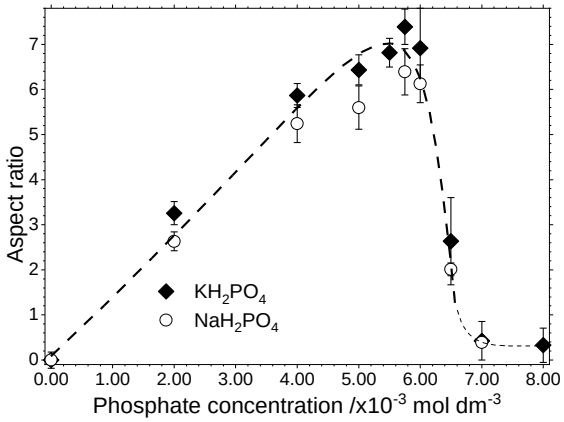

Figure 2-4: Graph of hematite nanoparticle aspect ratio as a function of potassium (or sodium) phosphate concentration. The figure demonstrates that the difference between the two cations is only just outside experimental error and the concentration limits of the approach are very similar. The dotted line is drawn to guide the eye. Errors were calculated from repeated measurements of ~ 100 nanoparticles for each point.

2.2.3 1,2 Propanediamine Promoted Nanorod Growth.

Figure 2-5(a) and (d) show the morphology of hematite nanoparticles obtained using 1,2 propanediamine as a structural promoter at 140 and 180 °C, respectively. At the lower temperature, the nanoparticles are generally spherical in shape but do show the beginnings of growth of rods perpendicular to the particle surface.

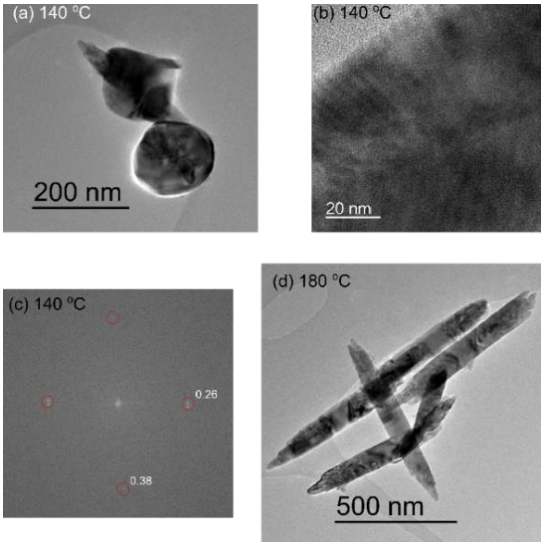

Figure 2-5: TEM of hematite nanoparticles synthesised at two different temperatures in the presence of 1,2 propanediamine as a structure-directing additive. (a) nanoparticles synthesised at 140 °C; (b) higher magnification of the 140 °C particles. Lattice fringes are

evident suggesting good crystallinity; (c) FFT analysis of the 140 °C particle; (d) nanoparticles synthesised at 180 °C showing the development of nanorods with aspect ratios much larger than those obtained from the phosphate directing agents.

At higher temperatures, the proportion of spherical nanoparticle intermediates decreases, and are replaced by more rod-like particles until, at 180 °C, the intermediate spherical type particles are absent. A median aspect ratio of 9.25 was measured for the nanorods at this temperature. Figure 2-5(a) shows 2 nanoparticles at different levels of growth at 140 °C, one with the hematite apexes protruding from the centre and another without any clear protruding crystals. However, within the body of the sphere lattice, fringes corresponding to hematite can already be seen. Figure 2-5Figure 2-5: TEM of hematite nanoparticles synthesised at two different temperatures in the presence of 1,2 propanediamine as a structure-directing additive. (a) nanoparticles synthesised at 140 °C; (b) higher magnification of the 140 °C particles. Lattice fringes are evident suggesting good crystallinity; (c) FFT analysis of the 140 °C particle; (d) nanoparticles synthesised at 180 °C showing the development of nanorods with aspect ratios much larger than those obtained from the phosphate directing agents.

(b) shows a magnified image of one of the crystal 'arms' and (c) shows the FTT of this image. Within the FFT there are 2 main maxima which, like the phosphate directed growth, corresponding to the hematite [104] and [012] planes. The nanorods generated at 180 °C show higher crystallinity than the equivalent rods produced by the phosphate directing agent. The effect of the temperature of ageing is shown in Figure 2-6, at 140 °C, the majority of particles are similar to those imaged in Figure 2-5Figure 2-5: TEM of hematite nanoparticles synthesised at two different temperatures in the presence of 1,2 propanediamine as a structure-directing additive. (a) nanoparticles synthesised at 140 °C; (b) higher magnification of the 140 °C particles. Lattice fringes are evident suggesting good crystallinity; (c) FFT analysis of the 140 °C particle; (d) nanoparticles synthesised at 180 °C showing the development of nanorods with aspect ratios much larger than those obtained from the phosphate directing agents.

(a) with only limited anisotropy. By 160 °C, the population of spherical type particles has reduced and a substantial number of rod-like particles has developed with a median aspect

ratio of ~8. Preparation at 180 °C gives almost exclusively nanorods with aspect ratios close to 9.25.

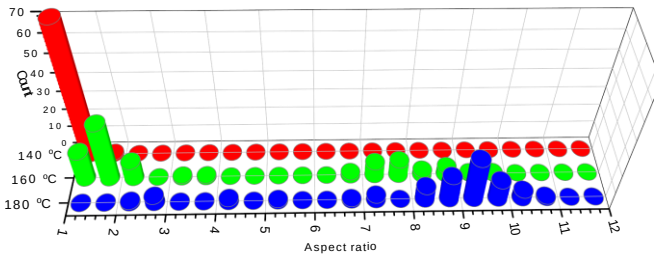

Figure 2-6: Variation of the nanorod aspect ratio as a function of ageing temperature in the presence of 1,2 propanediamine as a structure-directing agent. Data was collected from ~ 75 nanorods in each sample.

2.2.3 Powder XRD

The development of the nanorods synthesised under a range of conditions for both directing agents was studied by powder XRD, Figure 2-7. The characteristic hematite [012] and [104] reflections that were also found in the FFT from the TEM images, together with the [110] reflection, are evident in all the samples but most clearly in the phosphate and 1,2 propanediamine directed rods synthesised under standard conditions and aged for 8 hours or more: Figure 2-7,(a), (b), (f) & (g). For the phosphate directed rods, the quality of the hematite pattern degrades as the ageing time is shortened to the extent that the rods aged for only one hour have an extensive broadening of the [110] and [104] hematite reflections and strong evidence for the presence of akaganéite[15]. The rods developed in the absence of any directing agent but allowed to age for 16 hours give an XRD pattern indicating that akaganéite is the dominant state, Figure 2-7(e). At the other end of the scale, in the presence of 8 mM of phosphate, the XRD patterns show no evidence for akaganéite with hematite the only structure present. This is despite the TEM images showing no well-defined particles.

For the diaminopropane directed rods, reducing the ageing time also degrades the hematite pattern but even at 1 hour of ageing, the hematite structure is more distinct than is the case with the phosphate. The rods aged at 160 °C however, show additional peaks characteristic of the [110], [130] and [221] lines of α-FeOOH (goethite)[16].

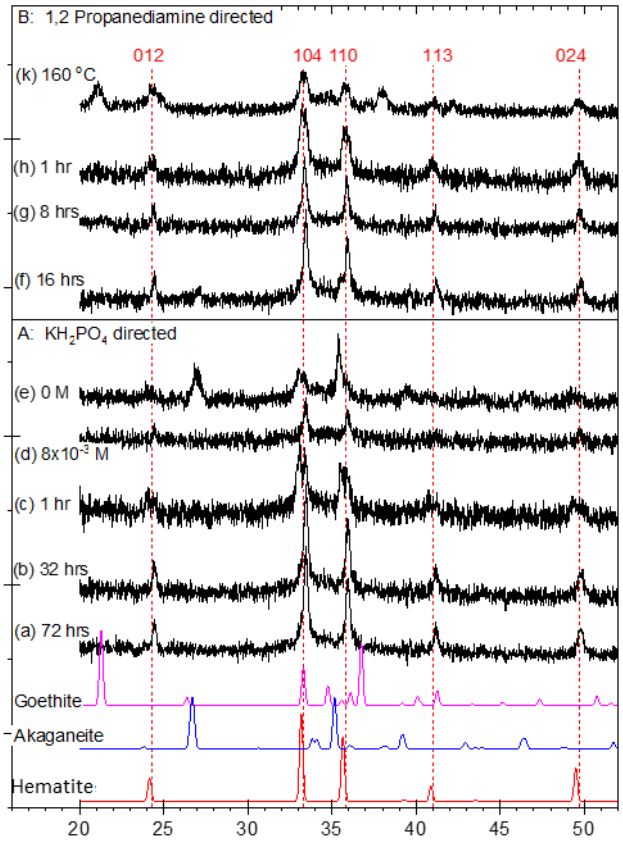

Figure 2-7: A comparison of XRD patterns from nanorods synthesised using the two structure directors with three standard materials from the ICSD library[15–17]. Phosphate directed rod, prepared at 100 °C: (a)-(c) prepared with 5.75×10-3 M phosphate solution and aged for (a) 72 hours; (b) 32 hours; (c) (1hour); (d) prepared with 8.00×10-3 M phosphate solution and aged for 72 hours; (e) prepared in the absence of phosphate ions, aged for 72 hours.
B. 1,2 propanediamine directed nanorods (f) aged for 16 hours at 180 °C; (g) aged for 8 hours at 180 °C; (h) aged for 1 hour at 180 °C; (k) aged for 24 hours at 160 °C.

2.2.4 Spectroscopy

2.2.3 Raman

Raman spectra of the hematite nanorods prepared using the two different structure-directing agents are shown in Figure 2-8. The spectrum for the 1,2 propanediamine promoted nanorods show a better signal to noise ratio than the phosphate directed rods, but this is probably related to the slightly higher concentration of rods in the sample. Both samples show four distinct peaks at ~220 cm^{-1}, ~300 cm^{-1}, ~410 cm^{-1} and ~ 500 cm^{-1} which match well with the phonon modes reported by Jubb and Allen for hematite at 229 cm^{-1} (A_{1g}), 295 cm^{-1} & 302 cm^{-1} (E_g), 414 cm^{-1} (E_g), and 500 cm^{-1} (A_{1g}). None of the peaks that identify maghemite (365 cm^{-1} (T_{2g}), 511 cm^{-1} (E_g), 700 cm^{-1} (A_{1g})) or magnetite (310 cm^{-1} (T_{2g}), 554 cm^{-1} (T_{2g}), 672 cm^{-1} (A_{1g})) are present.

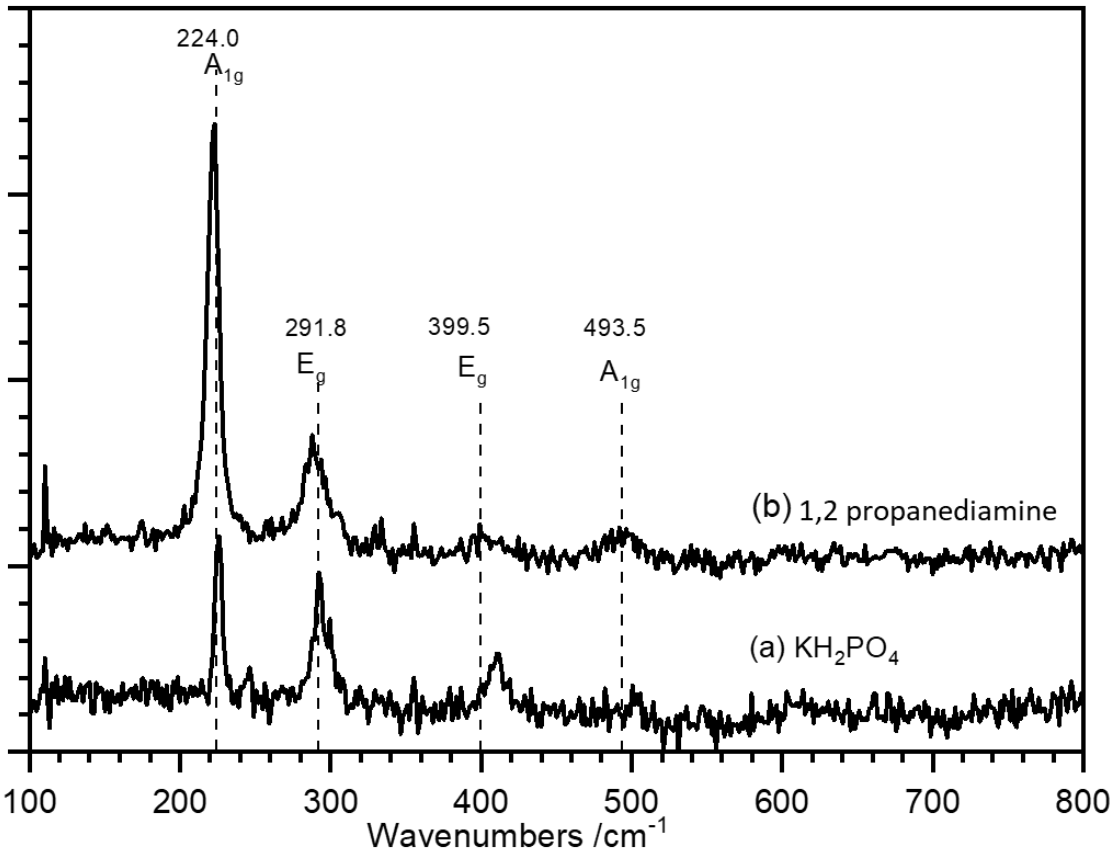

Figure 2-8: Raman spectra of hematite nanoparticles. (a) prepared at 100°C with 5.75×10-3 M phosphate solution present and aged for 72 hours; (b) 1,2 propanediamine directed nanorods prepared at 180 °C and aged for 16 hours.

It is also noticeable that the often-reported peak[18] at 660 cm^{-1} is not present in the spectra of either of the samples. This peak has been assigned to the longitudinal optical (LO) E_u mode of haematite, which is IR active but expected to be Raman forbidden. Its presence in Raman spectra of hematite has been attributed to the presence of significant disorder within the lattice and its absence here points to well-ordered crystalline structures[19]. The degree of crystallinity can also be inferred from the well-resolved peaks and relatively flat baseline suggesting the particles are predominantly crystalline although with some amorphous areas.

2.2.3 X-ray Photoelectron Spectroscopy (XPS)

The Fe(2p) region of the XP spectrum is known to discriminate between different iron oxides and hydroxides. In the present case, both the phosphate and 1,2 propanediamine directed rods show the Fe($2p_{3/2}$) peak at 710.7 eV, which matches literature values[20] and a reference

sample of haematite, Figure 2-9. The value of 710.7 eV is approximately 0.5 eV lower than expected for an iron hydroxide and the assignment to hematite is confirmed by the clear satellite feature at 718.6 eV which is characteristic of hematite rather than the hydroxide.

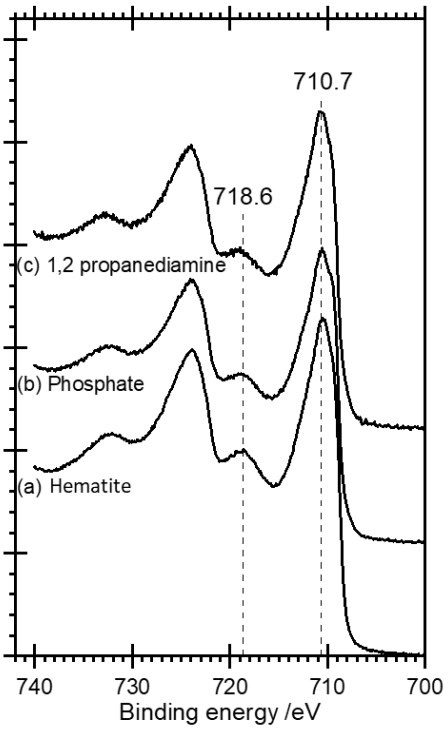

Figure 2-9: XPS: a comparison of the Fe(2p) region of the phosphate and 1,2 propanediamine directed nanorods with a hematite standard. (a) Hematite standard; (b) phosphate directed nanorods; (c) 1,2 propanediamine directed rods. To allow for the different sample sizes peaks are normalised in total area and a constant linear background subtracted from each.

2.2.3 X-ray Absorption Spectroscopic Studies (XAS)

XAS measurements were recorded of the nanoparticles at different stages of synthesis and with varying concentrations of structure-directing agents. Without the requirement for long-range order, XAS provides very complementary information on the iron coordination environment to XRD. Despite the very different conditions of each sample, the changes in the XAS are quite subtle, Figure 2-10. The clearest differences are evident in the XANES region, Figure 2-10A, where the spectrum of the phosphate directed sample that had been aged for just one hour is characteristic of akagneite[21] whereas the phosphate directed samples aged for 24 hours or longer show peak shapes characteristic of haematite[22]. These differences are also reflected in the Fe K-edge EXAFS Fourier transforms (FTs), Figure 2-10B, notably in the distances and relative intensities of the peaks associated with the Fe-O and Fe-Fe coordination. It is also clear from Figure 2-10A, that a reduction in the concentration of phosphate reduces the hematite character of the samples and increases the akaganéite

character, Figure 2-10B(d). The 1,2 propanediamine directed sample, which was synthesised at 180 °C, very closely matches the hematite spectrum and shows no evidence for ferric hydroxides.

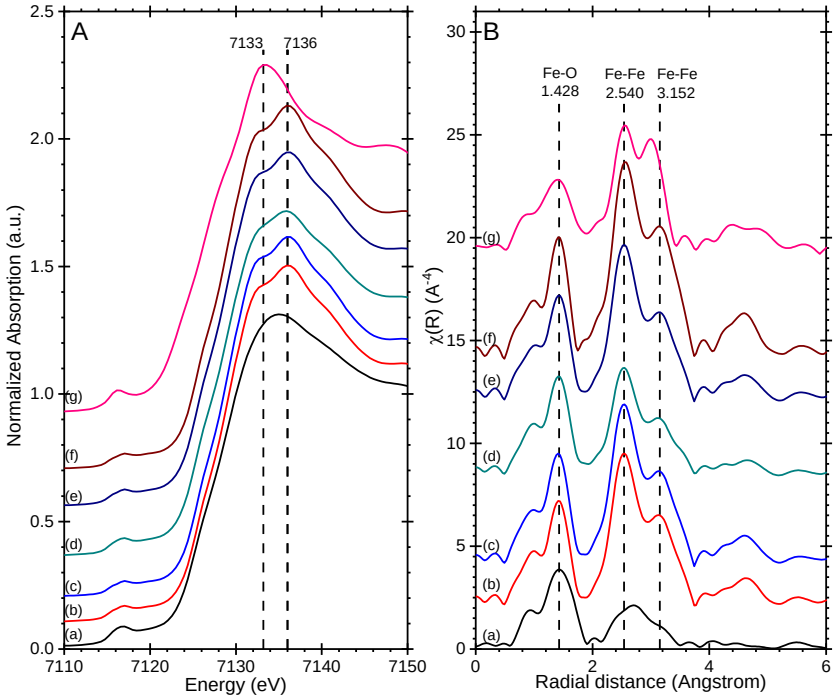

Figure 2-10: XAFS spectra of hematite samples obtained under a range of conditions: A: Normalized XANES spectra measured at the Fe K-edge. B: EXAFS Fourier transforms of k3χ(k). (a) 6×10-3 M phosphate directing agent aged for 1 hour; (b) as (a) but aged for 24 hours; (c) as (a) aged for 72 hours; (d) no phosphate directing agent, aged 24 hours; (e) 8×10-3 M phosphate directing agent aged for 24 hours; (f) 1,2 propanediamine directing agent aged for 16 hours; (g) phosphate directed nanorods reduced in H2/N2 at 200 °C to form magnetite rods.

2.2.3 Photo-induced Force Microscopy (PiFM)

PiFM combines atomic force microscopy and vibrational spectroscopy in a single instrument, providing simultaneous topography and chemical signatures at the nanometre scale[23]. In the present study, this technique allowed us to explore the distribution of specific species over the nanoparticles. The topography of four rods from different synthesis conditions are shown in Figure 2-11. Red crosses on the images show points at which the vibrational spectra are in Figure 2-12. were acquired whilst the images in Figure show intensity maps at specific wavenumbers, the intensity of the colour reflecting the strength of the specified frequency.

The background spectrum in Figure 2-12 (i), was recorded at the point shown in Figure 2-11, some distance from any nanoparticle. It is dominated by an intense peak at 1020 cm ^{1}, a

peak that also occurs, albeit at a weaker level, in all the other spectra. There is no matching peak in the IR spectra of haematite, akaganéite or goethite and mapping of 1020 cm^{-1} intensity across the samples shows maximum intensity on the mica surface rather than the nanoparticles, Figure 2-11 (b) & (e). We cannot identify this peak but assume it originates from the synthesis solution.

The spectra. (ii) & (iii) were recorded from the middle and apex positions on a growing 1,2 propanediamine directed rod, Figure 2-11 (a). A strong peak at 920 cm^{-1} in (ii) was mapped across the whole sample Figure 2-11Figure (c) and is present mainly around the central spherical part of the developing rod. Ruan et al. assigned a peak at 920 cm^{-1} to the OH deformation mode of goethite. In both (ii) & (iii) a medium intensity peak is also present at 1105 cm^{-1} which is only seen in the presence of the diamino, this can be assigned to the C-N stretch which in free 1,2 propanediamine occurs at ~ 1070 cm^{-1} but is perhaps shifted to higher frequencies by coordination to the nanoparticle surface. In the free molecule, a strong band is also expected at 1460 cm^{-1} due to the NH_2 deformation mode; its absence in the spectra of the nanoparticle suggests a strong interaction between the amine groups and the developing nanoparticle.

A peak at 1665 cm^{-1} could be characteristic of phosphate. This is not detected at point (v) on the sample synthesised under low phosphate concentration conditions but the intensity map of its distribution, Figure 2-11(h), shows it is present around the rim of the nanoparticle. On the particle synthesised in higher phosphate concentrations, Figure 2-11(m), the phosphate band is present over most of the surface although there is some evidence for higher intensities at the end of the nanoparticle.

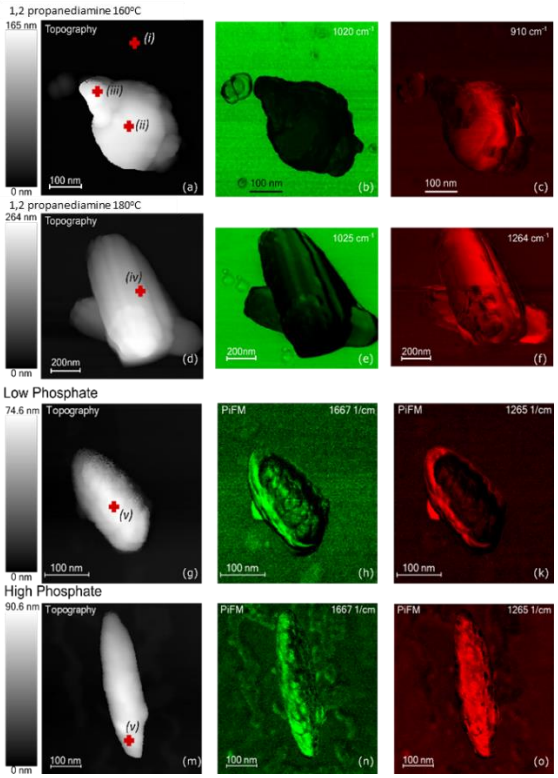

Figure 2-11: Topography (left-hand side) and PiFM intensity maps of three nanoparticles synthesised under different conditions. The frequencies at which the intensity maps were recorded are indicated on the images. (a)–(c) A 1,2 propanediamine directed particle was synthesised at 140 °C and therefore still in the process of forming the anisotropic rods. (d)-(f) Two 1,2 propanediamine directed particles were synthesised at 180 °C. (g), (h) & (k) a particle synthesised in the presence of $5x10^{-3}$ M phosphate solution and aged for 16 hours. (m), (n) & (o) A particle synthesised in the presence of $6x10^{-3}$ M phosphate solution and aged for 16 hours. The spectra in Figure 2-12 were recorded at the points indicated by crosses on the topographic image.

A medium strength peak at ~1265 cm^{-1} is present on both the diamino and phosphate directed rods but does not correspond to any previously reported band for mica, hematite, goethite or akaganéite[24–26]. The peak is at least 100 cm^{-1} too high in frequency to be assigned to either an adsorbed phosphate or the diaminopropane. A mapping of the 1265 cm^{-1} intensity distribution in Figure 2-11 (f),(k) & (o), confirms that the peak is not associated with the mica surface but is concentrated in selected areas of the nanoparticles. A possible assignment is to a carbonate generated by reaction of carbon dioxide with the iron hydroxide surface as suggested by Persson et al. [27] and this suggests an alternative assignment of the 1667 cm^{-1} peak to the asymmetric C-O stretch of adsorbed carbonate. Further investigation is needed, but the correspondence of carbonate with the rim of the particles (Figure 2-11 h, k, n & o) where one might expect growth to occur is suggestive of a marker for areas of iron hydroxide on the nanoparticles.

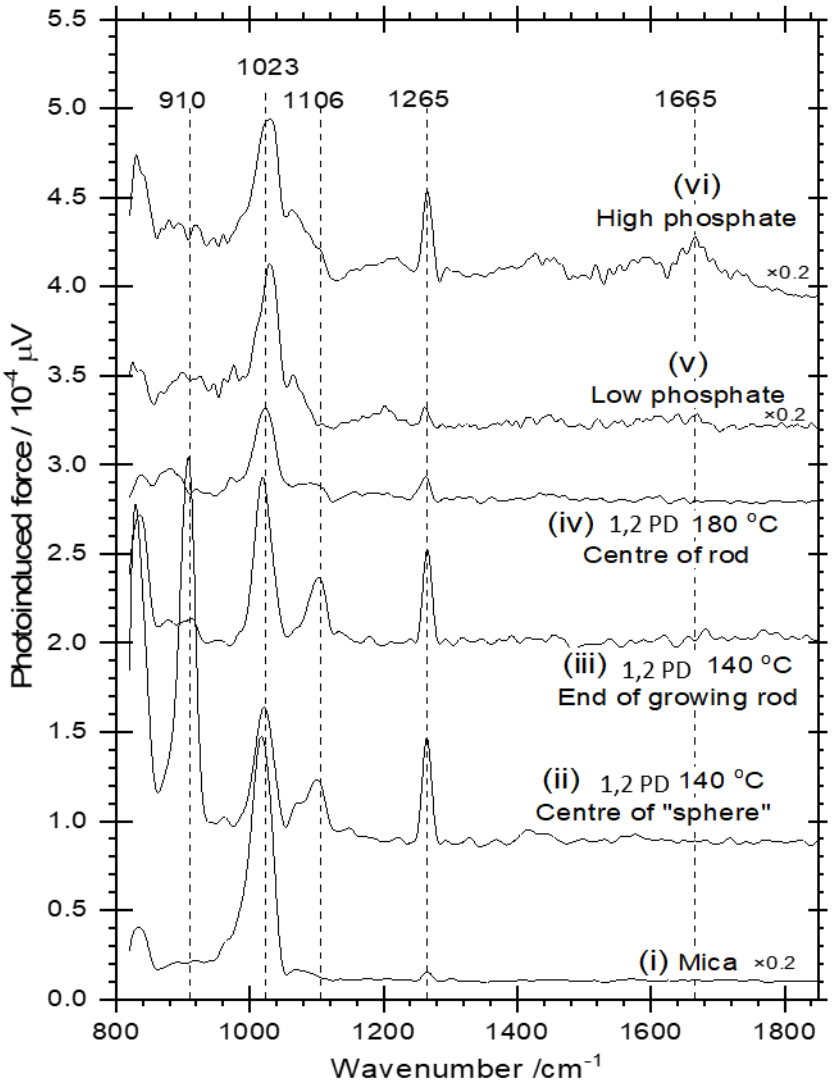

Figure 2-12: Vibrational spectra recorded using PiFM at the points indicated in the images in Figure 2-11. 1,2 PD indicates - 1,2 propanediamine.

Of most interest to this study is the strong peak at 910 cm−1 in (ii) assigned unambiguously to the OH deformation mode of goethite[24,28]; mapping of this peak's intensity across the whole sample (Figure 2-11(c)) shows that the goethite is present mainly around the central spherical part of the developing particle and interestingly, completely absent from the apex.

In the phosphate-directed rods, a new feature is observed near 1667 cm^{-1} and mapping the intensity of this peak across the two different nanorods (Figure 2-11 e, g) shows it to be most intense around the edges of the particle growing at low phosphate concentrations but concentrated at the ends of the nanorods grown under higher phosphate concentrations. The peak can be assigned to akaganéite[28–30], and its intensity map is interesting. On the particle synthesized under low phosphate conditions, where the aspect ratio of the rods is expected

to be low, akaganéite has a high concentration around the edge of the rod, but, as Figure 2-12(iv) shows, is virtually undetectable in the middle of the rod. Under higher phosphate concentrations, where much better aspect ratios are expected, the akaganéite is present at the apex of the rods. This is consistent with Frandsen et al. [31]. model of the development of the hematite rods in which growth occurs through the precipitation of hydroxide followed by conversion into hematite.

2.3 Flow Study

To attempt and exert more control over the ratio of $FeCl_3$:PO_4 over the full period of the reaction the addition of the two reactants was controlled with timed injections over an extended period. This would maintain a consistent phosphate concentration following the initial formation and aggregation of subunits. By doing so once the initial growth stages were complete, extra subunits could be formed and aggregate onto the already full-sized rods; the aim being to generate larger aspect ratios.

When controlling the flow rate of the reaction several issues are faced. Phosphate directed growth of hematite nanorods is carried out in a sealed glass reaction vessel at 100 ^{o}C, the resulting pressure of this reaction makes it difficult to set up and monitor a flow control experiment and a pressure balloon was required to fully prepare samples.

In most cases, no nanosized product was produced with TEM samples showing no evidence for the presence of any significant hematite structures. When injecting into a 5 mL hematite growth solution over a period of 48 hours, large rod-like structures were obtained on the cm-mm range, and the XRD patterns clearly show the presence of hematite (Figure 2-13)with four distinct peaks at ~220 cm^{-1}, ~300 cm^{-1}, ~410 cm^{-1} and ~ 500 cm^{-1} which match well with the phonon modes reported by Jubb and Allen for hematite at 229 cm^{-1} (A_{1g}), 295 cm^{-1} & 302 cm^{-1} (E_g), 414 cm^{-1} (E_g), and 500 cm^{-1} (A_{1g}).

While this experiment was unsuccessful in developing nanorods with larger aspect ratios, it did produce larger hematite particles. The degree of increase in size was significantly larger than expected. However, this result does suggest that the slow addition of additional iron precursor and phosphate will aid in the growth of the hematite structures.

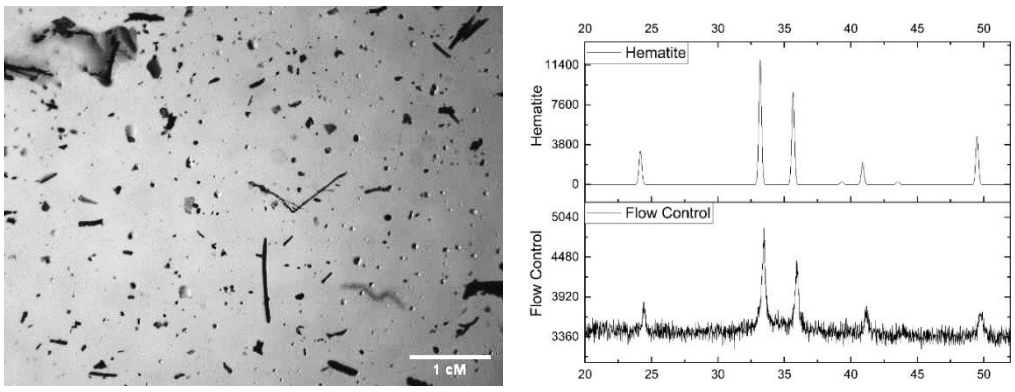

Figure 2-13. Microscope image of hematite structures formed by flow control. Phosphate flow controlled hematite formed at 100 ^{o}C compared to an ISCD hematite reference[15].

While these particles are anisotropic in nature, their size makes them unusable for industry as nanoparticles are needed. In addition, the preparation method was unreliable, often resulting in no consistent morphology across the product. This fact when coupled with the wide particle distribution makes the process unusable in this project for other applications and research in this area was not followed up.

2.4 Magnetite and Maghemite Nanoparticles

Magnetite and maghemite and hematite nanoparticles were successfully prepared through a process of reduction and oxidation steps performed on hematite rods formed by the phosphate method described above.

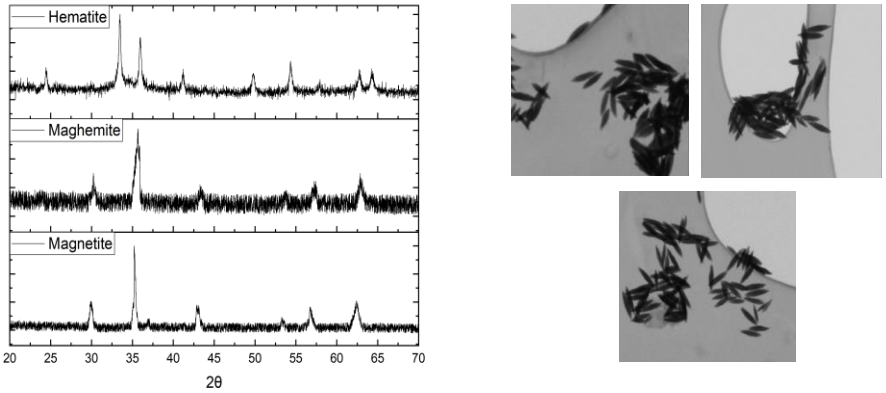

Figure 2-14:(Left) XRD spectra of hematite, magnetite and maghemite. (Right) SEM images of hematite, magnetite and maghemite

The particles were analysed with XRD, XPS and their magnetic susceptibility measured. During the redox process, the rod morphology of the particles was affected by the crystallographic rearrangements resulting in more spherical particles. When particles are soaked in phosphate solutions for several hours before freeze-drying, greater morphological stability was exhibited. Representative SEM images were obtained of all particles formed as their magnetic strength was too high for safe analysis within a TEM. Average aspect ratios showed only a small variation from that of the precursor hematite batch, with a typical loss of 0.3 in aspect ratio across the whole redox process. XRD and XPS of the particles confirm the formation of magnetite and maghemite, Figure 2-16 & Figure 2-17. The absence of the typical [110] hematite peak in the magnetite and maghemite particles suggests that they have been successfully formed.

However, differentiating between magnetite and maghemite can be more challenging since both show a [311] peak at approximately 35.4° accompanied with the [220], [400], [422],[511] and [440] planes of the cubic cell at 2θ of 30.0, 43,53.5, 57.0 and 62.5°, respectively.

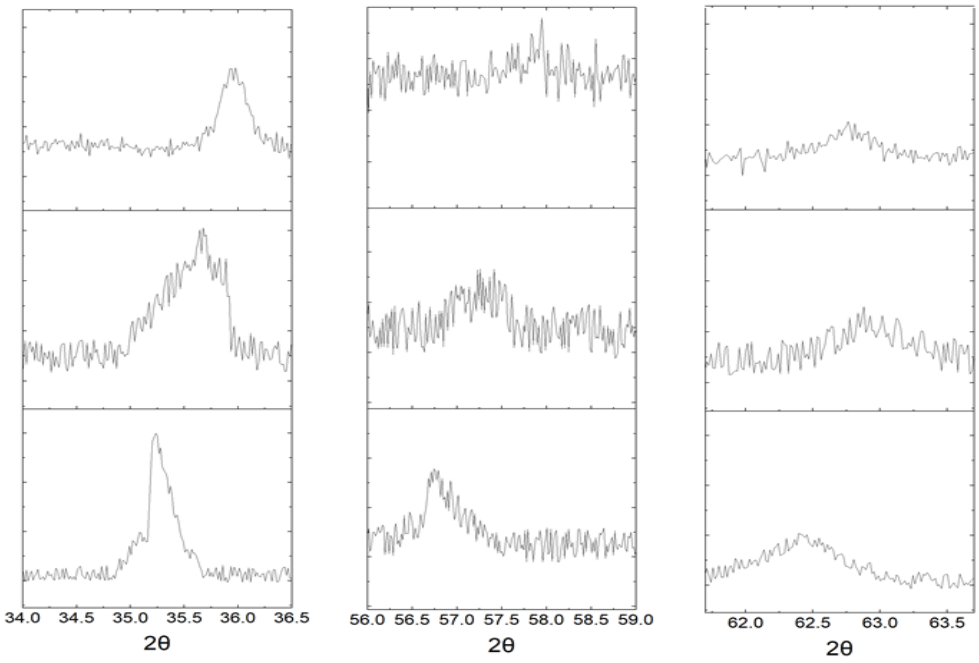

Figure 2-15: Sections of the XRD patterns, highlighting peaks from the [400], [511] and [440] crystal planes. Hematite (top), maghemite (middle), magnetite (bottom)

Close inspection of Figure 2-15 reveals that there is a shift in the diffraction angle as the redox process takes place. This shift has previously been identified in literature[32] and often shows approximately an increase of 0.2° between magnetite and maghemite. These shifts can be seen in the [400], [511] and [440].

This change in the crystal structure of the particles could be due to the smaller ionic radii of Fe^{3+} compared to that of Fe^{2+}. As magnetite is oxidised to form maghemite more Fe^{3+} content is formed resulting in holes in the lattice and hence causes a shift in the 2θ Pattern. This effect is seen further still in that of hematite which contains the largest proportion of Fe^{3+} ions so has the highest 2θ angles for its crystal lattices.

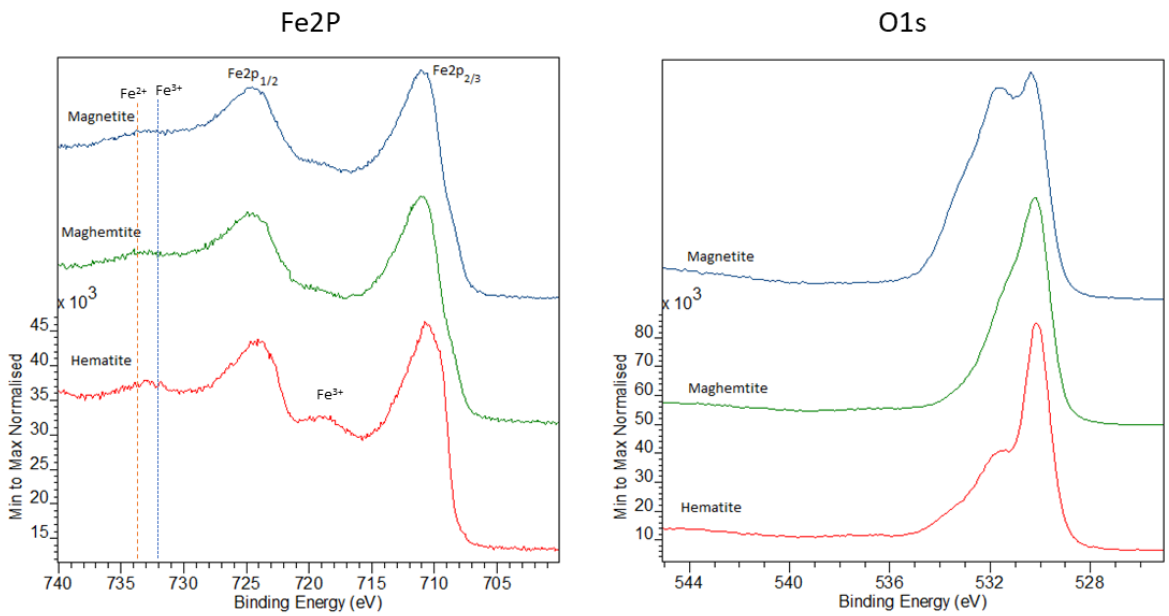

Figure 2-16: XP spectra of Hematite, Magnetite and Maghemite particles. (Left) Fe(2P) region (Right) O(1s) region.

XP spectra in Figure 2-16 show similar peaks across all particles. The Fe(2p) Region shows three important regions Fe^{3+} satellite, Fe($2P_{1/2}$) and Fe($2P_{2/3}$) at 718.6, 724.2 and 710.7 eV respectively. The Fe($2P_{1/2}$) and Fe($2P_{2/3}$) peaks are not significantly shifted between these three iron oxides and so the Fe^{3+} satellite is of particular importance. This is because maghemite and magnetite both possess the Fe^{2+} satellite approximately 2 eV upfield of the Fe^{3+} satellite, and when the Fe^{3+} and Fe^{2+} satellites combine, the resulting peak broadening can lead to the peak being lost to noise see Figure 2-17. This effect is particularly evident in magnetite and was shown well by the work of Radu et al. [32] Since magnetite and maghemite lack a distinct Fe^{3+} satellite region in their spectra, monitoring the Fe^{3+} satellite enables the transition from hematite to the other oxides to be confirmed.

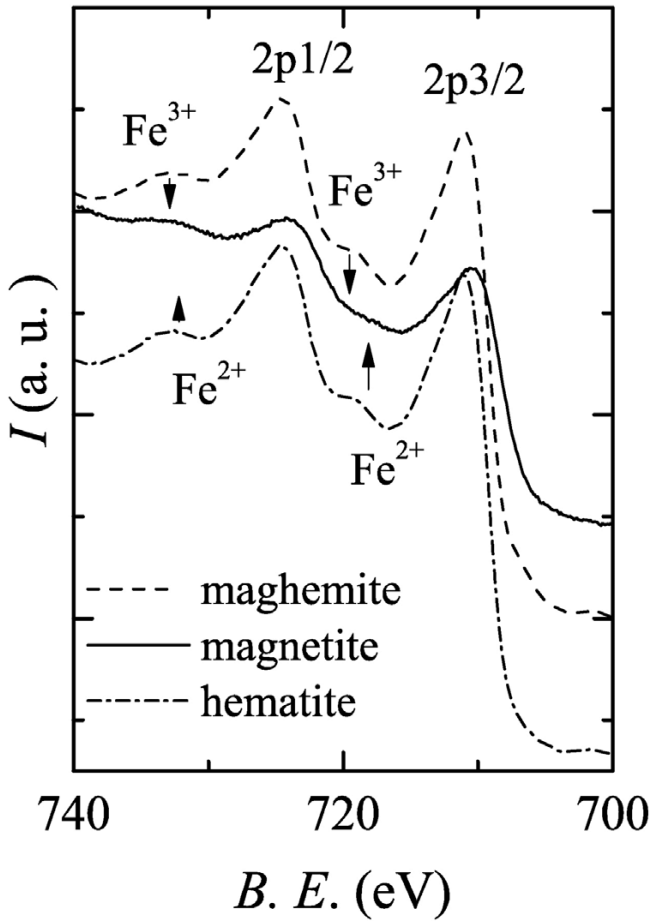

Figure 2-17: XP spectra illustrating differences between different iron oxide particles taken from Radu et al. [32]

The O1s region shows a typical Fe-O bond at 530.1 ev. The other signals at 532 and 533 eV in this region corresponds to an organic C-O bond and an OH bond. Both components decrease following heat treatment from hematite to maghemite. This is due to the thermal decomposition of organic contaminants on the surface of the particles.

2.4.1 Magnetic Measurements

Measurements of magnetic susceptibility were taken of the compounds using a Gouy balance. Typically, hematite has a susceptibility 3 orders of magnitude smaller than that of magnetite and maghemite, while the ferromagnetic family members tend to have susceptibilities of greater than 1000 $x10^{-4}cm^3g^{-1}$. The measurements obtained from these particles are given in Table 2.1 and show that there is a significant increase in magnetic susceptibility from the hematite particles to the magnetite and maghemite. However, the ferromagnetic particles have a susceptibility lower than their expected bulk values. This could be a result of size and morphology effects, but it is more likely that not all the particles were transformed from hematite in the redox process resulting in lower-than-expected molar susceptibility.

Material	Magnetic Susceptibility (X) ($x10^{-4}cm^3g^{-1}$)
Hematite	14.96
Magnetite	3067
Maghemite	2901

Table 2-1: Comparison of Iron oxide magnetic susceptibility obtained when nanoparticles are oxidised and reduced.

When combined with the XRD and XPS data the magnetic data confirms the formation of the three different forms of iron oxide but indicates that there has not been a full transformation of phases between the redox steps.

2.5 Discussion

Hematite, magnetite and maghemite nanoparticles were successfully prepared with an anisotropic morphology. Hematite was prepared through two sperate methods hydrothermal methods: one using phosphates and the other using 1,2 propanediamine. Each of the methods allowed a degree of aspect ratio tuning with a small particle size distribution. The morphology of the final product of each method was affected and tuned by different parameters. While they both resulted in morphologically similar hematite nanoparticles, their different relationships to temperature, reaction and reactant concentration implies they have different growth mechanisms. For example, the concentration of directing agent had a profound effect on nanoparticles produced in the presence of phosphates. Hematite prepared with low phosphate concentrations developed with more spherical morphologies. While in the presence of higher phosphate concentrations <7 mM the nanoparticles elongated forming anisotropic nanoparticles. There was a proportional relationship between aspect ratio and phosphate concentration between 0-6 mM phosphate resulting in an increase of aspect ratio from 0 to ~ 7. While the work of Li et al. [6] shows that there is much less of a relationship between aspect ratio and 1,2 propanediamine, in the absence of any 1,2 propanediamine spherical particles were formed, much like that of the phosphate method. However, between ratios, 3:1 to 1:5 $FeCl_3$ to 1,2 propanediamine rod morphology was obtained. Like phosphate directed hematite, there was a turning point for aspect ratio where when passing 1:1 ratio showing a reduction in length from a maximum 2800 nm to 600 nm. The temperature was a more important control for the preparation of 1,2 propanediamine hematite. Where a transition from spherical particles to rods could be affected with a simple change from 140 to 180 ^oC. This was reliably observed through TEM and the general population of nanoparticles can be seen

to transition between 140 ^{o}C and 180 ^{o}C perhaps with more delicate changes of temperature a greater degree of aspect ratio control could be exerted. Both forms of hematite show an order along their [104] and [012] planes which can be seen in their XRD and FFT likely since both phosphate and 1,2 propanediamine molecules are absorbed onto these planes. In most cases of hematite, the growth of the hematite structure is along the [001] plane as the surface hydroxyl groups are doubly bonded on the [001] plane while the [012], [104] and other crystal lattices have singularly bonded hydroxyl groups. Through the addition of the growth agents, these lattices are protected, and growth can only occur on the [001] axis. Since both phosphate and 1,2 propanediamine show a decrease in aspect ratio when passing a maximum amount of directing agent, this is likely at the point where a complete monolayer of directing agent has been formed on all the other surfaces and it has become favourable to bond to the [001] axis resulting in the shortening of the rods. The diameter of the 1,2 propanediamine rods is 3x that of hematite rods possibly suggesting that the 1,2 propanediamine has a less affinity for hematite than that of phosphate hence allowing more growth along with the non [001] axis. It was theorised that the length of a particle terminates in the phosphate method due to a lack of $FeCl_3$ this was examined in a flow control experiment, where additional growth solution was added to the reactant mixture slowly over a period of several days. This resulted in the formation of very large hematite structures ranging between the mm-cm scale. This suggests that the growth and aggregation of particles formed by the phosphate directed method can continue in solution as the additional growth solution resulted in larger structures. It is possible that rather than causing the extra nucleation of hematite onto the end of rods, that the aggregation of the nanoparticles seen in the growth mechanism would continue and form these larger structures.

The magnetic behaviour of all hematite particles was measured by Gouy balance. Both hematite structures had good magnetic susceptibility with agreed with literature with small discrepancies between the particles likely being due to shape and size affects resulting in electron holes. While these particles were suitably magnetic this study aimed to create a selection of particles with different magnetic susceptibilities. Magnetite and Maghemite were successfully prepared and resulted in significant increases in magnetic susceptibility of 3067 and 2901 $x10^{-4}cm^3g^{-1}$ respectively. These particles are magnetic however they would

pose a problem for magneto-optical diagnosis. These particles are so magnetically responsive that they would aggregate together in solution and rather than simply rotating in an external magnetic field they would be attracted to the magnet and each other.

2.6 Conclusion

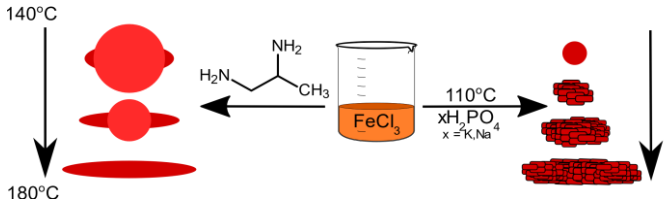

Figure 2-18: Illustration of the preparation of gold-coated hematite rods. The rods are synthesised in the presence of structure-directing phosphates or amines.

This study aims to compare the synthesis of anisotropic hematite nanoparticles using different structure-directing agents. The phosphate-based preparation procedure first described by Ozaki et al.[5] reproducibly creates hematite particles with narrow size distribution and our results show that the aspect ratio of the particles can be reproducibly tuned from zero to ~7.5 by increasing the phosphate concentration. Higher ratios cannot be achieved with this method, however, with phosphate concentrations above ~ 6 mmol inhibiting the anisotropic growth. TEM images confirm previous reports that the hematite rods formed under this entire range of conditions lack long-range crystallinity consistent with a formation mechanism involving the aggregation of subunits into the final “rice” shape. The growth mechanism proposed by Frandsen et al.[33] in which akageneite sub-units convert into hematite after coalescing was refined by Sugimoto et al. ’s[10] careful study showing that the hematite units are created initially by direct crystallisation from solution, with further growth by the dissolution of small akaganéite units and redeposition of oxide on the hematite particles. For our preparations at a temperature 10 °C higher than Sugimoto, the XPS, XANES, Raman and XRD data show the dominant phase to be hematite with only the samples prepared at the shortest ageing times or in the absence of phosphate showing any presence of akaganéite. This hints at a role for phosphate in accelerating the crystallisation of the hematite as well as directing the anisotropic growth. At the nanoscale, the PiFM data did not show any evidence for akaganéite on the phosphate directed particles. However, the presence of carbonate around the rim and tips of the growing particles is indicative of the presence of hydroxide at these sites. These two observations hint that there is a role for the hydroxide in the growth of the hematite and that the

phosphate may have a more significant role than simply blocking sites during the growth of the haematite. Further investigations should explore whether phosphate plays a role in accelerating the deposition of the hydroxide or the conversion of the hydroxide to the oxide.

In contrast to the phosphate directed rod growth, varying the concentration of diaminopropane gave much less control over the nanorod anisotropy with more of an effect on the yield of rods synthesised. The TEM and PIFM data support the growth mechanism suggested by Li et al. [6] for the diaminopropane directed rods with the initial formation of goethite spheres followed by recrystallisation of hematite on opposing sides of the sphere until the entire particle forms a hematite rod. The PiFM shows an 1105 cm^{-1} peak assigned to the diaminopropane concentrated on the outer regions of the recrystallised iron oxide rather than the goethite. It plays a role in directing the preferential growth of specific crystal faces of the haematite, whether it also inhibits the dissolution of the oxide compared to the hydroxide is an area that should be explored further.

2.7 References

1 T. Hyeon, *Chem. Commun.*, 2003, **3**, 927–934.

2 W. Wu, Q. He and C. Jiang, *Nanoscale Res. Lett.*, 2008, **3**, 397–415.

3 A. H. Lu, E. L. Salabas and F. Schüth, *Angew. Chemie - Int. Ed.*, 2007, 46, 1222–1244.

4 A. N. Ay, D. Konuk and B. Zümreoglu-Karan, *Nanoscale Res. Lett.*, 2011, **6**, 116.

5 M. Ozaki, S. Kratohvil and E. Matijević, *J. Colloid Interface Sci.*, 1984, **102**, 146–151.

6 Z. Li, X. Lai, H. Wang, D. Mao, C. Xing and D. Wang, *Nanotechnology*, 2009, **20**, 245603.

7 J. Chen, S. Macfarlane, C. Zhang, K. Yu and W. Zhou, *Cryst. Growth Des.*, 2017, **17**, 5975–5983.

8 Z. Ma, H. Han, S. Tu and J. Xue, *Colloids Surfaces A Physicochem. Eng. Asp.*, 2009, **334**, 142–146.

9 Z. Cai, E. S. P. Leong, Z. Wang, W. Niu, W. Zhang, S. Ravaine, N. L. Yakovlev, Y. J. Liu, J. Teng and X. Lu, *J. Mater. Chem. C*, 2015, **3**, 11645–11652.

10 H. Itoh and T. Sugimoto, *J. Colloid Interface Sci.*, 2003, **265**, 283–295.

11 M. Ocaña, M. P. Morales and C. J. Serna, *J. Colloid Interface Sci.*, 1995, **171**, 85–91.

12 Fairley N, *CasaXPS Manual: 2.3.15 Spectroscopy*, 2009.

13 F. A. Cicco AD, *The 14th Confrence on X-ray Fine Structure*, 2009.

14 B. Ravel and M. Newville, *J. Synchrotron Radiat.*, 2005, **12**, 537–541.

15 M. Pasero and N. Perchiazzi, *Mineral. Mag.*, 1996, **60**, 833–836.

16 Y. Hexiong, L. Ren, R. T. Downs and G. Costin, *Acta Crystallogr. Sect. E Struct. Reports Online*, 2006, **62**, I250–I252.

17 N. Pailhé, A. Wattiaux, M. Gaudon and A. Demourgues, *J. Solid State Chem.*, 2008, **181**, 2697–2704.

18 D. Bersani, P. P. Lottici and A. Montenero, *J. Raman Spectrosc.*, 1999, **30**, 355–360.

19 A. M. Jubb and H. C. Allen, *ACS Appl. Mater. Interfaces*, 2010, **2**, 2804–2812.

20 National Institute of Standards and Technology, *NIST X-ray Photoelectron Spectrosc. Database, Version 4.1*.

21 S. Jiang, M. G. Kim, I. Y. Kim, S. J. Hwang and H. G. Hur, *J. Mater. Chem. A*, 2013, **1**, 1646–1650.

22 A. Boubnov, A. Roppertz, M. D. Kundrat, S. Mangold, B. Reznik, C. R. Jacob, S. Kureti and J. D. Grunwaldt, *Appl. Surf. Sci.*, 2016, **386**, 234–246.

23 I. Rajapaksa, K. Uenal and H. K. Wickramasinghe, *Appl. Phys. Lett.*, 2010, **97**, 234–242.

24 H. D. Ruan, R. L. Frost, J. T. Kloprogge and L. Duong, *Spectrochim. Acta - Part A Mol. Biomol. Spectrosc.*, 2002, **58**, 967–981.

25 E. Darezereshki, *Mater. Lett.*, 2011, **65**, 642–645.

26 R. Parameshwari, P. Priyadarshini and G. Chandrasekaran, *Am. J. Mater. Sci.*, 2011, **1**, 18–25.

27 P. Persson, N. Nilsson and S. Sjöberg, *J. Colloid Interface Sci.*, 1996, **177**, 263–275.

28 M. Veneranda, J. Aramendia, L. Bellot-Gurlet, P. Colomban, K. Castro and J. M. Madariaga, *Corros. Sci.*, 2018, **133**, 68–77.

29 D. Vernekar and D. Jagadeesan, *Catal. Sci. Technol.*, 2015, **5**, 4029–4038.

30 E. Murad and J. L. Bishop, *Am. Mineral.*, 2000, **85**, 716–721.

31 C. Frandsen, B. A. Legg, L. R. Comolli, H. Zhang, B. Gilbert, E. Johnson and J. F. Banfield, *CrystEngComm*, 2014, **16**, 1451–1458.

32 T. Radu, C. Iacovita, D. Benea and R. Turcu, *Appl. Surf. Sci.*, 2017, **405**, 337–343.

33 C. Frandsen, B. a Legg, L. R. Comolli, H. Zhang, B. Gilbert, E. Johnson and J. F. Banfield, *Crystengcomm*, 2014, **16**, 1451–1458.

Chapter 3 Cerium Particle Growth

3.1 Introduction

In chapter 2 hematite was shown to have little preferential binding to gold upon its surface without the aid of surfactants such as 3-aminopropyl)triethoxysilane (APTES) or poly(vinylpolypyrrolidone) (PVP). However, ceria and other cerium compounds have long been known to possess strong support metal interactions which result in gold easily depositing upon the surface of ceria supports[1,2]. This chapter considers the preparation of cerium phosphate and oxide nanoparticles by hydrothermal synthesis using different directing agents for their growth, such as NaOH or $NaPO_4$. Ceria is diamagnetic and not an ideal prospect for the aims of this thesis but $CePO_4$ has potential for paramagnetism, and the aim is to prepare anisotropic nanorods by a simple hydrothermal method that can be tuned to accurately control the aspect ratio.

Cerium oxide and other lanthanide nanoparticles are of general interest in catalysis because of their 4f electrons facilitating switching between the Ce^{3+} and Ce^{4+} oxidation states. Over recent decades several 1D and 2D cerium oxide nanostructures have been prepared ranging from nanorods, nanobelts and nanopolyhedra[3–5]. The fluorite structure of CeO_2 is comprised of 8 coordinate Ce^{4+} and 4 coordinate O^{2-} ions and the Ce^{4+} /Ce^{3+} redox allows for oxygen migration in the [111], [110] and [100] crystal planes making them more active as they undergo the formation of oxygen vacancies. This property allows for the capture of oxygen into the fluorite lattice and is useful in catalysis, oxygen sensors and energy storage[6]. This effect also has uses in biomedical science where ceria's ability to scavenge reactive oxygen species gives it antioxidant properties[7].

There are several methods published by which cerium oxide nanoparticles can be formed including solid state reactions[8], hydrothermal[9], solvatothermal[10], coprecipitation[11] and reverse micelle[12]. However, the one-pot and one-step nature of hydrothermal methods make them preferable for developing nanoparticles with control over morphology[13,14]. Many hydrothermal methods are broadly similar with only slight changes across the synthesises. Most require the use of cerium precursors with counter-anions such as SO_4^{2-}, NO_3^-, and Cl^- which can play a significant role in the growth of cerium nanostructures and the ratio of Ce^{4+} /Ce^{3+} [15,16]. For example, Wu et al.[17] illustrated that halide counter ions are

more selective to rod morphology than nitrate ions. It was suggested that the halide ions themselves could act as a growth directing surfactants[13].

The production of high aspect ratio 1-D ceria nanostructures was first carried out in the presence of ethylene glycol since it can stabilize inorganic salts and has a high boiling point[18] . Varying reaction times were shown to tune the morphology from spheres to rods over a period of 20 minutes. The concentration of the precursor also played a part in the formation of the final product with increased concentrations resulting in larger polyhedra and nanocubes. Yan et al. [19,20] formed ceria nanorods, nanocubes and nano-polyhedra by carrying out a hydrothermal synthesis in the presence of NaOH. Again, varying the temperature and NaOH concentration resulted in the tuning of different morphologies. Table 3-1 shows the different morphologies that can be achieved through varying NaOH concentrations.

C_{NaOH} (mol/L)	T (°C)	Time (h)	Shape	Size (nm)
0.01	100	24	Polyhedra	10-15
0.01	180	24	Polyhedra	9-25
6	100	24	Rods	(8.5-10.7) x (50-200)
6	180	24	Cubes	29-43.2
9	100	24	Rods	(9.5-16.1) x (100-400)

Table 3-2: Ceria nanostructures formed under different conditions reproduced from Yan et al.[19,20]

This effect is having been attributed to the dissolution/recrystallization growth mechanism. Firstly $Ce(OH)_3$ is formed from the cerium precursor in the presence of NaOH. In low concentrations of NaOH and at low temperatures, the rate of dissolution/recrystallization is low, and the $Ce(OH)_3$ nuclei mature into polyhedra. With higher concentrations of OH^- the nuclei agglomerate by orientated attachment along the [110] direction to form nanorods. However, the highly basic solution and 155 °C temperature resulted in the dissolution of the $Ce(OH)_3$ nanorods to form CeO_2.NO_3^- or OH^- anions are selectively adsorbed onto the [100] plane of the CeO_2 inhibiting its growth rate and resulting in the formation of nanocubes[21].

Each nanostructure has different exposed crystal lattices: nanorods [110] and [100]; nanocubes [100] and the nanopolyhedra [111] and [100] where [111] has the lowest surface

energy. The surface energies are expected to show a trend of [110]>[100]>[111] suggesting nanorods would be the most strained crystal structure and hence the most reactive catalytically[22,23].

The ratio of Ce^{4+} /Ce^{3+} is an important metric to many cerium materials. For example materials with higher proportions of Ce^{4+} show more biological activity, preventing mitochondrial fragmentation for example, which can be used to aid neurodegenerative diseases[24]. Alternatively, The 5d-4f transitions in the Ce^{3+} ion give rise to strong absorption in the UV region and short luminescence lifetime, which can be used in developing sensors[24].

For use in magneto-optics cerium oxide would not be well suited as it is predominantly Ce^{4+} which is diamagnetic; Ce^{3+} on the other hand is a paramagnetic ion showing slight magnetic behaviour. However, magnetic properties have been observed in non-magnetic oxides such as Al_2O_3, ZnO, Ln_2O_3 and SnO_2, and Ro et al. [24] suggest this effect is a result of exchange interactions between unpaired electron spins in oxygen vacancies. This effect can be observed in the work of Tian et al.[25] where micron sized cerium oxide nanorods displayed weak magnetisation. This magnetisation was greatly increased through the addition of Mn ions into the lattice which increased the number of Ce^{3+} ions in the lattice.

3.2 Cerium Phosphate

Cerium phosphate is often an impurity found in cerium oxide nanorods formed in the presence of a capping agent with a phosphate counter ion such as trisodium phosphate or phosphoric acid,[26,27] and this is especially true at low temperatures. However, heavy metal phosphates such as $LnPO_4$, $BiPO_4$ and $CePO_4$ have become areas of significant interest in recent academic studies. $CePO_4$ has multiple uses across the fields of catalysis and fluorescence[28,29]. Furthermore, unlike cerium oxide which is formed from a combination of Ce(III) and Ce(IV) oxidation states, cerium phosphate is comprised of the paramagnetic Ce(III) oxidation state giving it a greater magnetic potential. Since this study focuses on the preparation of magneto-optical nanoparticles $CePO_4$ is the preferred product due to its increased Ce^{3+} content and consequently an increase in paramagnetism. The synthetic routes forming cerium phosphates and cerium oxides are often similar, with small variations in preparation temperatures or time[30]. A clear example of this is the work of Wen et al.[30] who added different concentrations of orthophosphoric acid to cerium nitrate and found

that at lower PO_4:Ce ratios, cerium oxide would be formed in an FCC structure but upon increasing the phosphate concentrations, cerium phosphate nanorods become the prevalent morphology. Similar work has been seen with other structures, for example, the cerium oxide 'hedgehog' structures formed by Xing et al[27]. and Xu et al.[31]. In both cases, the morphology of their nanoparticles consists of a central nano octahedron where rods grow from their surface. Upon increasing the concentration of the phosphate capping agents, cerium phosphate impurities become prevalent within the sample.

Heavy metal phosphates are known for having multiple natural crystal forms and cerium phosphate is no exception with its two naturally occurring crystal structures: hexagonal and monoclinic. Often the hexagonal form is hydrated and found with structural water, ($CePO_4.nH_2O$) and formed at low temperatures while the monoclinic form is entirely anhydrous and is formed at high temperatures. Tuning the crystal structure of such metal phosphates is not difficult and is often a matter of changing simple synthetic parameters such as pH, temperature, or pressure[32–35].

Xing et al.[36] formed cerium phosphate nanoparticles by reacting cerium nitrate with orthophosphoric acid, where the ratio of PO_4^-:$Ce^{3+/4+}$ was used to control the morphology of nanoparticles obtained. By changing the molar ratio between 10-600 they were able to tune the morphology from single rods to agglomerates of rods in a flower-like structure. The authors state that the rods grow hydrothermally through the selective adsorption of phosphate. The initial structures formed are hexagonal due to a lower ratio of Ce^{3+}:PO_4^{3-}. As the reaction continues the relative abundance of PO_4^{3-} increases the surface charge of the crystallites also increases. To attempt to reduce the surface charge the atoms on the surface undergo a lattice reorganisation. This results in the formation of the monoclinic phase of $CePO_4$ which acts as a seed for further monoclinic growth. This produces flower-like structures with monoclinic $CePO_4$ growing from the surface of hexagonal $CePO_4$.

The monoclinic and hexagonal forms of cerium phosphate show crystal specific properties. For example, Vinothkumar et al.[34] produced samarium doped cerium phosphate nanorods of both monoclinic and hexagonal structures and studied the luminescent properties of each phase as peroxidase mimetics and hydrogen peroxide sensors. The phase transition was easily achieved by heat treating hexagonal rods at 800 ^oC to form the monoclinic crystal structure. Results showed that the monoclinic form had a longer luminescent lifetime than

the hexagonal form which suffered from quenching due to structural water. The monoclinic form also showed higher catalytic activity in the presence of peroxidase due to its ability to create more hydroxyl radicals.

Pusztai et al.[35] synthesised cerium phosphate nanorods to test proton transport along the rods. It was found that the surfaces of the monoclinic rods and hexagonal rods were different with the hexagonal rods having a rougher surface. However, this may have been a result of hydrogen etching by the phosphoric acid used in the preparation. Due to this effect, the diameter of pore size present on the hexagonal samples were smaller than those of the monoclinic crystal structure. These smaller pores formed a rougher surface across the hexagonal samples resulting in a high surface area. When testing their abilities to adsorb nitrogen it was found that the monoclinic structure had a significantly lower surface area than that of the hexagonal form. The surface conductivity of the monoclinic form was also found to be 3 times higher than that of the hexagonal form. This difference was a function of the density of surface acidic sites and once normalised no clear difference could be seen. Ultimately, the authors concluded that surface acidity was the important factor, not the crystal structure and that the preparation method was a more significant effect than that of the crystal order.

3.2.1 Growth of Nanoparticles

Within large industrial scale chemistry, there are occasions where the rates of diffusion throughout a bulk solution are lower than the rates of the chemical reaction forming the growth species no matter the degree of agitation.[37] This is also true for biological species such as haemoglobin where the rate of oxygenation is mainly controlled by the rate at which oxygen and carbon monoxide can reach the active site in the large haemoglobin molecule[37,38]. This can be explained with Smoluchowski Theory and the Random walk.

The oxygenation and deoxygenation of haemoglobin (Hb) molecules relies upon three reactions:

1. $Hb + O_2 \rightarrow Hb.O_2$
2. $Hb + CO \rightarrow Hb.CO$
3. $Hb.O_2 \rightarrow Hb + O_2$

Reactions 1 and 2 entirely rely upon the movement of small atoms towards the larger haemoglobin and the rate of the chemical reaction between the two species is relatively fast. Therefore, the controlling aspect of the reaction is the time the molecules take to diffuse between the bulk and the surface-active sites of the haemoglobin. This can be visualised using a random walk where one molecule moves through the solution at defined equilibrium steps. When one of the steps on the path of the molecule is adjacent to a haemoglobin molecule there is a chance for an interaction between the two reactants. While the small molecule is in this position it will interact multiple times with the larger haemoglobin through movements such as vibrations and rotations, this is referred to as an encounter. Depending on the length of such an encounter two extremes are achievable: One where each encounter is long and thus each smaller molecule collides with the larger haemoglobin multiple times, essentially guaranteeing a successful reaction. In this case, the rate of encounters and hence reaction is diffusion controlled. The other extreme sees encounter only last for a short time and result in the smaller molecule continuing its path. In this case, most encounters are unsuccessful, and the rate is controlled by the reaction between the two species. Growth which is diffusion limited tends to have an activation energy between 0-20 $kJmol^{-1}$, while growth which is reaction or surface limited tends to have greater activation energies of 40-80 $kJmol^{-1}$ but can also be higher for less soluble species.[39,40]

The morphology and size distribution of nanoparticles depends upon the growth process of the nuclei. This process can be divided into four main steps:

(1) formation of the growth species

(2) diffusion of the species from the bulk solution to the crystallite surface

(3) adsorption of growth species upon the crystallite surface

(4) Incorporation of the growth species into the crystallite[41].

Therefore, the interactions which govern nanoparticle growth can be divided into two categories according to Smoluchowski Theory: those which are diffusion limited reactions and those which are reaction limited at the surface of the crystalite[42].

An example of diffusion limited growth is the formation of ZnO nanoparticles studied by Rao et al.[43] In Rao's study, the formation of ZnO nanorods was carried out in the presence and

absence of a PVP capping agent. When observing the growth of these nanorods the length of the particles would vary greatly over time and was dependent upon the presence of the capping agent. When PVP was absent the nanorods would grow from 19 to 52 nm in length and 8.3 to 12.3 nm in diameter over a period of 24 hours representing an aspect ratio change from 2.3 to 4.3. However, in the presence of PVP, the length changed from 19 to 77 nm with a relatively small change in diameter of 9.1 to 10.4 nm, which represents an aspect ratio change of 1.8 to 7.4 over 24 hours. The ZnO nanorods obtained showed a hexagonal structure consisting of a structure bound by six [1010] facets growing along the [0001] direction, which corresponds to the longest axis of the rod. The PVP selectively adsorbs upon the side [1010] facets allowing preferential growth along the [0001] crystal axis. In the absence of PVP, the [0001] still exhibits a preferential elongation due to the comparative growth rates of the axes involved where [0001]>[1011]>[1010], as the side [1010] surfaces are not capped without PVP a larger increase in diameter is seen. This data suggested that nanorods formed in the absence of a capping agent, grow mainly by a diffusion limited Ostwald ripening process. On the other hand, when ZnO nanorods were formed with a capping agent they grow by a more complex combination of mechanisms. This is probably because the PVP capping agent acts as a barrier for diffusion and subsequent assimilation of the growth species into the crystal. So, in these cases, the nanorods grew with a combination of surface and diffusion limited growth[43,44].

A similar example is the growth of goethite nanorods from precursors containing either sulfate or nitrate anions[45]. These particles grow by the oriented attachment of crystal subunits, which is subtly different to Ostwald ripening, in that there is a preferential crystal surface for the subunit to attach to before assimilation into the bulk. While ostwald ripening is driven by the surface energies of nanoparticles at different diameters, where those with a smaller diameter than a critical value are cannibalised by those with diameters larger[46]. When preparing nanoparticles with either anion the activation energy was low, at 23 and 43 $kJmol^{-1}$ for nitrate and sulfate ions, respectively. Morphologically the nanoparticles were similar, and both grew by a diffusion limited oriented attachment growth mechanism after nucleation. The difference in activation energies between the two samples was explained to be a result of the higher negative charge on the sulfate compared to the nitrate ion, illustrating the importance of anion effects upon the growth of crystal nanoparticles.

3.2.2 Aims

This chapter aimed to develop and study hydrothermal methods capable of producing cerium based anisotropic nanoparticles.

Several hydrothermal methods were analysed to identify a suitable process that was sufficiently reliable and simple. Each method was assessed based on the morphology and chemical composition of the product. The resulting particles were characterised with a combination of spectroscopic and surface techniques to identify the common features present in different morphologies.

This information was used to develop a procedure that produced particles where the morphology of the product was sensitive to parameters such as temperature and time. Resulting in a process that is highly tuneable and able to produce a range of aspect ratios reliably.

3.2.3 Method

In this chapter ceria-based nanostructures were formed by several methods, see Figure 3-1, to examine the effect of the synthesis route upon the morphology and chemical properties. One method was then used for doping to improve the magnetic properties of the ceria particles.

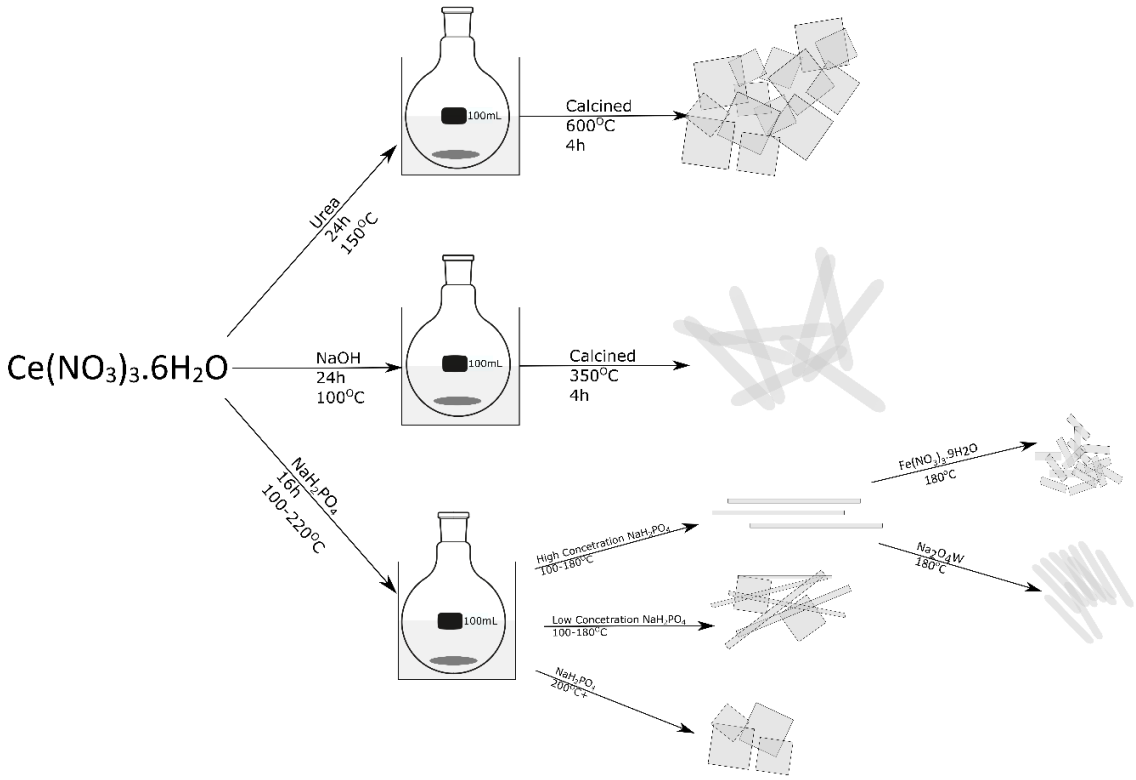

Figure 3-1: Illustration of different cerium particles formed under different conditions. Cerium particles were cubic when formed with urea, rod shaped with NaOH and a combination in the presence of phosphate. When adding Fe or W different morphologies were obtained.

3.2.3 NaOH Method

In a typical synthesis, 0.43 g of $Ce(NO_3)_3.6H_2O$ was added to a 6M NaOH solution of 20 mL in a 60 mL polyethylene beaker and stirred at 300 rpm for 30 minutes at room temperature (RT). After cooling to RT, the resulting white solution was transferred to a sealed pressure flask and placed in an oil bath at 100 ˚C for 24 hours. After heating the solution of nanoparticles, they were collected and cleaned in a centrifuge with approximately 10 mL of deionised water and ethanol to remove contaminants and unreacted chemicals. The precipitate was dried overnight in air at 70 ˚C to produce the ceria precursor as a deep yellow powder which was then calcined at 350 ˚C for 4 hours to produce ceria nanorods as a pale-yellow powder.

The above method is repeated but with 9 M sodium hydroxide for the '9 M NaOH' samples.

3.2.3 Phosphate Method

1.12 g $Ce(NO_3)_3.6H_2O$ was added to a $4.135x10^{-2}$ M solution of KH_2PO_4 or Na_3PO_4 of 40 mL and was stirred at 300 rpm for 5 minutes at RT. The white solution was transferred to a 90 mL Teflon-lined autoclave and heated at temperatures between 100-180 ^oC for 16 hours. After cooling to RT, the white solution was washed in a centrifuge with deionised water and dried at 70 ˚C overnight in air to produce a white powder of ceria.

3.2.3 Ceria Nanostructures

0.56 g $Ce(NO_3)_3.6H_2O$ was added to an $8.25x10^{-2}$ M solution of KH_2PO_4 or Na_3PO_4 of 20 mL and was stirred at 300 rpm for 5 minutes at RT. The white solution was transferred to a sealed pressure flask and heated at 170 ˚C for 24 hours. Upon cooling to RT, the white solution was washed in a centrifuge with deionised water and dried at 70 ˚C overnight in air to produce a white powder of cerium phosphate. Three other experiments using the same procedure were completed, except with a change in the phosphate concentration and these were as follows: a) $4.125x10^{-2}$ M; b) $1.65x10^{-2}$ M and c) $6.6x10^{-3}$ M.

3.2.3 Urea Method

0.87g of $Ce(NO_3)_3.6H_2O$ and 0.29g of urea were each separately added to 20 mL of deionised water and stirred for 30 minutes to form two stock solutions. 20 mL of the cerium nitrate solution was added to 12.5 mL of the urea solution into a glass vessel. This reactor was then sealed, heated to 150^oC, and left for 24 hours. The resulting solution was collected and allowed to cool to room temperature before being centrifuged. The solid was then re-suspended in 30 mL of water and centrifuged again in a washing step. This was then repeated 3 more times, once with water and twice with ethanol. The washed pelleted product was then allowed to dry overnight before being placed into a furnace and calcined at 600^oC for 4 hours.

3.2.3 Growth Study

To examine the growth of nanorods and to ascertain their rate of growth, both temperature and time were varied to examine how the aspect ratio and morphology would vary in concert. These experiments used the standard cerium phosphate rod conditions 180 ^oC with $8.25x10^{-2}$ M KH_2PO_4 stock.

3.2.3 Time

0.56g of $Ce(NO_3)_3.6H_2O$ was added to 20 mL of $8.25x10^{-2}$ M NaH_2PO_4 solution. The solution was poured into a sealed pressure flask and sonicated for 2 minutes, then heated in an oil bath at 180°C for between 2 - 20 minutes depending on the treatment. Each reaction

mixture was separated with centrifugation at 3450 rpm and washed with deionised water and ethanol and then dried at 80 °C overnight.

3.2.3 Temperature

0.56 g of $Ce(NO_3)_3.6H_2O$ was added to 20 mL of $8.25x10^{-2}$ M NaH_2PO_4. The solution was poured into a sealed pressure flask and sonicated for 2 minutes, then heated in an oil bath for the dictated temperature (as shown in Table 3-). The time for a colour change from white to cream/slightly transparent was noted.

Temperature of experiment (°C)	Time for removal (minutes)	Time for colour change (minutes)
100	120	72
110	120	49
120	120	26
130	120	22
140	60	23
150	60	12
160	60	12
170	60	6
180	60	6

Table 3-2: Table of reaction temperature & time taken for colour change.

3.2.4 Characterisation

Ceria and cerium phosphate particles were analysed with a combination of XPS, with electron microscopy used to confirm their morphology and chemical composition.

For mechanistic studies of the growth of the nanoparticles using XRD, and Raman and PiFM, the nanorods were extracted from solution by centrifugation and deposited on silica surfaces without further washing. For XPS, TEM and PiFM, the nanoparticles were isolated with a series of washing/ centrifugation steps and vacuum dried. TEM Samples were supported on copper support grids and analysed on a JEOL JEM-2100.

For XPS the dried nanorods were pressed onto conductive tape and analysed with a Kratos Axis Ultra-DLD photoelectron spectrometer with a monochromatic Kα x-ray source in the "hybrid spectroscopy" mode. The analysis area was approximately 700 × 300 µm. A pass-energy of 40 eV was used for high-resolution scans and 60 eV for survey scans. CasaXPS [47]was used to analyse the spectra. Binding energies are referenced to the largest C(1s) peak at 284.7 eV with an uncertainty of ~ 0.2 eV. Since intensities for powder samples are dependent on the surface area analysed, which can be poorly reproducible between

different powder samples, XP spectra in the figures are normalized to the point of maximum intensity.

Powder X-ray diffraction (XRD) was performed using a PANalytical X'Pert Pro diffractometer with a monochromatic Cu Kα source (λ = 0.154 nm) operated at 40 kV and 40 mA. The scans were recorded over the 2θ 10–80°

For the measurements with PiFM, the washed nanoparticles were deposited onto a mica sheet and allowed to dry before submitting for analysis. The measurements were made in the Molecular Vista laboratories by Dr. O'Reilly.

3.2.3 XPS Analysis of Ce Compounds.

In cerium compounds, the most useful region of the XP spectra is that of the Ce3d. Where both Ce(III) and Ce(IV) oxidation states can be observed and quantified. Upon first look, it can appear difficult to distinguish given that they have large areas of cross over. The Ce3d region is dominated by two multiplets corresponding to the $3d^{5/2}$ and $3d^{3/2}$ irrespective of the oxidation state [48]. These multiplets, u and v possess spin-orbit splitting of 18.6 and 18.2 eV for Ce(IV) and Ce(III) respectively. This results in a crowded but well-defined spectrum. The Ce(III) oxidation state has 4 distinct peaks within the 880-920 eV region where several overlap with peaks of Ce(IV)[49]. For example, both u,v and u^0,v^0 doublets for Ce(IV) and Ce(III) respectively are present at ~882 and 901eV. See Figure 3-20(a). For eV of each Ce species as an approximation from this data when normalised using the C1s at 285eV. However, One Indicator of the presence of Ce(IV) oxidation state is the presence of a peak occurring at 917.5 eV which is absent in the Ce(III) XP spectrum. When analysing the presence or absence of Ce(IV) the intensity within this region is a good indicator of its abundance within a final product When discussed in this report Ce(III) will be displayed in blue and Ce(IV) in red.

Ce(III)	Transition	Binding energy [eV]
u^0	$3d^{10}4f^1 \rightarrow 3d^9 4f^2(5d6s)^0$	882
v^0		901
u′	$3d^{10}4f^1 \rightarrow 3d^9 4f^1(5d6s)^1$	886
v′		904.5

Ce(IV)	Transition	Binding energy [eV]
u	$3d^{10}4f^0(5d6s)^0 \rightarrow 3d^9 4f^1(5d6s)^0$	882
v		901
u″	$3d^{10}4f^0(5d6s)^0 \rightarrow 3d^9 4f^0(5d6s)^1$	888
v″		907
u‴	$3d^{10}4f^0(5d6s)^0 \rightarrow 3d^9 4f^0(5d6s)^0$	898.8
v‴		917.5

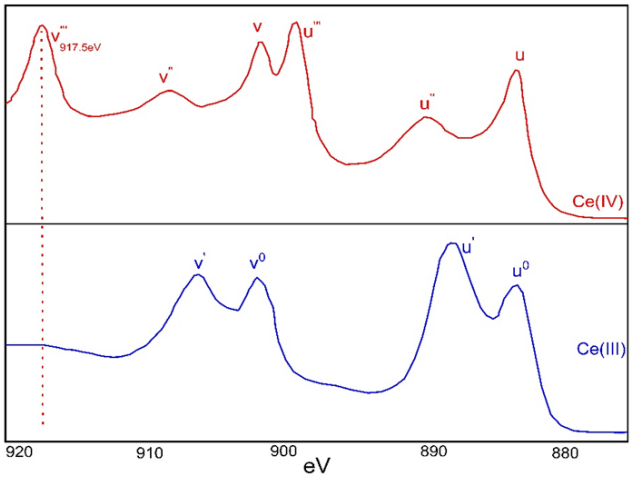

Figure 3-2: (a) Table[50]of Ce(III)/(IV) transitions within the Ce3d region of XP spectra (b) sketch of Ce3d region of XP spectra.

3.2.5 Urea method.

Urea has shown promise in assisting with the development of nanoparticles with anisotropic across several metal oxide systems. This included success in developing cerium based nanoparticles, one such example was the work of Zhang et al.[51] who prepared large ceria nanospindles in the presence of urea. The particles formed had dimensions of 800 nm diameter with lengths of up to 6 microns. While these particles are larger than ideal for this thesis the morphology is like that of the hematite structures formed in chapter 2 making it an interesting method to study.

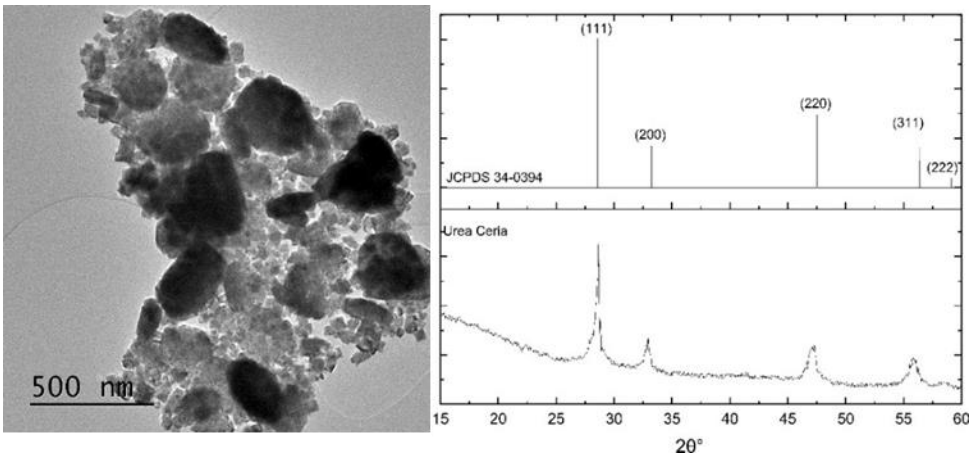

Figure 3-3: (a) TEM micrograph of ceria produced by urea method (b) XRD pattern of ceria formed with Urea and a Ceria reference JCPDS 34-0394

The cerium oxide nanoparticles obtained from reacting cerium nitrate with urea in a glass reactor did not yield anisotropic particles and resulted in a product with little morphological consistency and a particle size distribution varying between 20-350 nm. It is visible In Figure 3-3 (a) that the sample is a mixture of larger 350-200 nm round structures interlaced with smaller 50x50 nm cube structures. This suggests that urea did not selectively adsorb onto the [110] crystal surface to direct the growth of nanorods. Possibly the high concentrations of nitrate anion within the reaction medium directed the growth of cubic cerium oxide nanoparticles. During the 600 ^{o}C sintering step, these particles may have undergone phase transitions or sintering and aggregated to form larger less morphologically defined nanoparticles.

The XRD pattern in Figure 3-3 (b) match the ceria fluorite crystal system. However, the sample has a large full width to have maxima (FWHM). When analysed using the Scherrer equation (shown in equation 3-1) 52

Equation 3-12 $$\tau = \frac{K\lambda}{\beta \cos\theta}$$

Where τ is the mean size of crystal domains, K is the shape factor (0.89 for spherical particles and 0.95 for rods), λ is wavelength, β is the FWHM and θ is the Bragg angle. When calculated the crystallite size should be ~ 80 nm in size. However, this value is significantly smaller than that of other particles observed in Figure 3-3 (a) which within this study[52]. However, the average crystallite size across the entire sample may not be represented in the TEM micrograph.

3.2.3 XPS

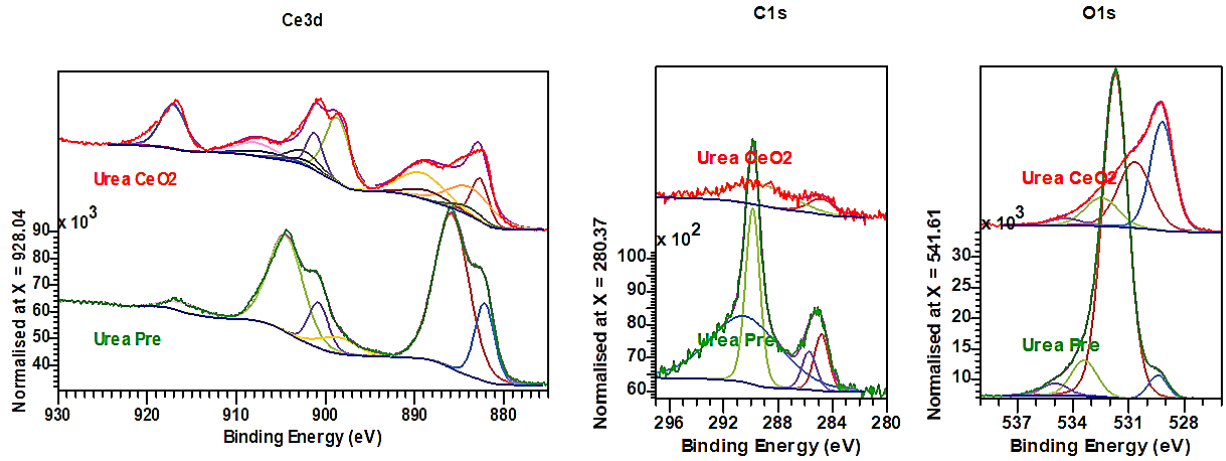

Figure 3-4 (a) XP spectra of Ce(3d) region of CeO2 and precursor formed in Urea assisted Method. (b) XP spectra of C(1s) and O(1s) regions of CeO2 and precursor formed in Urea assisted Method

XP spectra of the urea samples were collected before and after calcination at 600 ^{o}C. Samples were taken before calcination are referred to as “precursor” samples, while those following calcination are referred to as the “final product”, Figure 3-.

The characteristic Ce(IV) peak at 917.5 is present in both samples but greatly reduced in the precursor. The precursor is predominantly Ce(III) with small quantities of Ce(IV) present as indicated by the lack of significant intensity in the 888 and 907 eV region corresponding to the $3d^{10}4f^{0}\ (5d6s)^{0} \rightarrow 3d^{9}4f^{0}(5d6s)^{1}$ transition. In the final product, almost the entire spectrum is Ce(IV) with only small Ce(III) contributions. Cerium also shows a broad 4s component at 290.5 eV which is directly overlapping with the C(1s) region.

In the C(1s) scan there are four components present in the ‘precursor sample’, one corresponding to the Ce(4s). The other three components at 284.8, 289.9 and 285.7 eV are of interest. The peaks are 284.8 and 285.7 eV correspond to adventitious carbon contamination. The most prominent peak at 289.9 eV to a carbonate species, suggesting the presence of carbonate in the precursor[53,54]. The ‘final product’ has only one C(1s) at 284.8 eV corresponding to adventitious carbon.

The O1s of the precursor consists of 4 components at 529.4, 531.7, 533.4 and 535 eV , the primary peak at 531.72 eV has a binding energy like that expected of carbonates and hydroxyl groups this peak may be a combination of both. As when compared to the 289.9 eV C1s Carbonate component a C:O ratio of 1:4 is obtained suggesting the presence of the hydroxyl group. The 529.43 eV component is present in both the final product and

precursor. This component is due to the Ce-O oxygen atom present in CeO_2. The remaining peaks at 533.4 and 535 eV are likely caused by physisorbed water, with the latter having a degree of charge driving it to higher binding energies. The 'Final Product' has three oxygen components at 529.3, 531 and 532.9 eV. The first as discussed above is due to the Ce-O oxide oxygen atom. The peak at 532.9 eV is from absorbed water on the surface of the final product. The peak at 531 eV corresponds to hydroxyl groups on the surface of the product. This peak shows a shift in the binding energy of 0.7 eV resulting from the loss of carbonate from the surface which can be confirmed by the lack of a 289.9 eV C(1s).

Overall, this data indicates that the precursor compound is likely to be $CeCO_3OH$ which would agree with the ratio of 1:4 C:O mentioned above agreeing with previous literature. A comparison of peak areas indicates a ratio of Ce:O of 1:2.2 suggesting the product is CeO_2 with a degree of surface hydroxylation. Further characterisation would be needed to confirm the identification. However, previous work synthesising CeO_2 nanoparticles hydrothermally with urea with a calcination step has shown to undergo the formation of $CeCO_3OH$ by the following process[55].

1. $CO(NH_2)_2 + 2H^+ + H_2O \rightarrow 2NH_4^+ + CO_2$
2. $CO_2 + 4OH^- + 2NH_4^+ + H_2O \rightarrow 2\,NH_3 + 3H_2O + CO_3^{2-}$
3. $Ce^{3+} + H_2O \rightarrow [Ce(OH)\cdot(H_2O)_{n-1}]^{2+} + H_3O^+$
4. $[Ce(OH)\cdot(H_2O)_{n-1}]^{2+} + CO_2^{3-} \rightarrow CeCO_3OH + (n-1)H_2O$
5. $4CeCO_3OH + O_2 \rightarrow 4CeO_2 + 4CO_2 + 2H_2O$

3.2.6 Ceria Nanoparticles formed by NaOH method

Ceria nanoparticles were formed by a hydrothermal synthesis by reacting cerium nitrate with different concentrations of NaOH solution. The resulting solids were calcined at 350 ^oC. All products before calcination will be referred to as the precursor while the calcined compounds are called final products.

3.2.3 TEM Micrographs of NaOH Preparation Method

The TEM micrographs, Figure 3-5, confirm the formation of nanoparticles at both NaOH concentrations. Particles formed using 6 M NaOH displayed a spherical morphology, and it was not possible to obtain lattice fringes from the sample. These particles displayed a uniform distribution with a typical diameter of between 30-40 nm. Using a concentration of NaOH of 9 M resulted in the formation of ceria nanorods with an average aspect ratio of

5.18 and the crystal fringes evident in FFT of the TEM images showed d spacings consistent with the [111] and [311] planes of CeO_2 with a fluorite, Fm3m cubic crystal structure. This effect could be due to the selective adsorption of OH molecules onto the [110] plane to allow the growth of nanorods like the work of Yan et al.[19,20]. However, these results differ from Yan's work which only found rods at low temperatures of 100°C and cubes at 180°C with 6 M NaOH.

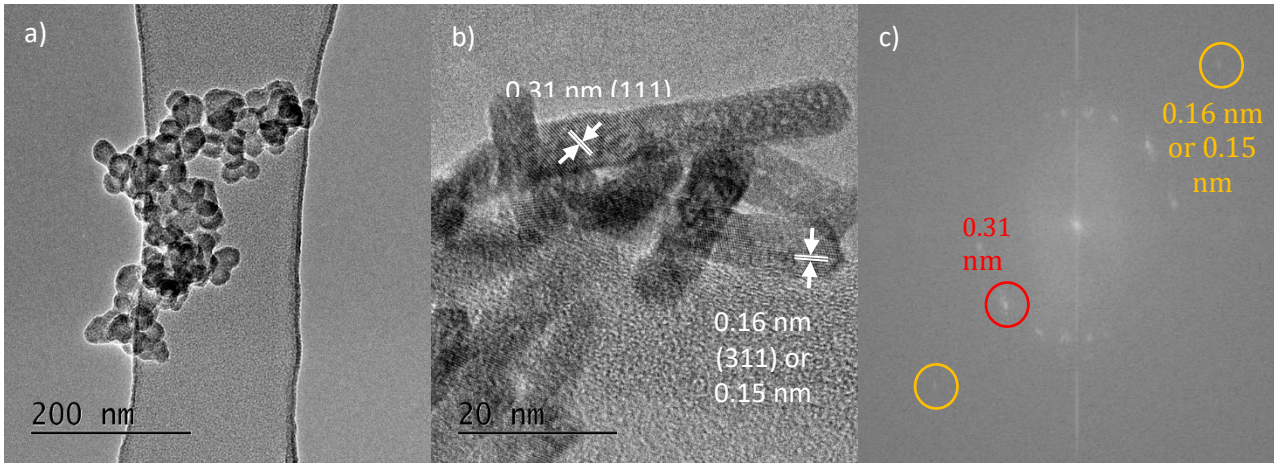

Figure 3-5:: TEM micrographs of nanoparticles formed when reacting CeCl3 (a) 6M NaOH (b) 9M NaOH (c) FFT 9M NaOH.

3.2.3 Raman Characterisation of Ceria by NaOH Method

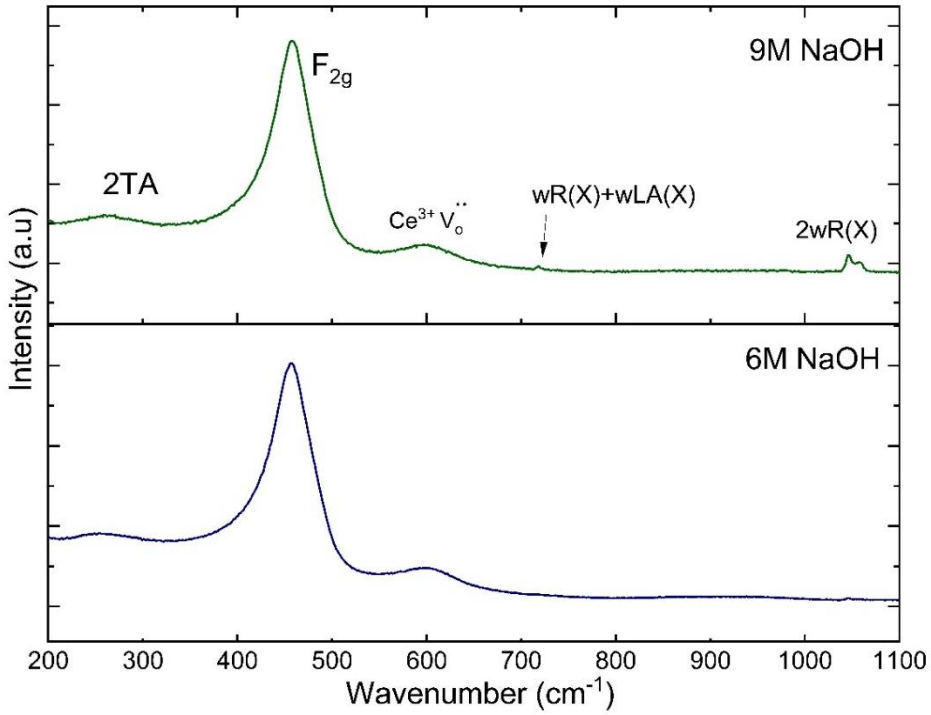

Figure 3-6: Raman spectra of a)6M NaOH and b) 9M NaOH with Raman peaks identified.

The Raman spectra in Figure 3-6 show 5 regions of interest that correspond to cerium oxide in a fluorite phase. The first wide peak at 260 cm^{-1} corresponds to 2TA while the peaks at 598 and 1030-1050 cm^{-1} correspond to second-order peaks[56–58]. The most prominent peak at 458 cm^{-1} corresponds to the triply degenerate Raman active phonon of ceria with a cubic structure. There is a slight shift in the frequency of this peak from 454 to 459 cm^{-1} which may be due to the slightly smaller nanoparticle diameter observed in TEM of 6 M NaOH. Other research has suggested that the 260c m^{-1} peak could relate to surface Ce-OH species[56] which would support the assignment of the ~531.4 eV peak in the XP spectra to the presence of OH. The peak at 595 cm^{-1} can be attributed to oxygen vacancies created in the crystallites due to size effects.

The peaks at 719 and 1030-1060 cm^{-1} could be a result of the cerium nitrate precursor remaining from the preparation. However, there is no evidence of nitrogen in the XP spectra. The peaks observed here would be at a significantly higher frequency if they corresponded to Cerium nitrate. To be exact they would occur approximately at 740, 1048 and 1071cm^{-1} representing a significant shift of 21, 5 and 15 cm^{-1} respectively[59–61].

3.2.3 XP Spectra of Ceria Nanostructures

When preparing ceria by the NaOH route, XP spectra were taken of both the precursor and the final product. At both stages, the Ce(3d), C(1s) and O(1s) scans were used to analyse the materials, shown in Figure 3-7. Upon first inspection, the presence of the prominent $3d^{10}4f^{0}(5d6s)^{0} \rightarrow 3d^{9}4f^{0}(5d6s)^{0}$ transition of Ce(IV) at 917 eV suggests that the samples are mainly comprised of Ce(IV). However small proportions of components due to $3d^{10}4f^{1} \rightarrow 3d^{9}4f^{1}(5d6s)^{1}$ and $3d^{10}4f^{1} \rightarrow 3d^{9}4f^{2}(5d6s)^{0}$ can be seen within the spectrum confirming the presence of a small number of Ce(III) atoms upon the surface. This is consistent with the Raman data which identified oxygen vacancies within the lattice resulting in the presence of Ce^{3+} ions.

The C(1s) scan of the precursor does not contain the typical Ce(4s) at 290.5 eV; there is a peal at 288.7 eV with a similar FWHM suggesting this peak has shifted down in binding energy. The spectra are comprised of 2 other components at 284.4, 286 eV, both corresponding to adventitious carbon and originates from being handled in the air during the preparation. The peak at 288.7 eV is likely due to a degree of carbonate species being present on the surface of the sample. While the final product C(1s) spectra are much similar containing a Ce(4s) region at 290.5 eV and the adventitious carbon peak at 284.4 eV.

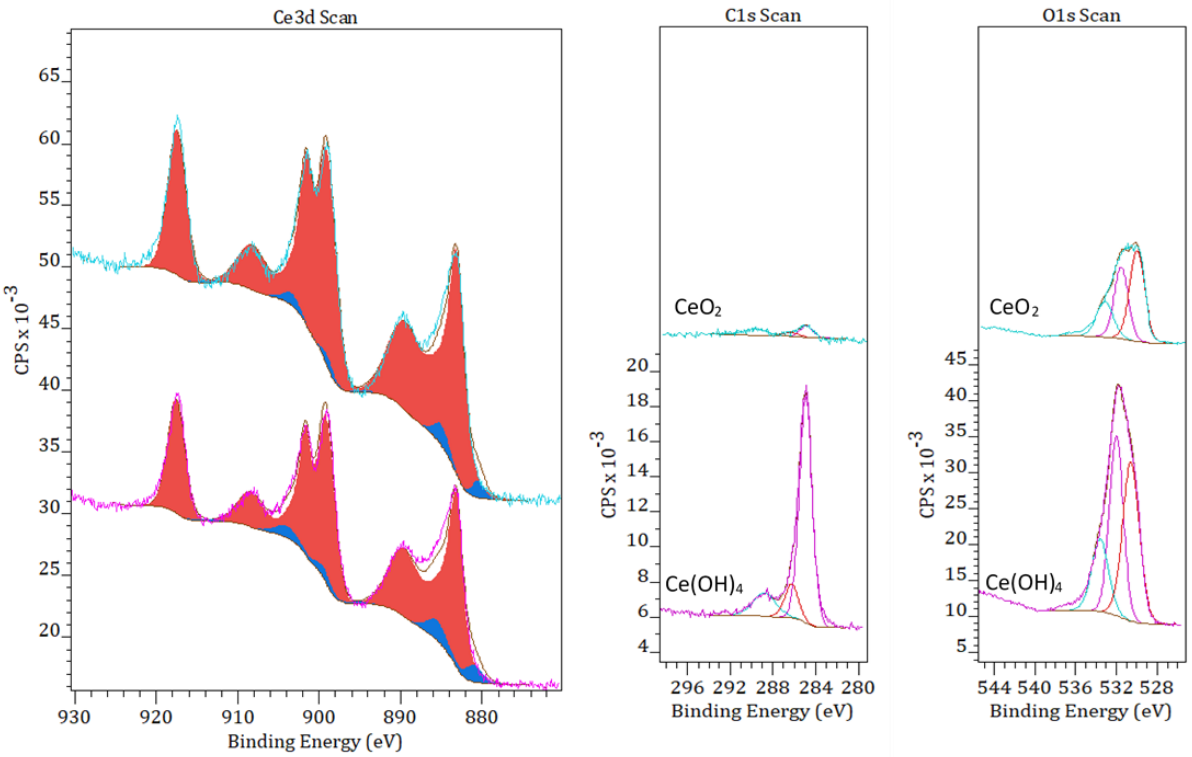

Figure 3-7: XP spectra of 6 M NaOH precursor and final product taken in the Ce(3d), Ce(1s) and O(1s) regions. The spectra have been labelled with CeO_2 for the final product and $Ce(OH)_4$ for the precursor.

The O(1s) spectra for the precursor and final product both show three fitted components. The components for the precursor occur at 529.7, 531.4 and 533.2 eV. While for the final product are at 530.1, 531.8 and 533.6 eV representing a 0.4 eV shift between the two compounds which could be due to a change in the proportion of the Ce(III) and Ce(IV) species between the two materials.

In the precursor the peaks at 533.2 eV correspond to absorbed water on the surface, the peak at 531.4 eV corresponds to the hydroxide species and the 529.7 eV peak corresponds to oxygen atom Ce-O. This is in agreement with the Raman data which suggests the presence of CeO_2 before calcination. Based on this information the precursor compound may be formed from a mixed phase of cerium oxide and cerium hydroxide. It is clear from the Raman and XPS that the hydroxide is by far the more prevalent species before calcination.

In the final product, the lower binding energy beak occurring 530.1 eV corresponds to a Ce-O metal oxide. This peak has dramatically increased in intensity between the precursor and the final product suggesting a shift from $Ce(OH)_x$ to the oxide form suggesting that CeO_2 is the major product of this method which agrees with data from the TEM and Raman. The

peaks at 531.8 and 533.6 eV are likely due to hydroxyl species and absorbed water, respectively. The presence of hydroxyl species suggests that not all $Ce(OH)_x$ has been removed from the final product through calcination.

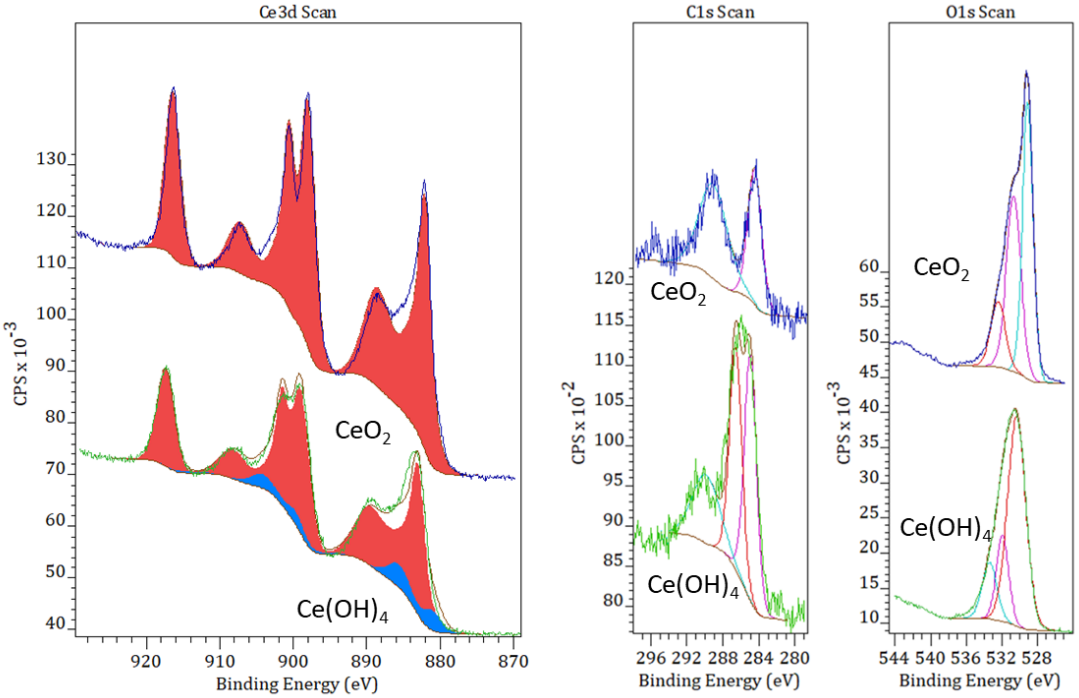

Figure 3-8: XPS spectra of 9M NaOH preparation route precursor and final product XP spectra of 6 M NaOH precursor and final product taken in the Ce(3d), Ce(1s) and O(1s) regions. The spectra have been labelled with CeO_2 for the final product and $Ce(OH)_4$ for the precursor.

Figure 3-8 shows the XPS spectra obtained for the 9 M NaOH preparation. The 9M and 6M samples appear to be very similar. Both concentrations show significant quantities of Ce(IV) oxidation state in both the precursor and final product Ce3d scans. However, the final product formed with higher concentrations of NaOH seems to be almost entirely Ce(IV).

C(1s) scans of the precursor compound is made from 3 components at 284.4, 285.9 and 289.8 eV. The 289.8 eV is likely due to the Ce(4s) shifting to a lower binding energy. The two remaining components are due to the same contamination observed in the 6M precursor. Corresponding to the similar peaks in the 6 M NaOH samples. The final product has only one C(1s) component at 284.4 eV from adventitious carbon where the other C(1s) contamination was lost from the high temperature calcination.

The O(1s) scan of the precursor is also very similar to that of the 6M method consisting of peaks at binding energies of 530.2, 531.7 and 534.4 eV that correlates to the oxygen atom in Ce-O, OH and absorbed water species, respectively. Like the results found at 6M NaOH the 531.7 eV hydroxyl species component can be seen to dominate the spectra in the precursor compound. In the final product, components are found at 529.1, 531.6 and 532,4 eV. The 529.1 eV peak corresponds to the Ce-O metal oxide oxygen atom. The 531.6 eV is the hydroxyl species while the 532.4 eV is caused by absorbed water species. Following calcination, the relative intensity of the Hydroxyl peak compared to the metal oxide is reduced. Further information can be found by analysing the peak areas within the O(1s) scan of CeO_2 the ratio of the metal oxide peak and. This shows a ratio of 2:1 suggesting that the surface of the sample is mostly oxidic. The $Ce(OH)_x$ species cannot be completely identified through XPS. However since Ce^{4+} is the only cerium oxidation state present within these samples, it stands to reason that the precursor is $Ce(OH)_4$ agreeing with the previous literature[55].

3.2.3 XRD characterisation of ceria

Ceria produced by the hydrothermal preparation with NaOH showed much wider XRD peaks than those of ceria produced by other methods, such as the phosphate mediated synthesis.

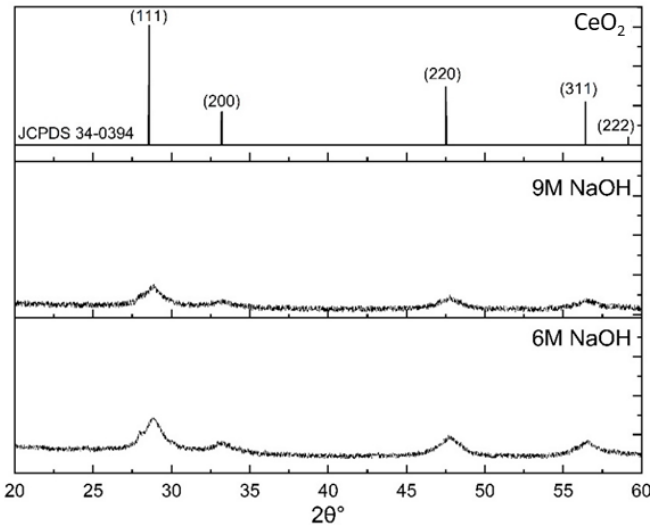

Figure 3-9: XRD pattern of the CeO_2 nanostructures produced via the 9M and 6M concentrations compared to a cerium oxide reference.

Figure 3-9 allows for a comparison between the two materials and a reference. Little difference can be observed between the 9 M and the 6 M preparation methods there are some slight changes in the FWHM of the peaks but no shifting in the 2θ values. A more

interesting comparison is between samples prepared by this method and those prepared by the phosphate method. When analysing their changes in FWHM it is evident that the peaks which correspond to the [111], [200], [220] and [311] planes are considerably broader in samples prepared by the NaOH method. This could be due to 2 reasons: 1) The NaOH formed ceria is less crystalline than that of the other methods or 2) the sizes of each crystallite are smaller for ceria produced using NaOH.

The TEM micrograph of NaOH derived ceria indicates that the nanostructures are very crystalline, and analysis of their lattice fringing (for the 9 M NaOH nanorods) is indicative of this. Additionally, these images also reveal that the same nanostructures are far smaller than the phosphate synthesised ceria, 30-40 nm diameter in comparison to the nanocubes of 250-1000 nm diameter of the phosphate derived samples. We can conclude that the peak broadening, in this case, is due to the much smaller relative size of the nanostructures synthesised.

3.2.3 Ceria and Cerium Phosphate Nanostructures via Phosphate Method

Ceria and cerium phosphate nanoparticles were formed from the hydrothermal treatment of cerium nitrate with potassium phosphate. This yielded several different morphologies, each of which was isolated and separately characterised.

3.2.3 TEM Micrographs of Ceria by the Phosphate method

TEM micrographs shown in Figure 3-10, confirm the formation of nanoparticles from the hydrothermal preparation at 200 ^{o}C with 4.125x10^{-2} M KH_2PO_4 above.

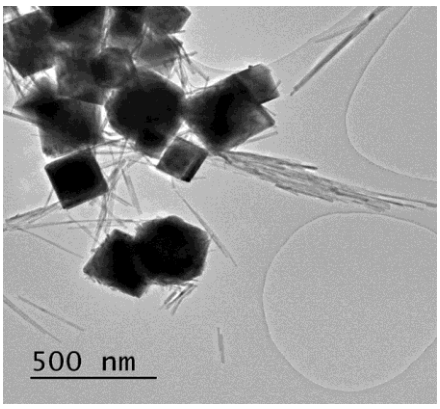

Figure 3-10: TEM micrographs of nanostructures synthesised by phosphate method at 200 ^{o}C with 4.125x10^{-2} M KH_2PO_4

The images show that a combination of two morphologies was formed ~200 nm wide nanocubes and anisotropic nanorods. Nanocubes have been reported previously and

attributed to the nitrate ions selectively adsorbing onto the [110] lattice [19,20]. In addition, anisotropic nanorods were also formed which had higher crystallinity than that of the NaOH CeO_2. This would suggest that PO_4^- groups selectively adsorb onto a crystal surface to direct the growth of this rod morphology.

An average aspect ratio of 29.2 was calculated for the nanorods which is a dramatic difference from the 9M and 6M NaOH cerium oxide nanostructures which had a maximum average aspect ratio of 5.18.

3.3 Morphological Control of Cerium Phosphate Rods

To obtain pure samples of one morphology, conditions such as reaction temperature and phosphate concentration were varied. decreasing temperatures led to an increased concentration of nanorods, whereas decreasing phosphate concentrations resulted in the formation of nanocubes.

3.3.1 Effect of Phosphate Concentration Variation

Figure 3-11 shows the effect of varying phosphate concentration with Large nanorods formed at higher phosphate concentrations and nanocubes become prevalent at lower concentrations of phosphate. Nanorods aspect ratios also increase as the phosphate concentration increases showing a change from 15 to 18.8.

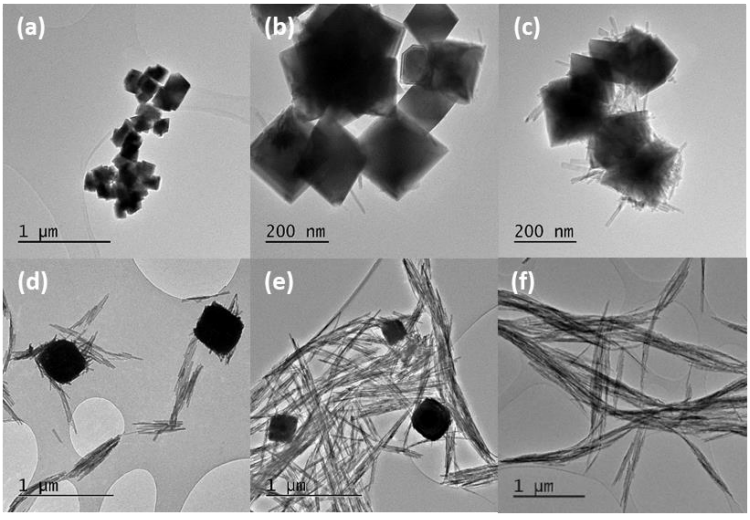

Figure 3-11: TEM micrographs of nanostructures formed by the phosphate method with varying concentrations of phosphate at 170 ˚C (a) 8.25×10^{-5} M; (b) 3.3×10^{-4} M; (c) 4.4×10^{-4} M; (d) 1.65×10^{-3} M; (e) 4.125×10^{-2} M; (f) 8.25×10^{-2} M.

XPS analysis of the Ce3d region confirms the formation of both Ce(III) and Ce(IV) species can be formed by this method depending on the concentration of phosphate. Where there is

between 0.0825 x 10^{-3} M and 0.33 x 10^{-3} M phosphate reactions show an almost 100% yield of Ce(IV) on the surface of the sample based on the $3d^{10}4f^{0}$ $(5d6s)^{0}$ → $3d^{9}4f^{0}(5d6s)^{0}$ Transition found at 917.5eV. By tracking this region and the $3d^{10}4f^{1}$ → $3d^{9}4f^{2}(5d6s)^{0}$ transition at 901 and 882 eV of Ce(III) it is possible to see that at concentrations between 0.66x10^{-3} M and 6.6x10^{-3} M a mixture of the two oxidation states is obtained while after this point over 85% of the surface is in Ce(III) form, See Figure 3-12.

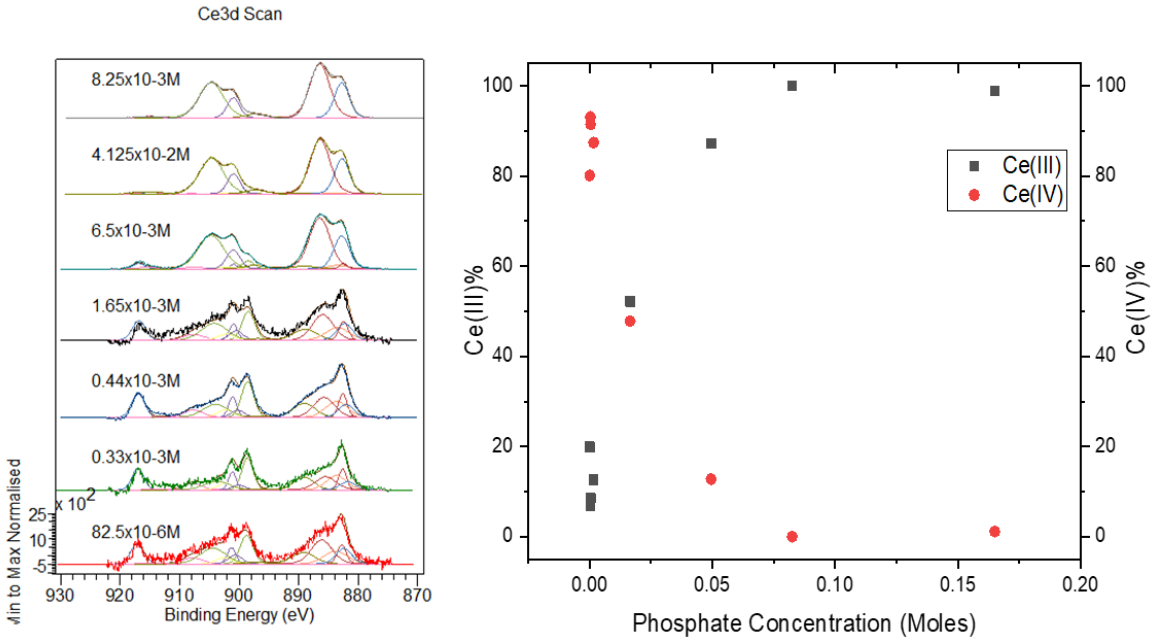

Figure 3-12: (Left) XP spectra of Ce(3d) region of nanoparticles formed with different concentrations of potassium phosphate. (Right) Comparison of Ce oxidation state at each concentration of phosphate.

This suggests that lower concentrations of phosphate the balance of oxidation lies in favour of the Ce(IV) species which in turn corresponds to the cubic nanostructures observed in the TEM micrographs. The concentration of 16.5x10^{-3}M potassium phosphate seems to correspond to an almost 50:50 mixture of the two oxidation states; TEM micrographs at this concentration shows a mixture of rods and cubes. The graph suggests that concentrations of 0.08 M phosphate would result in almost 100% Ce(III).

Figure 3-13 shows the O(1s) and P(2p) scans for cerium nanostructures produced at all concentrations. The P(2p) scan shows a gradual increase in phosphorus on the surface, at a binding energy of ~ 133.5 eV . Previous studies have shown ($CePO_4$) monazite has a P(2p) peak between 132-134 eV [62,63]. The O(1s) region shows 3 components at 529.3, 532.2 and 535.5 eV. the lowest binding energy peak at 529.3 eV corresponds to the metal oxide state and is only found in products formed with low concentrations of phosphate.

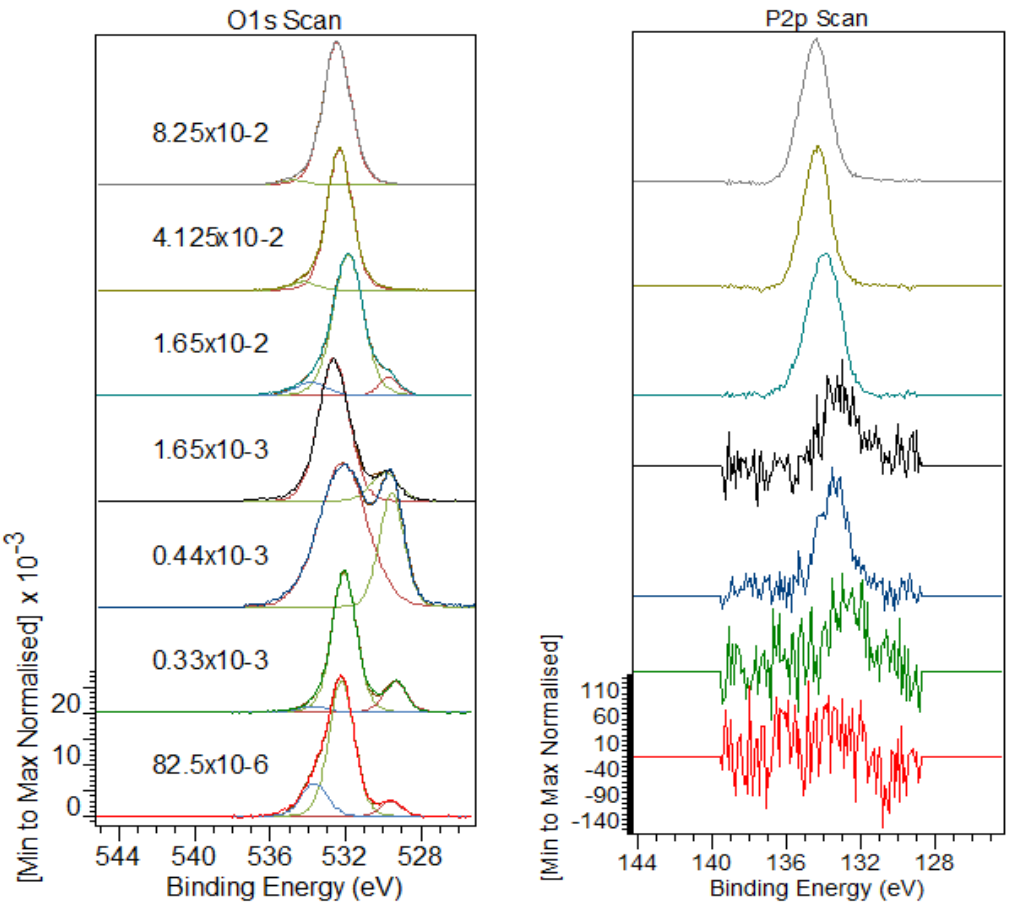

Figure 3-13. O(1s) and P(2p) Xp spectra for cerium nanoparticles formed at different concentrations of phosphate directing agent.

The peak ranging between 532 and 533 eV can be attributed to the P-O nonbridging oxygen bond which typically can shift up to 1.7 eV higher in binding energy than that of the Ce-O[62]. The highest energy component has been assigned to a Ce-O-P bridging oxygen species[64]. Together with the change in oxidation states suggests that the higher phosphate concentration products consist mainly of $CePO_4$. When comparing peak areas and quantifying the XP Spectra of 8.25 x 10^{-2} M and 4.125 x 10^{-2} M $CePO_4$ a ratio of Ce:P:O of 1:1:4 was obtained for both samples.

3.3.2 XRD Analysis

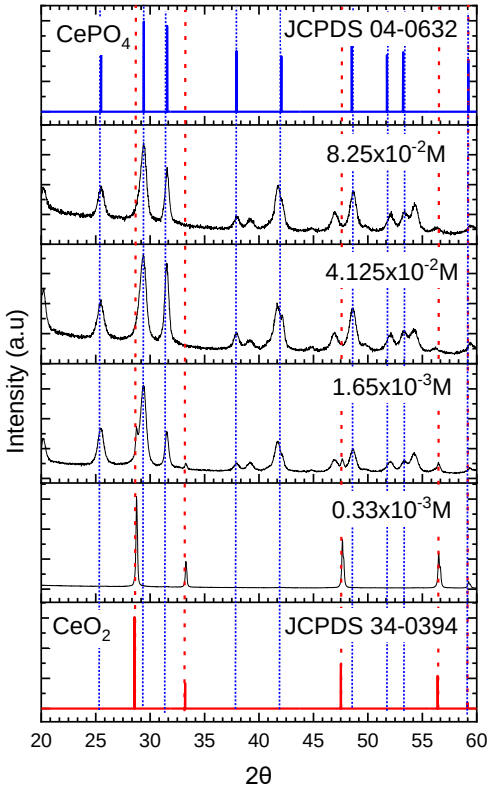

Figure 3-14: XRD patterns of cerium nanoparticles obtained at different concentrations of phosphate with reference for CeO_2 and hexagonal $CePO_4$ in blue and red, respectively.

Figure 3-14 confirms the presence of both cerium oxide and cerium phosphate with the particles formed at lower potassium phosphate concentrations displaying XRD patterns corresponding to that of cerium oxide with intense [111] and [220] peaks indicating a cubic fluorite Fm-3m space group[65]. At higher concentrations, 12 peaks are observed, with the [200], [102] and [211] being the most intense. When compared against reference samples these indicate the presence of $CePO_4$ in its hexagonal form with a $P6_222$ space group. The monoclinic phase of $CePO_4$ shows a significantly more complex XRD pattern than that of the hexagonal form, however, the most intense peaks in the hexagonal pattern, the [200] and [102], overlap with the most intense peaks of the monoclinic phase ([120] and [012]) so the possibility of a mixed phase cannot be eliminated[66,67]. Hexagonal cerium phosphate can occur in both its anhydrous and hydrated (rhabdophane) forms. A comparison of the XRD patterns of these forms of cerium phosphate shows little difference other than slight shifts in 2θ. As a result, it isn't possible to differentiate between the two forms of monazite[66,68]. However, monazite only dehydrates at temperatures exceeding 250 ^oC and so it is likely that

the bulk of the sample exists in the hydrated form. In the case of cerium nanoparticles formed in the presence of $1.65x10^{-3}$ M phosphate, a mixture of both CeO_2 and $CePO_4.xH_20$ is evident, agreeing with XPS and TEM micrographs further indicating that the large 1 µm nanocubes are cerium oxide and the rods are monazite.

3.3.3 Vibrational Spectroscopy

3.3.3 Raman

Comparison of the products formed under different concentrations in Raman sheds significant light on the crystallographic order of the samples. Figure 3-15 shows that the products formed at low concentrations of phosphate possess the typical CeO_2 pattern with an intense F_{2g} first order phonon at 459 cm^{-1} corresponding to the fluorite crystal system. There are also two weak peaks at 260 cm^{-1} and 1065 cm^{-1} caused by the 2TA and a second order phonon. Upon closer examination, a weak PO_4^- symmetric stretching band at 979 cm^{-1} can be detected corresponding to the presence of monazite in the sample.

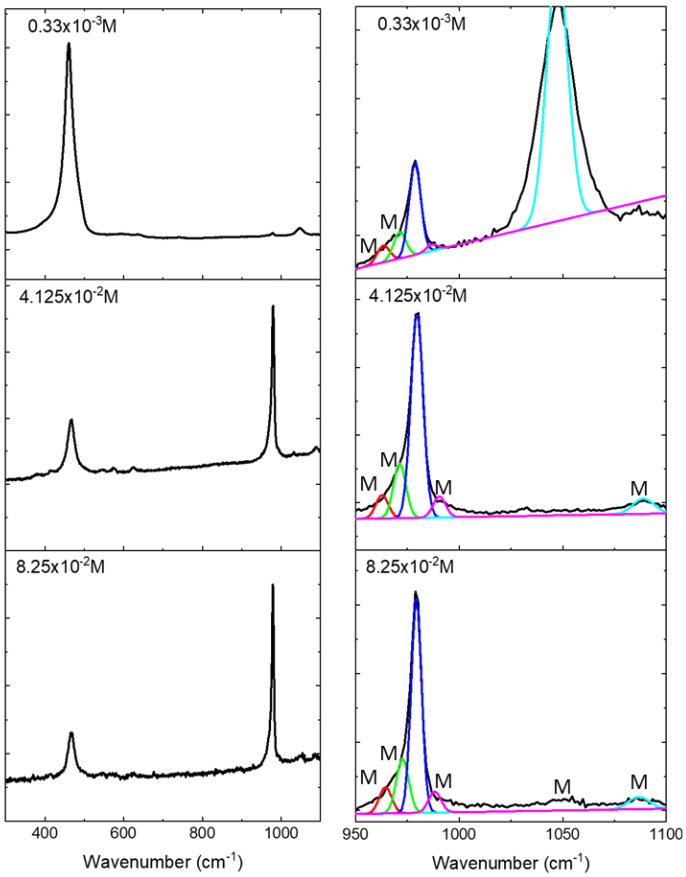

Figure 3-15: (Left) Raman spectra for cerium nanoparticles formed with different concentrations of potassium phosphate. (Right) magnification upon the PO_4 stretching region of the spectra where monoclinic and hexagonal components have been fitted. M labels monoclinic features of the spectra.

$CePO_4$ has four Raman active modes corresponding to the PO_4 stretching and bending modes shown in Table 3-4. The most intense peak in the spectra is at 468 cm^{-1} due to the v_2 mode and is seen in both the monoclinic and hexagonal phosphates but also overlaps with a cerium oxide band and so the presence of CeO_2 annot be ruled out from the final products. The most intense peak of monazite is found in the 900-1100 cm^{-1} region of the spectra and is caused by the symmetric and anti-symmetric stretching of the phosphate group. The presence of peaks in both of the 468 and 900-1100 cm^{-1} regions in the absence of other peaks, particularly the absence of the 1065 cm^{-1} peak observed in the ceria samples, indicates the preparation of relatively pure monazite at higher concentrations of phosphate. Identifying the exact species of monazite is more difficult. Hexagonal $CePO_4$ has only 2 peaks in the 900-1100 cm^{-1} region while the monoclinic form has 5, Table 3-3 and Table 3-4

IR- Spectroscopy Frequencies /cm^{-1}		
Hexagonal	**Monoclinic**	**Assignment**
	1104	V_3
	1096	
1052	1062	
1020	1025	
	995	
967	956	V_1
615	623	V_4
569	579	
542	567	
	542	

Table 3-3: Experimentally observed infrared values for monoclinic and hexagonal cerium phosphate.

Raman – Spectroscopy Frequencies /cm^{-1}		
Hexagonal	**Monoclinic**	**Assignment**
1085	1070	V_3
	1054	
	1024	
	990	
976	969	V_1
624	618	V_4
573		
466	466	V_2
377	414	

Table 3-4: Experimentally observed Raman values for monoclinic and hexagonal cerium phosphate.

The spectra suggest that most of the products formed have the hexagonal structure but there is evidence for small contributions from the monoclinic structure with peaks in the spectra at 414 and 396 cm^{-1}. There are also clear shoulders within the 900-1100 cm^{-1} region of the spectra which, when fitted, clearly indicate the presence of the monoclinic form. The

absence of evidence for the monoclinic structure in the XRD could be due to its relative lack of abundance in the samples or perhaps a small domain size.

The FT-IR spectrum of $CePO_4$ is like the Raman with 3 active modes corresponding to shown in Table 3-3. The monoclinic and hexagonal crystal structures are significantly different in the IR, the monoclinic form possessing more peaks for the v_3, anti-symmetric stretch of the phosphate group. One key difference between these two forms of monazite is the ability of the hexagonal form to be hydrated while the monoclinic does not exist in a hydrated form and so lacks any IR bands at 1620 cm^{-1} [69,70]. Cerium oxide presents very few peaks in the mid-IR range of 400-4000 cm^{-1} with only a weak peak corresponding to the Ce-O stretching mode at approximately 500 cm^{-1}. Any other peaks in this region can be assigned to adsorbed hydroxyl or carbonyl groups[71,72]. A few reports have assigned a peak between 870 and 850 cm^{-1} to the cerium oxide Ce-O bond [73–75] however, others report this as a polydentate carbonate group on the ceria.[76–78]

3.3.3 PiFM

PiFM enables the simultaneous examination of topographical and spectral information. Samples of rods formed at higher concentrations of phosphate and samples with mixed morphology were examined. Topographically PiFM indicated the presence of rods and a nanostructure consisting of nanorods associated with cerium oxide nanocubes. The rod structures formed with 8.25×10^{-2}M phosphate displayed typical cerium phosphate vibrational peaks at 970, 1020 and 1052 cm^{-1} suggesting the formation of a mainly hexagonal form of cerium phosphate, see Figure 3-16. Close inspection reveals further components at 1093, 999 and 1100 cm^{-1} which are indicative of monoclinic cerium phosphate.

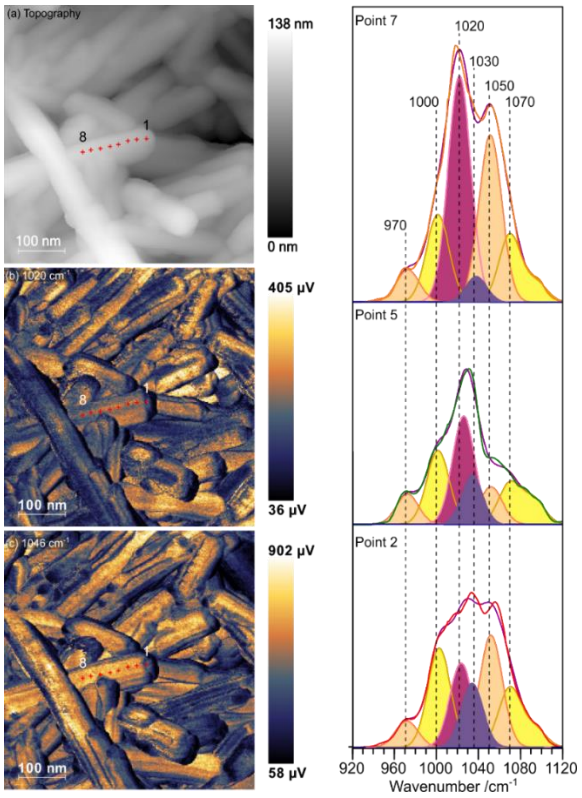

Figure 3-16: (Left) PiFM image of Topography and maps for 1620, 1046 and 1409cm^{-1} across the surface. (Right) IR spectrum obtained from different positions along a cerium phosphate rod.

From the PiFM vibrational spectra the proportions of monoclinic and hexagonal monazite change across the length of the cerium phosphate rod. The peak map of 1046 cm^{-1} cannot be used to determine differences between crystal phases as it sits between the 1052 cm^{-1} component of the hexagonal monazite and a 1033 cm^{-1} component that can probably be assigned to a surface carbonate. However, the map does indicate the presence of subunits

across the surface. The hexagonal crystal structure of cerium phosphate contains structural water when synthesised at low temperatures while the monoclinic is completely anhydrous. This relationship can be seen by comparing the 1620 cm^{-1} peak for water and the 1052 cm^{-1} peak of the hexagonal phase.

Mapping the 1620 cm^{-1} component across the sample highlights the subunits across the rod surface. Following the assumption that the 1620 cm^{-1} region indicates the presence of hexagonal monazite, it is probably that these show the distribution of the hexagonal and monoclinic phases across the particle surface.

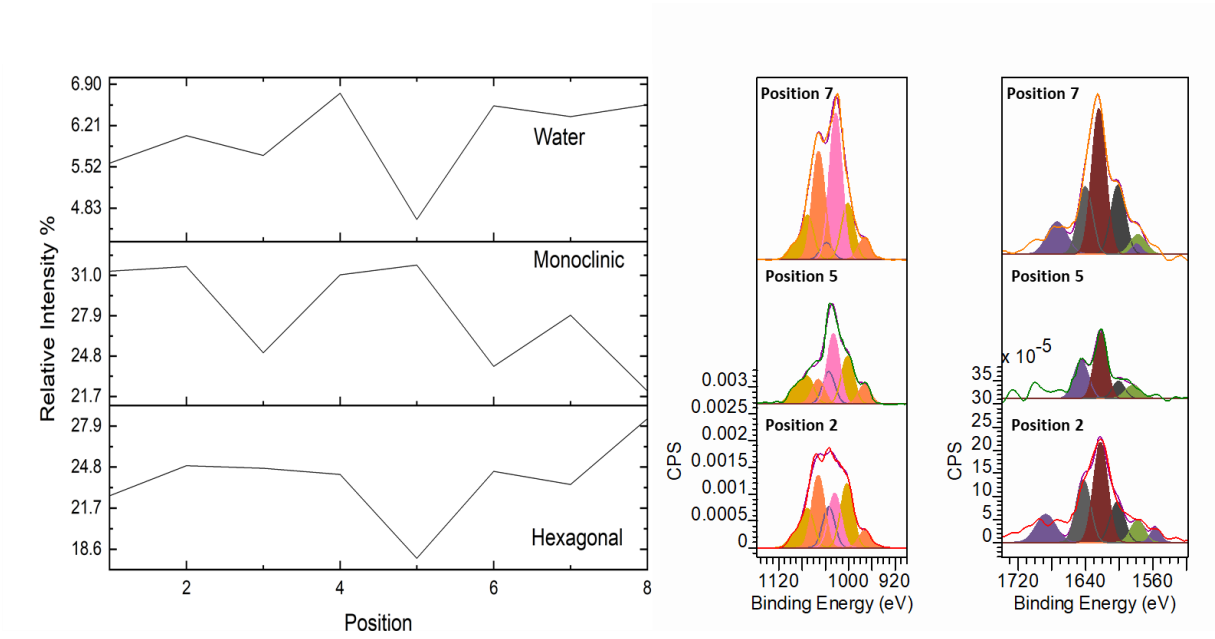

Figure 3-17: (Left) Graph showing the relative component intensities at different positions across the cerium phosphate rod. Hexagonal is 1052 cm^{-1} while hexagonal is 999, 1073 and 1101 cm^{-1}. (Right) magnified PiFM spectra for the 800-1350 cm^{-1} and 1600 cm^{-1} regions.

Carbonates adsorbed at a cerium surface in a bidentate fashion typically[79] display peaks in 5 regions of the IR spectrum 1460, 1390-1365, 1033, 850 and 835 cm^{-1} , although some studies have found the ~1400 cm^{-1} peak shifted downfield to 1410 cm^{-1} which is approximately what is observed in these PiFM measurements[80]. The PiFM data in Figure 3-17 shows peaks corresponding to all expected regions of a bidentate carbonate and when mapped topographically upon the particle, the areas which are high in the hexagonal phase display a lesser carbonate component. There is strong evidence that the bidentate carbonates tend to highlight the areas that correspond to the monoclinic lattice hinting at the possibility that the carbonates are selectively adsorbing upon the monoclinic species.

FThe PiFM topography maps of samples formed in the presence of $1.65x10^{-3}$ M phosphate agree with the XRD and TEM results indicating a mixture of the two morphologies of cerium nanoparticles. Slight components corresponding to cerium phosphate can be seen on the surface of the cube suggesting that small amounts of the phosphate phase exist upon the ceria surface, shown in Figure 3-18.

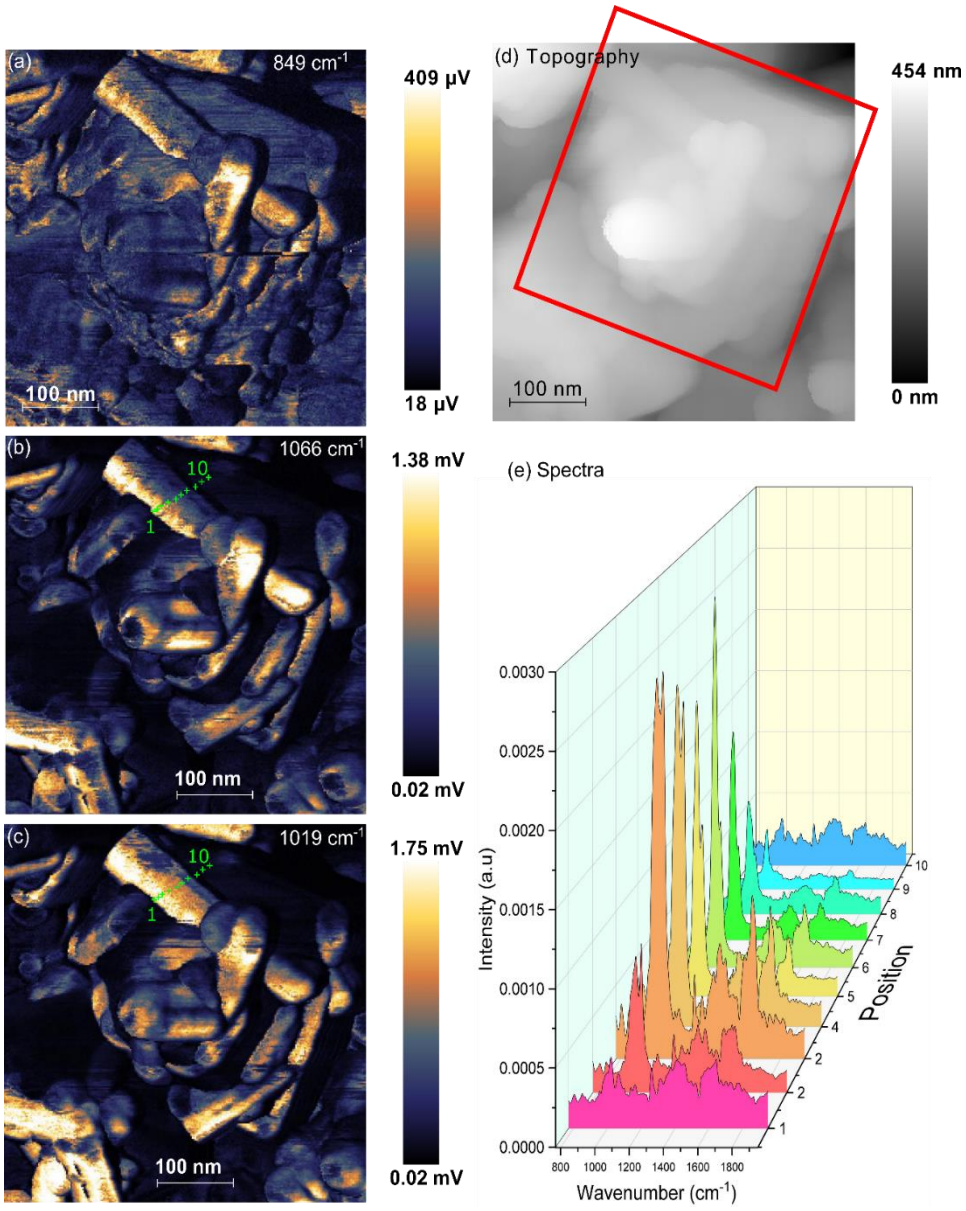

Figure 3-18: (left) PiFM topography and maps of cerium nanoparticles formed at $1.65x10^{-3}$ M Phosphate solution. (Right) PiFM spectra from positions across a nanoparticle.

The map of the 1066 cm^{-1} frequency corresponding to the V_3 peak of the monoclinic phase, suggests the presence of areas that are high in the monoclinic form. This component is in an area where the 1054 cm^{-1} peak of hexagonal cerium phosphate could interfere. However, mapping this region topographically shows that it highlights the cerium phosphate rod

structures. The map of the 1620 cm^{-1} region shows the entire sample possess water on the surface, there appear to be slight subunits along the rods, but they are less clear than in the higher concentration sample. The rods seem to show a less evident mixture of the monoclinic and hexagonal phases. The entire samples show carbonate peaks across both the cubes and rods.

3.3.4 Effect of Synthesis Temperature

Temperature also plays a significant part in the synthesis of cerium nanoparticles and by varying the temperature of the synthesis, significantly different morphologies and aspect ratios could be obtained.

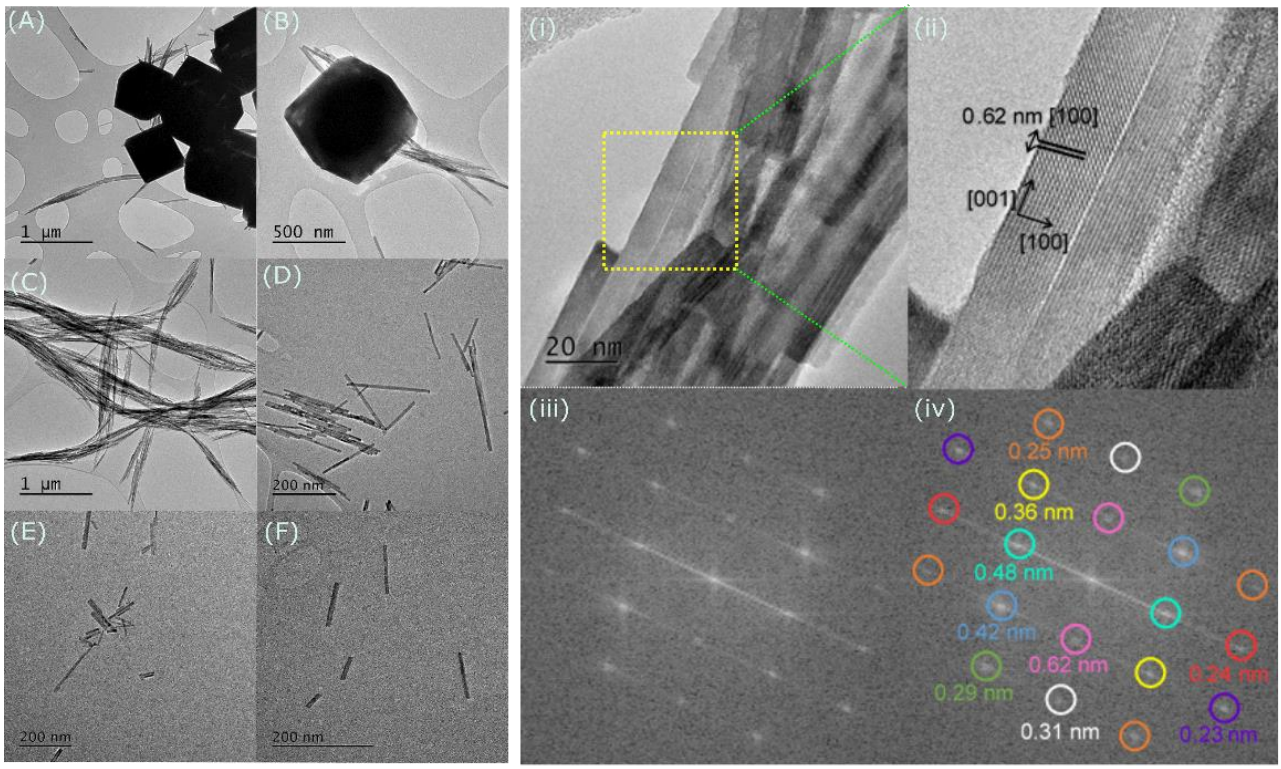

Figure 3-19. TEM micrographs of cerium nanoparticles formed at (A) 220 °C (B) 200 °C (C) 180 °C (D) 140 °C (E) 120 °C (F) 100 °C (i) 170 °C (ii) magnified image of cerium phosphate rods formed at 170 °C (iii) and (iv) show the FTT and annotated FTT, respectively.

The TEM micrographs in Figure 3-19 indicate that similar results are obtained when maintaining the concentration of sodium dihydrogen phosphate ($8.25x10^{-2}$ M) and varying the temperature between 100 and 220 °C. When decreasing temperature, the morphology of the product is changed from nanocubes to nanorods. The size of the nanoparticles increases with temperature, irrespective of their morphology.

hkl	Hexagonal d spacing (Å)	Monoclinic d spacing (Å)
[100]	6.1	n/a
[101]	4.43	4.1
[111]	3.1	3.5
[200]	3	3.3
[102]	2.8	n/a
[210]	2.3	3
[211]	2.1	2.5

Table 3-5. lattice parameters for monoclinic and hexagonal monazite

When the Lattice fringes of the nanorods in Figure 3-18 were examined where preferential growth along the [001] axis was found and the d spacing found from the FFT is consistent with literature values of cerium phosphate with a hexagonal crystal (Table 3-5)[70].

XP spectra illustrate the transition from cerium phosphate nanorods to ceria nanocubes showing a steady decrease of Ce(III) within the sample as the temperature is increased. This can be observed by the intensity of the 917.5 eV peak corresponding to the Ce(IV) oxidation state which is plotted in Figure 3-20. When fitted the XP spectra shows that the switch in preference to form Ce(III) over Ce(IV) at 8.25×10^{-2} M would occur at approximately 190 °C.

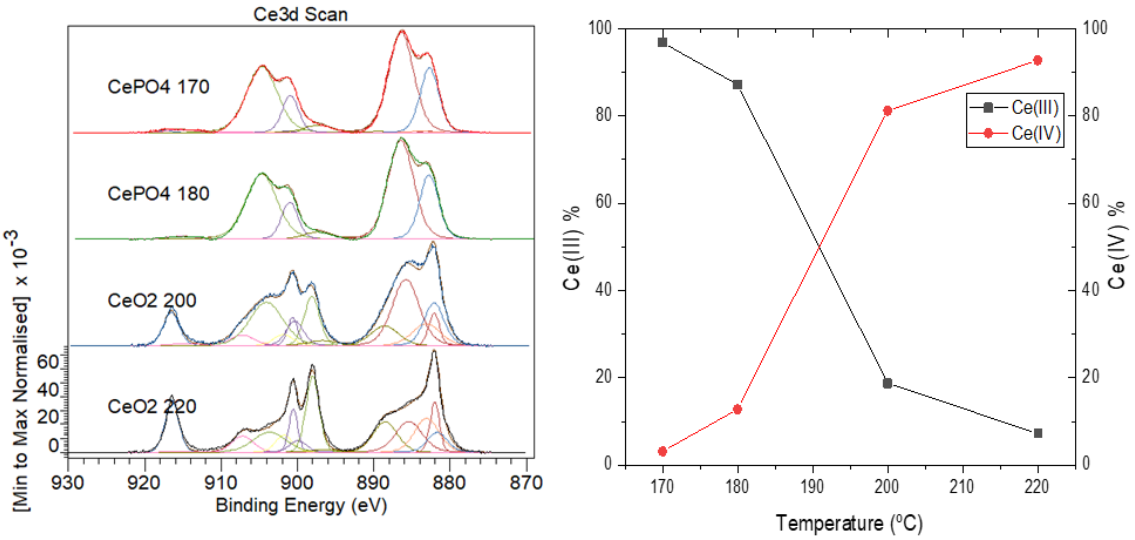

Figure 3-20: (left) XP Spectra of Cerium (3d) region across 4 different synthesis temperatures. (right) graph of Ce ion species as temperature differs.

XP spectra of the O(1s) and P(2p) (See supporting information 1) show a similar change. O(1s) shows the presence of three oxygen components across the three samples. These are at 530.39, 531.9 and 533.35 eV and correspond to oxygen atoms present in Ce-O metal oxide, A bridging Ce-O-P and a P-O bond, respectively. The metal oxide peak can be seen to

shift from 529.5 eV up to a maximum of 530.39 eV as the temperature is decreased. This shift is consistent in which the shift changes in the proportion of Ce^{4+} to Ce^{3+} and is due to both a change in oxidation state and the Ce-O-P/P-O bond shifting the region upwards. The phosphate scan only indicates one distinct peak which across all synthesis temperatures at 129.9 eV corresponding to the P-O within the phosphate group. This suggests that there are small portions of $CePO_4$ formed across all temperatures where 220 ^oC shows 98% Ce^{4+} upon the surface of the sample.

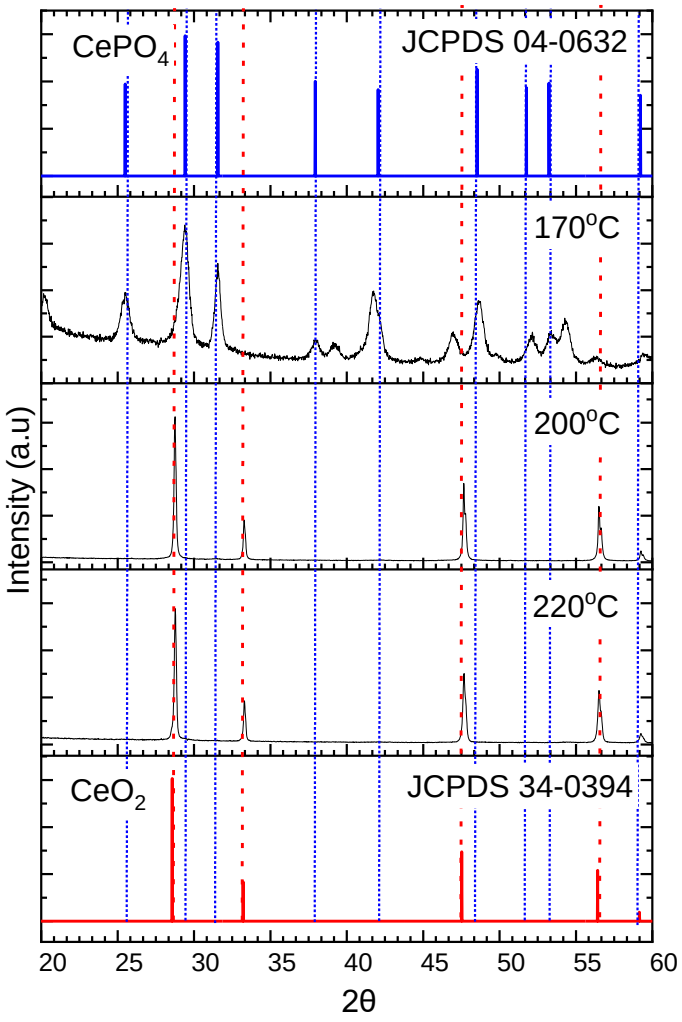

Figure 3-21. XRD for Cerium nanoparticles prepared at 220,200,170^oC with 8.25x10^{-2} M potassium phosphate. With reference samples from the ICDMS database for hexagonal $CePO_4$ and CeO_2

XRD in Figure 3-21 shows good purity of the nanoparticles where all peaks correspond to either CeO_2 or $CePO_4$ little difference can be seen when decreasing temperature from 220 to 200 ^oC suggesting that the small change of 98% to 86% Ce^{4+} is mainly a surface change as the bulk of these samples display no significant evidence of cerium phosphate peaks. This Is

slightly at odds with the TEM micrographs which indicate the presence of several cerium nanorods, which have previously been assigned as cerium phosphate by PiFM and Raman. A slight degree of wideness to the base of the [111] peak could suggest a slight degree of [200] from the hexagonal phase as the two most intense phases overlap. The particles formed at 170 °C show peaks which can be identified as the hexagonal form of monazite. As mentioned above the hydrated and anhydrous formed of $CePO_4$ are difficult to distinguish so the presence of either cannot be excluded. This data generally agrees with the lattice information obtained from the TEM and suggests that little monoclinic phase is present within the bulk. When comparing the FWHM of the peaks it is evident that the cerium particles formed at higher temperatures either tend to have larger crystal units or have a narrower size distribution.

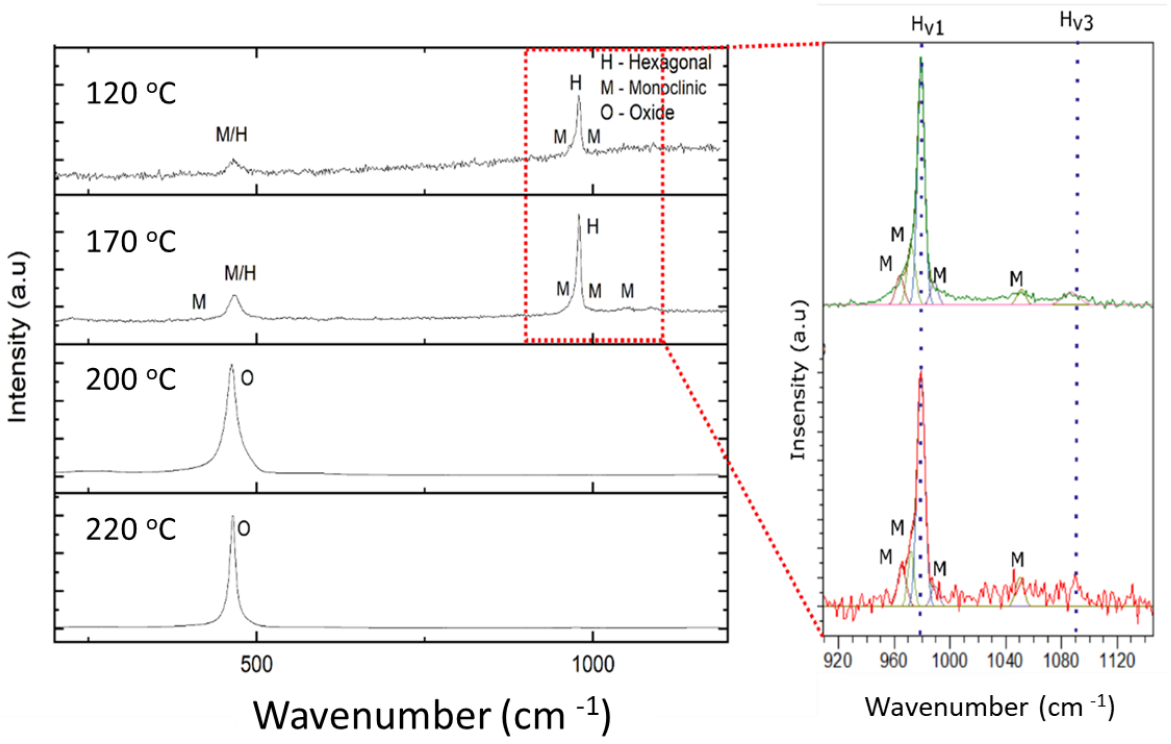

Figure 3-22. Raman spectra of cerium nanoparticles formed at temperatures between 220-120 °C after 16 hours with 8.25×10^{-2} M potassium phosphate. Magnified 930-1130 cm^{-1} region shows monoclinic and hexagonal components.

The Raman spectra of the samples formed at temperatures varying between 220-120 °C show a transition from cerium oxide to hexagonal cerium phosphate which agrees with the XRD and TEM data. The micrographs in Figure 3-22 show mainly consist of cubes that possess the signature F_{2g} phonon of the oxide. Unlike previous samples, no intensity was

found within the 900-1200 cm^{-1} region which corresponds to the phosphate stretches. Upon lowering the temperature, the characteristic hexagonal cerium phosphate 980 cm^{-1} V_1 phonon is visible. Small components from the monoclinic structure can be seen at 969, 990 and 1054 cm^{-1}. The overlap of the F_{2g} and V_4 phosphate phonon means that the presence of small quantities of the oxide form cannot be eliminated. The loss of intensity observed in the lower temperature samples is a function of the poor stability of the cerium phosphate samples which would decompose under the laser when exposed to the same conditions as other samples. This could be due to the hydrated form of cerium phosphate that tends to form at lower temperatures being less stable than its anhydrous counterpart.

3.3.5 Nanoparticle length

Temperature variation also caused changes in the dimensions of the cerium phosphate nanoparticles obtained. Those formed at lower synthesis temperatures would form significantly shorter nanorods than those formed at higher temperatures, see Figure 3-23. These particles were all formed after a period of 16 hours in the presence of 4.125×10^{-2} M potassium phosphate. At temperatures of 220°C nanoparticles have a length of 795.6 nm but when the temperature was decreased to 100 °C the particle' average length was 98.7 nm corresponding to an aspect ratio change from approximately 27 to 3.

Temperature (°C)	Average nanoparticle length (nm)
100	98.7
120	160.4
140	172.9
180	430.6
220	795.6

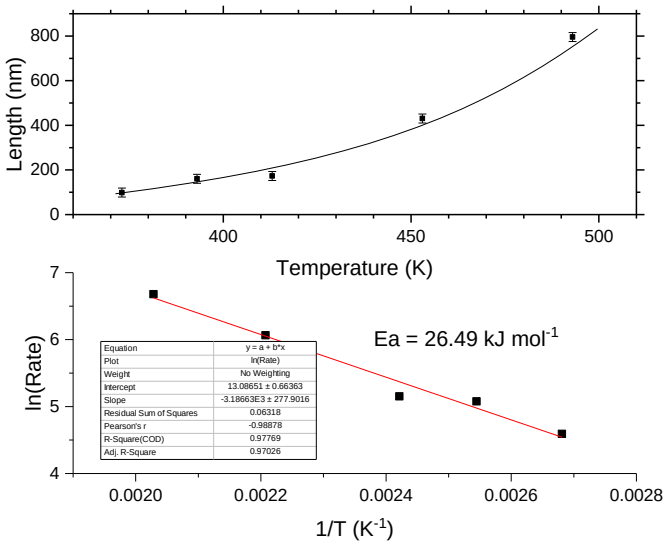

Figure 3-23: (left) Table of preparation temperature and average particle length based on a sample of 100 nanoparticles. (Right) Top – Graph of nanoparticle length against temperature. Bottom – Arrhenius plot.

An Arrhenius plot indicates activation energy of the nanoparticle growth is found to be 26.5 kJ mol^{-1}. The growth of such nanorods is likely limited by two processes: (1) the diffusion of

the reactant to the surface of the cerium subunit. (2) The reaction between the surface of the subunit and the reactant[81]. Activation energies below 40kJmol^{-1} normally indicate a diffusion-controlled reaction, while those above 40kJmol^{-1} are normally chemically controlled[82,83]. This suggests that the activation energy to nucleate $Ce(OH)_2$ seeds is low, so they form in excess. The reaction is controlled by the time taken for each of these seeds to diffuse to each other and then form $CePO_4$ through 'coarsening' this process is called ostwald ripening. In a reaction such as this, the aspect ratio of the nanoparticle is a function of the motion of these primary particles. Therefore the length of nanoparticles formed by this mechanism is proportional to the reaction time[84,85].

Similar results are obtained when studying the colour change from cloudy to a solid white during the preparation method. This change seems to correspond to the change of cerium nitrate to cerium phosphate, samples were taken after the colour change and allowed to cool contain the two characteristic peaks of cerium phosphate in Raman spectra, see supporting information 2.

3.4 Conclusion

Several hydrothermal methods of producing cerium based anisotropic nanoparticles were analysed. The NaOH and Urea methods both resulted in the formation of ceria particles however their aspect ratios were not more than those found in chapter 2. These two methods relied on the preparation of a cerium-based soft template that is heated to produce ceria. These were likely in the form of $Ce(OH)_4$ and $CeCO_3OH$ which when exposed to high temperatures will decompose to the oxide form. In the case of the Urea method, which formed $CeCO_3OH$ as its precursor no anisotropic particles were successfully produced with the product consisting of two separate particles, large nanoparticles with lengths >400nm which had a more spherical morphology and small nanocubes with dimensions of approximately 50nm. When compared to the other nanocubes obtained in the phosphate method, these were probably nanocubes of CeO_2. While the NaOH method allowed for a degree of aspect ratio tuning. Showing a change from spherical particles to nanorods when varying NaOH concentrations from 6 M to 9 M this method was not reliable and could not be easily replicated.

The one-pot hydrothermal synthesis of cerium phosphate nanorods proved a more tuneable method while being simpler to complete. The chemical composition of nanorods and cubes

was carried out with a combination of surface and spectroscopic techniques allowing for the characterisation of CeO_2 nanocubes and $CePO_4$ nanorods. The method was optimised to produce the best yield of nanorods through phosphate concentration. The combination of reaction time and the temperature was used to tune the method to produce a range of aspect ratios between 3 - 27.

3.4.1 Growth Mechanism

The combination of data obtained in this chapter suggests two competing growth mechanisms for the cerium phosphate system with the cerium hydroxide nuclei being the point of divergence. One preferentially forms cerium oxide nanocubes and the other cerium phosphate nanorods. It is suggested that at low concentrations of phosphate groups the NO_3^- counter ion directs growth by selectively adsorbing onto $Ce(OH)_2$ nuclei. Based on the following reaction:

step 1: $Ce(NO_3)_3 + H_2O \rightleftharpoons Ce(OH)_2+ + 3NO_3- + H+$

step 2: $Ce(OH)_2+ + 3NO_3- + H+ + H_2NaPO_4 \rightleftharpoons CePO_4 + NaOH + 3HNO_3$

When there is insufficient phosphate, step two does not occur and instead the $Ce(OH)_2$ undergoes a process of dissolution-crystallisation forming CeO_2 nanoparticles which selectively adsorb NO_3^- ions onto the [100] plane stunting growth and resulting in the formation of ceria nanocubes[86–88]. A illustration of a possible growth mechanism is below in Figure 3-24.

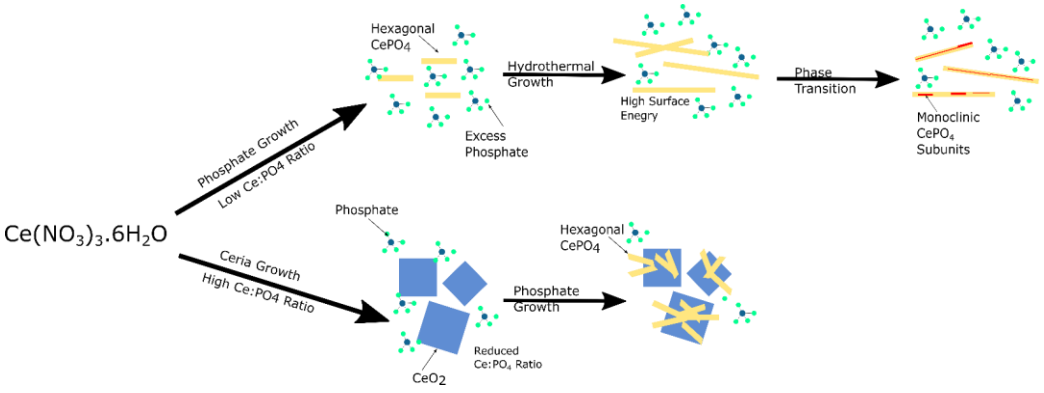

Figure 3-24: Illustration of the suggested growth mechanism of cerium nanoparticles based on phosphate concentration.

However, as the ratio of Ce: PO_4 begins to decrease the position of equilibrium between the phosphate selective adsorption mechanism and the dissolution crystallisation changes allowing for the nucleation of $CePO_4$ on the surface of the cerium oxide nanocubes which

develop into the two-phase agglomerates of ceria nanocubes and cerium phosphate nanorods.

When the phosphate concentration is sufficiently high, the position of equilibrium lies entirely towards the formation of cerium phosphate nanorods shown by the presence of only Ce^{3+} in the XPS spectra and the lack of ceria defining peaks in XRD. These rods form and when phosphate is in excess, they adsorb the phosphate groups to their surface which at highly acidic pH results in a region of high surface energy across the nanorods. These regions undergo crystallographic rearrangement to the monoclinic phase to reduce their surface energy resulting in the formation of monoclinic monazite subunits across the nanorod structure. This is less clear in rods that form upon ceria nanocubes as the phosphate concentration isn't high enough to trigger this transition to the same extent[89].

Higher temperatures direct growth towards the formation of cerium dioxide nanocubes which were not detected below 180 ^{o}C. This has been explained by the growth of cerium dioxide nanocubes proceeding by a dissolution-crystallisation mechanism; at the higher temperatures, the solubility of ceria increases in the solution until the solution becomes super saturated and results in the nucleation of ceria nanocubes. These cubes then undergo a process of ostwald ripening resulting in the formation of larger cerium oxide nanoparticles[90].

3.5 References

1 Y. Lin, Z. Wu, J. Wen, K. Ding, X. Yang, K. R. Poeppelmeier and L. D. Marks, *Nano Letters*, 2015, **15**, 5375–5381.

2 N. Ta, J. (Jimmy) Liu, S. Chenna, P. A. Crozier, Y. Li, A. Chen and W. Shen, *Journal of the American Chemical Society*, 2012, **134**, 20585–20588.

3 N. W. Kim, D. K. Lee and H. Yu, *RSC Advances*, 2019, **9**, 13829–13837.

4 T. Naganuma, *Nano Research*, 2017, **10**, 199–217.

5 F. Gu, Z. Wang, D. Han, C. Shi and G. Guo, *Materials Science and Engineering B: Solid-State Materials for Advanced Technology*, 2007, **139**, 62–68.

6 W. X. Tang and P. X. Gao, *MRS Communications*, 2016, 6, 311–329.

7 G. Pulido-Reyes, I. Rodea-Palomares, S. Das, T. S. Sakthivel, F. Leganes, R. Rosal, S. Seal and F. Fernández-Pinãs, *Scientific Reports*, 2015, **5**, 1–14.

8 M. Lykaki, E. Pachatouridou, E. Iliopoulou, S. A. C. Carabineiro and M. Konsolakis, *RSC Advances*, 2017, **7**, 6160–6169.

9 C. Y. Cao, Z. M. Cui, C. Q. Chen, W. G. Song and W. Cai, *Journal of Physical Chemistry C*, 2010, **114**, 9865–9870.

10 J. H. Pang, Y. Liu, J. Li and X. J. Yang, *Rare Metals*, 2019, **38**, 73–80.

11 M. Farahamndjou, M. Zarinkamar and T. Firoozabadi, *Revista Mexicana de Física*, 2016, **62**, 496–499.

12 S. Sathyamurthy, K. J. Leonard, R. T. Dabestani and M. P. Paranthaman, *Nanotechnology*, 2005, **16**, 1960–1964.

13 Z. Ji, X. Wang, H. Zhang, S. Lin, H. Meng, B. Sun, S. George, T. Xia, A. E. Nel and J. I. Zink, *ACS Nano*, 2012, **6**, 5366–5380.

14 C. Sun, H. Li and H. Zhang, *Nanotechnology*, 2005, **16**, 2502.

15 H. X. Mai, L. D. Sun, Y. W. Zhang, R. Si, W. Feng, H. P. Zhang, H. C. Liu and C. H. Yan, *Journal of Physical Chemistry B*, 2005, **109**, 24380–24385.

16 M. Hirano and E. Kato, *Journal of the American Ceramic Society*, 2005, **79**, 777–780.

17 W. Wang, J. Y. Howe, Y. Li, X. Qiu, D. C. Joy, M. P. Paranthaman, M. J. Doktycz and B. Gu, *Journal of Materials Chemistry*, 2010, **20**, 7776–7781.

18 K. S. Lin and S. Chowdhury, *International Journal of Molecular Sciences*, 2010, 11, 3226–3251.

19 H.-X. Mai, L.-D. Sun, Y.-W. Zhang, R. Si, W. Feng, H.-P. Zhang, H.-C. Liu and C.-H. Yan, *J. Phys. Chem. B*, 2005, 24380–24385.

20 K. Zhou, X. Wang, X. Sun, Q. Peng and Y. Li, *Journal of Catalysis*, 2005, **229**, 206–212.

21 C. Dong, Y. Zhou, N. Ta and W. Shen, *CrystEngComm*, 2020, **22**, 3033–3041.

22 P. X. Huang, F. Wu, B. L. Zhu, X. P. Gao, H. Y. Zhu, T. Y. Yan, W. P. Huang, S. H. Wu and D. Y. Song, *J. Phys. Chem. B*, 2005, 19169–19174.

23 R. Si and M. Flytzani-Stephanopoulos, *Angew. Chem. Int. Ed*, 2008, **47**, 2884–2887.

24 A. Gupta, S. Das, C. J. Neal and S. Seal, *Journal of Materials Chemistry B*, 2016, **4**, 3195–3202.

25 C. Xia, C. Hu, P. Chen, B. Wan, X. He and Y. Tian, *Materials Research Bulletin*, 2010, **45**, 794–798.

26 L. Yan, R. Yu, J. Chen and X. Xing, *Crystal Growth and Design*, 2008, **8**, 1474–1477.

27 B. Xu, Q. Zhang, S. Yuan, M. Zhang and T. Ohno, *Applied Catalysis B: Environmental*, 2015, **164**, 120–127.

28 L. Qian, W. Du, Q. Gong and X. Qian, *Materials Chemistry and Physics*, 2009, **114**, 479–484.

29 K. Rajesh, P. Mukundan, P. K. Pillai, V. R. Nair and K. G. K. Warrier, *Chemistry of Materials*, 2004, **16**, 2700–2705.

30 X. Wen, C. Li and F. Meng, *Journal Wuhan University of Technology, Materials Science Edition*, 2014, **29**, 229–232.

31 L. Yan, R. Yu, J. Chen and X. Xing, *Crystal Growth and Design*, 2008, **8**, 1474–1477.

32 Y. P. Fang, A. W. Xu, A. M. Qin and R. J. Yu, *Crystal Growth and Design*, 2005, **5**, 1221–1225.

33 A. Ochiai and S. Utsunomiya, *Minerals*, 2017, **7**, 84.

34 G. Vinothkumar, I. L. Arun, P. Arunkumar, W. Ahmed, S. Ryu, S. W. Cha and K. S. Babu, *Journal of Materials Chemistry B*, 2018, **6**, 6559–6571.

35 P. Pusztai, H. Haspel, I. Y. Tóth, E. Tombácz, K. László, Á. Kukovecz and Z. Kónya, *ACS Applied Materials and Interfaces*, 2015, **7**, 9947–9956.

36 Z. Ji, X. Wang, H. Zhang, S. Lin, H. Meng, B. Sun, S. George, T. Xia, A. E. Nel and J. I. Zink, 2012, **6**, 5366–5380.

37 R. G. C. C.H. Bamford, C.F.H. Tipper, *Diffusion-Controlled Reactions in Solution*, Elsevier, 1985, vol. 25.

38 E. Ackerman, R. L. Berger, W. L. Blair and G. K. Strother, *Biophysical Journal*, 1963, **3**, 469–478.

39 J. W. Mullin, *Crystallisation*, American Chemical Society (ACS), 2002, vol. 6.

40 M. Widdrat, E. Schneck, V. Reichel, J. Baumgartner, L. Bertinetti, W. Habraken, K. Bente, P. Fratzl and D. Faivre, . *Phys. Chem. Lett.*, 2017, **8**, 1132–1136.

41 G. Cao and Y. Wang, *Nanostructures and Nanomaterials*, WORLD SCIENTIFIC, 2011, vol. 2.

42 K. M. Carroll, A. W. Knoll, H. Wolf and U. Duerig, *Langmuir*, 2018, **34**, 73–80.

43 K. Biswas, B. Das and C. N. R. Rao, *Journal of Physical Chemistry C*, 2008, **112**, 2404–2411.

44 P. Gao, M. Grätzel, M. K. Nazeeruddin, A. J. Nozik, G. Conibeer, M. C. Beard, P. Gao, M. Grätzel, M. K. Nazeeruddin, M. Gra, D. Ginley, Y. Okada, W. Van-Sark, A. Bett, S. Glunz, T. Gessert, L. M. Peter, M. K. Nazeeruddin, N.-G. Park and A. Zaban, *Advanced Concepts in Photovoltaics*, Royal Society of Chemistry, 2014, vol. 11.

45 T. A. Vu, M. M. Reagan, D. Li, B. Legg, J. J. De Yoreo, J. F. Banfield and H. Zhang, *CrystEngComm*, 2014, **16**, 1466–1471.

46 N. T. K. Thanh, N. Maclean and S. Mahiddine, *Chem. Rev.*, 2014, **114**, 7610–7630.

47 Fairley N, *CasaXPS Manual: 2.3.15 Spectroscopy*, 2009.

48 E. Bêche, P. Charvin, D. Perarnau, S. Abanades and G. Flamant, *Surface and Interface Analysis*, 2008, **40**, 264–267.

49 L. Li, Y. Diao and L. Xin, *Journal of Rare Earths*, 2014, **32**, 409–415.

50 R. Eloirdi, P. Cakir, F. Huber, A. Seibert, R. Konings and T. Gouder, *Applied Surface Science*, 2018, **457**, 566–571.

51 D.-E. Zhang, X.-J. Zhang, X.-M. Ni, J.-M. Song and H.-G. Zheng, *ChemPhysChem*, 2006, **7**, 2468–2470.

52 J. I. Langford and A. J. C. Wilson, *Journal of Applied Crystallography*, 1978, **11**, 102–113.

53 X. Feng, H. Chen, F. Jiang and X. Wang, *Catalysis Science and Technology*, 2019, **9**, 2849–2857.

54 J. Stoch and J. Gablankowska-Kukucz, *Surface and Interface Analysis*, 1991, **17**, 165–167.

55 J. Luo, F. Meng, L. Wang and Y. Jiang, *Micro & Nano Letters*, 2013, **8**, 19–22.

56 R. Zamiri, H. A. Ahangar, A. Kaushal, A. Zakaria, G. Zamiri, D. Tobaldi and J. M. F. Ferreira, *PLoS ONE*, , DOI:10.1371/journal.pone.0122989.

57 W. H. Weber, K. C. Hass and J. R. McBride, *Physical Review B*, 1993, **48**, 178–185.

58 M. Radović, Z. Dohcevicr-Mitrovic, N. Paunović, M. Šćepanović, B. Matović and Z. V. Popović, *Acta Physica Polonica A*, 2009, **116**, 84–87.

59 J. P. Mathieu and M. Lounsbury, *Discussions of the Faraday Society*, 1950, **9**, 196–207.

60 R. C. Deus, R. A. C. Amoresi, P. M. Desimone, F. Schipani, L. S. R. Rocha, M. A. Ponce, A. Z. Simoes and E. Longo, *Ceramics International*, 2016, **42**, 15023–15029.

61 A. Filtschew, K. Hofmann and C. Hess, *Journal of Physical Chemistry C*, 2016, **120**, 6694–6703.

62 E. Bêche, P. Charvin, D. Perarnau, S. Abanades and G. Flamant, *Surface and Interface Analysis*, 2008, **40**, 264–267.

63 S. Sisira, L. A. Jacob, K. P. Mani, P. R. Biju, N. V. Unnikrishnan and C. Joseph, *Journal of Materials Science: Materials in Electronics*, 2019, **30**, 11354–11367.

64 A. Kumar and R. Srivastava, *Sustainable Energy and Fuels*, 2019, **3**, 2475–2489.

65 K. Deori, D. Gupta, B. Saha, S. K. Awasthi and S. Deka, *Journal of Materials Chemistry A*, 2013, **1**, 7091–7099.

66 M. Llusar, B. Escuder, J. López-Castro, S. Trasobares and G. Monrós, *Gels*, 2017, **3**, 23.

67 P. Pusztai, T. Simon, Á. Kukovecz and Z. Kónya, in *Journal of Molecular Structure*, 2013, vol. 1044, pp. 94–98.

68 J. F. Lima, P. C. De Sousa Filho and O. A. Serra, *Ceramics International*, 2016, **42**, 7422–7431.

69 N. Ekthammathat, T. Thongtem, A. Phuruangrat and S. Thongtem, *Journal of Nanomaterials*, 2012, **2012**, 1–6.

70 J. Bao, R. Yu, J. Zhang, X. Yang, D. Wang, J. Deng, J. Chen and X. Xing, *CrystEngComm*, 2009, **11**, 1630–1634.

71 Y. H. Liu, J. C. Zuo, X. F. Ren and L. Yong, *Metalurgija*, 2014, **53**, 463–465.

72 A. S. Dezfuli, M. R. Ganjali, H. R. Naderi and P. Norouzi, *RSC Advances*, 2015, **5**, 46050–46058.

73 S. Phoka, P. Laokul, E. Swatsitang, V. Promarak, S. Seraphin and S. Maensiri, *Materials Chemistry and Physics*, 2009, **115**, 423–428.

74 K. Babitha, A. Sreedevi, P. K P, B. Sabu and T. Varghese, *Indian Journal of Pure and Applied Physics*, 2015, **53**, 596–603.

75 P. S. E. Kumar1 ï€ª and K. Balasubramanian3, *Recent Research in Science and Technology*.

76 S. Agarwal, X. Zhu, E. J. M. Hensen, B. L. Mojet and L. Lefferts, *Journal of Physical Chemistry C*, 2015, **119**, 12423–12433.

77 S. Agarwal, X. Zhu, E. J. M. Hensen, L. Lefferts and B. L. Mojet, *Journal of Physical Chemistry C*, 2014, **118**, 4131–4142.

78 S. Agarwal, L. Lefferts, B. L. Mojet, D. A. J. M. Ligthart, E. J. M. Hensen, D. R. G. Mitchell, W. J. Erasmus, B. G. Anderson, E. J. Olivier, J. H. Neethling and A. K. Datye, *ChemSusChem*, 2013, **6**, 1898–1906.

79 F. Bozon-Verduraz and A. Bensalem, *Journal of the Chemical Society, Faraday Transactions*, 1994, **90**, 653–657.

80 M. Cargnello, N. L. Wieder, T. Montini, R. J. Gorte and P. Fornasiero, *Journal of the American Chemical Society*, 2010, **132**, 1402–1409.

81 R. Viswanatha, P. K. Santra, C. Dasgupta and D. D. Sarma, *Growth mechanism of nanocrystals in solution: ZnO, a case study*, 2007.

82 G. Uğuz and F. Geyikçi, *KUJES*, 2019, **5**, 1–15.

83 J. E. Crooks, *Annual Reports Section "C" (Physical Chemistry)*, 1984, **81**, 258–289.

84 K. Biswas, B. Das and C. N. R. Rao, *Journal of Physical Chemistry C*, 2008, **112**, 2404–2411.

85 R. Viswanatha, P. K. Santra, C. Dasgupta and D. D. Sarma, *Growth mechanism of nanocrystals in solution: ZnO, a case study*, 2007.

86 Q. Wu, F. Zhang, P. Xiao, H. Tao, X. Wang, Z. Hu and Y. Lü, *Journal of Physical Chemistry C*, 2008, **112**, 17076–17080.

87 H. X. Mai, L. D. Sun, Y. W. Zhang, R. Si, W. Feng, H. P. Zhang, H. C. Liu and C. H. Yan, *Journal of Physical Chemistry B*, 2005, **109**, 24380–24385.

88 C. Dong, Y. Zhou, N. Ta and W. Shen, *CrystEngComm*, 2020, **22**, 3033–3041.

89 J. Bao, R. Yu, J. Zhang, X. Yang, D. Wang, J. Deng, J. Chen and X. Xing, *CrystEngComm*, 2009, **11**, 1630–1634.

90 Z. Yang, K. Zhou, X. Liu, Q. Tian, D. Lu and S. Yang, *Nanotechnology*, 2007, **18**, 185606.

Chapter 4 Plasmonic Coating Optimization

4.1 Introduction

When using metal nanoparticles, the morphology of the particles is key to their properties. Different morphologies result in different crystal surfaces and atoms being available for reaction[1] and this effect is important whether preparing catalysts[2,3], photonics[4,5], or other materials[6,7]. The effect is key in both typical particles and particles with coatings, such as core-shell. The morphology, thickness and roughness of a metal coating in a core-shell particle contribute to the overall material properties[8]. In the field of catalysis, particle size distribution can dramatically affect the selectivity and activity of a catalyst. Understanding the relationships between the surface and the supported coat or nanoparticle is imperative in preparing consistent and reproducible catalysts which can be optimised for given reaction systems.

When developing optically active particles there are clear parameters that can be optimised to impact their behaviour, such as the metal, morphology of particle and surface roughness, e.g. a large spherical silver nanoparticle will have different optical behaviour to a small gold nanorod[9,10]. Core-shell particles have additional preparation challenges as developing suitable coatings for the nanomaterials can be difficult. In terms of photonics, it is important due to the surface sensitivity of plasmon resonance[11].

There are several methods to successfully form coatings such as thin films including, but not limited to, chemical vapour deposition[12], spin coating, and dip coating[13]. However, vacuum methods such as PVD and CVD struggle to coat the more complex 3D geometries of nanorods and other morphologies. This originates from the fact that the deposition species must interact with the core from all directions. To overcome this difficulty, more complex methods are needed and generally, these are carried out in solution relying on the functionalisation of surfaces with molecules to induce electrostatic attraction between the deposition particle and the core[14]. Often the controlled reduction of precursor molecules onto a functionalised particle is used[15]. This approach has two key advantages: 1) Allows for the control of the interactions between metal precursor and the functionalising agent. 2) Small changes in method parameters such as pH, temperature and time can allow precise control of film thickness and morphology[14].

This chapter focuses on these synthetic routes using functionalisation to produce metal coatings on several different surfaces. Several different variables contribute to the successful coating, including:

- The surface-coating interaction. The affinity of a metal-to-metal oxide bond between the metal oxide support and the metal adatom.
- The ratio of surface area: metal. This is decided by a few factors such as morphology and porosity of the metal oxide support. The amount of metal precursor capable of forming a coat is a function of the volume of the precursor and its concentration.

While the ratio of surface area to metal is relatively simple to change through minor variations in concentration or volume, the affinity between any given material and its coating is an inherent property of that system. However, this limitation may be overcome through the functionalisation of a surface with molecules that possess functional groups that can increase the attraction between the two mediums. Such systems are often complex and require careful optimisation. To that effect, in this chapter, a model surface is used to study the interactions of gold when supported on hematite in the presence of different surfactants. The most promising combination of these was then used on a real nanoparticle system.

4.2 Method

4.2.1 Model Surfaces

Single crystal hematite samples were deemed unsuitable surfaces to optimise coatings since such samples are expensive and are unrealistic surfaces. Furthermore, the results discussed in Chapter 2, showed that hematite nanoparticles are generally composed of an aggregation of different crystal subunits. Polycrystalline samples would therefore better emulate the nanoparticle surfaces. Realistic hematite surfaces were obtained by taking geological hematite samples and cutting them to 2 mm in thickness so that they could be analysed on AFM and XPS. These samples were then smoothed and polished to a degree that their surfaces were flat. The processing of the samples was carried out by the school of Geology at Cardiff University. These were then further polished using diamond paste. Each sample was treated with one droplet of each treatment and allowed to dry for a period of 6 hours in sequence.

4.2.2 Nanoparticle Preparation

As mentioned above, controlled reduction with a functionalised surface is a reliable and optimisable method to produce thin films upon 3D particles. One such method was first used by Wang et al.[16,17] on hematite nanorice particles. The gold coating is developed in two stages; firstly, gold "seed" particles approximately 5 nm in diameter are adhered to the hematite surface using 3-aminopropyl triethoxysilane (APTES). The gold coating was then grown from the seeds by precipitating gold from the solution, Figure 4-1.

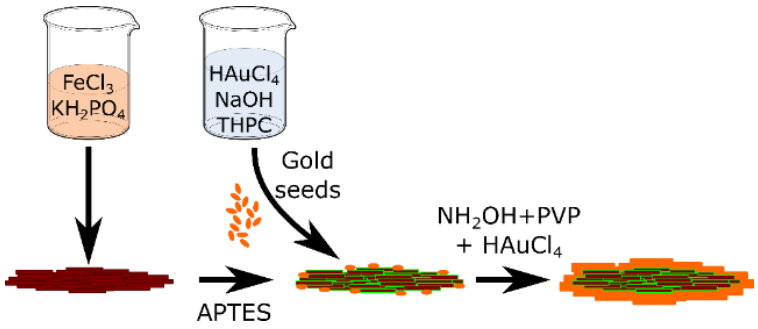

Figure 4-1. Illustration of the preparation of gold coated hematite rods. The rods were synthesised in the presence of structure directing phosphates and subsequently coated treated with 3-aminopropyl triethoxysilane (APTES) which helped bond separately synthesised ~ 5 nm diameter gold seeds to the surface. The coating layer was then precipitated onto the rods by reduction from solution with hydroxylamine in the presence of polyvinylpyrrolidone (PVP).

4.2.3 Phosphate Hematite Preparation

Hematite nanorice were prepared by precipitation from 50 mL of 40 mM ferric chloride solution ($FeCl_3$), 10ml of potassium dihydrogen phosphate (H_2KPO_4) varying concentration from 0 to 70 mM with an additional 40 mL of deionised water before being sealed and heated in an oil bath for up to 72 hours at 110 ^oC Following this, the hematite particles are carefully washed in a centrifuge using ethanol and water to remove impurities and narrow particle size distribution.

4.2.3 1,2 Propanediamine Hematite

7 mL of 0.86 M $FeCl_3$ were added to a glass pressure reactor and stirred in an ice bath. 7 mL of 1,2 propanediamine was added slowly to the flask and allowed to stir in the ice bath for 15 minutes. The flask was then sealed and heated at 180 °C for 16 hours. After cooling, the nanoparticles were separated by centrifugation and washed thoroughly with ethanol and water before freeze-drying.

4.2.3 APTES Functionalization of Nanoparticles

30 mg of hematite rods were suspended in 25 mL of ethanol and 6 mL of 3-aminopropyl triethoxysilane (APTES) in a 120 mL sealed plastic bottle and allowed to stir overnight. The resulting solution is centrifuged to separate the treated nanorods which were washed with additional ethanol before being re-suspended in 30 mL of EtOH and stored in a 50 mL plastic centrifuge tube.

4.2.3 Gold Seed Preparation

93 mL of DI H_2O was placed into a 120 mL plastic bottle followed by 3 mL of 0.2 M NaOH solution and 2 mL of tetrakis (hydroxymethyl) phosphonium chloride (THPC) solution before 2 mL (50 mM) of $HAuCl_4$ solution was added. The solution turned into a tea-coloured solution within few seconds. The solution was stirred for 30 seconds longer and the bottle with the freshly synthesised seed gold spheres was stored in the fridge for 1 hour before use.

4.2.3 Decoration of Hematite Nanorods

The APTES functionalised material was pelleted using a centrifuge and suspended in 20 mL of the seed gold sphere solution and stored for 6 hours. The partly decorated rods were then separated with a centrifuge and the first step was repeated. The gold decorated rods were extensively washed in deionised water and suspended in 20 mL of ethanol.

4.2.3 Gold Shell Synthesis

40 mg polyvinylpyrrolidone (PVP) was added to 32.5 mL deionised water in a 50 mL plastic bottle and PVP was then dissolved in water by sonication for 1 hour. The gold coating solution was prepared by adding 60 mg of K_2CO_3 to 22 mL of deionised water and 3 mL of 50 mM $HAuCl_4$ solution. The coating solution rested for 6 hours before treating the nanoparticles. 5 mL of the gold coating solution was added to 0.5 mL of decorated hematite rods and the solution was mixed in a sonication bath before 2.5 mL of hydroxylamine solution was added. The bottle was then immediately mixed by shaking and then left undisturbed for 60 min at room temperature. The suspension was washed, extracted by centrifuge, and re-suspended in water. The gold coating of the silica coated particles followed an identical procedure.

4.2.3 Silica Shell Synthesis

20 mg of hematite was re-suspended in 10 mL of deionised water and treated with the addition of 0.243 g PVP. The solution was left to rest for an hour before being centrifuged at 8000 rpm for 30 minutes to remove any remaining un-reacted surfactant. The solid was then re-suspended in 100 mL of ethanol in a 250 mL plastic bottle. 6 mL of the particle solution was taken and added to 1.2 mL of deionised water and 0.05 mL of tetramethylammonium hydroxide, (TMAH). Tetraethyl orthosilicate, (TEOS) was added stepwise to the system while under sonication for 8 hours. The total volume of TEOS stated in Figure 4-24 corresponds to the sum of equal volumes added every two hours whilst stirring.

4.2.3 Cerium Phosphate Rod Coatings

4.2.3 PVP Functionalisation

50 mg of $CePO_4$ nanorods was suspended in 20 mL of deionised water. 0.65g of PVP was dissolved in 20 mL of deionised water in a glass beaker. The two solutions were combined and allowed to stir for 1 hour at room temperature. The $CePO_4$/PVP product was separated with centrifugation at 4350 RPM for 1-hour. The pellet of $CePO_4$/PVP was resuspended in 30 mL of ethanol and stored in a 50 mL plastic centrifuge tube.

4.2.3 Coating of PVP Functionalised Rods

10 mL of $CePO_4$/PVP solution was and diluted with 6.7 mL of ethanol. 1 mL of deionised water and 0.034ml of TMAH was added to $CePO_4$/PVP solution the then sonicated for 5 minutes. 0.1 mL of was added TEOS at a rate of 0.1 mL per 30 minutes while under constant sonication. This was repeated until the total volume of TEOS reached 0.5 mL an additional 0.5 mL of TEOS was to the solution and allowed to rest for 30 minutes. The final solution is centrifuged and washed with ethanol before being pelleted and suspended in 20 mL of ethanol.

4.2.4 Decoration of $CePO_4/SiO_2$/PVP Nanorods with Gold Seeds

4.2.3 APTES Functionalisation

36mg of $CePO_4/SiO_2$/PVP was suspended in 20 mL of ethanol under sonication. 150 µL was added to the solution and refluxed at 80 °C for 3 hours. The solution was stirred and cooled to room temperature for 24 hours. The $CePO_4/SiO_2$/PVP/APTES was separated by

centrifugation and washed with ethanol and deionised water. The product was then suspended in 4 mL of deionised water producing a 9 mg/mL solution.

4.2.3 Gold Seed Loading

1 mL of the $CePO_4/SiO_2$/PVP/APTES solution was suspended in a 10 mL centrifuge tube. The solution was sonicated, and the gold seed solution was added dropwise over 1 hour. The product was separated by centrifugation and washed with deionised water. The $CePO_4/SiO_2$/PVP/APTES/Au-seed rods were then dispersed in 13.5 mL of deionised water forming a 0.666 mg/mL solution.

4.2.3 Coating of $CePO_4/SiO_2$/PVP/APTES/Au Seeded Nanorods with Gold

Gold growth solution was prepared 24 hours before the coating step by dissolving 0.26g of K_2CO_3 in 90 mL of deionised water and 10 mL 50mM of $HAuCl_4$ solution. A 5% wt solution of PVP and 10% CH_2O solution were also prepared.

200 µL of the $CePO_4/SiO_2$/PVP/APTES/Au-seeded solution was added to 1 mL of the gold growth solution and 25 µL of the 10% CH_2O solution under sonication. Further additions 1 mL gold growth solution and 25 µL of the 10% CH_2O were added at 2-minute intervals until a total volume of 8 mL of gold growth solution was added. For each 3 mL of gold growth solution, 50 µL of the PVP solution was added and at the end, the solution was treated with 500 µL of PVP. The product was washed with water and ethanol by centrifugation and resuspended in 4 mL of deionised water.

4.2.5 Characterisation

Functionalised and coated particles or surfaces were analysed with a combination of XPS, with electron microscopy used to confirm their morphology and chemical composition. TEM the nanoparticles were isolated with a series of washing/ centrifugation steps and vacuum dried. Samples were supported on copper TEM support grids and analysed on a JEOL JEM-2100 TEM

For XPS the dried nanorods were pressed onto conductive tape and analysed with a Kratos Axis Ultra-DLD photoelectron spectrometer with a monochromatic al. Kα x-ray source in the "hybrid spectroscopy" mode. Model hematite surfaces were treated in the same manner. The analysis area was approximately 700 × 300 µm. A pass-energy of 40 eV was used for high-resolution scans and 60 eV for survey scans. CasaXPS[18] was used to analyse the spectra. Binding energies are referenced to the largest C(1 s) peak at 284.7 eV with an uncertainty of ~ 0.2 eV. Since intensities for powder samples are dependent on the surface area analysed, which can be poorly reproducible between different powder samples, XP spectra in the figures are normalized to the point of maximum intensity.

Hematite model surfaces were first prepared and analysed to identify their surface properties ensuring that the hematite models would be suitable for analysis. This analysis confirmed the absence of other adatoms on the model surfaces and samples were limited to those with a less than 20 nm average variation in their surface height as measured by A Bruker Multimode 8 AFM.

4.3 Results.

4.3.1 Hematite Model Surfaces

The dispersion and consistency of gold islands formed on the hematite surface were compared to reference hematite surfaces with no treatment. The chemical composition, morphology and oxidation state of these islands were analysed using AFM and XPS.

'Clean' reference hematite surfaces were prepared by a process of polishing and sonication to ensure the absence of other atoms before being exposed to treatment. When exposed to a 50 mM gold solution, very few islands were observed in the AFM images but increasing the concentration to 500 mM resulted in a small number of gold islands. These particles were few, with only 5 per μm^2 with nanoparticle heights in the range of 10-16 nm. 5 gold

islands per μm^2 is a considerably lower coverage of gold compared to other treatments and suggests that gold has little affinity to the hematite surface without a degree of surface functionalisation.

Based on previous literature, several possible treatments were chosen to increase the extent of the nucleation of gold at the hematite surface. These conditions are adaptions of the typical seeded immobilisation method mentioned in the introduction.

Two main areas of optimisation were investigated:

1. A surfactant to functionalise the hematite surface to facilitate the support-metal interaction. Amines, thiols, and carboxylic acids are often used in this context and are attached to organosilanes due to their ability to polymerise into thin coatings upon the surface of nanoparticles.
2. Stabilizing agents which can act as a guide to metal deposition.

Poly(vinylpyrrolidone) (PVP) has been used as a stabiliser for gold nanoparticles by forming a coating around the particles and preventing their aggregation[19]. This comes at the cost of the PVP changing the optical behaviour of the gold nanoparticles[20]. PVP is also known for the difficulty associated with its removal once applied to a surface and so polyvinyl alcohol (PVA) was also investigated as a potential alternative stabiliser that might overcome such synthetic issues[21].

Two examples of functionalisation agents were examined in this study: 3-aminopropyl triethoxysilane (ATPES) and 3-(mercaptopropyl) trimethoxysilane (MPTMS), both of which have been used in seed-mediated coating of hematite previously.

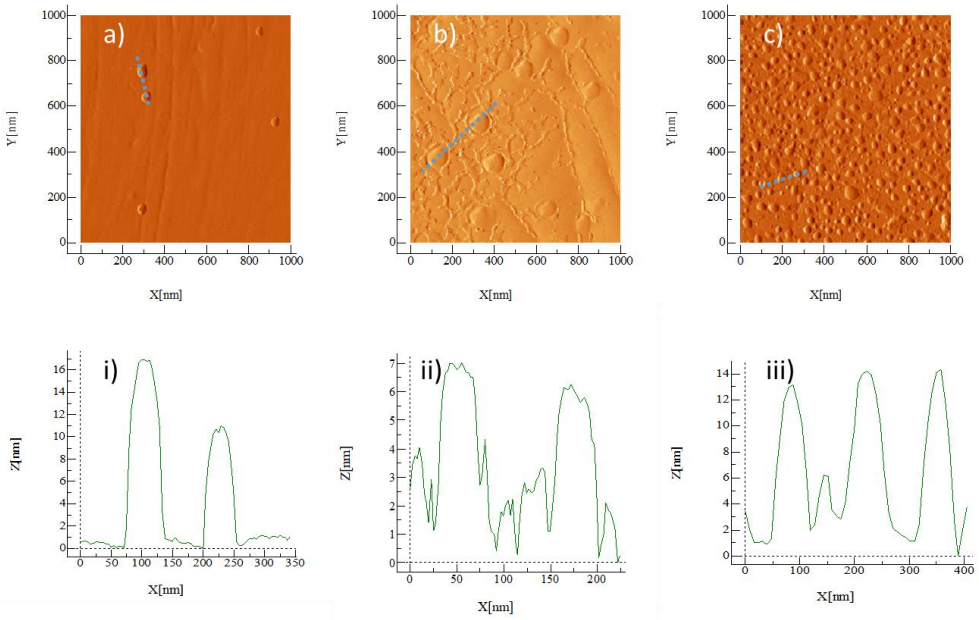

Figure 4-2. (Top) AFM data for (a) Fe_2O_3/$HAuCL_4$. (b) Fe_2O_3/PVA/$HAuCL_4$ (c) Fe_2O_3/PVA/$HAuCL_4$. (Bottom) Height profile of i) Fe_2O_3/$HAuCL_4$ ii) Fe_2O_3/PVA/$HAuCL_4$ iii) Fe_2O_3/PVA/$HAuCL_4$. The Blue dotted line shows where the height profile was taken.

Figure 4-2 illustrates how gold is deposited upon functionalised and unfunctionalised hematite surfaces. When a hematite surface was first functionalised with PVP the gold loading of the surface increased to a distribution of gold across the surface from 5 gold islands per μm^2 to 413 gold islands per μm^2. This represents an increase of gold coverage of over 80-fold. Island dimensions were very similar for Fe_2O_3/$HAuCL_4$ and Fe_2O_3/PVP/$HAuCL_4$ with an average diameter of 52 nm and heights of 16 nm. Fe_2O_3/PVA/$HAuCL_4$ suggested that PVA had less of an impact on gold coverage with an increase from 5 gold islands per μm^2 to 12 gold islands per μm^2. This represents a more moderate increase in surface affinity to gold, furthermore, these islands were much flatter than those of Fe_2O_3/$HAuCL_4$ and Fe_2O_3/PVP/$HAuCL_4$ with an average height of 6.2 nm. The surface of Fe_2O_3/PVA/$HAuCL_4$ also had a network of smaller structures which were between 1 and 3 nm in height which surrounded the gold nanoparticles and could be PVA.

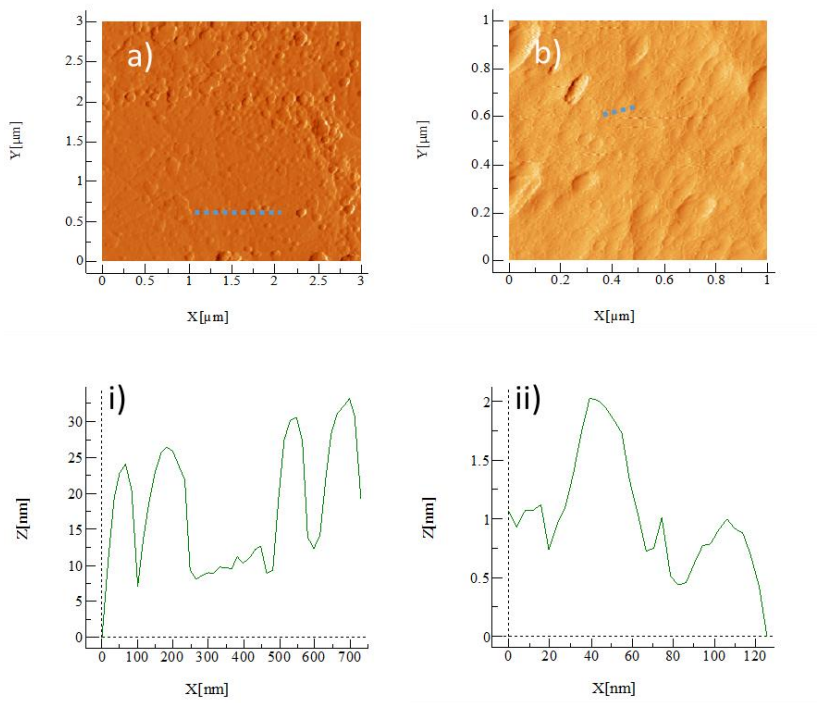

Figure 4-3. AFM data for (a) Fe_2O_3/APTES/PVP (b) Fe_2O_3/MPTMS/PVP(Bottom) Height Profile of i) Fe_2O_3/APTES/PVP ii) Fe_2O_3/MPTMS/PVP_4. The Blue dotted line illustrates the area height profile was taken.

Hematite functionalised with only silanes such as APTES and MPTMS showed very little evidence of organisation like those seen in the PVP and PVA treatments, see Figure 4-3. Fe_2O_3/APTES/$HAuCL_4$ had much larger structures on the surface than those of treatments in the absence of a silane. A portion of this increase could be due to the presence of a silane polymer coating across the surface of the hematite as when treatments of Fe_2O_3/APTES/PVP and Fe_2O_3/MPTMS/PVP were measured, a change in the surface morphology was observed. Fe_2O_3/APTES/PVP showed a significant change of surface morphology with the introduction of a large number of features with a height of 30 nm. These features were not equally distributed across the sample with sections being denser than others. For example, the upper right quadrant of Figure 4-2 having coverage of 32 islands per μm^2 compared to 17 islands per μm^2. These features are less pronounced on the surface of Fe_2O_3/MPTMS/PVP which indicates the possible presence of several features across the surface with heights lower than 3 nm and while in this sample the presence of MPTMS had little effect on the height of the sample it is possible that on other areas of the hematite plate, dense silane polymer particles could be found.

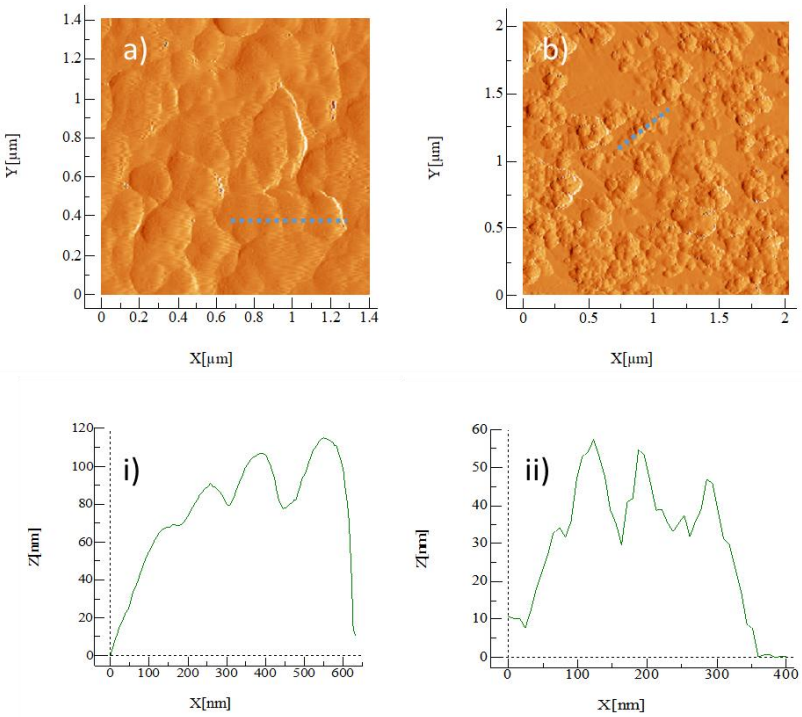

Figure 4-4. AFM data for (a) Fe_2O_3/APTES/$HAuCL_4$. (b) Fe_2O_3/MPTMS/$HAuCL_4$(Bottom) Height Profile of i) Fe_2O_3/APTES/$HAuCL_4$ ii) Fe_2O_3/MPTMS/$HAuCL_4$. The Blue dotted line illustrates the area height profile was taken.

A portion of the height increase of Fe_2O_3/APTES/$HAuCL_4$ and Fe_2O_3/MPTMS/$HAuCL_4$ can be attributed to the silanes. The height profiles of these samples have increased by at least 80 nm and 30 nm respectively through the addition of gold when compared to the corresponding uncoated surfaces. Furthermore, the morphology of the surface features in Figure 4-4 is different to other treatments of Fe_2O_3/APTES or Fe_2O_3/MPTMS and Fe_2O_3/PVP/$HAuCL_4$. They have increased in width from approximately 50 nm to 100 nm while remaining relatively circular in shape. The surface of Fe_2O_3/MPTMS/$HAuCL_4$ is less ordered than other treatments but seems to have a less homogenous coverage of gold particles across the surface with large areas of between 0.2 and 1 µm of bare hematite.

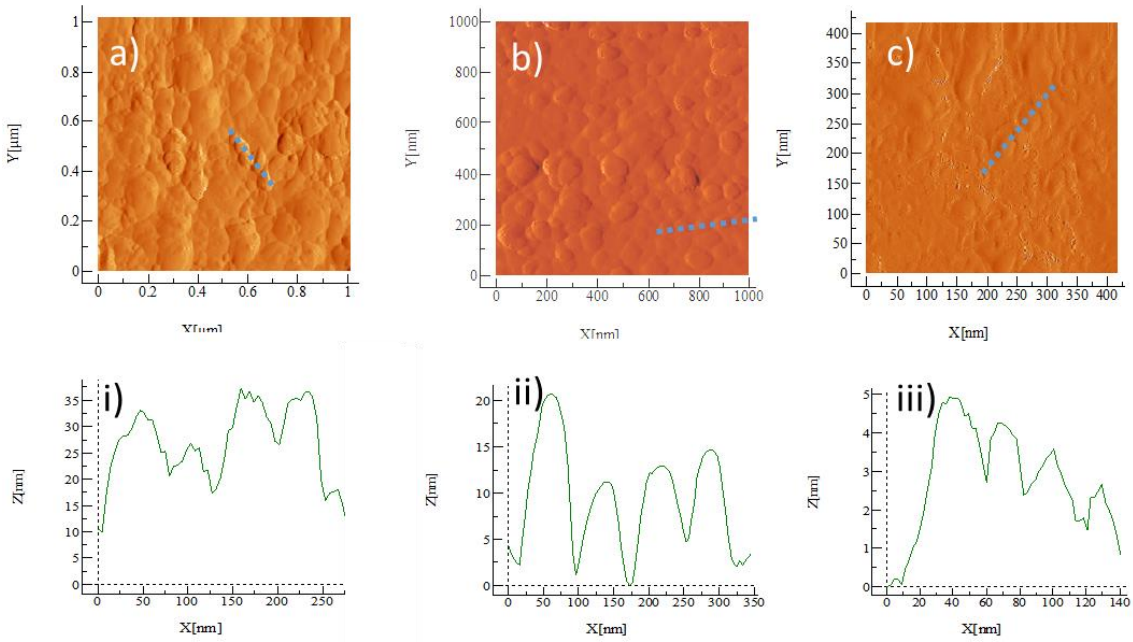

Figure 4-5. (Top) AFM data for (a) Fe_2O_3/PVP/APTES/$HAuCL_4$. (b) Fe_2O_3/PVP/MPTMS/$HAuCL_4$ (c) Fe_2O_3/PVA/MPTMS/$HAuCL_4$. (Bottom) Height Profile of i) Fe_2O_3/PVP/APTES/$HAuCL_4$ii) Fe_2O_3/PVP/MPTMS/$HAuCL_4$ iii) Fe_2O_3/PVA/MPTMS/$HAuCL_4$. Blue dotted line illustrates area height profile was taken.

.

. To achieve better control of the deposition of gold onto the surface of the hematite models a combination of all the above treatments was carried out. Figure 4-5 shows a comparison of different functionalisation combinations on a hematite surface. The combination of polymers and silanes results in less disordered surfaces with lower height profiles than those obtained in the absence of PVP or PVA such as Fe_2O_3/APTES/$HAuCL_4$. The Fe_2O_3/PVP/APTES/$HAuCL_4$ treatment has decreased in height from the 120 nm maximum seen in Fe_2O_3/APTES/$HAuCL_4$ with particle diameters being approximately 50 nm. The height profile shows no drops below 15 nm suggesting the presence of a layer 15 nm thick on top of the hematite surface. Fe_2O_3/PVP/MPTMS/$HAuCL_4$ and Fe_2O_3/PVA/MPTMS/$HAuCL_4$ both have height profiles which indicate that the deposition of gold is not in a full coat but rather individual islands however the islands that are present. In the case of Fe_2O_3/PVP/MPTMS/$HAuCL_4$, these particles can be seen to be approximately 13 nm in height and are like the morphology of gold found in earlier treatments such as Fe_2O_3/PVP/$HAuCL_4$ and Fe_2O_3/ $HAuCL_4$.

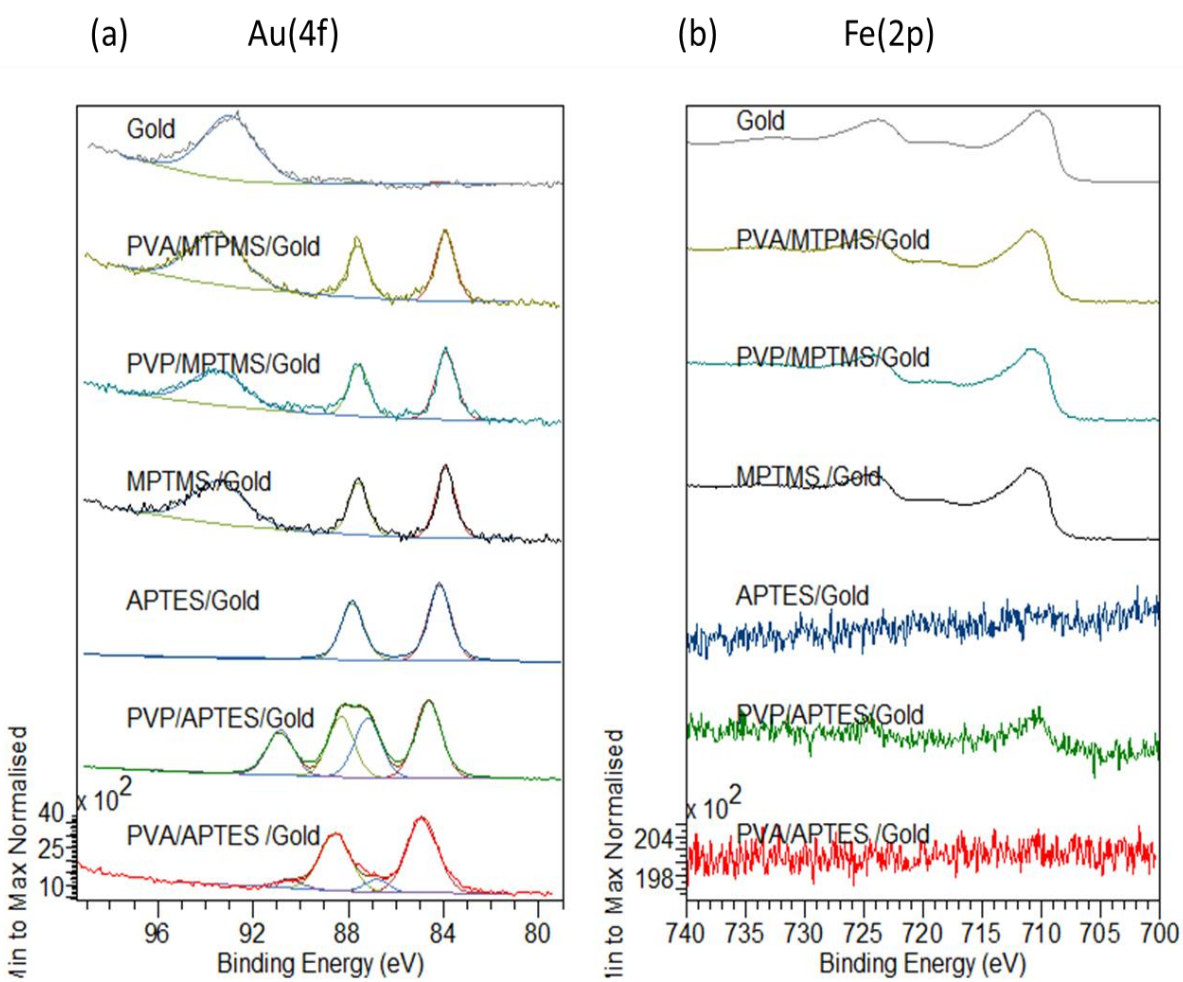

Figure 4-6 XP Spectra model hematite surfaces functionalised with combinations of PVA, MPTMS, APTES and PVP. (a) Au(4f) (b) Fe(2p)

Surfaces treated with silanes and a combination of PVP or PVA with a silane showed a significant increase in gold intensity compared to $HAuCl_4$ alone. In the absence of the silane and the polymer, no gold is evident in the XP spectra; only the Fe(3s) peak originating from the hematite surface is evident with a binding energy of 93.3 eV.

When comparing MPTMS and APTES treatments the Au(4f) scan indicates that APTES results in a fuller coat across the surface of the hematite. This is visible through the lack of a Fe(3s) peak at 93.3 eV in the Fe_2O_3/PVP/APTES/$HAuCl_4$ and Fe_2O_3/PVA/APTES/$HAuCl_4$ treatments and the significant reduction of a signal in the Fe(2p) region. This can be attributed to the formation of a silane polymer coat across the surface of the hematite which AFM indicated to be up to 30 nm in thickness. This silane coat acts as an intermediate between the hematite surface and the gold, increasing the gold affinity for the surface resulting in a greater degree of gold deposition. MPTMS does not polymerise to form a silane coat across

the surface of the hematite and as a result, gold has a lower affinity to surfaces treated with MPTMS than APTES. APTES treatments are unique through the presence of Au(0) and Au(III) species on their surface, while all other treatments only possess Au(0). The dominance of the Au(0) species is expected as APTES, PVP, PVA and MPTMS can act as reducing agents in the formation of metal nanoparticles[22–24]. The presence of Au(III) however is more interesting. Previous research has indicated that the ratio of Au(III) to Au(0) on a surface may be a function of the amount of gold deposition on the surface[25]. Perhaps in this study, as a full adlayer of gold is formed all of the reducing potential of the surface is exhausted and the remaining gold deposits in the form of Au(III) which would be the predominant gold species in $HAuCl_4$[26]. Fe_2O_3/APTES/$HAuCl_4$ was shown by AFM to have a large coating of a maximum thickness of 120 nm significantly larger than observed with other treatments. Based on the XPS above and literature, the absence of Au(III) indicates that most of this coat was silane polymer and less gold was deposited on the iron oxide surface in the absence of PVP and PVA controlling the deposition.

Fe_2O_3/PVP/APTES/$HAuCl_4$ had more Au(III) relative to Au(0) compared to Fe_2O_3/PVA/APTES/$HAuCl_4$ this is possibly due to the hydroxylation of the hematite surface in the presence of PVA. PVA has high-density hydroxyl groups and would be more reducing in nature than that of PVP. Similar results were obtained on carbon surfaces where treatment with PVA resulted in the reduction of Au(III) to Au(0) [26].

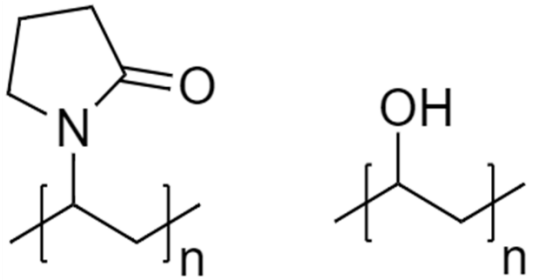

Poly(vinylpyrrolidone) (PVP)

Polyvinyl Alcohol (PVA)

Figure 4-7 illustrations of the chemical structure of PVA and PVP

The combination of XPS and AFM suggests that previous literature is valid and that both silane and a stabilising agent would yield the best gold deposition upon a hematite surface. APTES results in the deposition of thick silane polymer coats which vastly increases the affinity of gold to the surface. However, in this project, the aspect ratio and morphology of

the core nanoparticle is important and as coating thickness increases there are risks of changes in optical behaviour[27,28]. The magnetic behaviour can also be affected with silica coatings as thin as 2 nm in thickness. This was illustrated by Husain et al. who coated magnetite spherical nanoparticles of approximately 15 nm in size with coatings varying between 1 – 7 nm. The magnetic response of those particles was more than halved, with the magnetisation reducing from 77 emu g^{-1} to 34.7 emu g^{-1} [29]. Therefore, the preference for APTES to form a polymer coat across the surface of hematite could be problematic for developing magnetically responsive nanoprobes. MPTMS treatments result in a lower overall deposition of gold and, based upon the Fe(3s) and Fe(2p) scans, do not create full monolayers of gold or silane across the surface of the hematite so may also not be suitable for the development of coatings on nanorice particles. Since a combination of silane and PVP gave the best result, these were examined on hematite nanorods.

4.3.2 Hematite Nanorod Coating

Hematite nanorice has been used as a core for the seed-mediated growth of a gold coating in the previous literature[29]. However, there is no previous literature discussing the coating of hematite rods made with 1,2 propanediamine as a directing agent. While the particles are similar chemically, they have different morphological and crystal features which can affect the surface-metal interactions of a core-shell particle. To best optimise the coating method of these anisotropic nanoparticles, the seed-mediated coating of hematite prepared in the presence of phosphate will be examined first and optimised before examining 1,2 propanediamine hematite nanorods.

4.3.3 Unfunctionalized Nanorods

To be consistent with the work described above on the model surfaces, the coating of the nanoparticles was first carried out in the absence of gold seeds as nucleation points for gold growth. These treatments were carried out on 20 mg of hematite rods using 5 mL of untreated $HAuCl_4$.

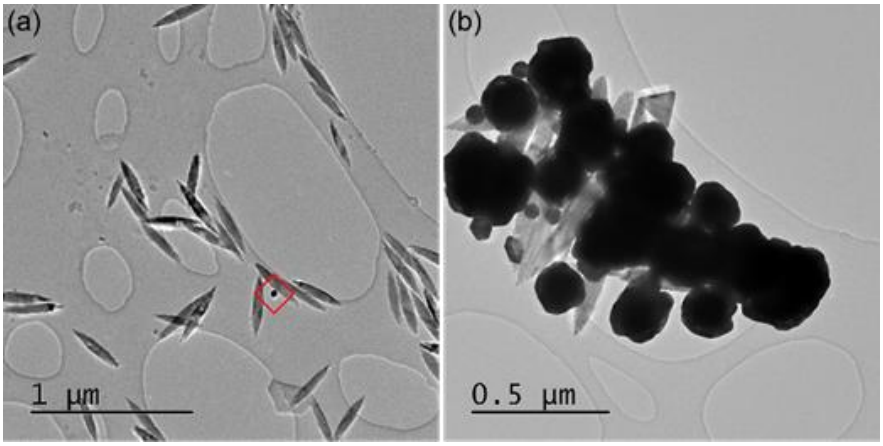

Figure 4-8. Gold particle growth on hematite surfaces: (a) TEM of bare hematite nanorods following deposition of gold in the absence of APTES; the red box highlights an unattached gold nanoparticle. (b) APTES functionalised hematite coated with gold in the absence of seed particle

In the absence of the silanes such as APTES or MPTMS and gold seeds Figure 4-8 (a) illustrates that no gold nanoparticles are adsorbed on the hematite surface but a small number of independent gold particles are observed which, have deposited with the nanorods when the solution is dried onto the TEM grid. These gold nanoparticles may be initially nucleated on the surface of hematite but are too weakly bound to remain beyond the washing step. Furthermore, because the centrifugation step separates the heavier gold particles from the hematite nanorods, the reaction likely generates many more gold nanoparticles than are seen in the image.

When the surface is functionalised with APTES before coating, but without the pre-adsorption of gold seeds on the hematite surface, gold growth also failed to coat the surface effectively; Figure 4-8 (b) shows a sample in which the gold was nucleated in the absence of the gold seeds. It is not clear whether the large gold nanoparticles are adsorbed on the nanorod particle surfaces or simply co-deposited with them on the TEM grid, but it is evident that gold is growing as crystalline nanoparticles rather than as a coating for the hematite.

The solution to these issues is to follow the seed-mediated method illustrated in the literature where previously prepared gold nanoparticles of 2-3 nm are supported on the functionalised surface of a hematite nanorice which are bound to the amine and thiol groups of APTES and MPTMS.

4.3.3 MPTMS

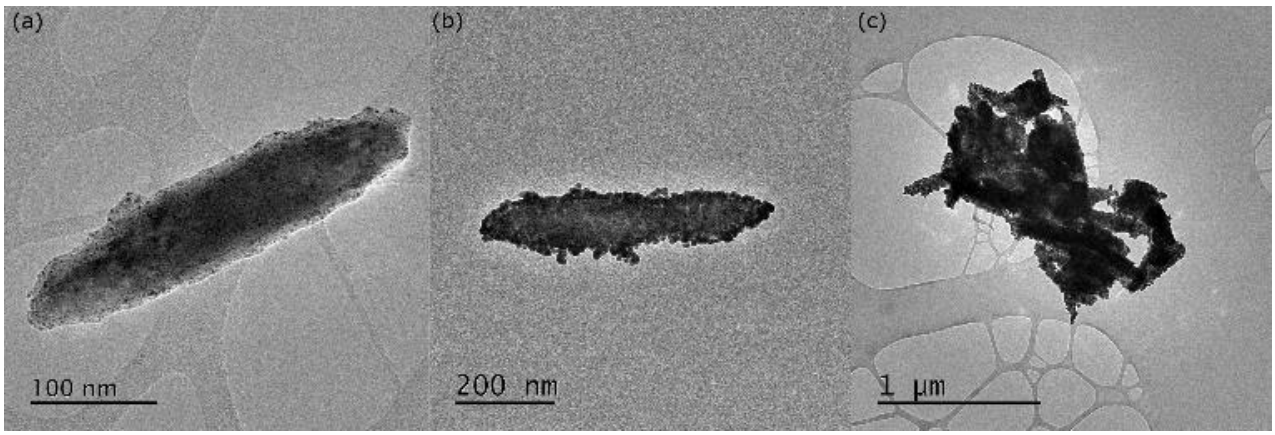

Figure 4-9. (a) Hematite rod with MPTMS functionalisation and supported gold seeds. (b) A coated Au/Fe_2O_3 nanoparticle (c) Cluster of nanoparticles

The Fe_2O_3/MPTMS treatment of nanorods results in the formation of a 5 nm thick coating of silane polymer across the surface of the nanoparticle. This is thicker than the 2 nm networks identified on the AFM of the model hematite surfaces and is more like APTES. This coat formed in an uncontrolled manner and varied between 3 – 6 nm in thickness across the surface of the particle. This morphology of the coat would ultimately inhibit the growth of a smooth gold coat by giving an uneven foundation for the nucleation and propagation of gold across the surface which can be seen in Figure 4-9. Furthermore, as discussed above, the presence of an unwanted silane coat could have significant effects on the magneto-optical effects of the nanoparticles. Between the functionalisation and the coating step, the nanoparticles have agglomerated into larger structures of up to 1 µm in size. This is observed because the coating formed in the absence of any sonication, and the particles are pelleted and dried between functionalisation and gold coating. Silica coatings will adhere to each other when dried or polymerise together during the process of a silica coat forming.

While MPTMS functionalisation did increase the affinity of nanorice for gold deposition, treatment did not result in the easy and reliable coating process needed to develop consistent nanoprobes. Because of the necessary steps of centrifugation and drying, the tendency for MPTMS to polymerise across the surface of hematite and consequent aggregation, this treatment was not studied further.

4.3.3 APTES

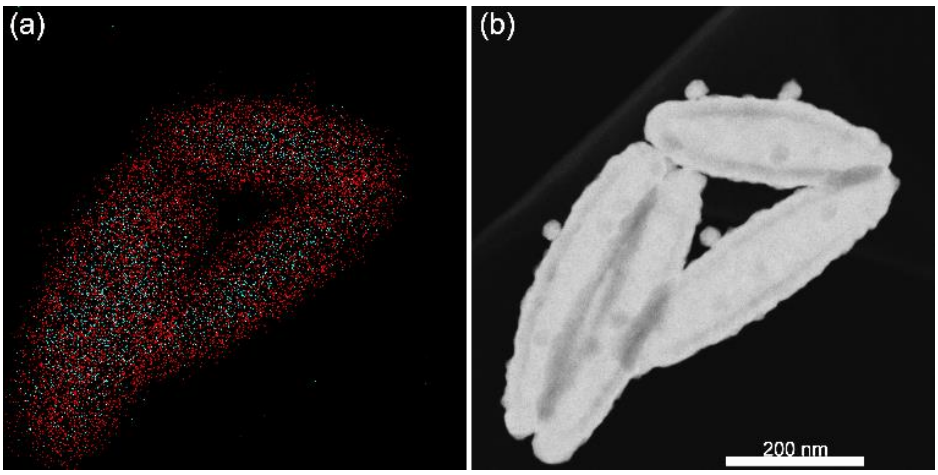

Figure 4-10: Hematite nanorods with smooth gold coating. (a) EDX data of the same image showing gold (red) uniformly coating the particles with the iron signal (blue) showing most strongly in the centre of the particle. (b) SEM image of four particles. The hematite/gold boundary is distinguishable.

The SEM and EDX images in Figure 4-10, demonstrate that relatively smooth gold coatings with small variations in height of 20 nm can be deposited on hematite nanorods using APTES as the surface modifier. Figure 4-10 (b) shows that while smooth coatings are obtained there are additional gold spheres supported on the gold coating. This is because there is a key balance that must be struck between the quantity of growth solution and the number of seed particles used when coating hematite nanorods with the seed-mediated model. Figure 4-11 illustrates the effect of situations of too many, or too few gold seeds in the coating process. In the case of low quantities of gold seeds, the lack of overall coverage across the surface is a contributing factor to the coating morphology giving rise to multiple individual particles supported across the surface of the nanoparticle. The resulting particles are not in close enough proximity to coalesce to a smooth coat and instead form larger supported spherical particles when exposed to gold growth solution. At the other extreme, gold seeds are in such abundance that a complete monolayer of gold nanoparticles is supported on the surface. However, because the gold seeds are in surplus, they cannot all pack onto the surface of the hematite core and instead stack onto other gold particles. These additional seeds compete with the surface stabilised seeds for growth solution, resulting in all seeds either growing at much slower rates and merging into other gold morphologies such as pyramids or cuboids. As a result, the final coating is very rough.

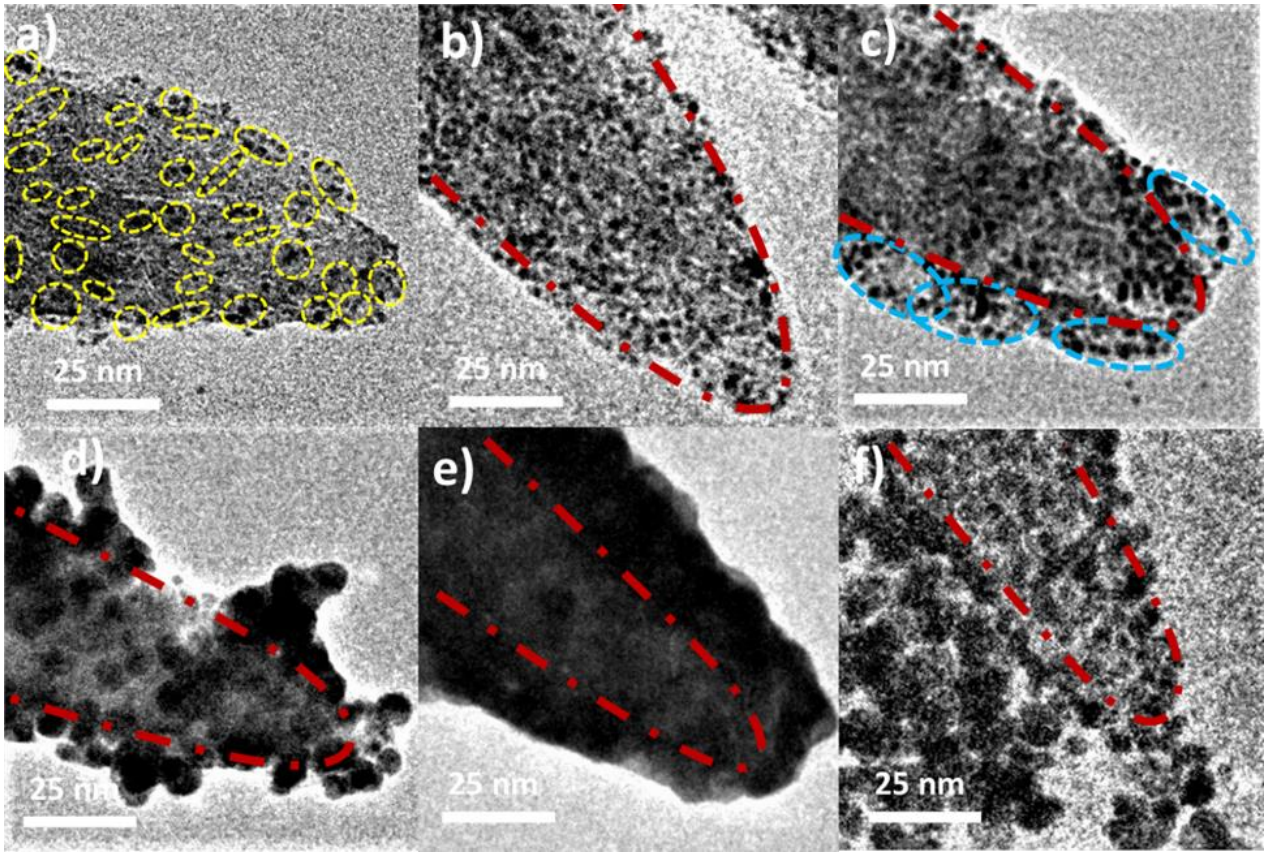

Figure 4-11: Gold particle growth on hematite surfaces with different amounts of seeds before and after the addition of 5 mL gold growth solution. (a) and (d) 6 mL of seed solution before and after treatment with 5 mL gold growth solution. (b) and (e) 13 mL of seed solution before and after treatment with 5 mL of gold growth solution. (c) and (f) show 25 mL of seed solution before and after treatment with 5 mL of growth solution. Red lines outline the surface of hematite particles. The Blue circle highlights seed particles protruding from the hematite particle surface. Yellow shows clusters of particles less than 1.5 nm away from each other.

The XPS (See supporting information) of the coated hematite particles shows that, unlike the model surfaces, Au(0) is the only state deposited in all cases. This is probably due to the presence of reducing agents such as PVP and APTES. Unlike the model hematite surfaces, the gold solution is aged in an alkali solution caused by the KCO_3 added to the growth solution. This favours the reduction of the gold from Au(III) to Au(0). The second important aspect is the quantity of gold growth solution used in any given treatment this is explored in Figure 4-12. In effect, this can be visualised as controlling the growth of the individual seeded particles since the amount of growth is proportional to the gold solution concentration.

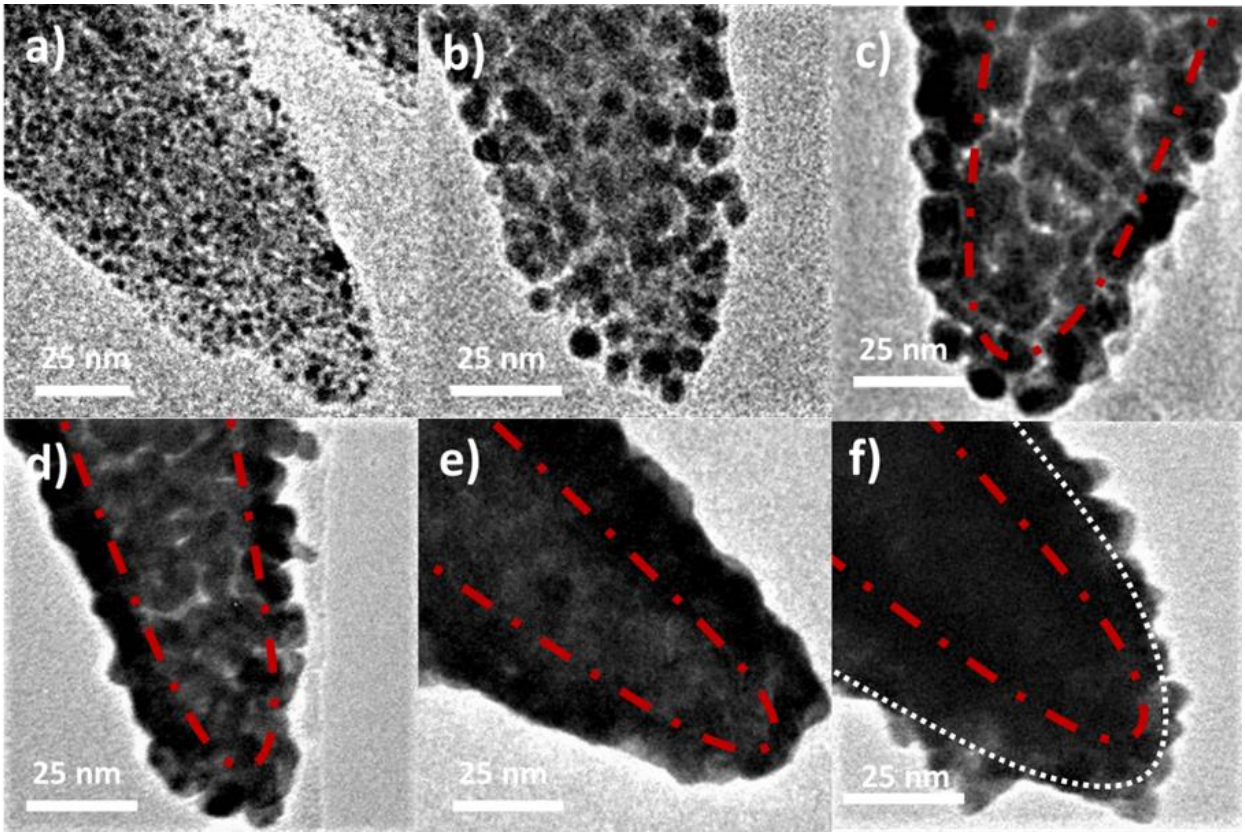

Figure 4-12: (left) Fe_2O_3 rods functionalised with APTES and 20 mL of gold seed particles exposed to increasing volumes of the aqueous $AuCl_4$ coating solution (a) 0 mL; (b) 0.25 mL; (c) 2.5 mL; (d) 4 mL; (e) 5 mL (f) 6.5 mL (right) XP Spectra of hematite nanorice particles coated with different amounts of aqueous $AuCl_4$ coating solution.

This effect can be divided into two stages. The “coalescence” stage and the “gold: gold” stage. At first, the gold particles grow until they coalesce into one coat. However, once these particles reach a size that each they start to coalesce into a film, the growth changes with the formation of the new monolayer. This layer has significantly less interaction with the hematite core and is in more of gold: gold growth. The TEM images show that the PVP and APTES have little control over the gold growth at this stage and instead, island formation begins, consistent with typical gold growth forms in the shape of spherical particles and pyramids. If the aim is to generate a “smooth” coating, this growth stage needs to be avoided.

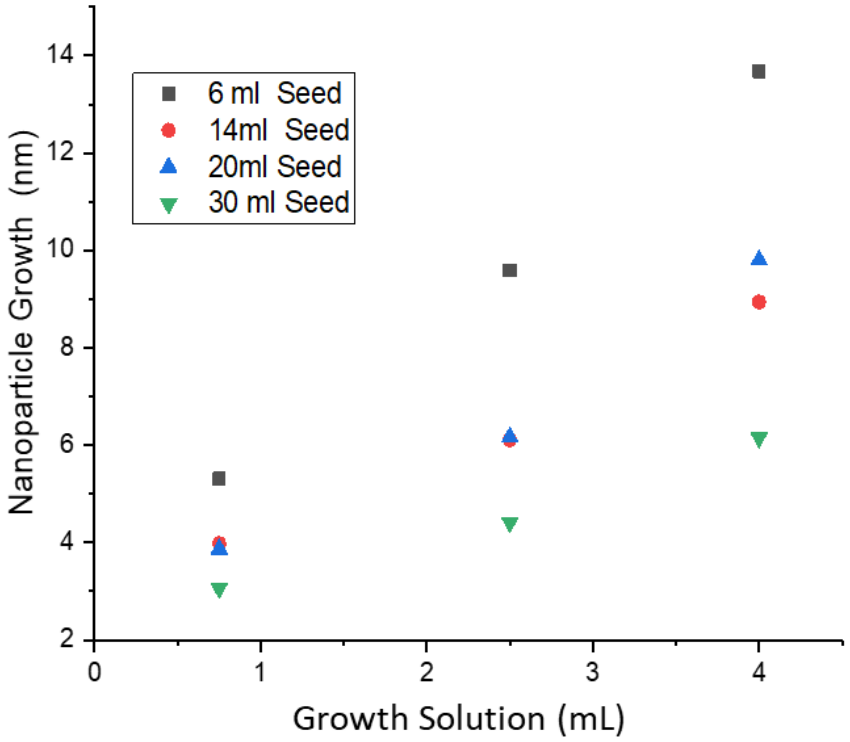

Figure 4-13: Graph of particle growth as a function of the growth solution added to different seed treatments. Measurements of particle growth were calculated as the average height of a selection of 50 gold nanoparticles on a hematite surface. Growth was calculated by using the average seed size calculated from average diameters. Volumes greater than 4 mL were not measured as particles begin to coalesce into coats at this point.

Figure 4-13 shows the linear relationship between the nanoparticle size and the amount of gold growth solution added to seeded hematite nanorice. The data shows that when more seeds are present, as in the case of 30 mL seed treatment, the overall growth of the seeds is less over the growth period compared to a sample with fewer gold seeds. In summary, the more seeds there are present, the more gold solution is needed to grow those seeds to the same extent. This underlines the importance of accuracy in the number of seeds deposited to the ability to grow a smooth coating.

4.3.3 1,2 Propanediamine Directed Hematite Rods

The information learned from coating the model hematite surface and the well-studied phosphate directed hematite nanorod system was applied to study the coating of two more complex hematite systems: 1,2 propanediamine directed nanorods and sphere intermediates prepared at 140 °C and 180 °C.

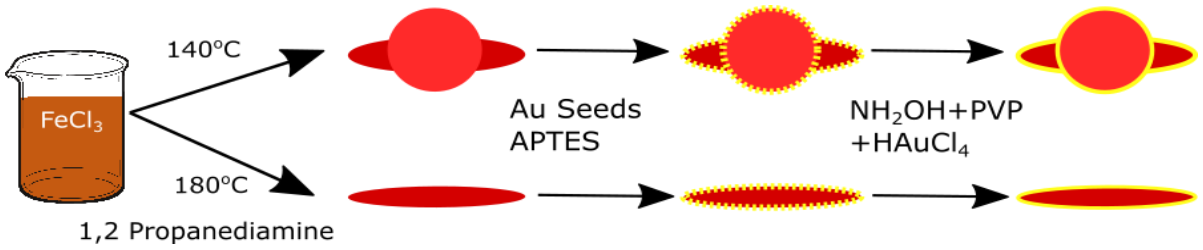

Figure 4-14: illustration of 1,2 propanediamine rods being coated in gold with the APTES assisted seed-mediated method.

These systems were both prepared from 1,2-propanediamine and their growth and synthesis were examined in Chapter 2. The particles had two morphologies, rods and sphere intermediates with the shape controlled by the temperature of the preparation method. Coating these particles posed more of a challenge due to their different morphologies and the presence of hematite precursors such as goethite on their surface. However, they are of interest as different morphologies have different magnetic responses and optical properties.

Figure 4-14 is a basic illustration of the coating method which is similar to that used for phosphate directed rods. However, the propanediamine method was adapted from the phosphate assisted rods. However, the functionalisation method differed: The typical APTES functionalisation seen in the phosphate rods requires 6 mL of APTES being added directly to the hematite rods. However, the new method uses 120 µl of APTES and reflux at 80 °C for three hours. While this method is slightly more complicated than that used in the phosphate assisted rods the reduction in silane use by 50 times is overall more cost-effective while taking less time.

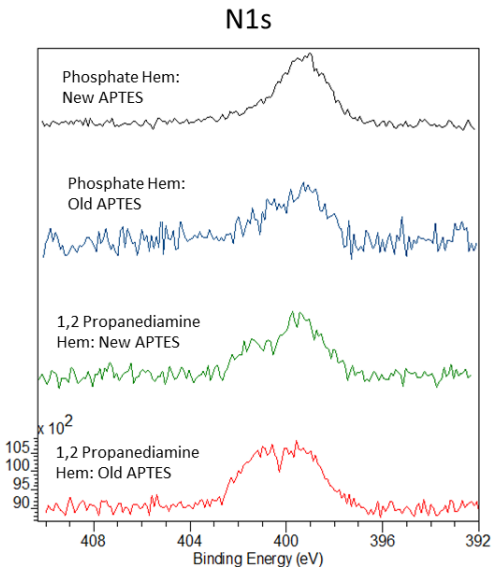

Figure 4-15: XP spectra of the N1s region of comparing nanorods prepared by the phosphate and propanediamine assisted methods using different functionalisation methods. the old method adds 6 mL of APTES to a solution of hematite and is stirred overnight. The new method uses 120 µl of APTES in reflux at 80 °C for three hours.

The XP spectra, Figure 4-15, shows the two types of rods show clear peaks for the nitrogen present within the APTES at ~ 399 eV but in addition, the spectra of the 1,2 propanediamine rods also show a peak at 401.5 eV due to the presence of the nitrogen within the 1,2 propanediamine which remains upon the surface. The XP spectra confirm the presence of APTES on both hematite rods proving that the reflux method successfully functionalised the surface. This is confirmed by the successful support of gold seeds and a gold coat upon the 1,2 propanediamine rods in TEM micrographs from Figure 4-17 and Figure 4-16

The surface areas of each solution were calculated as a function of its density and the average particle dimensions of that sample. These estimates are shown in Table 4-1.

Particle Type	Particle Surface Area (m^3)	Volume of single nanoparticle (m^3)	Mass of nanoparticles in solution (mg)	Total Surface Area (m^3)	Predicted Growth Solution (mL)
Phosphate[1]	$1.09x10^{-13}$	$1.4x10^{-21}$	30	295000	5
1,2 propanediamine 180°C[2]	$2.15x10^{-13}$	$4.45x10^{-21}$	60	367500	6
1,2 propanediamine 160°C[2]	$2.45x10^{-13}$	$11.74x10^{-21}$	60	159000	2.5

Table 4-1 table of predicted surface area and calculated prediction of gold growth solution needed for a full coat when using 20 mL of gold growth solution. Phosphate nanorods were estimated to have the volume and surface area of an oblate spheroid. 1,2 propanediamine 180 oC were assumed to be a simple cylinder while 1,2

propanediamine 160 oC were calculated as the combination of a sphere and two cones 1 phosphate hematite nanorice with an aspect ratio of 6.2.

The general trend of gold coating growth observed in the phosphate directed nanorice is repeated in the two 1,2 propanediamine samples. Irrespective of the morphology or surface area, the seed-mediated growth appears to progress by the same mechanism with seed particles progressively increasing in diameter until coalescing into a coat.

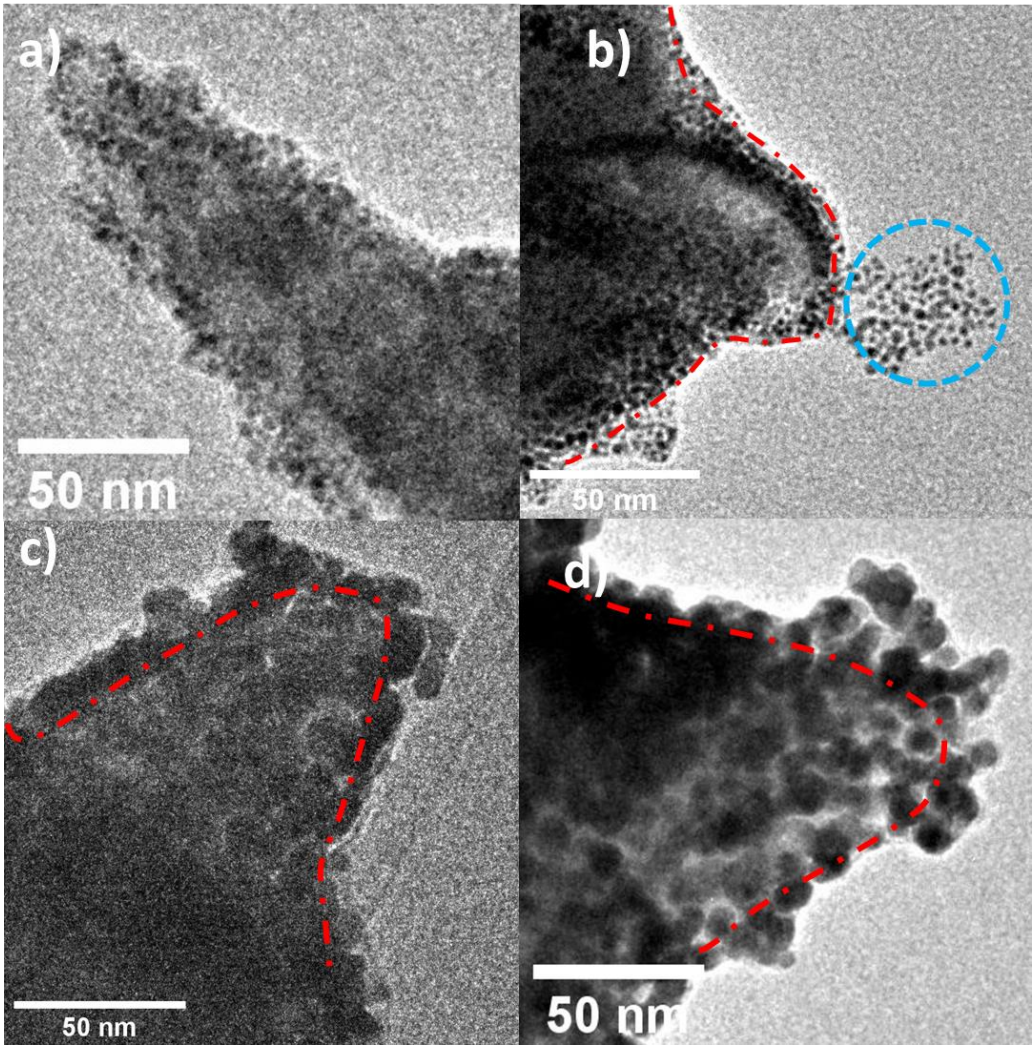

Figure 4-16: TEM Micrographs of 1,2 propanediamine nanostructures of APTES functionalised hematite prepared at 160 ^{o}C and treated with (a) – (b) 20 mL of seed solution before (i) and after (ii) exposure to 4 mL of gold growth solution. (c) – (d) 30 mL of seed solution before (c) and after (d) exposure to 4 mL of gold growth solution. Red lines outline the surface of hematite particles. The Blue circle highlights seed particles protruding from the hematite particle surface.

1,2 propanediamine nanoparticles hematite particles prepared at 160 ^{o}C were treated with between 10-30 ml of seed solution. TEM micrographs of these particles are shown in Figure 4-16. When 20 ml of seed solution was and 2.5 mL of gold growth solution the surface

stabilised seed particles grew from an average particle diameter of 2.13 nm to 4.13 nm. This increase was insufficient for nanoparticles to reach an appropriate size to coalesce. However, increasing the gold growth solution from 2.5 mL to 4 mL a more successful coat was obtained with an average thickness of 12.27 nm across the hematite surface. When using 30 or 10 ml of seed particles rough surfaces were obtained which are like those in phosphate particles. Comparing Figure 4-16 (c) to a successfully coated nanorice particle, it is clear the surface is rougher. The coating resembles one achieved in the presence of too many seeds (see for example Figure 4-11 and Figure 4-17) so perhaps a slight reduction in seed solution would result in a more homogenous coat. These results imply that the approximation in Table 4-1.

was inaccurate as 4 mL of gold growth solution was needed to form a coat. The reason for this difference could be a result of the particle size distribution of the hematite intermediates. When prepared at 160 ^{o}C, a combination of rods and sphere intermediates are formed. These intermediates are at varying degrees of growth and while centrifugation is a good method of removing unwanted hematite rods the particle size distribution is still wide.

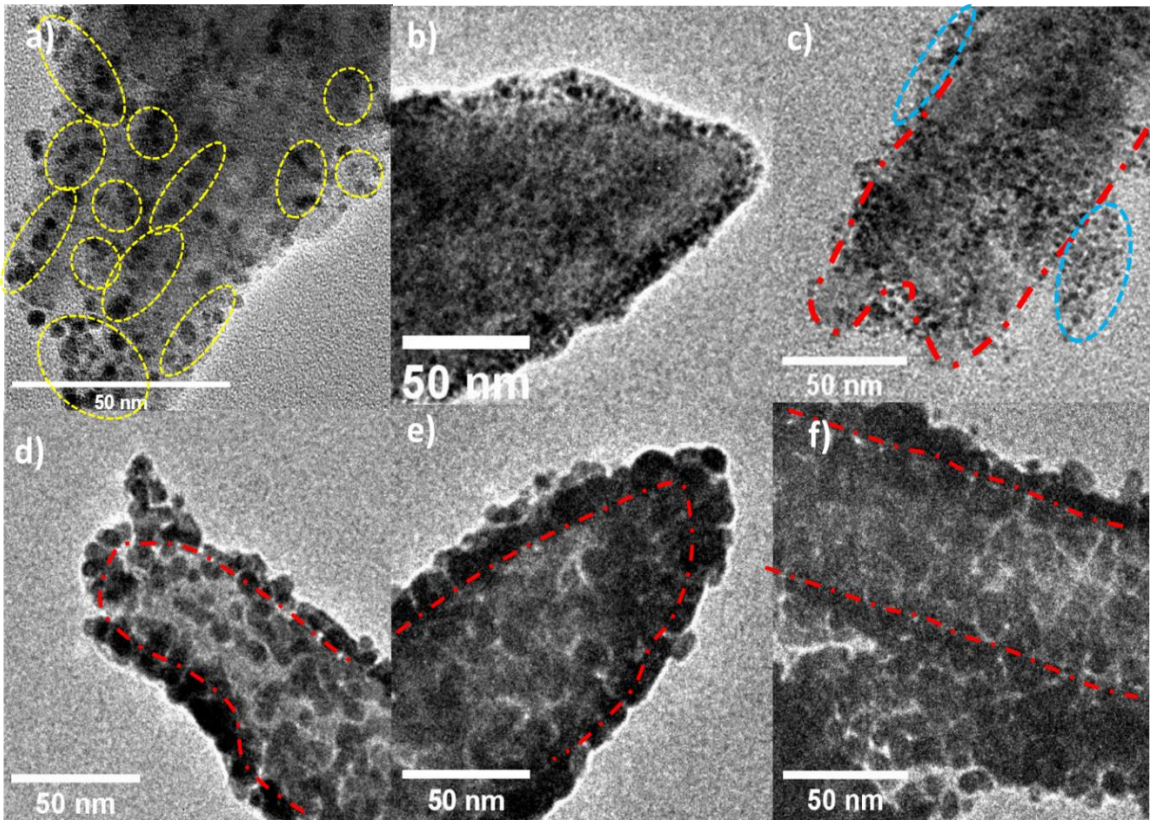

Figure 4-17: TEM Micrographs of 1,2 propanediamine nanostructures functionalised seeded with different amounts of gold seed solution: APTES functionalised hematite prepared at 180 ^{o}C (a) – (d) 6 mL of seed solution before (a) and after (d) exposure to 6 mL of gold growth solution. (b) – (e) 20 mL of seed solution before (b) and after (e) exposure to 6 mL of gold growth solution. (c) – (f) 30 mL of seed solution before (c) and after (f) exposure to 6 mL of gold growth solution Red lines outline the surface of hematite particle. The Blue circle highlights seed particles protruding from the hematite particle surface. Yellow shows clusters of particles less than 1.5 nm away from each other.

Based on the approximations in Table 4-1., 1,2 propanediamine nanorods prepared at 180 ^{o}C were treated with different amounts of seed solution varying between 6 – 30 mL and the coat was grown with 6 mL of gold growth solution. As in the case of the phosphate assisted rods, the number of seeds stabilised at the nanoparticle surface is integral to the formation of a smooth coat. Figure 4-17 (c) – (f) illustrated that more gold growth solution is needed overall for 1,2 propanediamine direct nanorods to develop a full coat of gold. Since Figure 4-17 (e) is the seed treatment analogous for an ideal coat on a phosphate directed nanoparticle. While Figure 4-17(e) shows a successful coat, there was a degree of roughness on the surface which suggested a surplus of seed particles as discussed above. To reduce the amount of seeding a quantity of 18 mL of seed solution was attempted and the addition of PVP was also increased from 40 to 60 mg, see Figure 4-18. The coating was then optimised using the predicted gold solution from Table 4-1.

Figure 4-18 (b) illustrates large channels and holes between seed particles which can be seen to decrease in size as more gold growth solution is added.

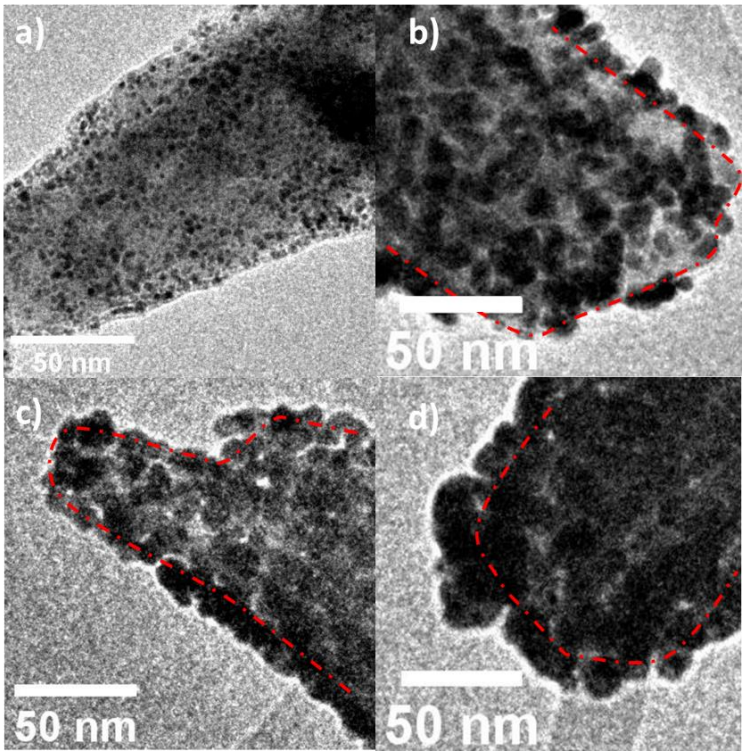

Figure 4-18: TEM micrograph of 1,2 propanediamine 180°C hematite nanoparticle seed with 18 mL of gold seed solution and being treated (a) 0 ml (b) 0.5ml (c) 5ml (d) 6ml of gold growth solution. Red lines outline the surface of the hematite rod.

The PVP plays an important part in the growth of a gold coating by preventing the aggregation of gold nanoparticles. Increasing the quantity of PVP results in a greater disaggregation effect preventing the supporting of additional gold seeds to the surface. The gold growth showed a similar relationship to the gold solution seen in phosphate hematite with the gold seed particle diameter proportional to the amount of gold seed solution added. Table 4-2 shows the average shell thickness for each type of particle. Despite the addition of more gold growth solution, the coating thickness of the 1,2 propanediamine hematite nanoparticles was thinner than that seen in the phosphate directed nanorice.

Nanoparticle	Average Coating Thickness (nm)
Phosphate[1]	24.3
1,2 Propanediamine 180 °C	16.8
1,2 Propanediamine 160 °C	12.3

Table 4-2 table of average coating thickness on hematite particles coated with gold through the seed-mediated method. were calculated as the combination of a sphere and two cones 1 phosphate hematite nanorice with an aspect ratio of 6.2

A possible explanation for the decrease in shell thickness could be that twice the mass of propanediamine nanoparticles (60 mg) are coated with gold compared to the phosphate directed particles (30 mg). While the solutions have similar amounts of gold solution added, in the case of 1,2 propanediamine 180 °C, the number of particles and hence the total surface area is greater, so more gold solution is needed to develop a full shell. Another possible explanation could be that the decrease in the quantity of APTES in the 1,2 propanediamine nanorod preparation may influence how the gold coat is formed

4.3.3 Gold Growth Mechanism

The growth of thin gold films has been shown to progress through steps of growth and coalescence. However, detailed growth mechanisms of these seed-mediated coats are lacking, with the effects of parameters such as the number of seeds not fully understood Brown et al. [30] supported 12nm gold colloids on MPTMS functionalised glass. These particles were exposed to fresh gold solution multiple times. As time progressed the average particle diameter increased from 12 to 75 nm with particles forming a collection of rods and spheres. The radius of the seed particles is controlled by the amount of growth solution added where the reduction of Au^{3+} from solution to Au^{0} the surface of the seeds was the main form of growth. Preston et al. showed that when gold seeds were immobilised with ATPES on silica spheres the seed particles would first coalesce into islands. These islands would then grow in diameter until coalescing into a full coat[31]. Similar results were obtained in this study, where the radius (r) of gold particles upon the surface of hematite was controlled through the addition of gold growth solution. Pashley et al[32] showed that gold islands deposited upon the surface of glass would grow in size until forming holes and channels in their coat, this was a direct result of the interfacing of islands, but there being

insufficient growth for full coalescence. As growth continued, channels would form holes and eventually a full coat was formed.

The overall effect of seed solution on film morphology is shown in Figure 4-11 and Figure 4-17. Clusters of gold seeds on the surface of hematite treated when treated with low volumes of seed solution. These clusters have separations between them varying between 2 - 18 nm. The isolated clusters may form through a preferential binding to specific crystal lattices and are present in both forms of hematite rod. Clusters become less prevalent upon the hematite surfaces as the amount of seed solution is increased with the overall separations decreasing. However, when adding excess quantities of seed solution are added to functionalised rods. Groups of seeds can be seen protruding up to 10 nm from the surface of the rods.

Phosphate 100°C	Particles per 25 nm^2	
Seed Solution Added (Vol)	Before Growth	After 5 ml gold growth solution
6 ml	12±5	4±3
20 ml *	25±4	0
30 ml	33±3	7±5

1,2 Propanediamine 160°C	Particles per 25 nm^2	
Seed Solution Added (Vol)	Before Growth	After 5 ml gold growth solution
10 ml	14±3	4±3
20 ml	28±5	1±1
30 ml	35±6	6±2

1,2 Propanediamine 180°C	Particles per 25 nm^2	
Seed Solution Added (Vol)	Before Growth	After 5 ml gold growth solution
10 ml	18±4	4±3
20 ml	24±5	2±2
30 ml	30±3	5±1

Table 4-3 Table of particle number at different seed solutions before and after particle growth. Measurements were taken over 3 25 nm^2areas and averaged across all hematite samples* Taken after 5 ml of growth solution corresponds to a full coat when seeded with 20 ml of solution

Table 4-3 Illustrates how increasing the seed solution quantity increases the distribution of gold nanoparticles across the surface and that as the gold solution is added to the seeded particles the total number of surface particles decreases. This change corresponds to the coalesce of gold seeds as they increase in size. As the growth of the films progress the formation of channels and holes can be seen. These are formed from areas where the separation between clusters of seeds is larger than the lateral growth of nanoparticles leaving channels between the coalesced clusters. As these clusters also grow, they close these channels until only holes remain and eventually a full film is formed. These results agree with the findings of Pashley et al[32].

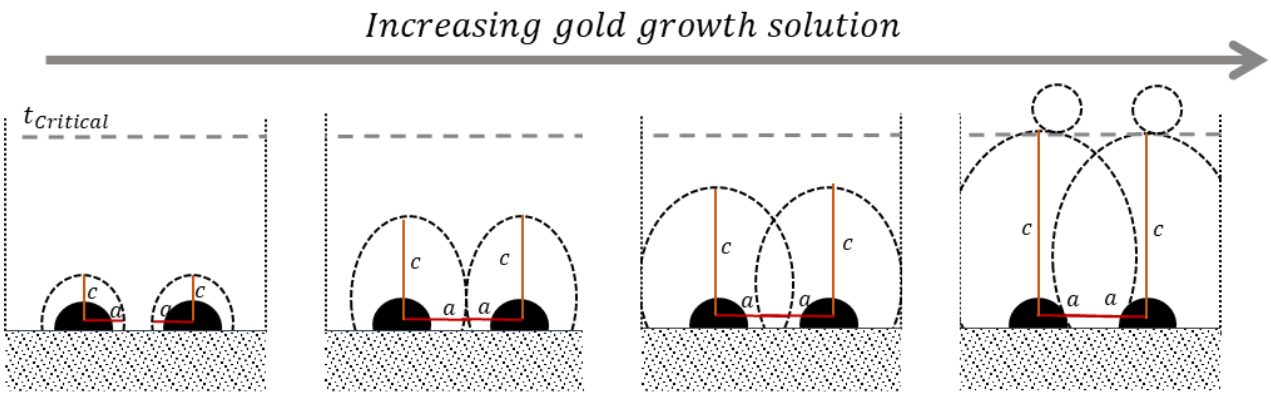

Figure 4-19: Illustration of seed particle growth through a prolate sphere model towards a critical thickness.

When gold seed particles are functionalised to the surface of hematite nanorods. They grow from a spherical morphology into a smooth coat. TEM images show that after being exposed to gold growth solution, seed particles grow in diameter while maintaining a semi-circle morphology. This growth continues until the seeds contact another gold island, at which point coalescence occurs, illustrated in Figure 4-19. Stranksi-Krastanov mechanism indicates that as the film thickness increases the attraction between the substrate and the gold decreases. This has been termed overgrowth. The original gold seed is immobilised upon the substrate surface with the silane intermediate. As this seed grows its lattice is placed under strain to bond to the substrate. When a Critical thickness of the coat is reached interactions between the substrate and the gold is so low that it switches to a gold growth dominated system. At this point the newly deposited particles grow with a lattice with its original crystal structure, resulting in the formation of triangle and cubic structures rather than a smooth coat.

When modelling growth based on the Stranksi-Krastanov mechanism it becomes apparent that the separation of seed particles must be smaller than the critical height if you are to obtain a smooth coat.

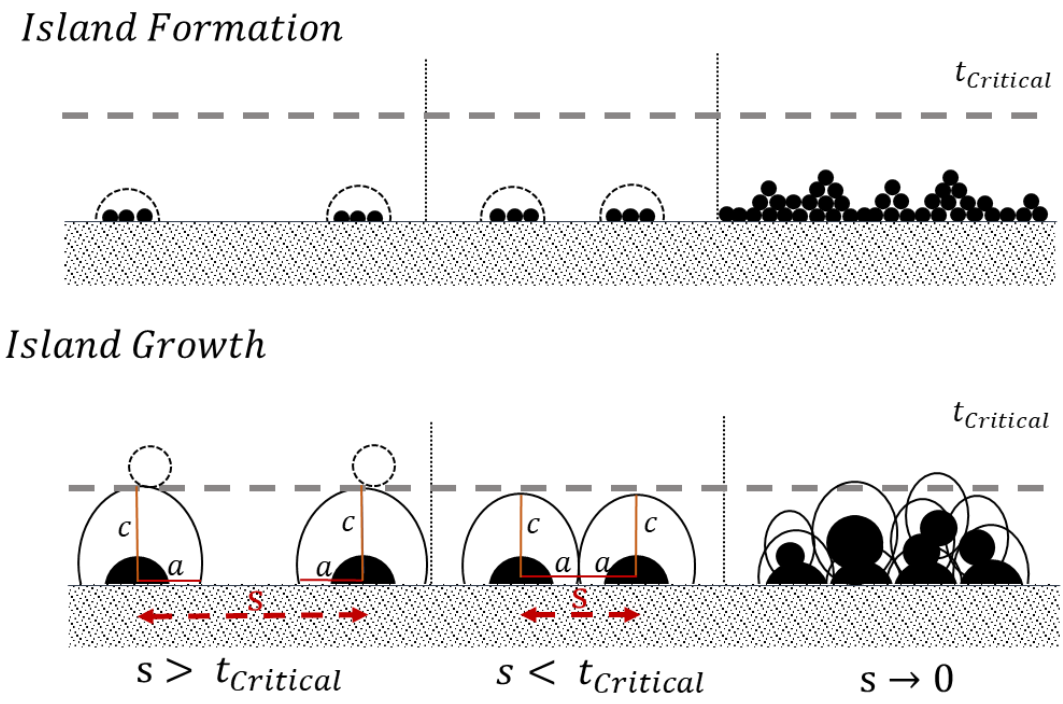

Figure 4-20: Illustration of seed particle coalescence into islands based upon their relative proximity. 'S' shows separation between particles. When large separations are present the lateral growth cannot bring the particles into contact before reaching critical thickness.

Figure 4-20 is an illustration of how seed numbers affect the growth mechanism of a gold coat. When too few seeds are immobilised upon the surface, the separation between the seed atoms, s, is so large that the increase in radius needed for the seeds to encounter is higher than the critical thickness. In this case, the gold seeds grow in a spherical fashion until their size is large enough that the silanes do not affect the deposition of new atoms. At which point gold: gold growth predominates. In this situation, it is likely impossible to control the growth of gold islands sufficiently for them to coalesce. When the separation of seeds is less than the critical thickness, the gold seeds can grow in radius sufficiently that they can form a contact between the two particles and coalesce into a smooth coat. Gold will be continued to be deposited upon the surface, depending on the volume of growth solution used and can still get thicker than the critical thickness. When seeds are used in great excess the separation between seeds on the surface decreases to approximately zero. At this point, there is insufficient space for further deposition of seeds, so they begin to form a second layer. This results in the formation of clusters of seeds that act as islands of different sizes across the surface and therefore result in a rough coat.

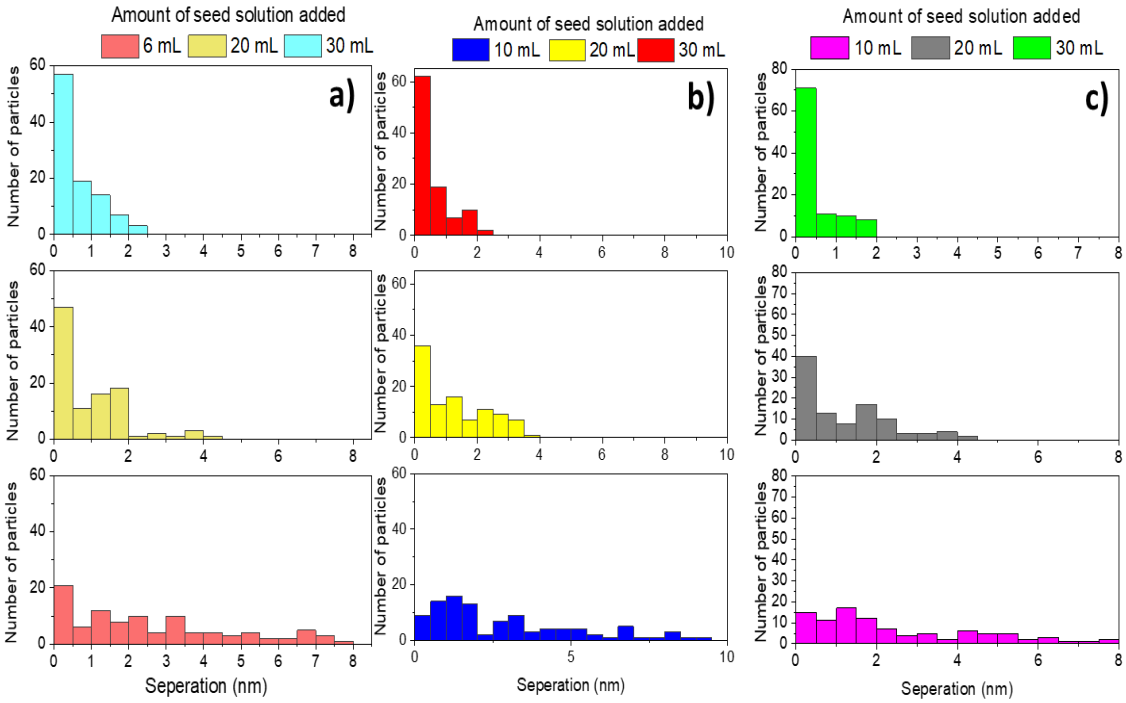

Figure 4-21: Distribution of the distance between gold seed particles supported on APTES functionalised hematite nanorods when treated with between 6 – 10 ml of seed solution. (a) Phosphate (b) 1,2 Propanediamine 160°C (c) 1,2 Propanediamine 180°C

When analysing the average separation between gold particles supported on phosphate hematite rods between 6-30 ml of seed solution treatments a median separation of 2.3, 0.7 and 0 nm can be calculated for However, this average is reduced by the large number of particles existing in clusters. A cluster is described as a group of particles with less than 1.5nm separation between them. When the separation of clusters is measured a considerably starker comparison can be seen with the average separation being 4, 1.8 and 1.7 nm respectively. With the % of these separations only being 25% and 11% for the 20 and 30 ml treatments. Similar data is obtained with 1,2 Propanediamine shown in Table 4-4.

1,2 Propanediamine 160°C	Separation (nm	
Seed Solution Added (Vol)	Seeds	Clusters
10 ml	1.7	3.9
20 ml	0.8	2.2
30 ml	0.0	1.7

1,2 Propanediamine 180°C	Separation (nm)	
Seed Solution Added (Vol)	Seeds	Clusters
10 ml	1.7	3.5
20 ml	1.0	2.5
30 ml	0.0	1.8

Table 4-4 Table separation between particles and clusters at different quantities of seed for 1,2 Propanediamine hematite particles formed at 180 and 160 °C. Measurements were taken over 100 particles and cluster separation was measured by removing all measurements below 1.5 nm.

This data indicates that while there are small channels of separation between clusters formed in the higher seed treatments, they are relatively few and considerably smaller when compared to those found in the 10 and 6 ml seed treatments. The small separations obtained in higher seed quantities can be overcome through the lateral growth of the gold seeds along the surface of the hematite resulting in a complete coat. When using too few seeds, however, the separation is too large, and channels are formed which cannot be filled before reaching the critical thickness and overgrowth occurs.

This proposed growth mechanism can be expressed mathematically by comparing the growth in height (c) and the radius (a) of the gold seeds. These particles grow preferentially along their height axis as gold: gold growth is preferred to the gold: hematite interaction with the surface of the nanoparticles. This growth results in gold nanoparticles similar in geometry to prolate spheres where c > a which is shown in Figure 4-22.

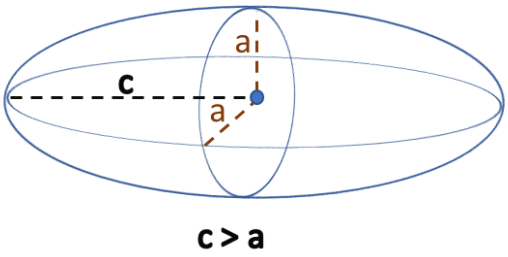

Figure 4-22 Illustration of a prolate spheroid

The surface area of a prolate sphere can be described as:

$$\text{Equation 4-1: } \text{Surface Area(A)} = 2\pi a^2 \left(1 + \frac{c}{ae}\arcsin(e)\right) \text{ where } e^2 = 1 - \frac{a^2}{c^2}$$

Assuming that the increase in the c axis is twice that of a axis the following equation for the surface area can be obtained:

$$\text{Equation 4-2: } \text{Surface Area(A)} = 2\pi a^2 \left(1 + \frac{4}{\sqrt{3}}\right)\left(\frac{\pi}{3}\right)$$

Therefore the change in the area can be obtained through derivation:

$$\text{Equation 4-3: } \frac{dA}{da} = 4\pi a \left(1 + \frac{4\pi}{3\sqrt{3}}\right)$$

$$\text{Equation 4-4: } \therefore \; dA = da \,.\, 4\pi \left(1 + \frac{4\pi}{3\sqrt{3}}\right)$$

The rate of change in the area is equal to:

$$\text{Equation 4-5: } \frac{dA}{dt} = \frac{da}{dt}.\, 4\pi \left(1 + \frac{4\pi}{3\sqrt{3}}\right)$$

The rate of growth of the total area is proportional to the current surface area and a rate constant “kA”

$$\text{Equation 4-6: i. e. } \frac{dA}{dt} = k_A A$$

By substituting

Equation 4-2 into Equation 4-10 for surface area (A):

$$\text{Equation 4-7: } \frac{dA}{dt} = k_A 2\pi a^2 \left(1 + \frac{4\pi}{3\sqrt{3}}\right)$$

From Equation 4-5:

$$\text{Equation 4-8: } 4\pi a \left(1 + \frac{4\pi}{3\sqrt{3}}\right)\frac{da}{dt} = k_A 2\pi a^2 \left(1 + \frac{4\pi}{3\sqrt{3}}\right)$$

$$\text{Equation 4-9: } \therefore \; \frac{da}{dt} = \frac{k_A a^2}{2}$$

integrating Equation 4-9 allows for the isolation of the magnitude of at time 0 and t:

$$\text{Equation 4-10: } \int_{a_0}^{a_t} \frac{2}{a^2}\, da = \int_{t_0}^{t_t} k_a\, dt$$

$$\text{Equation 4-11: } \left[\frac{-2}{a}\right]_{a_0}^{a_t} = k_a t \; \therefore \; \frac{2}{a_0} - \frac{2}{a_t} = k_a t$$

However since: $a = \frac{c}{2}$:

Equation 4-12: $\frac{4}{c_0} - \frac{4}{c_t} = k_a t$

The thickness of a film at time t can be described:

Equation 4-13: $\therefore\ c_t = \frac{4c_0}{4\text{-}k_a c_0 t}$

The dimensions of 100 nanoparticles on both phosphate hematite and 1,2 propanediamine hematite were prepared at 100 and 180 ^{o}C respectively. The radius (a) was often between 1.5 – 2 times smaller than that of the height of a single particle, supporting the growth mechanism suggested above. Furthermore, when plotting the average radius and height for the two nanorods they fit well to Equation 4-13. The first data points of lo volume fit less well with the equation, this is since initially the seed particles are spherical and become more prolate in nature as growth continues. However, this model is limited as particles begin to coalesce and lose their prolate geometry.

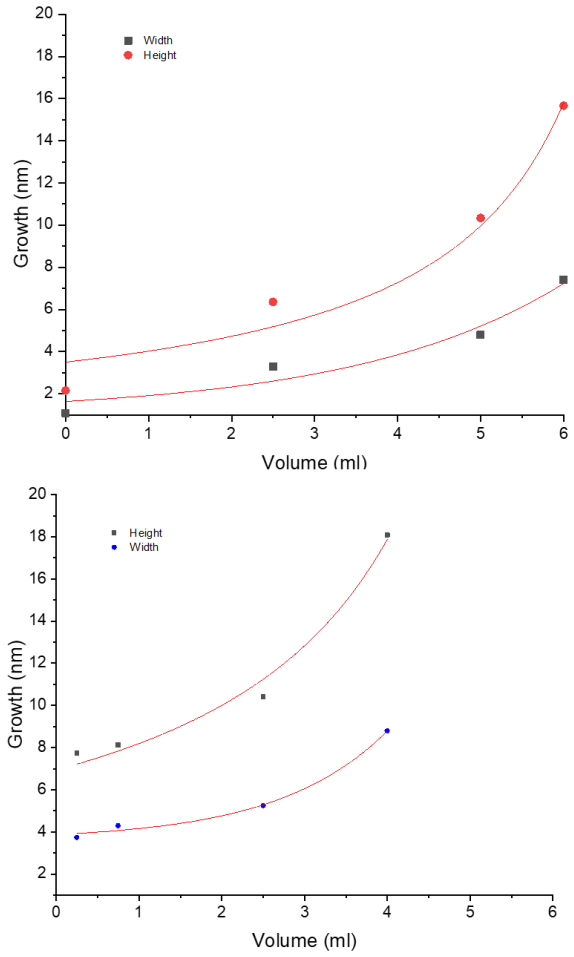

Figure 4-23: Graphs of average radius and height take from 100 seed particles at different volumes of gold growth solution fitted with Equation 4-13. (Top) 1,2 propanediamine 180^{o}C (bottom) Phosphate 100^{o}c

Figure 4-23 shows a good fit between the growth data and the mathematical model. Using the model the value of the rate constant kA can be deduced as 0.088 and 0.15 for 1,2 propanediamine 180^{o}C and Phosphate 100^{o}c respectively. The difference in rate constant could be a result of the different methods of APTES functionalisation across the two rods or could be a result of the difference in crystal orientation between the rods.

4.3.3 Silica Coating

Hematite nanoparticles were coated with silica using a modified Stöber process which involves decomposing TEOS in the presence of tetra-methyl ammonium hydroxide (instead of ammonia used in the standard Stöber process) and with PVP previously adsorbed on the hematite surface. Silica coatings of increasing thickness were prepared by simply increasing volumes of TEOS (added stepwise over 8 hours). A selection of TEM images of the resultant coated particles is shown in Figure 4-24 (a)-(g).

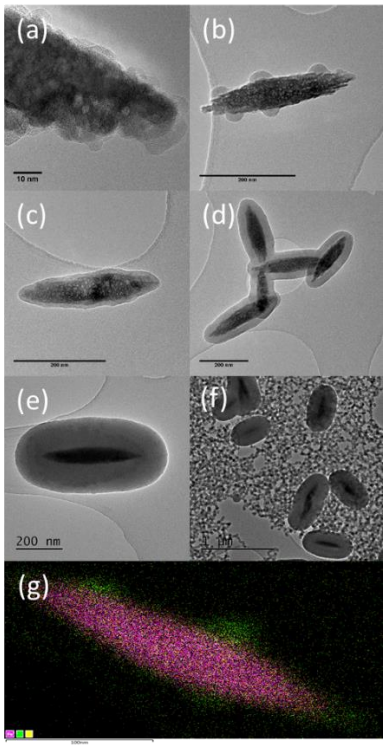

Figure 4-24 TEM and EDX images of a selection of phosphate directed hematite nanorods coated with increasing volumes of TEOS. (a) After coating with 0.05 mL TEOS with particles separated from solution after < 5 minutes; (b) After coating with 0.05 mL TEOS and equilibrated in solution for ~8 hours; (c) 0.1 mL TEOS; (d) 0.5 mL TEOS; (e) 4 mL TEOS. (f) 12 mL TEOS (g) EDX atomic map of (a) showing discontinuous silica shell surrounding the particle, red dots indicate iron, green indicates silicon.

Total volumes of TEOS less than 0.1 mL result in a discontinuous coverage of silica on the nanoparticle, but a complete coating with a thickness of ~5 nm was obtained with a total TEOS volume of 0.1 mL. However, under these conditions the coatings were not

homogenous, exhibiting larger island structures of silica upon the surface Figure 4-24 (a)-(c). With volumes of TEOS of 0.25 mL or greater, smooth silica shells were obtained which increased in thickness with the increasing TEOS: hematite ratio. The increasing shell thickness affects the aspect ratio, with the shell tending to a spherical shape. The thickness of the silica shell (at its thinnest point) grows to ~165 nm before plateauing and at this stage, further deposition of silica on the shell becomes unfavourable compared to nucleating nanoparticles of silica in solution. The latter is clearly illustrated by Figure 4-24(f).

The thickness of the silica coat increases rapidly as the ratio of TEOS added to a fixed volume of nanoparticles increases, but the rate of growth decays exponentially to the maximum thickness of ~165 nm. Yang's recent study of the effect of ammonia concentration on silica nucleation in the Stöber process shows a similar growth curve and proposes two competing pathways: (i) nucleation and growth of small silica particles via homogeneous condensation and (ii) condensation of silanol monomers onto the preformed silica particles. We were unable to fit the present thickness data with any combination of growth curves based on a competition of two processes (nucleation on the iron oxide vs nucleation of pure silica for example) suggesting that a third contribution affects the growth curve, perhaps a decreasing heat of adsorption at the nanorod surface as the diameter increases. An empirical fit to the function $T = L(1-\exp(-R/\beta))$ is shown in Figure 4-25, where T is the coating thickness, L is the limiting thickness of the coating, R is the TEOS / nanorod ratio and β is a constant, often called a time constant with this kind of function. The data gives a value of 165.82 nm for the limiting thickness and a β value of 0.131.

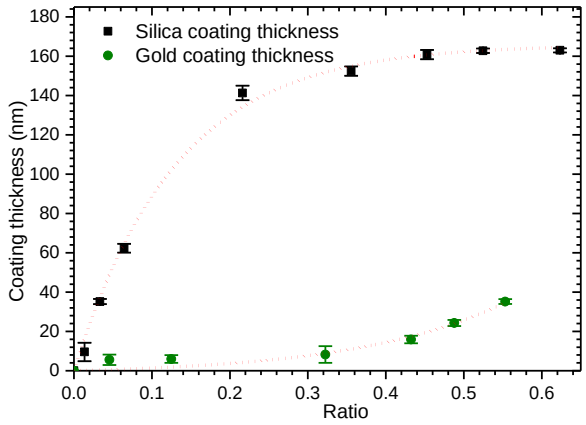

Figure 4-25 Measured silica and gold shell thicknesses on hematite nanorods as a function of the ratio of coating precursor concentration to hematite nanoparticles.

The gold coating on the hematite particles shows different behaviour to that of the silica, with an increasing rate of thickness growth as the ratio of gold concentration to hematite rods. However, this data only considers gold films with coatings up to ~ 40 nm, we have not been able to grow smooth gold coatings at greater thicknesses to explore the behaviour at higher ratios.

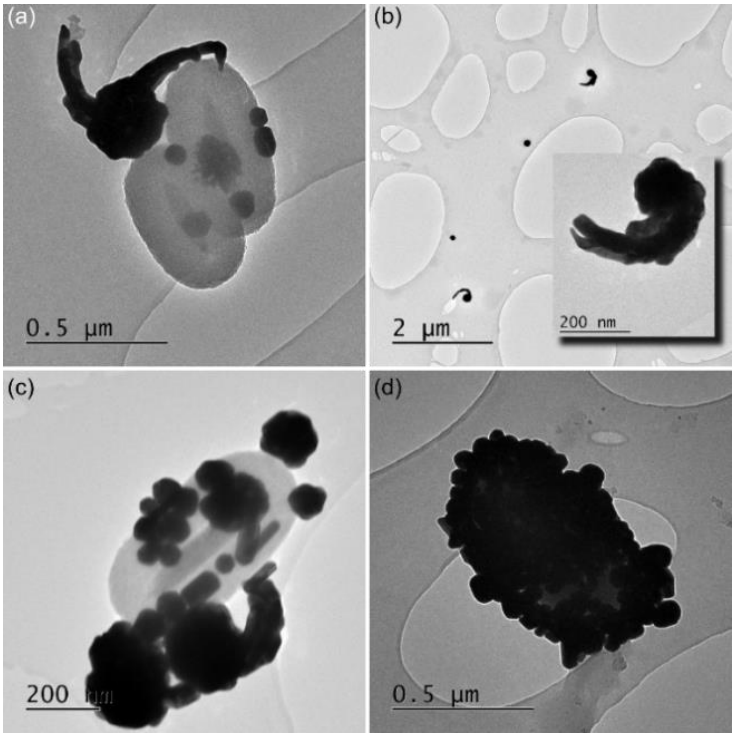

Figure 4-26: Growth of gold nanoparticles on silica coated hematite. (a) Gold particles observed upon silica shell at 5 mL gold solution; (b) Gold particles seen in solution at 5 mL gold solution; (c) Gold particles observed upon silica coat at 8 mL gold solution; (d) Fe_2O_3 / SiO_2 /Au formed with 25 mL Au solution.

It is interesting to compare the growth of gold coatings on silica surfaces with that on the hematite. Nucleation is less favourable on silica; no identifiable gold features could be seen on the silica shell until at least 10 mL of gold solution was added, as seen in Figure 4-26. However, gold particles with a "comma" shaped morphology were observed in solution for samples using at least 5 mL of the gold coating solution, From the similarity of these shapes to those observed at higher gold solutions and associated with the hematite particles, we surmise that these distinctive particles in solution have detached during the centrifugation step and been removed in the supernatant liquid.

4.3.3 Cerium Phosphate Rod Coating.

The cerium phosphate nanoparticles prepared in Chapter 3, have an interesting promise for their optical properties. Since the emission wavelength of plasmonic nanoparticles is

directly proportional to its aspect ratio, the $CePO_4$ nanoparticles would be an ideal core substrate due to their range of possible aspect ratios. Equation 4-14 shows this linear relationship in a nanorod, where R is the nanoparticle aspect ratio.

Equation 4-14 $$\lambda_{max} = 95R + 420$$

$CePO_4$ nanorods were synthesised with aspect ratios of between 3 and 27 in Chapter 3, which from Equation 4-1 predicts a possible λ_{max} range of 705 – 2985 nm. While the hematite systems would only cover a range of 600 - 1100 nm.

Since the seed-mediated growth had been successful in both hematite methods a similar method was adopted for the new system of $CePO_4$. Previous coating proportions and estimates were replicated in this section, for example, the reflux APTES functionalisation step piloted on the 1,2 propanediamine nanoparticles. However, one must be careful in drawing parallels between chemically different surfaces and morphologically different rods.

4.3.3 Direct Gold Coating

The preparations of $CePO_4$ were carried out in a similar method to that of 1,2 propanediamine hematite where 50 mg of $CePO_4$ nanorods were functionalised with 120 µl APTES before supporting between 3 – 20 mL of seed solution.

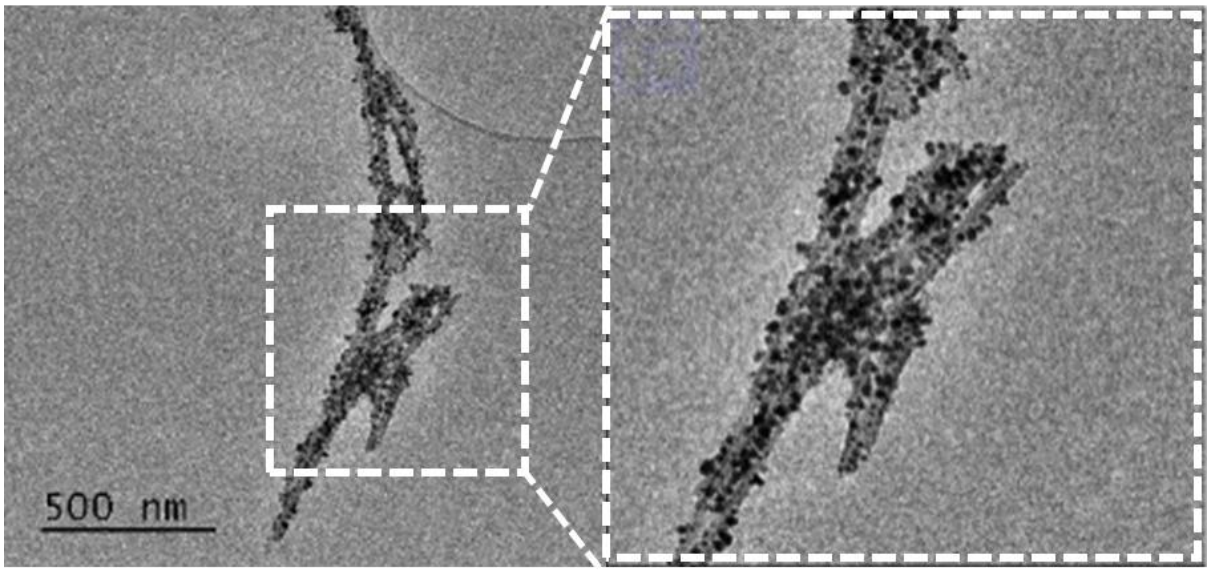

Figure 4-27: TEM micrographs showing seeded -$CePO_4$ nanoparticles following the addition of 5 mL of gold growth solution.

Figue 4-27 shows the results of the coating $CePO_4$ seed mediated growth. While gold islands were successfully supported on the surface of the rods they were not well distributed across the surface, with only 10 particles per 100 nm^2. These poorly distributed particles grew from 3.89 nm to an average of 14.87 nm in diameter whilst a few gold nanoparticles on the cerium phosphate surface grew to over 25 nm in diameter which is larger than the average $CePO_4$ nanoparticle width of 16.2 nm. While previous data would indicate this was through a lack of seed particles being supported on the surface leading to large gold particles, this result was obtained across all seed treatments.

The APTES functionalised $CePO_4$ surfaces the average gold seed n size was 3.89 nm which corresponds to greater than 24 % of the width of one cerium phosphate nanoparticle. It is theorised that since the ratio of nanorod surface to seed particle size is so small there is insufficient room for space for nanoparticles to pack onto the surface to fully coat the $CePO_4$ nanorods. When the seeds are so large in comparison to the core, each seed represents a significant increase in width and can radically change morphology. For example, if we assume a $CePO_4$ nanorod is cylindrical in shape the circumference of one rod would be 50.89 nm only allowing for 13 seeds to be along one circumference. Ultimately, this predicts that there is considerably less room and opportunity for nanoparticles to be functionalised to the surface of a $CePO_4$ nanorod compared to a hematite nanorod. As a result, the few seeds which do stabilise upon the surface grow unevenly and cannot coalesce.

4.3.3 Silica Coated $CePO_4$

To overcome the issues faced Figure 4-27 a modified coating method utilising silica as an intermediate was developed like that of Wang et al. who created $Fe_2O_3/SiO_2/Au$ sandwich structures through first coating hematite with the Stöber method and then taking a more controlled approach to the seed-mediated gold growth[33].

Figure 4-28: Diagram showing how $CePO_4$ nanorods are prepared for the seed-mediated coating of gold.

This method can be divided into two key steps:

1. The silica coating of $CePO_4$ with the Stöber method.
2. A modified seed-mediated stepwise gold coat growth.

By introducing a controlled silica coat the average diameter of a nanorod can be increased meaning more gold seeds can be supported on any single rod. While gold does not have a significant affinity for silica, the APTES reflux step makes it possible to support gold seeds on the surface of silica.

Since the thickness of a silica coat can have effects on the magneto-optical properties of nanorods the Stöber method was studied on $CePO_4$ nanoparticles to produce different shell thicknesses. Like the results obtained on hematite nanorice, the amount of TEOS added to the reaction was directly proportional to the thickness of the silica coat. Therefore, small amounts of TEOS were added to the $CePO_4$ nanorods to prepare thin coatings which would have the least effect on the magneto-optical properties of the nanoparticles.

This step was carried out under sonication as in the absence of agitation nanoparticles would aggregate into larger structures. The maximum thickness of the silica coating obtained on $CePO_4$ in this study was 21.3 nm. TEOS added at speeds faster than 0.1 mL every 30 minutes resulted in separate silica particles Figure 4-29 (d) rather than a silica coat on the $CePO_4$ surface. An additional rate of 0.1 mL every 30 minutes would result in more than 5 hours to deliver TEOS volumes greater than 1 mL, and it was deemed not time effective.

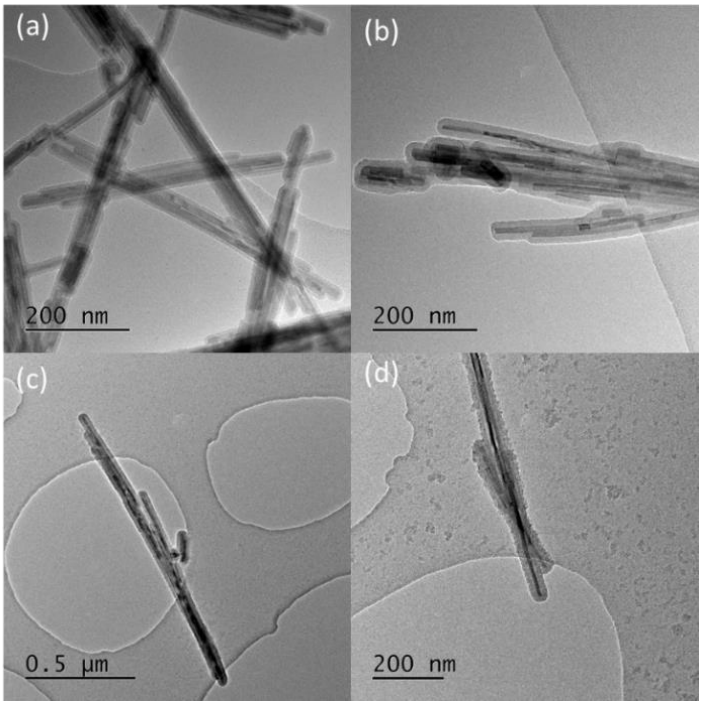

Figure 4-29: A) 0.1 mL TEOS added in 30 mins B) 0.5 mL TEOS added over 2.5 hours C) 1 mL of TEOS over 5 hours. D) 1 mL TEOS over 1 hour at 0.5 mL per 30 minutes.

As the ratio of $CePO_4$:SiO_2 increases, the morphology of the nanostructures changes from a more rectangular prism-like morphology to an elliptical morphology. Such changes in geometry can have profound changes on the optical properties of nanostructures since plasmon emission tends to occur from corners and edges[34]. This geometry has some distinct optical advantages over the more rectangular form. As discussed in the introduction surface plasmons have two modes: The longitudinal and the transverse. As a rod-shaped nanoparticle is similar in morphology to a spindle the coupling of these two modes is greater in a rod than in a rectangular prism[35]. As corners of a cuboidal nanoparticle are rounded the two modes shift closer together with the most intense mode shifting down in wavelength and increasing in intensity and sharpness[36]. However, Sburlan et al. predicted that rectangular prism-shaped nanorods have a greater degree of light scattering than a rod with rounded corners. This may be because by rounding the corners of a rod, you are effectively decreasing the length of the particle[37], which can reduce the intensity of the transverse component.

TEOS Volume (ml)	Coating Thickness (nm)	Total Diameter (nm)	Aspect ratio *
0.1 mL	5.8 nm	27.8	21
0.5 mL	16.1 nm	48.4	12
1 mL	21.3 nm	58.8	9.9

Table 4-5: Comparison of $CePO_4$ nanoparticle morphology and aspect ratio when coated with different quantities of TEOS. * $CePO_4$ nanoparticles were formed at 170 ^oC with an average length of 563 nm and an average diameter of 16.2 nm corresponding to an aspect ratio of 34.5.

Optical and magnetic properties will be negatively affected with an increasing coat thickness, irrespective of corner rounding. For optical properties, this is because the growth of a silica coat significantly increases diameter as coating thickness increases. This is illustrated in Table 4-5 where a coat of 16.1 nm thickness can effectively reduce aspect ratio by 65% which would hugely impact optical sensitivity. Consequently, it is important to balance all these effects when selecting a suitable coat. The coat achieved in this study, at 5.8 nm, was selected for supporting seeds. While this coating seems small, it has a large effect on the circumference of the nanoparticle. This coating resulting in an increase in circumference from 50.89 nm to 87.34 nm which would allow for 22 seed particles along one cross-section of a rod while providing an intermediate to increase gold affinity.

The $CePO_4/SiO_2$ rods with a coating thickness of 5.8 nm were functionalised with APTES under reflux and 20 mL of seed solution was used to support gold seeds on their surface. The coating of the rods was undertaken by a modified seed-mediated method. This method introduces the gold growth solution in a stepwise manner. Under constant sonication 1 mL of gold growth solution was added every 2 minutes until a total gold solution volume of 8 mL was reached. To better control, the growth in these sequential additions, 50 µl of PVP was added every 4 minutes followed by 500 µl when at the end of the additions. This method through the slow addition of gold and PVP sequentially allowed for the deposition of gold in a constant PVP stabilised environment which should prevent the aggregation of unwanted gold seeds in solution.

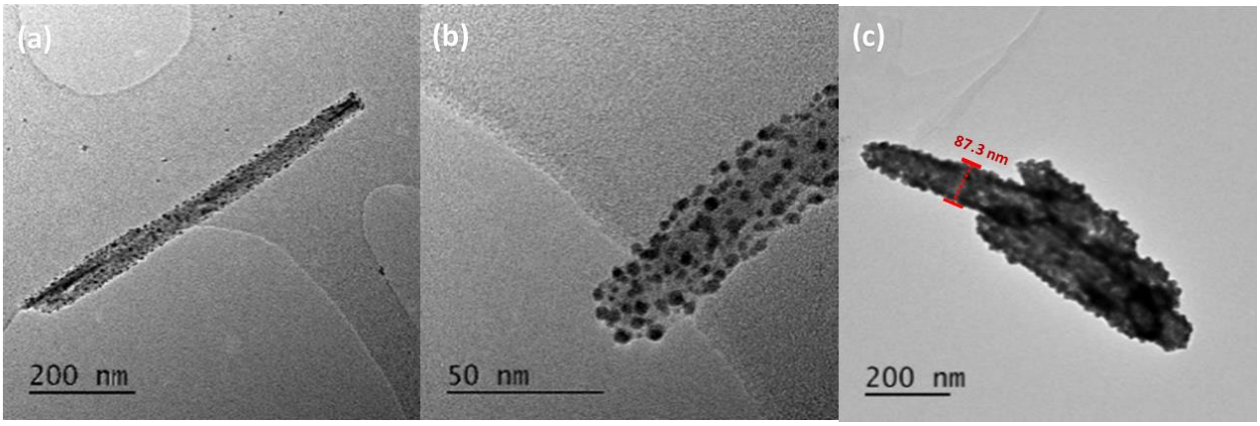

Figure 4-30: TEM Micrographs of $CePO_4/SiO_2$/Au particles prepared with 14 mL of seed solution and coated using the modified seed-mediated method. The micrographs were taken at different stages of their preparation. a-b) seeded silica coated nanorods c) cluster of $CePO_4/SiO_2$/Au. The Red line shows the diameter of one $CePO_4/SiO_2$/Au nanostructure.

$CePO_4$ nanorods were successfully seeded with gold nanoparticles with an average size of 3.9 nm these particles were well distributed across the surface with an average of 74 per 100nm, a large increase from 10 per 100 nm without the silica. Figure 4-30 (c) shows the product of the $CePO_4/SiO_2$/Au coating. While the particles have successfully been coated in a 13.5 nm gold shell, the coat is not smooth and has clear bumps from seed particles on the surface. However, the nanoparticles have a surprisingly large average diameter of 86.6 nm which is not accounted for by the increase in the SiO_2 and Au coats. The predicted average particle size for a $CePO_4/SiO_2$/Au particle with a 5.8 nm silica coat and a 13.5 nm gold coat would lie at approximately 54 nm. Figure 4-30 (c) shows an example diameter measurement of one of these nanoparticles. The gold interface between the core and the gold coating can be easily identified on the micrograph and has a width of 14 nm, leaving a core size of approximately 59 nm which probably corresponds to two aggregated $CePO_4$ nanorods.

It is possible that during the gold coating step, multiple $CePO_4$ rods adhered to each other and as a result were encapsulated by the gold coat. This has a dramatic effect on the nanocomposites formed, changing their diameters, and hence reducing the aspect ratio. These nanoparticles formed with an average aspect ratio reducing from 21 to 6.7.

4.3.4 Discussion

The preparation procedures described here, reproducibly create four different gold coated nanostructures using the seed-mediated method. These particles each have their challenges which result from their morphology and surface chemistry. Through the study of functionalisation and producing sandwich structures, each particle was successfully coated in gold. However, while each of their coatings was different, some general trends and relationships were uncovered when using the seed-mediated method.

In the absence of any other functionalisation, gold had a low affinity for all the surfaces studied here ($CePO_4$, Fe_2O_3 and SiO_2) but it has been shown that smooth coatings of gold can be achieved in the presence of seed particles. In the absence of seed particles particle growth is more three dimensional and a possible explanation for this behaviour is that lateral growth on the three surfaces is stabilised by the presence of the seeds. This could occur if the initial growth of gold on the surface is strained but stabilised by the presence of the seed. The strain in the adlayer becomes unfavourable where growth on the surface occurs too far away from the gold nanoparticles and so three-dimensional growth occurs in preference. In other words, the seed nanoparticles provide a network of anchors on the surface. Once the adlayer is established, growth becomes more even and thicker gold adlayers develop with increasing volumes of gold solution added. Therefore we can conclude that understanding the relationship between the number of seeds present and that the volume of gold solution added is imperative for forming a smooth coat. When few seeds are present there is an insufficient network of “scaffolding” for the building of a coat and as a result, a rough surface develops. On the other hand, when too many seeds are present the seed particles form large groups which, when exposed to gold growth solution, gow into individual nanoparticles rather than forming a coating.

The effect of morphology and crystallinity was examined through the use of particles formed by two different structure directors: 1,2 propanediamine and phosphate. As discussed in chapter 2, the nanoparticles of phosphate-directed hematite, are formed through the aggregation of hematite subunits, while 1,2 propanediamine directed nanorods are formed from a single crystal. When these different types of particles are coated the overall relationship of coating thickness and seed growth was similar for both types of rod. The increase in seed particle size, and hence coating thickness, was proportional to the

amount of gold growth solution added to the rods. However, the total surface areas of the two types of rods were different as a result of their different morphologies. Since 1,2 propanediamine rods were larger with surface areas calculated to be almost twice that of the phosphate directed rods, they required more gold solution for the seed particles to coalesce. Ultimately, because more gold solution was needed a larger degree of gold stabilisation was required to prevent the unwanted gold: gold growths, this was achieved with the addition of extra PVP.

The morphology of the final coat formed upon both hematite systems relied heavily on the amount of gold growth solution added and the number of seed particles on the surface. When using a gold seed solution, the seed particles appear to cluster into groups of several seeds. When increasing the volume of seed solution these particles become more homogeneously dispersed across the surface and have significantly lower separations. When using an excess of gold seeds, there is insufficient space for seeds to be immobilised upon the surface and instead, they stack protruding from the surface of the hematite rod. The number of particles present on the surface of the hematite decreases as the growth solution is added. The growth of gold seeds can be successfully modelled as prolate spheres where the lateral growth of seed particles is half the rate of the film thickness. Separation data suggests that maximum separations between nanoparticles should be no more than 3.9 nm to achieve a smooth coat.

The challenge of coating silica with gold is to increase the affinity of the surface to the gold seeds even further than in comparison to the hematite surfaces. This could be a result of APTES not functionalising the surface of the SiO_2 as favourably as it did on hematite. When gold growth solution was added to the seeded - Fe_2O_3/SiO_2 nanorods it resulted in the independent growth of gold nanoparticles into morphologies such as triangles and rods. This could be due to two different effects. (1) there is insufficient seeds on the surface. (2) the growth was not controlled well enough as all gold was added in one step. When coating seeded-$CePO_4/SiO_2$ particles this was done in a stepwise manner with additional PVP being added to prevent gold: gold growth as was seen in the hematite samples.

Clean $CePO_4$ surfaces were difficult to coat in gold even when functionalised with APTES. When this was carried out very few gold particles, only 7 per 100 nm would adhere to the surface of the nanoparticles. It was suggested that this was a product of the narrow

diameter of these nanoparticles, in the region of 16 – 21 nm, which allows for very few 3.89 nm particles to fit onto one face of these rods. As discussed above these seed particles form a network that acts as a foundation for the eventual gold coat and since there is so little room, the particles cannot disperse themselves favourably across the surface. When using a silica intermediate the quantity of seeds supported on the surface increases from 7 to 74 per 100 nm indicating a clear increase in affinity for the surface with silica is functionalised with larger quantities of APTES. However, while these coats allow for the easier functionalisation and seeding of $CePO_4$ rods, they may also be causing the aggregation of nanoparticles between treatments. The effect of this can be seen in the final $CePO_4/SiO_2$/Au product where multiple rods would agglomerate into larger structures.

4.4 Conclusion

Gold coating of silica and iron oxide and cerium phosphate surfaces has been investigated and compared. While gold coating was relatively straightforward on a hematite surface, silica and cerium phosphate surfaces required extra control in their seed-mediated coating. Several nanoparticles of differing aspect ratios were successfully coated in gold however their coatings differed in thickness and roughness, See Table 4-6.

	Average		
Particle Type	**Coating Thickness (nm)**	**Coating Roughness (nm) [1]**	**Aspect ratio [2]**
Phosphate Hematite	24.3	5.7	5.2
1,2 propanediamine 180°C	16.8	8.2	6.1
1,2 propanediamine 160°C	12.3	10.4	2.26
$CePO_4$	13.5	13.5	6.6

Table 4-6: Table comparing the morphology of gold coatings obtained on different nanoparticles. 1 Coating roughness is found by measuring the average variation in height across the particle. 2 Aspect ratio is calculated assuming that each particle has its average dimensions.

The phosphate hematite rods have the smoothest gold coating of all particles formed; however, this coating is also the thickest. A thick coat can affect the magnetic properties of nanoparticles, so such a thick coat may have negative effects on the magneto-optical effects. The highest aspect ratio nanoparticles formed were $CePO_4$ which gives the potential to have a plasmon peak with the most intensity. However, these also have the highest surface roughness and therefore may not have consistent emission spectra between

batches. 1,2 propanediamine 180 ^{o}C possess the balance of all these properties. They have a large aspect ratio, without too thick or too rough a coat.

4.5 References

1 S. A. Afolalu, S. B. Soetan, S. O. Ongbali, A. A. Abioye and A. S. Oni, in *IOP Conference Series: Materials Science and Engineering*, Institute of Physics Publishing, 2019, vol. 640, p. 012065.

2 M. G. Taylor, N. Austin, C. E. Gounaris and G. Mpourmpakis, *ACS Catal.*, 2015, **5**, 6296–6301.

3 S. J. Hoseini, M. Bahrami, M. Zanganeh, M. Roushani and M. Rashidi, *RSC Adv.*, 2016, **6**, 45753–45767.

4 G. Oberdörster, E. Oberdörster and J. Oberdörster, *Environ. Health Perspect.*, 2005, **113**, 823–839.

5 M. Rothe, Y. Zhao, G. Kewes, Z. Kochovski, W. Sigle, P. A. van Aken, C. Koch, M. Ballauff, Y. Lu and O. Benson, *Sci. Rep.*, 2019, **9**, 1–12.

6 H. Jeon and K. Lee, *Colloids Surfaces A Physicochem. Eng. Asp.*, 2019, **579**, 123651.

7 A. Bendahou, H. Kaddami and A. Dufresne, *Eur. Polym. J.*, 2010, **46**, 609–620.

8 K. S. Kumar, V. B. Kumar and P. Paik, *J. Nanoparticles*, 2013, **2013**, 1–24.

9 W. Shi, J. Casas, M. Venkataramasubramani and L. Tang, *ISRN Nanomater.*, 2012, **2012**, 1–9.

10 X. Chen and L. Jensen, *J. Opt. (United Kingdom)*.

11 N. Daneshfar, *Phys. Plasmas*, 2014, **21**, 063301.

12 M. J. Powell, R. Quesada-Cabrera, W. L. Travis and I. P. Parkin, *J. Mater. Chem. A*, 2015, **3**, 17241–17247.

13 M. Israelowitz, J. Amey, T. Cong and R. Sureshkumar, *J. Nanomater.*

14 H. Hofmeister, P. T. Miclea and W. Mörke, *Part. Part. Syst. Charact.*, 2002, **19**, 359–365.

15 A. Dokoutchaev, J. Thomas James, S. C. Koene, S. Pathak, G. K. Surya Prakash and M. E. Thompson, *Chem. Mater.*, 1999, **11**, 2389–2399.

16 H. Wang, D. W. Brandl, F. Le, P. Nordlander and N. J. Halas, *Nano Lett.*, 2006, **6**, 827–832.

17 J. C. Y. Kah, N. Phonthammachai, R. C. Y. Wan, J. Song, T. White, I. Ahmad, C. Sheppard and M. Olivo, *Gold Bull.*, 2008, **41**, 23–36.

18 Fairley N, *CasaXPS Manual: 2.3.15 Spectroscopy*, 2009.

19 V. A. Dhumale, R. K. Gangwar, S. S. Datar and R. B. Sharma, *Mater. Express*, 2012, **2**, 311–318.

20 H. Shen, B. L. Cheng, G. W. Lu, D. Y. Guan, Z. H. Chen and G. Z. Yang, *J. Phys. D. Appl. Phys.*, 2005, **39**, 233.

21 R.-Y. Zhong, J.-W. Yang, Z. Hu and B.-Q. Xu, *ACS Appl. Nano Mater.*, 2019, **2**, 5720–5729.

22 A. K. Thompson, C. Hackett, T. L. Grady, S. Enyinnia, Q. C. Moore and F. M. Nave, *Polymers (Basel).*

23 K. W. Shah and L. Zheng, *Materials (Basel).*

24 K. M. Koczkur, S. Mourdikoudis, L. Polavarapu and S. E. Skrabalak, *Dalt. Trans.*, 2015, **44**, 17883–17905.

25 B. Bowden, M. Davies, P. R. Davies, S. Guan, D. J. Morgan, V. Roberts and D. Wotton, *Faraday Discuss.*, 2018, **208**, 455–470.

26 X. F. Hoo, K. A. Razak, N. S. Ridhuan, N. M. Nor and N. D. Zakaria, in *AIP Conference Proceedings*, 2017, vol. 1877, p. 39.

27 F. Ye, S. Laurent, A. Fornara, L. Astolfi, J. Qin, A. Roch, A. Martini, M. S. Toprak, R. N. Muller and M. Muhammed, *Contrast Media Mol. Imaging*, 2012, **7**, 460–468.

28 W. L. Liu, F. C. Lin, Y. C. Yang, C. H. Huang, S. Gwo, M. H. Huang and J. S. Huang, *Nanoscale*, 2013, **5**, 7953–7962.

29 H. Husain, B. Hariyanto, M. Sulthonul, W. Klysubun, D. Darminto and S. Pratapa, *Mater. Res. Express*, 2019, **6**, 086117.

30 K. R. Brown, L. A. Lyon, A. P. Fox, B. D. Reiss and M. J. Natan, *Chem. Mater.*, 2000, **12**, 314–323.

31 T. C. Preston and R. Signorell, *ACS Nano*, 2009, **3**, 3696–3706.

32 D. W. Pashley, M. J. Stowell, M. H. Jacobs and T. J. Law, *Philos. Mag.*, 1964, **10**, 127–158.

33 X. Wang, J. Feng, H. Yu, Y. Jin, A. Davidson, Z. Li and Y. Yin, Anisotropically Shaped Magnetic/Plasmonic Nanocomposites for Information Encryption and Magnetic-Field-Direction Sensing.

34 X. Bin Xu, J. S. Luo, M. Liu, Y. Y. Wang, Z. Yi, X. B. Li, Y. G. Yi and Y. J. Tang, *Phys. Chem. Chem. Phys.*, 2015, **17**, 2641–2650.

35 D. C. Tzarouchis, P. Ylä-Oijala, T. Ala-Nissila and A. Sihvola, *Appl. Phys. A Mater. Sci. Process.*, 2016, **122**, 1–7.

36 A. Agrawal, I. Kriegel and D. J. Milliron, *J. Phys. Chem. C*, 2015, **119**, 2021.

37 S. E. Sburlan, L. A. Blanco and M. Nieto-Vesperinas, *Plasmon excitation in sets of nanoscale cylinders and spheres*, American Physical Society, 2006, vol. 73.

Chapter 5 Magnetic Behaviour of Nanorods

5.1. Introduction

Magnetic anisotropic nanoparticles possess different properties to those of simple spherical morphology, their anisotropic nature can give rise to several direction-dependent magneto-optical properties such as Faraday rotations, circular dichroism and nonlinear optical behaviour[1]. These unique properties offer several potential uses across several applications including drug delivery[2], catalysis[3], and communications[4]. The symmetry and elongated shape of nanorods result in magnetic anisotropy which leads to an S like hysteresis loop when the magnetic field is in line with the short axis and a square shaped hysteresis loop when in line with the long axis[5,6].

One example of multi-functional magneto-optical nanorods is found in the case of Fe_3O_4/SiO_2 core-shell nanoparticles which have been linked in the literature to a wide array of possible uses, for example, the development of Crystal Colloidal Arrays (CCA). These systems can detect magnetic fields and when sandwiched between two polarisers can act as anti-counterfeiting materials. At smaller film thicknesses the CCA colour becomes dependent on the magnetic field and this could allow for the design of smart windows, which can change the transmittance of light into a room based on an external magnetic input[7,8]. Fe_3O_4/SiO_2 composites can also be used as theranostic agents in magnetic resonance imaging and targeted cancer treatment. When functionalised with folic acid the composite uptake by cancer cells was significant with a high selectivity ideal characteristics for the particles to act well as a targeted medicine. Furthermore, the optical properties of the nanoparticles mean that they exhibit a photothermal effect killing the cancerous cells[9] when exposed to long-wavelengths (650-900 nm).

Magnetic nanoparticle sensors rely upon the behaviour of nanoparticles in solution while being manipulated by an external magnetic field. These sensors can take several shapes and sizes. Magnetic Relaxation switches (MRSws) can be used as contrast agents in MRI imaging[10]. These sensors rely upon a change in the T_2 relaxation time caused by a switch between aggregated and non-aggregated nanoparticles[11]. Nanoparticles are functionalised with molecules that bind to specific target molecules. When these target molecules are present the magnetic nanoparticles bind to them, forming agglomerates of multiple nanoparticles surrounding the target molecules. This causes local magnetic field

inhomogeneities which dephase the proton spins around them resulting in the relaxation of the medium increasing. One example of these 'relaxometers' uses Mn-doped ferrite nanoparticles between 10 – 16 nm in length to detect approximately 2 cancer cells per µL of solution[12].

The above example indicates the sensitivity of magnetic particles but does not rely on magneto-optical properties. However magnetic and optical properties can be coupled for many different uses as Table 5- shows.

Nanoparticle Type	Magneto-optical principal	Potential Application	Ref
Fe_3O_4/SiO_2/Au Nanocomposite	Faraday Effect	Magnetic Field Sensor	13
Ni & cobalt nanorods	Faraday Effect	Magnetic Rotational Spectroscopy	14
Ni nanorods	Magneto-optical Diffraction	Optofluidic Illuminator	15
Ni nanodiscs	Kerr Effect	Magneto-Plasmonic Ruler	16
Ni nanorod	Induced polarization & Rotational Dynamics	Protein Detection	17
Fe_3O_4 magnetic nanobead	Induced Polarization & Rotational Dynamics	DNA Detection	18

Table 5-1: Table of different magneto-optical nanoparticles and their potential uses.

Zubritskaya et al. used the magneto-optical Kerr effect to obtain accurate measurements of distances on the nanoscale with Ni nanodiscs[16]. This was achieved by measuring the extinction coefficient of different distances between the Ni nanodiscs, as they came closer together more intense signals were obtained. The intensity of the signal was proportional to the distance between the two discs. This allowed the light guided assembly of nanostructures in solution. The other uses in Table 5- rely on the movement or rotation of nanoparticles in solutions caused by an external magnetic field. Wang et al. used plasmonic nanocomposites of Fe_3O_4/SiO_2 that would respond accurately to an external magnetic field and orientate themselves appropriately[13]. Tokarev et al. used a suspension of Ni nanorods of different lengths to examine the effects of drag upon their rotation[15]. They found that as the aspect ratio increased the ability of a nanorod to follow an external magnetic field decreased. This is because when an external magnetic field is rotating there is a lag between the particle rotation and the magnetic field. This can be described by considering the magnetic torque t_m exerted on a particle and the drag felt by that particle:

Equation 5-1 $$t_m = \mu_{eff} B \sin\theta = \gamma 2\pi f$$

Where μ_{eff} is the effective magnetic moment, f is the frequency of rotation, θ is the angle between the nanorod and the rotating magnetic field B and γ is the drag constant[19,20].

The drag γ is determined by a combination of the nanoparticle length l, diameter d, and viscosity η of solution.

Equation 5-2

$$\gamma = \frac{\pi\eta l^3}{3\ln\left(\frac{l}{d}\right)\text{-}2.4}$$

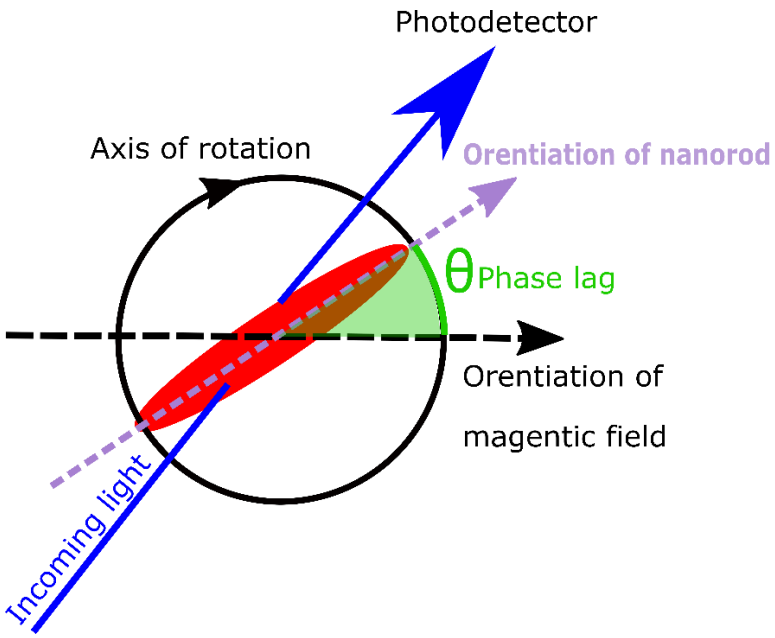

Figure 5-1: Illustration of nanorod rotation acting as a sensor. Θ indicates the lag between the nanoparticle and magnetic field orientation.

Equation 5-1 and Equation 5-2 while showing the relationship between nanoparticle rotation and several key parameters. Firstly, the drag forces felt by a nanoparticle and the lag between a nanoparticle. This means that the phase lag between a nanoparticle and the magnetic field is proportional to the particle length, its diameter and the viscosity of the solution. Secondly, in magneto-optical uses, the amplitude of light transmitted through the solution is a function of the phase. A particle suspension with a greater net orientation between the particle axis and the magnetic axis will deliver higher amplitudes compared to a suspension where particles have lesser net orientation. Therefore, changes in particle movement can be measured through two modes, changes in the amplitude of light and changes in the phase lag for any given suspension (Illustrated in Figure 5-1).

The properties and measurements above enable other applications listed in Table 5-., which can be classified under two different types: Those which measure changes in viscosity and those which measure changes in the nanoparticle surface.

Changes in the viscosity of a solution will have an obvious effect on the drag experienced by a particle. Increasing the viscosity will increase the drag forces and hence lead to a greater phase lag. This enables rotational magnetic spectroscopy with anisotropic nanoparticles. These probes could be used to measure the rheology of surface droplets[21]. However, there are also biological applications, where the viscosity of a solution can be used to indirectly detect the presence of target molecules[21].

The other mode of action allows for target molecules to bind to the surface of functionalised nanoprobes to detect DNA and different proteins. These methods rely upon effective changes in the nanorod diameter. Schrittwieser et al. used cobalt nanorods coated in platinum and gold as sensors[21]. The particles when functionalised had an average diameter of 15 ± 9.5 nm, and the best detection was for small analytes in the region of 2- 15 nm. Thus the binding of such analytes to the surface would result in changes in the diameter of between 15 -100 % which would have a significant effect on the drag forces.

5.5 Bacterial Endotoxin Detection

Cotton Mouton Diagnostic Ltd., (CMD) the industrial partner in this research project, rely upon similar technology to those described above to test for the presence of bacterial endotoxins (BET). Bacterial endotoxins are lipopolysaccharides present in the walls of gram-negative bacteria[22]. These molecules can cause liver damage, heart problems and have been linked to neurodegenerative disease[23]. The European Union sets limits for these molecules at 0.25 endotoxin units per mL (EU/mL) to which all pharmaceutical companies must adhere. However, testing for these molecules can also be used as diagnostics. BET play a significant role in sepsis and are present in a large number of patients suffering from the condition[24]. Therefore detecting the presence of BET in the blood of patients suspected to be suffering from sepsis could act as a diagnostic test for the condition[25]. One test for the presence of BETs is often carried out with Limulus Amebocyte Lysate (LAL), an extract from the blood cells of the horseshoe crab. When BETs react with LAL it causes the formation of a clot. In a 'Gel clot LAL test' the presence of BETs is confirmed qualitatively by leaving the mixture of the two reagents to incubate for an hour at 37 ^{o}C. Following this, the sample is

inverted by 180° and if a clot is observed, BET is present[25]. The LAL gel method varies between 0.1-1 EU/mL and quantitative methods such as the chromogenic and turbidimetric have detection limits of 0.01 and 0.005 EU/mL, respectively[26].

CMD can quantify the presence of BET through its reaction with LAL to a limit of 0.001 EU/mL in 30 minutes. This is achieved through the magneto-optical rotation of nanoparticles in a solution of LAL. The rotation of the particles is sensitive to small changes in viscosity caused by the clotting of the LAL. This causes an increase in drag and can be monitored through the amplitude and phase of the optical signal.

In this chapter, the doping of $CePO_4$ nanorods formed in chapter 3 with different metal ions is discussed and their magnetic properties assessed. The behaviour of nanoparticles of different morphology has been tested to examine if they can be rotated in aqueous media to produce magneto-optical signals. The particles' rotational dynamics were also tested in model viscous solutions of aqueous glycerol, to determine whether they can be used to detect changes in viscosity.

5.2. Method

5.5 Hematite Nanorice

Hematite nanorice are prepared by precipitation from 50 mL of 40 mM ferric chloride solution, 10 mL of potassium dihydrogen phosphate with a concentration varied from 0 to 70 mM with an additional 40 mL of deionised water before being sealed and heated in an oil bath for up to 72 hours at 110 ^{o}C the hematite particles are then carefully washed in a centrifuge using ethanol and water to remove impurities and narrow the particle size distribution by removing larger and smaller particles.

5.5 Hematite Nanorods

7 mL of 0.86 M $FeCl_3$ was added to a glass pressure reactor and stirred in an ice bath. 7 mL of 1,2 propanediamine was added slowly to the flask and allowed to stir in the ice bath for 15 minutes. The flask was then sealed and heated at 180 °C for 16 hours. After cooling, the nanoparticles were separated by centrifugation and washed thoroughly with ethanol and water before freeze-drying.

5.5 Doping of Cerium Phosphate

Doping of cerium phosphate nanorods was carried out at the optimised cerium phosphate nanorod conditions of 180 °C with 8.25×10^{-2} M KH_2PO_4 stock. To this, different amounts of dopant were added.

5.5 $Mn(NO_3)_2.4H_2O$ Doping

0.7 g of $Mn(NO_3)_2.4H_2O$ was added to 50 mL of deionised water to form a 13.94 mg mL^{-1} stock solution. In a sealed pressure flask, 0.56g of $Ce(NO_3)_3.6H_2O$ was dissolved in 10 mL of deionised water and 5 mL of $8.25x10^{-2}$ M NaH_2PO_4 stock solution was added. To this, between 10 and 1300 µL of $Mn(NO_3)_2.4H_2O$ stock solution was added (Shown in Table 5-2), depending on doping amount, and enough deionised water to bring the final volume of the reaction mixture to 20 mL. After sonication, the solution was heated in an oil bath at 180 °C for 24 hours. Each reaction mixture was separated with centrifugation and washed with deionised water and ethanol then dried at 80 °C overnight.

Wt % of metal component	**$Mn(NO_3)_2.4H_2O$ Stock (µL)**
0.03	12
0.05	20
0.15	60
0.4	160
0.6	240
0.9	365
1.2	490
3	1240

Table 5-2: table showing volumes of $Mn(NO_3)_2.4H_2O$ stock solution added to 0.56 g of $Ce(NO_3)_3.6H_2O$ to achieve different wt% doping.

5.5 $Co(NO_3)_2.6H_2O$ Doping

2.1g of $Co(NO_3)_2.6H_2O$ was added to 50 mL of deionised water to form a 41.6 mg mL^{-1} stock solution. In a sealed pressure flask, 0.56 g of $Ce(NO_3)_3.6H_2O$ was dissolved in 10 mL of deionised water and a 5 mL aliquot of $8.25x10^{-2}$ M NaH_2PO_4 stock solution was added (Shown in Table 5-3). To this, between 50-500 µL of $Co(NO_3)_2.6H_2O$ stock solution was added depending on doping level with deionised water to bring the final volume of the reaction mixture to 20 mL. After sonication, the solution was heated in an oil bath at 180 °C for 24 hours. The reaction mixture was separated with centrifugation and washed with deionised water and ethanol before being dried at 80 °C overnight

Wt % of metal component	**$Co(NO_3)_2.6H_2O$ stock (µL)**
0.03	4
0.05	7
0.15	20
0.3	45
0.7	95
1	135
1.3	175
3.4	475

Table 5-3: table showing volumes of $Co(NO_3)_2.6H_2O$ Stock added to 0.56 g of $Ce(NO_3)_3.6H_2O$ to achieve different wt% doping.

5.5 $Ni(NO_3)_2.6H_2O$ Doping

2.0g of $Ni(NO_3)_2.6H_2O$ was added to 50 mL of deionised water to form a 40.6 mg mL^{-1} stock solution. In a sealed pressure flask, 0.56 g of $Ce(NO_3)_3.6H_2O$ was dissolved in 10 mL of deionised water and 5 mL of $8.25x10^{-2}$ M NaH_2PO_4 stock solution was added. To this, between 45-500 µL of $Ni(NO_3)_2.6H_2O$ stock was (Shown in Table 5-4), with deionised water added to bring the final volume of the reaction mixture to 20 mL. After sonication for 5 minutes, the solution was left to heat in an oil bath at 180 °C for 24 hours. The reaction mixture was separated with centrifugation (and washed with deionised water and ethanol before being dried at 80 °C overnight.

Wt % of metal component	**$Ni(NO_3)_2.6H_2O$ Stock (µL)**
0.03	4
0.05	7
0.15	20
0.3	45
0.7	95
1	135
1.25	175
3.3	475

Table 5-4: table showing volumes of $Ni(NO_3)_2.6H_2O$ stock added to 0.56 g of $Ce(NO_3)_3.6H_2O$ to achieve different wt% doping.

5.5 $Fe(NO_3)_3.9H_2O$ Doping

0.56 g of $Ce(NO_3)_3.6H_2O$ was added to an $8.25x10^{-2}$ M NaH_2PO_4 solution in 20 mL of deionised water. To this between 0.03 and 0.65g of $Fe(NO_3)_3.9H_2O$ was added (Shown in Table 5-5). The solution was poured into a sealed pressure flask, sonicated for 5 minutes, and heated in an oil bath at 180 °C for 24 hours. Each reaction mixture was separated with centrifugation and washed with deionised water and ethanol before being dried at 80 °C overnight.

Wt% of component metal	**Mass of $Fe(NO_3)_3.9H_2O$ (g)**
5.00	0.031
12.00	0.078
22.00	0.156
36.00	0.311
52.00	0.622

Table 5-5: Mass of $Fe(NO_3)_3.9H_2O$ added to 0.56 g of $Ce(NO_3)_3.6H_2O$ to achieve different wt% doping.

5.5 Na_2O_4W Doping

0.56 g of $Ce(NO_3)_3.6H_2O$ was added to an 8.25×10^{-2} M NaH_2PO_4 solution in 20 mL of deionised water. To this, 0.38 g Na_2O_4W was added. The solution was poured into a sealed pressure flask, sonicated for 5 minutes, and heated in an oil bath at 180 °C for 24 hours. The reaction mixture was separated with centrifugation and washed with deionised water and ethanol before being dried at 80 °C overnight.

5.5 Characterisation of doped nanorods

Ceria and cerium phosphate particles were analysed with a combination of XPS, with electron microscopy used to confirm their morphology and chemical composition.

For mechanistic studies of the growth of the nanoparticles using XRD, and Raman and PiFM, the nanorods were extracted from solution by centrifugation and deposited on silica surfaces without further washing. For XPS, TEM the nanoparticles were isolated with a series of washing/ centrifugation steps and vacuum dried. TEM Samples were supported on copper support grids and analysed on a JEOL JEM-2100.

For XPS the dried nanoparticles were pressed onto conductive tape and analysed with a Kratos Axis Ultra-DLD photoelectron spectrometer with a monochromatic al. Kα x-ray source in the “hybrid spectroscopy” mode. The analysis area was approximately 700 × 300 µm. A pass-energy of 40 eV was used for high-resolution scans and 60 eV for survey scans. CasaXPS[27] was used to analyse the spectra. Binding energies are referenced to the largest C(1 s) peak at 284.7 eV with an uncertainty of ~ 0.2 eV. Since intensities for powder samples are dependent on the surface area analysed, which can be poorly reproducible between different powder samples, XP spectra in the figures are normalized to the point of maximum intensity.

Powder X-ray diffraction (XRD) was performed using a PANalytical X’Pert Pro diffractometer with a monochromatic Cu Kα source (λ = 0.154 nm) operated at 40 kV and 40 mA. The scans were recorded over the 2θ 10–80°

5.5 Magnetic Measurements

A combination of magnetic analyses was used across the nanorod doping experiments. This was carried out using a Gouy balance to find the effective susceptibility of each nanorod. Those with high susceptibility were treated differently to those with lower susceptibility. In some cases, a 1 tesla magnet was used to examine how the nanoparticles would interact with a strong magnetic field. The sample was suspended in a solution with a sonicator and allowed to settle in the presence of a 1 tesla magnet. When a magnetically susceptible sample was placed in contact with the magnet, the sample should be drawn to the magnet more than the bottom of the flask and stick to the sides of the flask. A 1 tesla magnet was selected to match the maximum strength of the magneto-optical rig.

5.2.10.1 Magneto-optical Rig

Samples found to be sufficiently magnetically susceptible were analysed in the Cotton-Mouton Diagnostics (CMD) magneto-optical rig. The rig analyses the rotation frequency of nanoparticles to an external magnetic field. The frequency of rotation is varied between 10-80 Hz with the amplitude of the optical signal being measured. The optical amplitude is used to develop a sine wave and hence deduce the phase shift between the particles and the magnetic field. Measurements were carried out in two different modes:

1) The magnetic response of $CePO_4$ nanorods was measured on a rig with a 1 T magnet, the phase difference between the optical signal and the magnetic field modulation is measured. This was carried out in solutions of different viscosities described below.
2) The rotational dynamics of hematite particles were measured on a rig with variable a variable magnetic field at 0.1 T. The amplitude of the optical signal was measured at different rotational frequencies to determine the frequency most sensitive to changes in viscosity. This was achieved by measuring the optical signal of the particles while suspended in different concentrations of glycerol solution. The difference in amplitude was then used to develop a calibration curve.

Viscosity sensing was measured with 10 mg of nanorods being suspended in a 1 mL cuvette containing glycerol solution. Three different glycerol solutions were examined,Table 5-6:

Glycerol wt%	Literature Viscosity (cP)	Ref
0	1.002	25
10	1.328	28
20	1.844	
30	2.516	
40	3.720	

Table 5-6: Table of different viscosity values of glycerol solutions prepared

5.3. Results

5.5 Electron Microscopy

The morphology of the nanoparticles formed was analysed with transmission electron microscopy, See Figure 5-2. In the cases of Co, Ni and Mn doping little change to the morphology rod morphology was seen each showing the typical rod-like morphology with an average particle diameter of 20 nm, like that of undoped $CePO_4$. There was some variation in the average length of the nanoparticles at 422 nm, 416 and 404 nm respectively for Co, Mn and Ni.

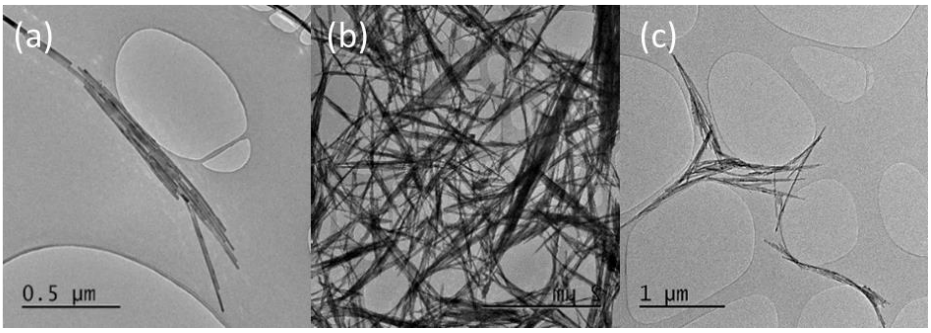

Figure 5-2: TEM micrographs of $CePO_4$ nanorods treated with 0.15 % of (a) $Co(NO_3)_2.6H_2O$ Stock (b) Ni (d) Mn.

More substantial changes in morphology were seen in the cases of Fe and W doped rods, probably due to their larger dopant %. Fe doped particles lost their morphological consistency forming particles that ranged in size from 20 to 400 nm depending on the extent of doping. For example, in the case of 12%, $FeCl_3$ doping produces a mixture of longer of 380 nm length nanorods with 16 nm diameter resembling those formed without doping and lower aspect ratio rods with lengths of 40 nm and diameters of 20 nm which are like the hematite subunits obtained in chapter 2. Overall, this results in a vast reduction in particle length from 430 nm to 42.3 nm. The nanoparticles formed from high concentrations of iron had no long $CePO_4$-like nanorods present. However, the morphology was not consistent and varied between that of rods and spheres which can be seen in Figure 5-3(e) and (f).

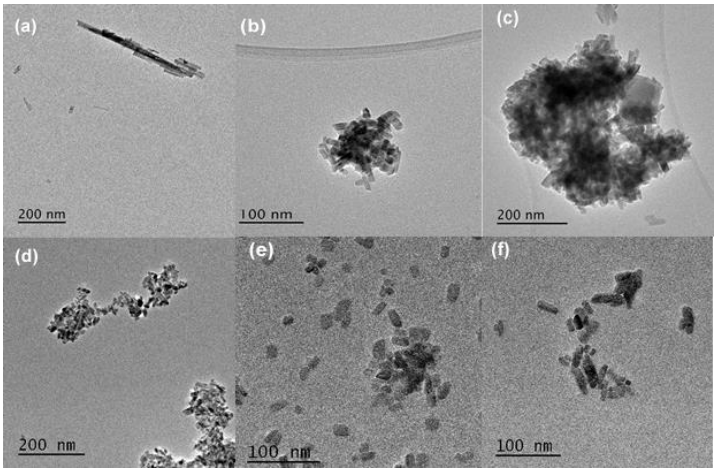

Figure 5-3: TEM micrographs of $CePO_4$ nanoparticles formed when doped with different amounts of Fe(NO3)3.9H2O. (a) 12% Fe Doped $CePO_4$ (b)– (c) 21% Fe Doped $CePO_4$ (d) 36% Fe Doped $CePO_4$ (e)- (f) 52% Fe Doped $CePO_4$.

A general reduction in the length of all nanoparticles formed can be seen when doping cerium phosphate, see Figure 5-4.

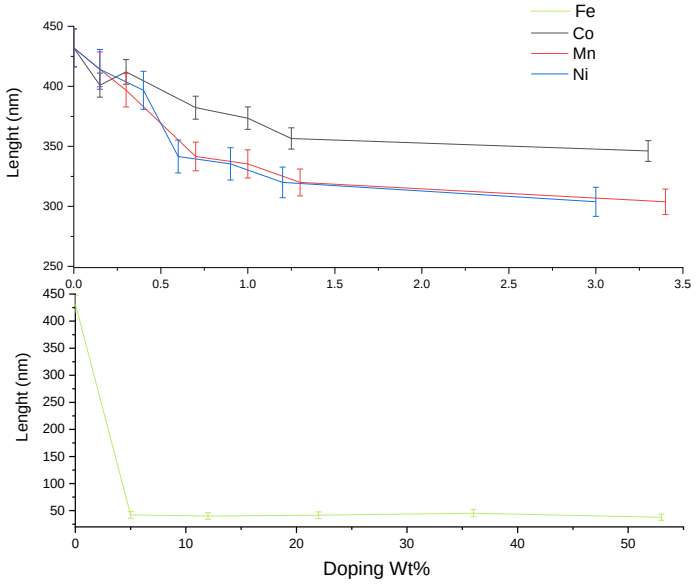

Figure 5-4: Graph of rod length change as dopant wt% Increases. Error is calculated based on the average percentage variation within each data set at Fe ± 15%, Ni ± 5%, Co ±2.6% Mn ±3.8%.

When doping cerium phosphate with tungsten, morphological changes are observed but the nanoparticles adhered to each other when drying on the TEM plates and so it is difficult to analyse this sample. However, the TEM micrographs in Figure 5-5 show that a mixture of nanorods and other morphologies have been formed. The dominant morphology, nanorods, have lengths varying between 50-100 nm with a consistent width of approximately 20 nm.

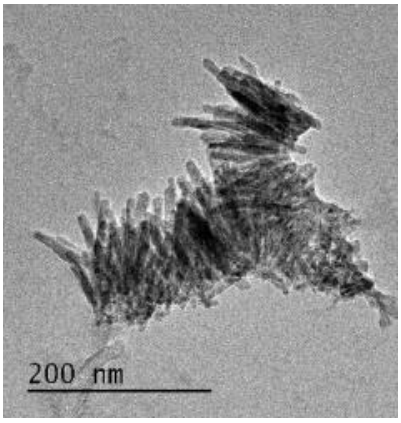

Figure 5-5: TEM micrographs of $CePO_4$ nanorods doped with 40.5 wt% Tungsten.

The above data suggest that the addition of foreign metal ions affects the growth of nanorods. With Ni, Co and Mn all reducing the aspect ratio compared to an undoped cerium phosphate rod. The larger doping concentrations used for W and Fe result in more dramatic changes in shape and size, but it is unclear from the data presently available whether these changes are due to the incorporation of the respective metal ions or are due to kinetic and equilibrium changes through the addition of another reactant.

5.5 Raman Spectroscopy

A selection of samples with wt% dopants between 0.15 and 3.5% was analysed with Raman spectroscopy for Co, Ni and Mn doped cerium phosphate rods. Raman can give an insight into small changes in crystal order.

Wavenumber of Raman peaks for cerium phosphate structures (cm^{-1})		**Assignment**
Hexagonal	**Monoclinic**	
1085	1070	V_3
	1054	
	1024	
	990	
976	969	V_1
624	618	V_4
573		
466	466	V_2
377	414	
	396	

Table 5-7: Literature values for different Raman vibrations found in hexagonal and monoclinic $CePO_4$.

As mentioned in Chapter 3, a key identifier between the monoclinic and hexagonal $CePO_4$ is the difference between the single V_3 signal seen in the hexagonal structure compared to the several peaks shown in the monoclinic. The difference in the spectra is shown in Table 5-7.

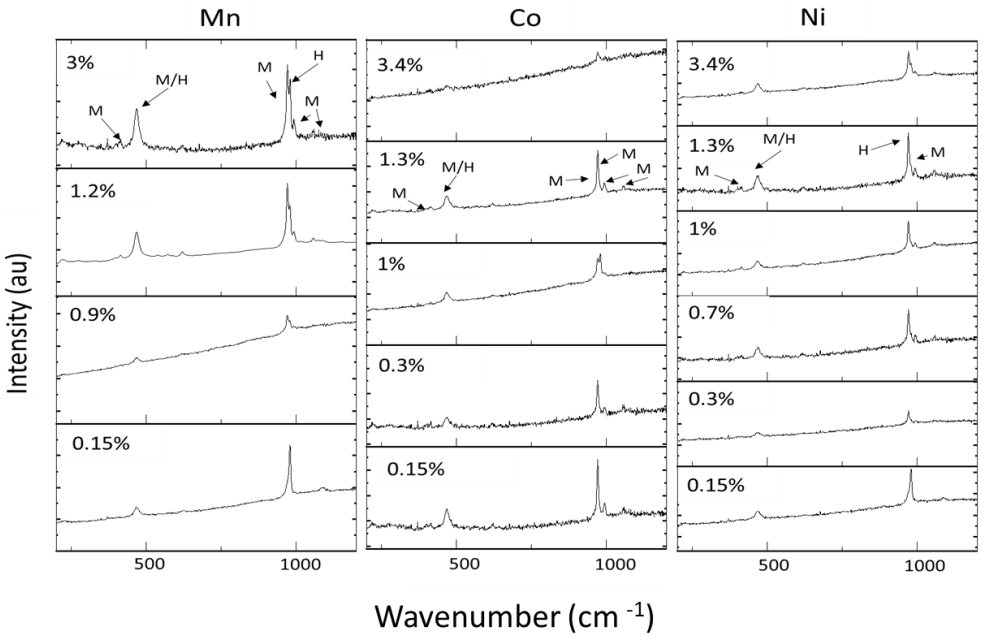

Figure 5-6: Raman spectra of Mn, Co and Ni doped cerium phosphate

Figure 5-6 shows that the Co, Ni and Mn doped cerium phosphate rods contain the typical V_3 peaks between 990 – 1080 cm^{-1} and the V_4 peaks characteristic of cerium phosphate. There are no clear additional Raman signals which correspond to the introduction of dopants. However, when treating cerium phosphate rods with Co, Ni and Mn precursors, a switch between the hexagonal and monoclinic phases does occur. This can be seen in the increasing complexity in the V_4 region of the spectrum. This change becomes increasingly evident upon increasing the % of dopants. For example, 2% dopant in all cases results in the clearest monoclinic spectra. Note also that due to the overlap of the F_{2g} and V_4 phonons the presence of cerium oxide within the sample cannot be eliminated.

When analysing Figure 5-7, at first glance, the Raman spectra of Fe doped cerium phosphate appear to be radically different to those obtained in pure, Ni, Co, and Mn doped cerium phosphates. However, there are some key similarities.

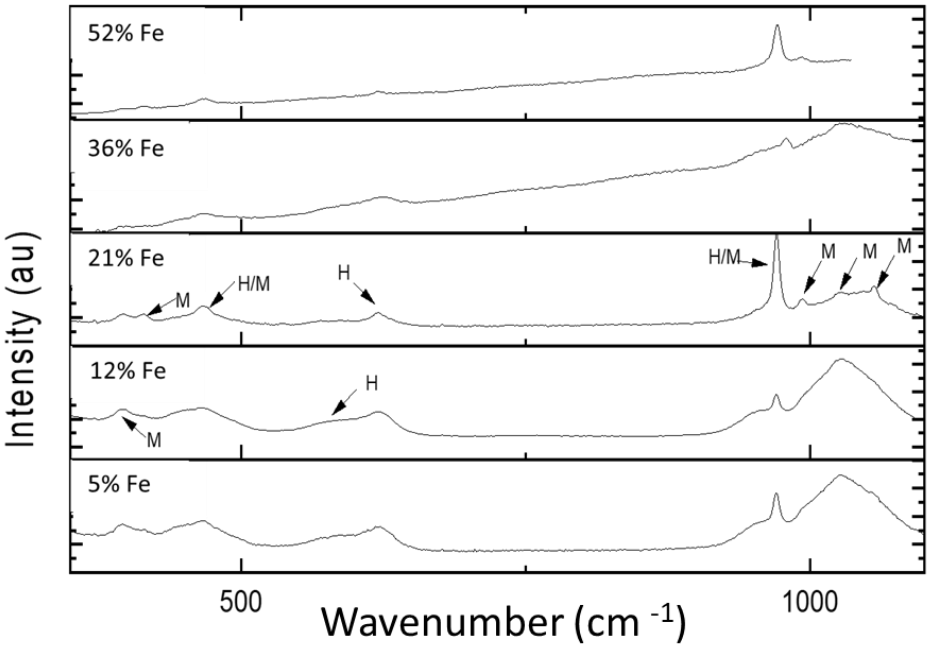

Figure 5-7: Raman Spectra of Fe doped cerium phosphate nanoparticles.

The spectra can be easily analysed by splitting into two separate regions (1) 350-650 cm^{-1} (2) 950-1100 cm^{-1}.

(1) 350-650 nm region consists of 5 clear phonons at 396.23,414.42, 447.04, 586.74, 622.51 cm^{-1} each of which can be attributed to a V_3 or V_4 vibration of either monoclinic or hexagonal cerium phosphate. This region of the spectrum is often less well defined in other samples.

(2) 950-1100 nm region consists of 4 clear phonons at 971.08, 993.34, 1028.23, 1055.41 cm^{-1}. Except for the sample with 21 wt% doping, this region consists of a very broad peak covering 1000-1100 cm^{-1}. However, in the 21%, it is easier to analyse. Each of the 4 peaks corresponds directly to monoclinic and hexagonal phosphate vibrations V_3.

This set of spectra is made more difficult through a change in intensities and a broadening of phonon areas. This is most likely due to the radically different morphology of the nanoparticles obtained by the doping since particle lengths below 50 nm result in optical phonon confinement which causes peak broadening.

Tungsten doped nanoparticles resulted in a Raman spectrum (Shown in Figure 5-8) like that of the control hexagonal $CePO_4$ despite the changes in morphology. Clear V_2 and V_1 phonons are observed at 466 and 970 cm^{-1} respectively.

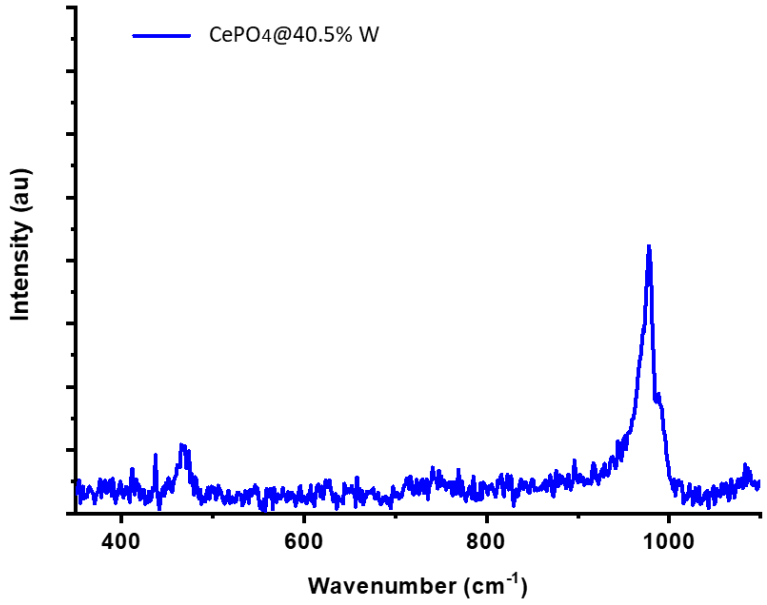

Figure 5-8: Raman spectra of W doped cerium phosphate.

The background noise of the spectrum makes it difficult to locate any clear phonons indicating the doping of tungsten species into the lattice of $CePO_4$. Mioc et al. report that cubic WO_3 materials possess characteristic bands at 805 and 706 cm^{-1} originating from a W-O-W stretching mode[29]. Araujo et al. reported that doping with WO_3 caused a doublet at 900 and 940 cm^{-1} associated with W=O or W-O^- bond vibrations, with either four-, five- or six-coordinate W atoms. Finally, based on the Raman spectrum of pure tungsten oxide, a band at 830 cm^{-1} can be assigned to a W–O single bond stretching vibrations within W–O–W-bonded units. However, the Raman spectrum does not show any of the vibrations mentioned above. It is possible that the doublets corresponding to the W=O or W-O^- could be integrated into the intensity of the V_3 peak of $CePO_4$. This implies that there is no significant amount of WO_3 present on the surface of the nanorods.

5.5 X-ray photoelectron Spectroscopy

Co, Mn and Ni doped nanoparticles XP spectra closely matched those of $CePO_4$, with the Ce(3d) region containing only the features typical of Ce(III). The Ce(III) oxidation state has 4 distinct peaks within the 880-920 eV region which have been labelled: U^o, U^1, V^o, and V^1 at 882, 885, 901, and 904.5 eV respectively. In the XP spectra of all samples containing Co, Mn and Ni dopants, these characteristic Ce(III) peaks dominate, confirming the Raman evidence that $CePO_4$ has been formed and that there is little cerium oxide present within the samples. Furthermore, no signals are obtained in the XP spectra for Ni, Mn, or Co, (see Figure 5-9 for

example), indicating the absence of any dopant atoms on the surface of the particles although they may be present in the bulk.

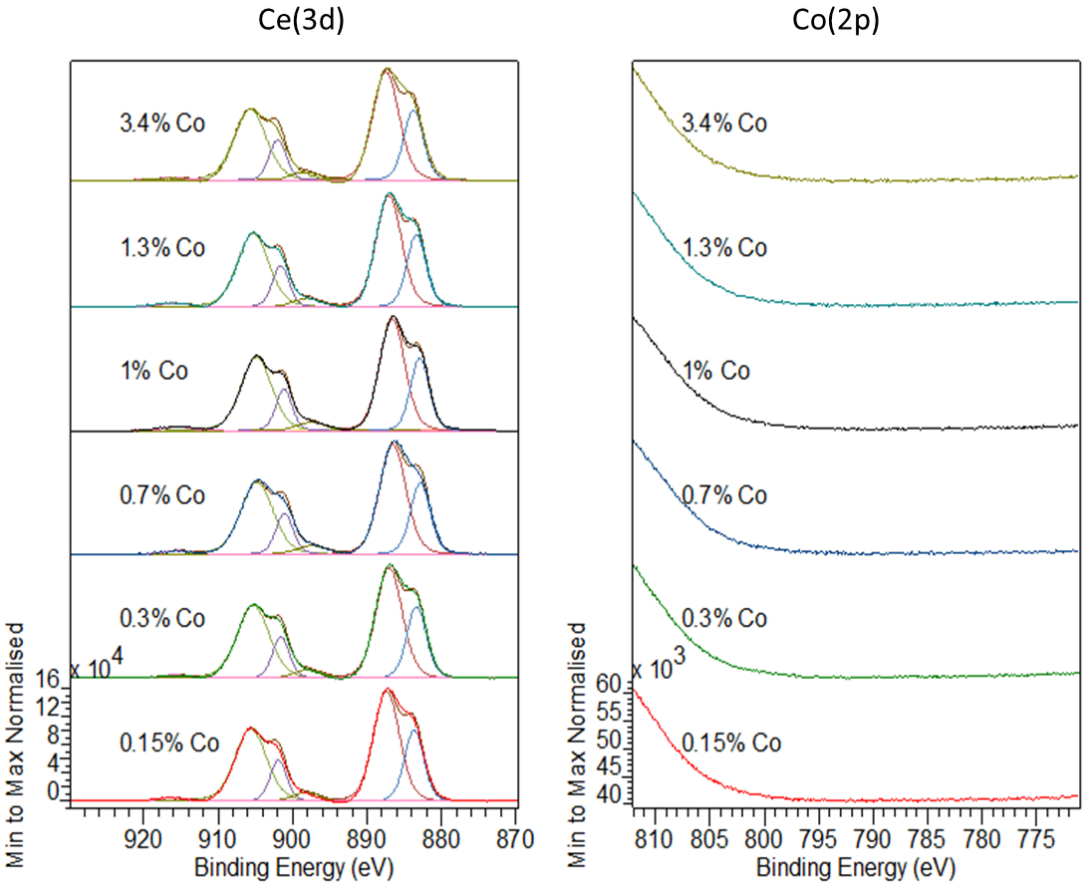

Figure 5-9: XP spectra of Co doped cerium phosphate nanoparticles. For spectra of Ni and Mn view supplementary information.

The Fe doped nanoparticles show more variation in their XP spectra, Figure 5-10. While little change to the Ce(3d) spectra is seen and Ce(III) appears to be the dominant cerium species with strong signals at 882, 885, 901, and 904.5 eV a peak is obtained in the Fe(2p) region.

There are 4 peaks of interest in the 745-700 eV region; the peaks occurring at 720 and 735 eV correspond to Ce satellites, the other peaks at 725.96 eV and 712.5 eV correspond to $Fe(2p_{1/2})$ and $Fe(2p_{3/2})$. The intensity of the Fe components in the spectra corresponds directly to the expected wt% Fe present.

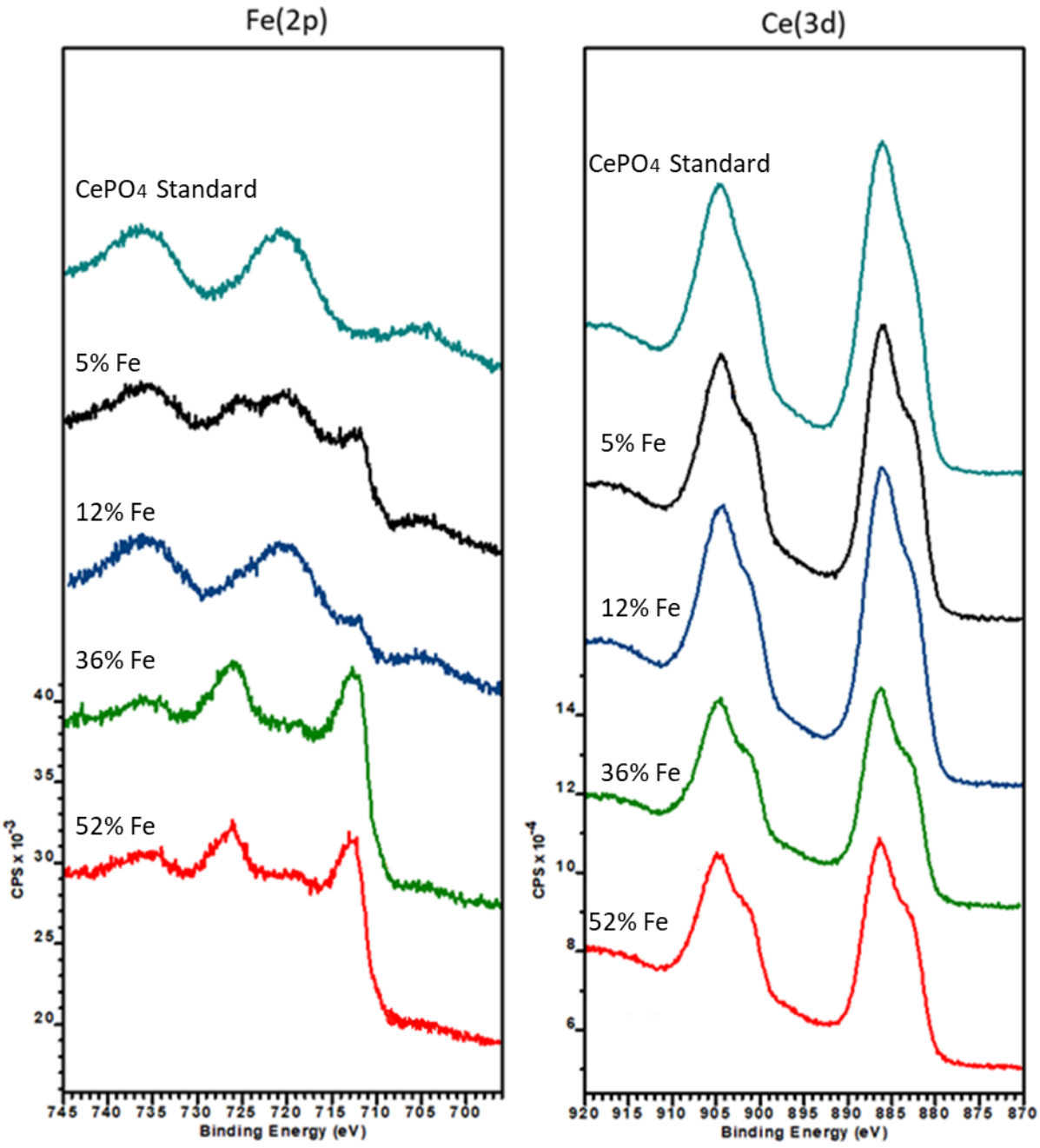

Figure 5-10: XP spectra of Ce(3d) and Fe(2p) for Fe doped cerium phosphate nanoparticles. Where 52% is the predicted wt%

While the iron could be integrated into the $CePO_4$ lattice, Fe(2p) peaks such as these are present in the spectra of $FePO_4$[30] suggesting that the iron peaks do not originate from the $FeCl_3$ species when paired with the lack of a signal in the Cl region.

XP spectra of WO_3 treated cerium phosphate nanoparticles, Figure 5-11, also indicate the prevalence of Ce(III) with strong intensity at 882, 885, 901, and 904.5 eV but with a degree of peak broadening compared to a $CePO_4$ standard suggesting the environment may be more variable in comparison to a standard $CePO_4$ rod. While only slight changes to the

Ce(3d) region are observed, the W($4d_{5/2}$) and W($4d_{3/2}$) peaks are present at 246.5 and 261.5 eV. (Note the usual method of identifying tungsten species using the W(4f) region is not possible here because of an overlap with the Ce(5s))

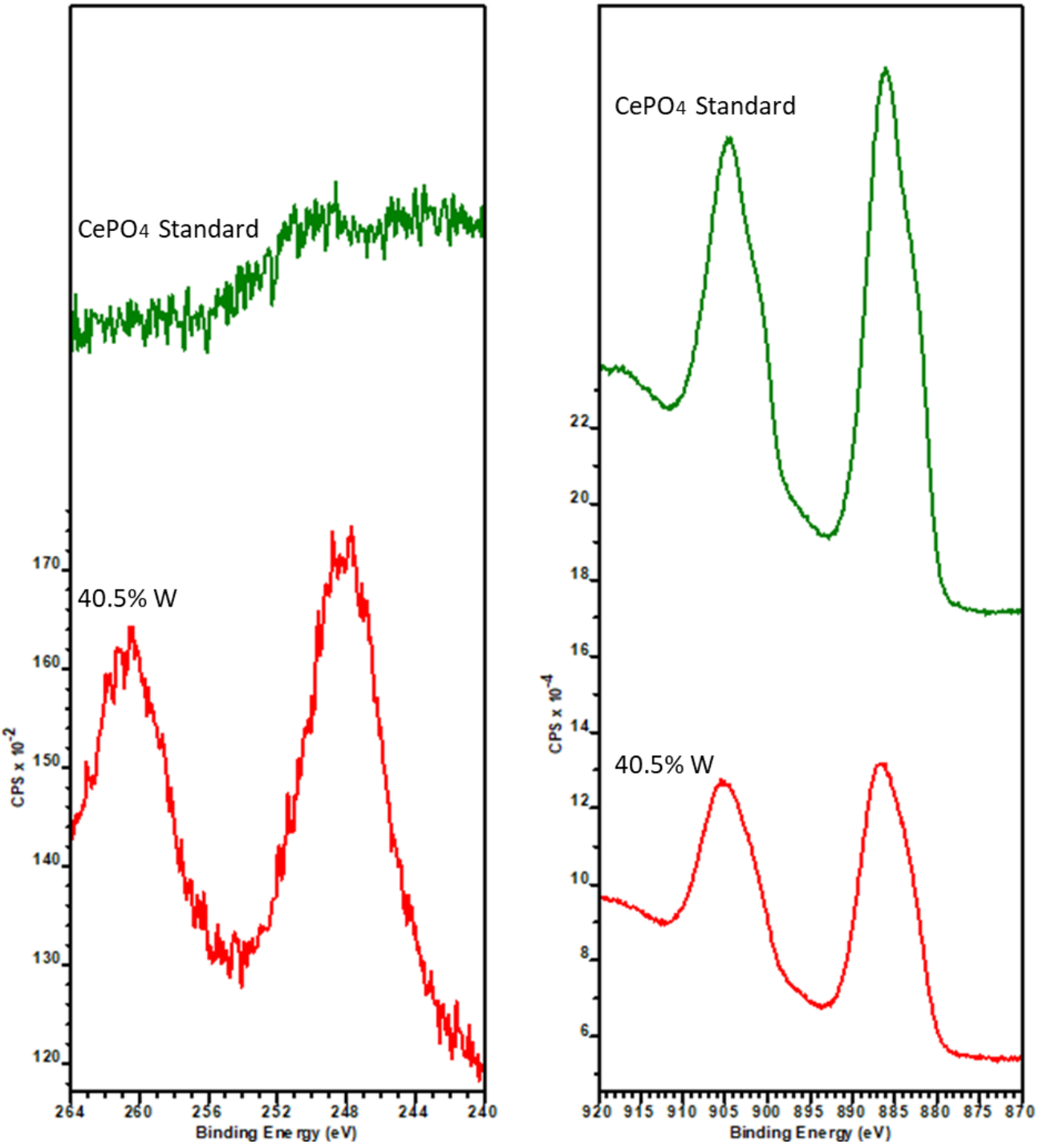

Figure 5-11: XP spectra of W doped cerium phosphate nanoparticles in the W(4d) and Ce(3d) regions of the XP spectra.

5.5 Magnetic Measurements

5.3.4.1 Gouy Balance

Gouy balance measurements were taken to compare the magnetic susceptibility of nanoparticles formed by doping to those without a dopant. These measurements have been displayed in Table 5-8. Only small changes are observed, but Mn for wt% ≥ 0.6%, W and Fe at very high wt% do show increases of ~20% in magnetic susceptibility.

Sample & vol% doping	Magnetic susceptibility X ($x10^{-4}$ cm^3 g^{-1})	Susceptibility Ratio Hematite:$CePO_4$	Susceptibility Ratio Undoped $CePO_4$: Doped
Pure $CePO_4$	1.714	0.11	1.00
Mn 0.15%	1.621	0.11	0.95
Mn 0.4%	1.926	0.13	1.12
Mn 0.6%	2.143	0.14	1.25
Mn 0.9%	2.098	0.14	1.22
Mn 1.2%	2.264	0.15	1.32
Mn 3%	1.934	0.13	1.13
Co 0.15%	1.443	0.10	0.84
Co 0.3%	1.622	0.11	0.95
Co 0.7%	2.003	0.13	1.17
Co 1%	1.954	0.13	1.14
Co 1.3%	1.396	0.09	0.81
Co 3.4%	1.462	0.10	0.85
Ni 0.15%	1.743	0.12	1.02
Ni 0.3%	1.854	0.12	1.08
Ni 0.7%	1.982	0.13	1.16
Ni 1%	1.876	0.13	1.09
Ni 1.25%	1.864	0.12	1.09
Ni 3.3%	1.965	0.13	1.15
Fe 5%	1.987	0.13	1.16
Fe 12%	2.031	0.14	1.18
Fe 22%	2.094	0.14	1.22
Fe 36%	1.934	0.13	1.13
Fe 52%	2.056	0.14	1.20
W 40.5%	2.145	0.14	1.25

Table 5-8: Magnetic susceptibility of each nanoparticle prepared measured by Gouy balance and compared to that of hematite and undoped $CePO_4$.

Hematite is significantly more susceptible to a magnetic field than any of the doped $CePO_4$ rods but small changes are apparent when compared to the $CePO_4$ standard rods, Figure 5-12.

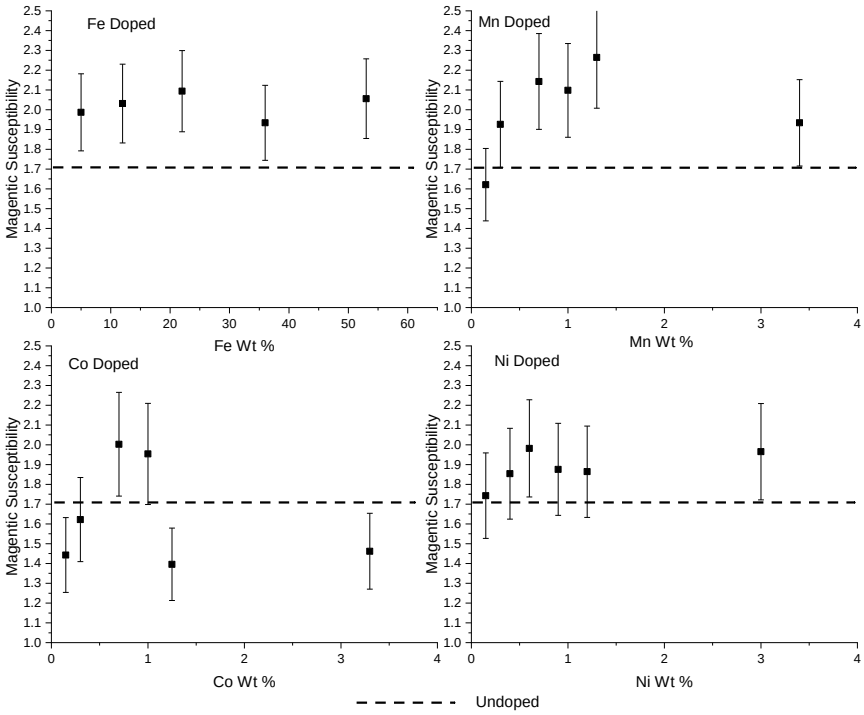

Figure 5-12: Graphs of doped cerium phosphate molar susceptibility as a function of dopant concentration

When smaller dopant precursor percentages are used, such as in the case of Co Mn and Ni there are slight effects to molar susceptibility with increased dopant ions although the error in the measurements is relatively high (~$0.3\pm\times10^{-4}$). Co doping indicates there is little effect on the magnetic susceptibility with all changes being within error. There is less scatter in the Ni and Mn data with samples showing an increase in susceptibility which is above the error of the measurements implying that treatment over 1% can increase the magnetic susceptibility of $CePO_4$ nanorods. Since neither the Raman nor XPS data show evidence of any additional metal ions these changes in magnetism may be linked to chemical changes in solution which impacted the nucleation of the nanoparticles. Following this conclusion, a higher dopant % was studied in the cases of tungsten and iron.

Comparing the iron doped samples to those of Co, Mn and Ni, the scatter is significantly lower and every addition increases molecular susceptibility. However, it appears that adding an increasingly high % of Fe does not result in significant changes to the molar susceptibility of the nanoparticle. The iron doping results in a general increase in molar susceptibility of between 15-20%. When this information is combined with morphological changes from the TEM and the XPS data a degree of doping may have occurred. Similar changes can be seen in

the case of the 50% tungsten sample which resulted in a 25% increase in molar susceptibility. It is possible that since both the tungsten and iron samples have significantly different morphologies, changes to the molar susceptibility could be a result of magnetic shape and size effects.

The best candidates for further examination on the magneto-optical rig and with a 1 tesla magnet were the Fe 5-52% and W 40.5% samples.

5.3.4.2 1 Tesla Magnet Separation Test

Since the magnetic susceptibility of $CePO_4$ doped nanorods is relatively low a study was carried out to measure their response to a 1 tesla (T) magnet which corresponds to the maximum magnetic field that can be used in this study. To ensure that the nanorods would react to the external magnetic force in the optical rig, a nanoparticle suspension of 10 mg mL^{-1} was placed in a 5 mL glass vial and allowed to separate over a period of 1 minute. If the nanoparticles were sufficiently susceptible, they would be attracted to the magnet and stick to the glass rather than falling to the bottom of the glass through gravity, See Figure 5-13(c).

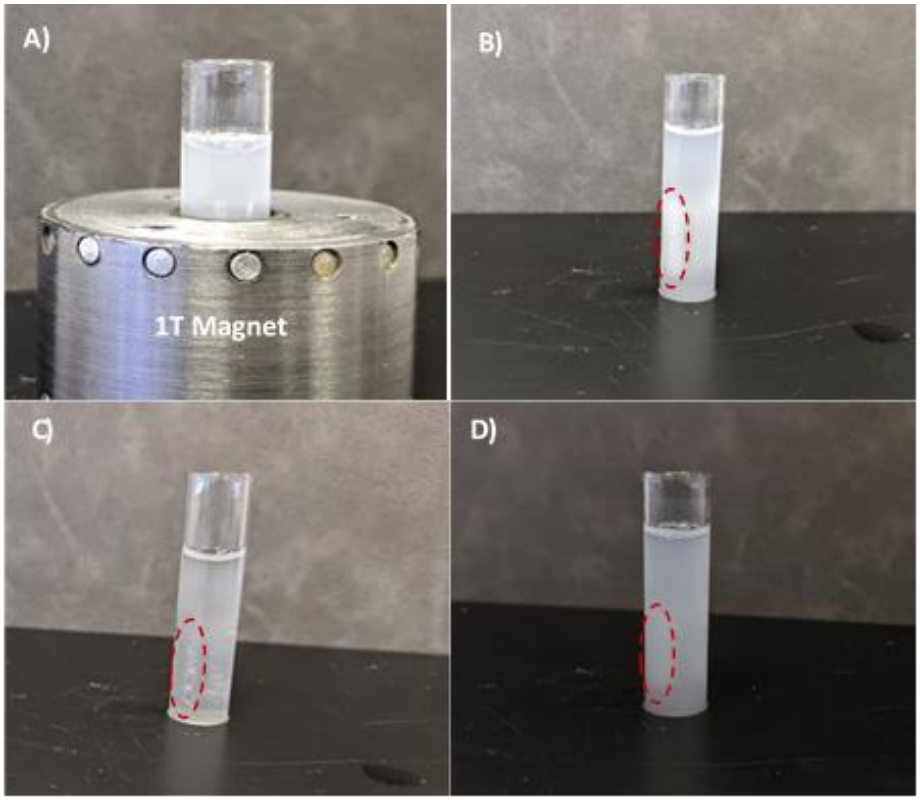

Figure 5-13: A) Image of 1T magnet around sample vial; B) Image of 21% Fe doped $CePO_4$; C) Image of 40.5% W; D) Image of 52% Fe after 1 minute exposed to the magnetic field.

All the samples tested separated from the dispersion and formed collections of particles on the glass, indicating they were attracted to the magnet within the given time. In agreement with the Gouy balance results, samples of 50% W and 90% Fe doped $CePO_4$ separated faster than the others, with no material falling to the bottom of the vial and these two were selected for further study in the magneto-optical rig. (Note: the 36% Fe/$CePO_4$ sample contained separate brown sediment which was strongly attracted to the magnet. This is likely to be an iron oxide side product that had not been successfully removed during washing procedures and was discounted from the present investigations).

5.3.4.3 Viscosity Measurements

As Equation 5-2 and Equation 5-3 describe the ability for a nanoparticle to match the rotation of the magnetic field depends upon several factors, including the viscosity of the solution. By fixing all other variables, such as magnetic field strength and aspect ratio we can use anisotropic nanoparticles to sense small changes of viscosity in a solution. In this section, we focus on using glycerol to control the viscosity of nanoparticle suspensions and determine how accurately nanoparticles can detect this change.

The $CePO_4$ and Fe_2O_3 nanorods were measured differently. The reason for this can be examined in the Curie Weiss Law which examines the relationship between effective magnetic moment (μ_{eff}) and the magnetic susceptibility(χ_A)[29].

Equation 5-3: $$\mu_{eff} = \left[\frac{3kT\chi_A}{N\beta^2}\right]^{1/2}$$

Where k is the Boltzmann constant, T is temperature, N is Avogadro constant and β is the Bohr magneton.

Equation 5-4: $$t_m = \mu_{eff} B \sin\theta = \gamma 2\pi f$$

Equation 5-4 shows that the rotational force t_m experienced by a nanorod is proportional to the effective magnetic moment in the axis of rotation. The magnetic moment is, in turn, a function of the material's magnetic susceptibility. The amount of rotational force exerted on a $CePO_4$ nanorod will be significantly less than that of a hematite nanorod under the same magnetic field. Therefore, a more powerful magnetic is needed to rotate $CePO_4$ rods than is needed for the hematite. Hence, the $CePO_4$ and Fe_2O_3 were tested in two different

magneto-optical rigs with a 1 tesla magnet used to test the $CePO_4$, and a variable magnetic field, with a maximum of 0.1T, used for the hematite rods.

5.3.4.4 Cerium Phosphate Particles

In the presence of a 1 T external magnetic field, all samples of $CePO_4$ produced an optical signal, indicating that the nanoparticles were successfully rotated in solution by the magnetic field. However, some doped particles had large phase differences between the magnetic field and the nanoparticle. These samples experienced a greater degree of drag in water compared to those with smaller phase differences. These particles were inappropriate to study for their viscosity sensing as they would possess a smaller range for the phase difference to be measured across.

Two systems were identified for viscosity measurements because of their greater synchronisation with the magnetic field in the absence of glycerol; the 36% Fe doped-$CePO_4$ and the 40.5% W-doped $CePO_4$. The desynchronisation of the nanoparticles and the magnetic field is visualised in Figure 5-14.

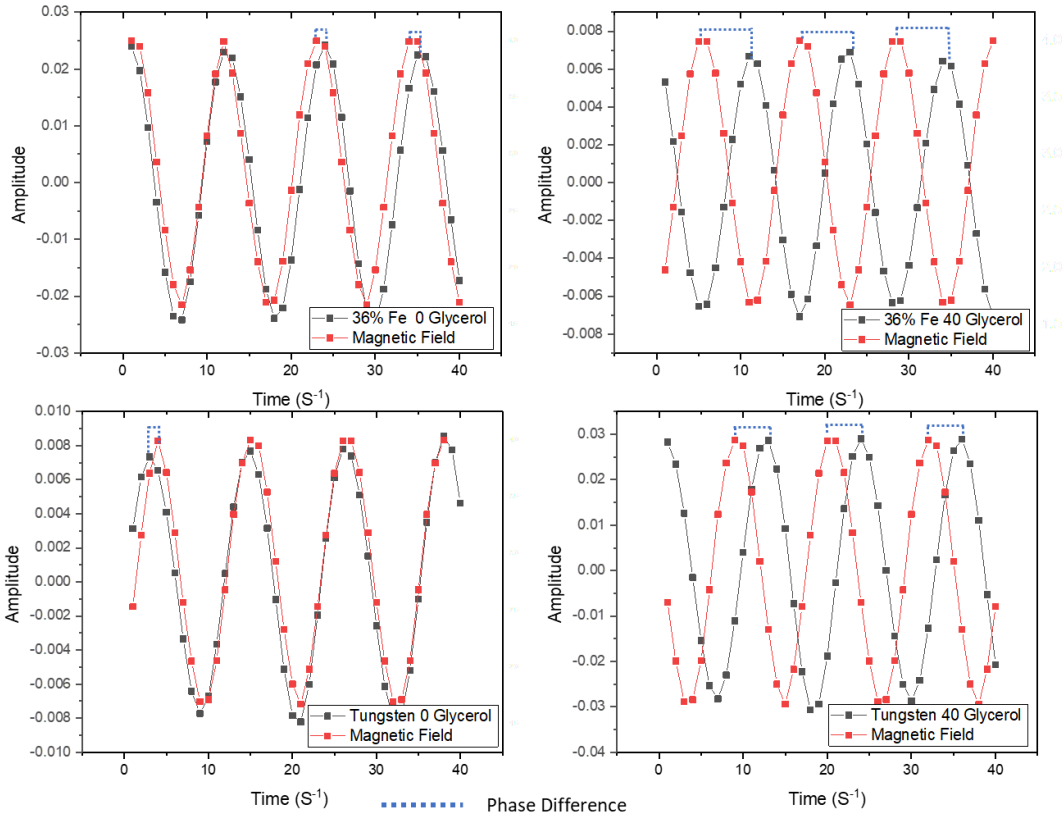

Figure 5-14: Magneto-optical signals obtained from (left) 36% Fe doped-$CePO_4$ and 40.5% W-doped $CePO_4$ in water. (right) 36% Fe doped-$CePO_4$ and 40.5% W-doped $CePO_4$ in 40% glycerol solution.

The difference in time Δt between the peaks of the magnetic field and the optical signal is directly proportional to the phase shift θ.

Equation 5-5 $\theta = \frac{360^{*}\Delta t}{\tau}$

Where τ is the period of one wave.

Since the time difference and the phase difference are proportional, the time difference has been used in the following analysis. At low viscosities, there is little drag force acting upon the nanoparticles and so the phase difference is minimal resulting in the optical signal and magnetic signal being superimposed. However, As the viscosity increases with the glycerol wt% the particles suffer from increased drag and are less able to rotate at the same speed as the external magnetic field. This causes an increase in the lag between the magnetic field and rotation of the nanoparticles causing the phase difference to increase.

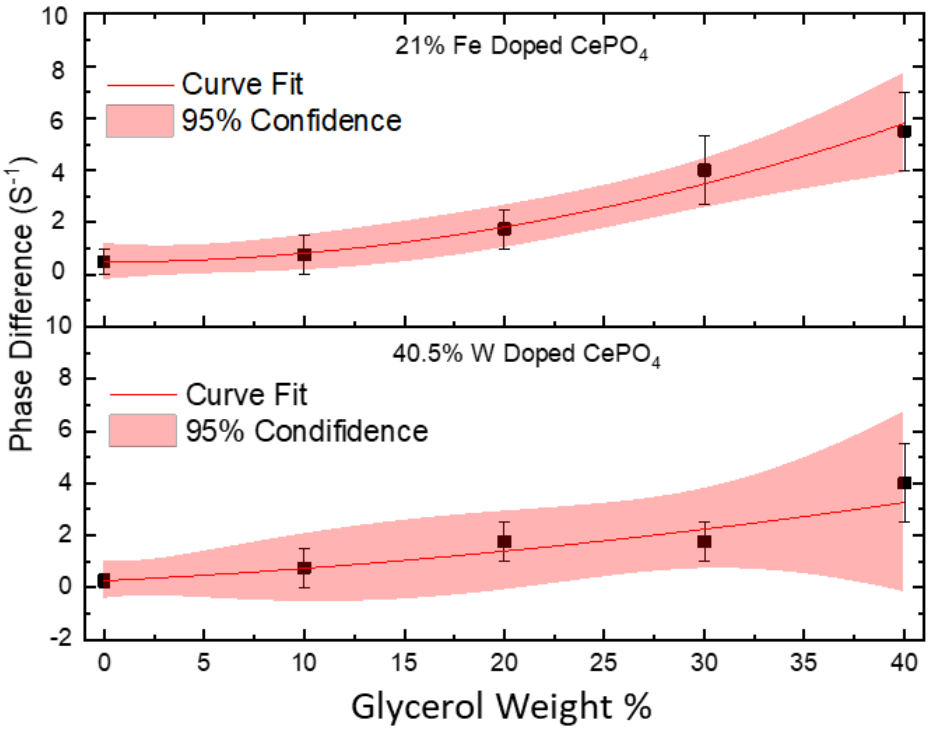

Figure 5-15: Calibration graphs of glycerol wt% and time difference for 36% Fe doped-$CePO_4$ and 40.5% W-doped $CePO_4$ nanorods rotating in solutions varying between 0-40% glycerol. The error in these measurements is based on the error in the magneto-optical rig.

The calibration curve shows that this relationship does not appear to be linear, Figure 5-15. There is a large degree of error in the data and further study is needed to fully quantify

viscosity with these particles. However, from this current data, It appears that 36% Fe doped-$CePO_4$ could sense changes in viscosity. The 40.5% W-doped $CePO_4$ particles also showed a net increase in phase difference as the concentration of glycerol was increased. However, these particles were less sensitive to these changes showing a smaller increase of 3 s^{-1}over the viscosity range compared to 4.9 s^{-1} in the 36% Fe doped-$CePO_4$ samples.

5.3.4.5 Hematite Nanoparticles

The magnetic susceptibilities of each type of nanoparticles have been tabulated in Table 5-9. The susceptibility of the 1,2 propanediamine directed hematite rods is significantly greater than that of phosphate directed hematite with an increase of 1.76 x10^{-4} cm^3 mol^{-1}, corresponding to an 11.7% increase. The change may be due to differences in size and morphology, oxygen holes on the surface of the nanoparticles creating more Fe^{3+} for example would increase magnetic susceptibility, or it may be related to the greater crystallinity which allows for larger magnetic domains to develop in the 1,2 diaminopropane directed rods.

Sample & Vol% doping	**Magnetic susceptibility, (X) (×10^{-4} cm^3 g^{-1})**
Cerium Phosphate	1.74
Phosphate Fe_2O_3	14.96
1,2 propanediamine Fe_2O_3	16.72

Table 5-9: Magnetic susceptibility of hematite nanorods synthesised by different methods.

Both phosphate and 1,2 propane diamine directed hematite nanorods were tested for their ability to detect changes in viscosity affected by increasing glycerol concentration. In the experiment, the amplitude of light transmitted through the nanoparticle suspension is plotted against the magnetic field rotation frequency. The light amplitude is directly related to the spin of the nanoparticles and varies based on the net orientation of nanoparticles with the magnetic field. A higher amplitude would suggest more light being transmitted through the nanoparticle suspension and hence less of a phase lag. While a decrease in amplitude would indicate less light transmission caused by a loss of nanoparticle orientation and hence an increase in phase lag. As the viscosity of the solution increases the drag forces exacted upon the nanoparticles increases.

However, this is not the only way to affect the phase lag of nanoparticles. Equation 5-1 shows that the phase shift θ is also a function of the rotational frequency of the

nanoparticles. As the rotational frequency of a nanoparticle increases so does the phase shift. This can be visualised as the nanoparticles struggling to maintain their speed of rotation in comparison to the external magnetic field. Therefore, the changes in phase shift will be different depending on the rotational frequency.

In this section, the ability of hematite rods to indirectly sense changes in viscosity will be examined at different rotational frequencies.

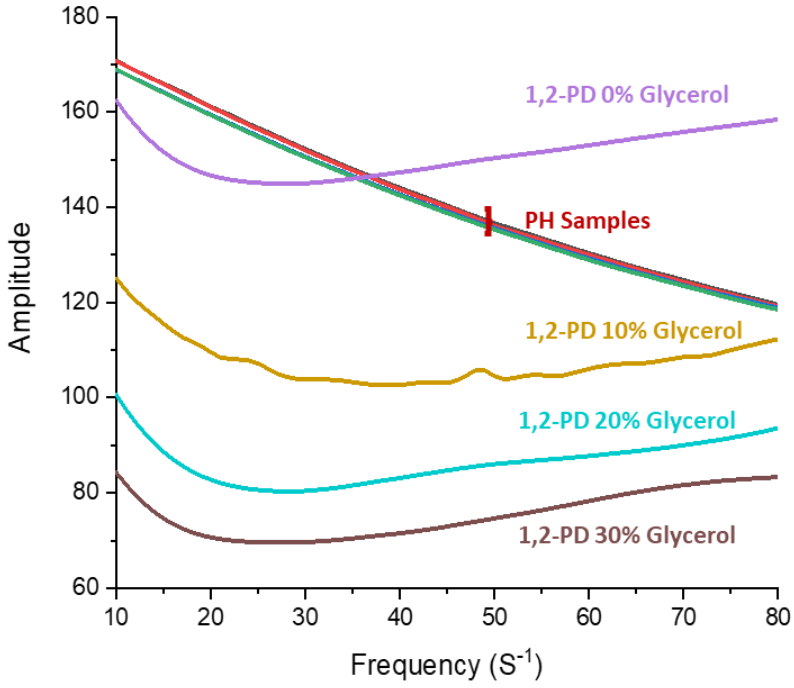

Figure 5-16: Graph of amplitude against frequency for all hematite nanoparticles measured. PH samples refer to phosphate directed hematite nanorods; 1,2-PD refers to 1,2 Propanediamine.

The effect of drag on the amplitude of the optical signal can be observed in the signals of the 1,2 propanediamine hematite samples, see Figure 5-16. As the glycerol concentration increases the amplitude of the optical signal decreases significantly over the 0-30% range. Changes in the amplitudes can also be observed as a function of frequency with the average differences in amplitude at approximately 20 s^{-1}. The large differences in amplitude imply that the 1,2 propanediamine nanorods are very sensitive to changes in solution viscosity. The difference between the 1,2 propanediamine and phosphate hematite is stark. The difference amplitude of the phosphate directed hematite is not comparable on the scale of the 1,2 propanediamine. This would suggest that over the 0-30% glycerol range that 1,2

propanediamine hematite is the most sensitive. A net decrease in the amplitude of the phosphate samples is seen as the frequency of rotation is varied between 10-80s^{-1} indicating that an increase in the phase shift is obtained through varying the rotational speeds of the phosphate directed hematite rods. However, this is not the case for the 1,2 propanediamine samples which appear to have a different relationship with frequency. The amplitude of the 1,2 propanediamine signal follows a more U-shaped pattern with the lowest amplitudes being obtained between 20-30 s^{-1}.

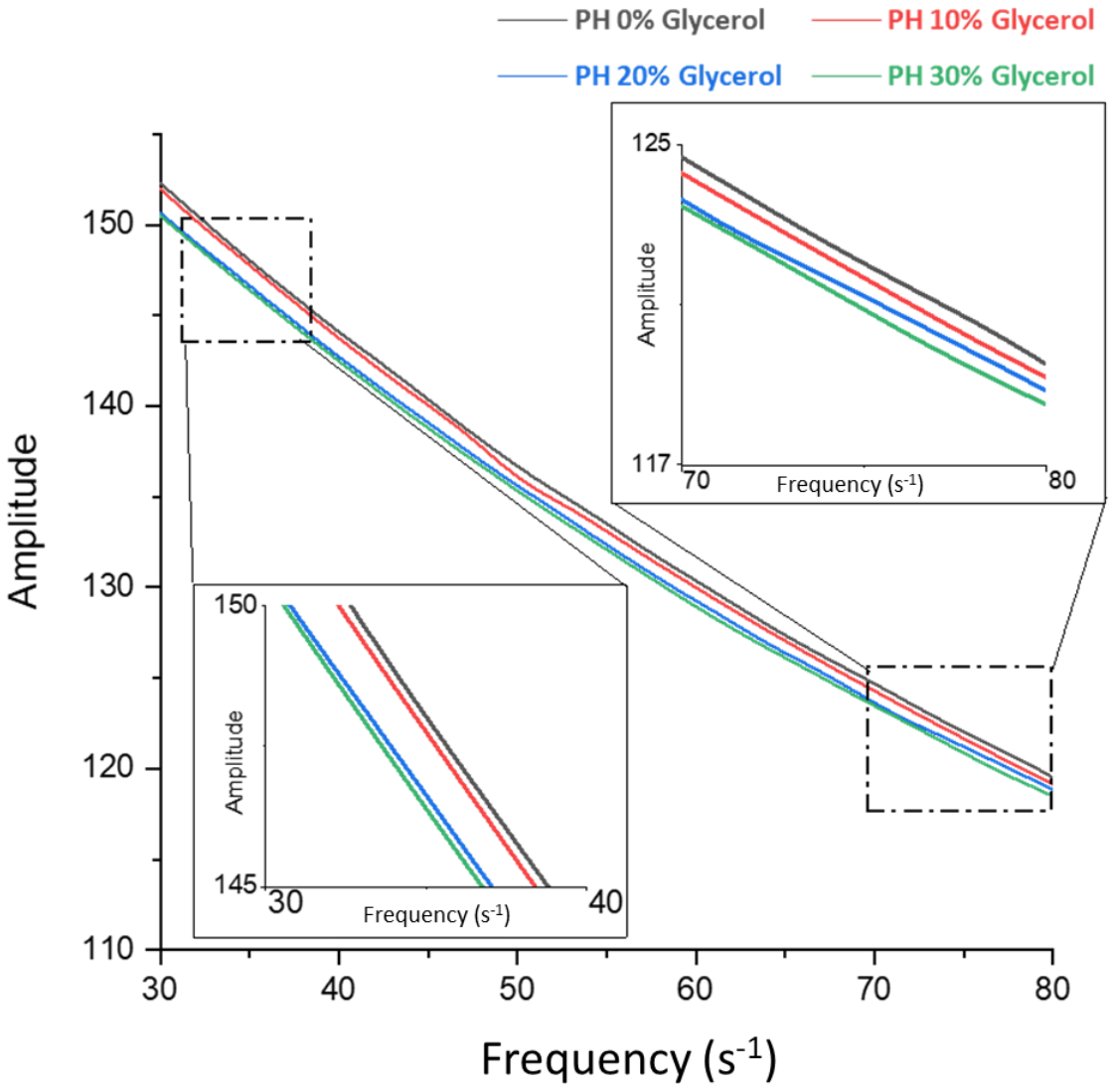

Figure 5-17: Amplitude versus rotation frequency of phosphate grown hematite between 40 and 80 s^{-1}**.** PH referring to phosphate hematite.

Figure 5-17 examines the sensing capabilities of the phosphate directed hematite over a small amplitude range. It indicates that the relative sensing capabilities of the two types of hematite rods are not quite so black and white as suggested above. The phosphate directed

hematite p1articles are a much better example of the effect of rotational frequency. At low frequencies such as < 30 $s^{-1,}$ there is no significant difference between the 0 and 10% glycerol solutions or the 20 and 30% solutions. These signals have differences which are approximately 0.007 au which is between 5000 -11,000 times smaller than that those seen in the 1,2 propanediamine. While these differences are small at higher frequencies of < 75 s^{-1} the nanoparticles' signals begin to separate indicating that the combined drag effects and increased frequency can affect the sensing capabilities of these rods. When examining the relationship of amplitude difference to glycerol % at high frequencies, the relationship appears to become almost linear which would be ideal for a sensor.

In a comparison of the changes in amplitude caused by viscosity at different frequencies, it becomes apparent that the 1,2 propanediamine and phosphate hematite have different relationships.

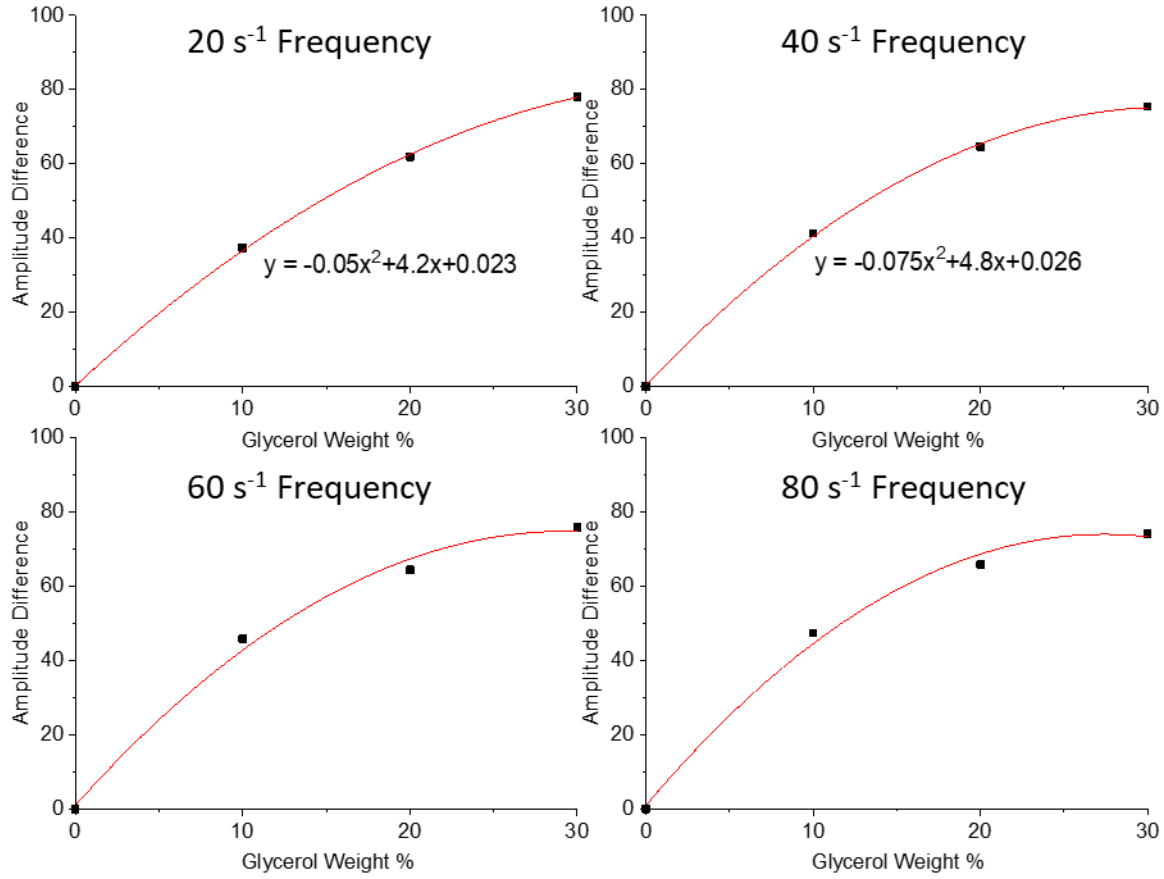

Figure 5-18: Graphs of amplitude difference compared to the amplitude of 1,2 propanediamine in 0% glycerol at different rotational frequencies of 10, 30, 50 and 70 s^{-1}.

Figure 5-18 shows the relative amplitude differences between different glycerol rates at 10, 30, 50 and 70 s^{-1}. Comparing the sensitivity of 1,2 propanediamine nanorods at different frequencies shows that the difference in frequency has little effect. However, greater differences in amplitude can be seen at lower frequencies. These provide a good calibration curve for predicting the viscosity of a solution. Whereat 10 or 30 s^{-1} the glycerol % of a solution could be predicted using the equations in Figure 5-18. The difference in amplitude begins to decrease as glycerol % is increased across all frequencies. This suggests that the 1,2 propanediamine rods would be less sensitive in concentrations greater than 20% glycerol and would probably not give a significant difference in amplitude for solutions above 30% glycerol.

Figure 5-19 shows the relationship between glycerol concentration and amplitude at different frequencies. As mentioned above, at low frequencies the phosphate directed hematite rods are not able to differentiate between 0% and 10% glycerol or 20% and 30% glycerol. However, there is a large increase in amplitude difference between the 10% and

20% solutions at frequencies between 10-40 s^{-1}. This sharp change in amplitude could suggest that the phosphate hematite may be very sensitive to viscosity changes between 1.328 and 1.844 cP.

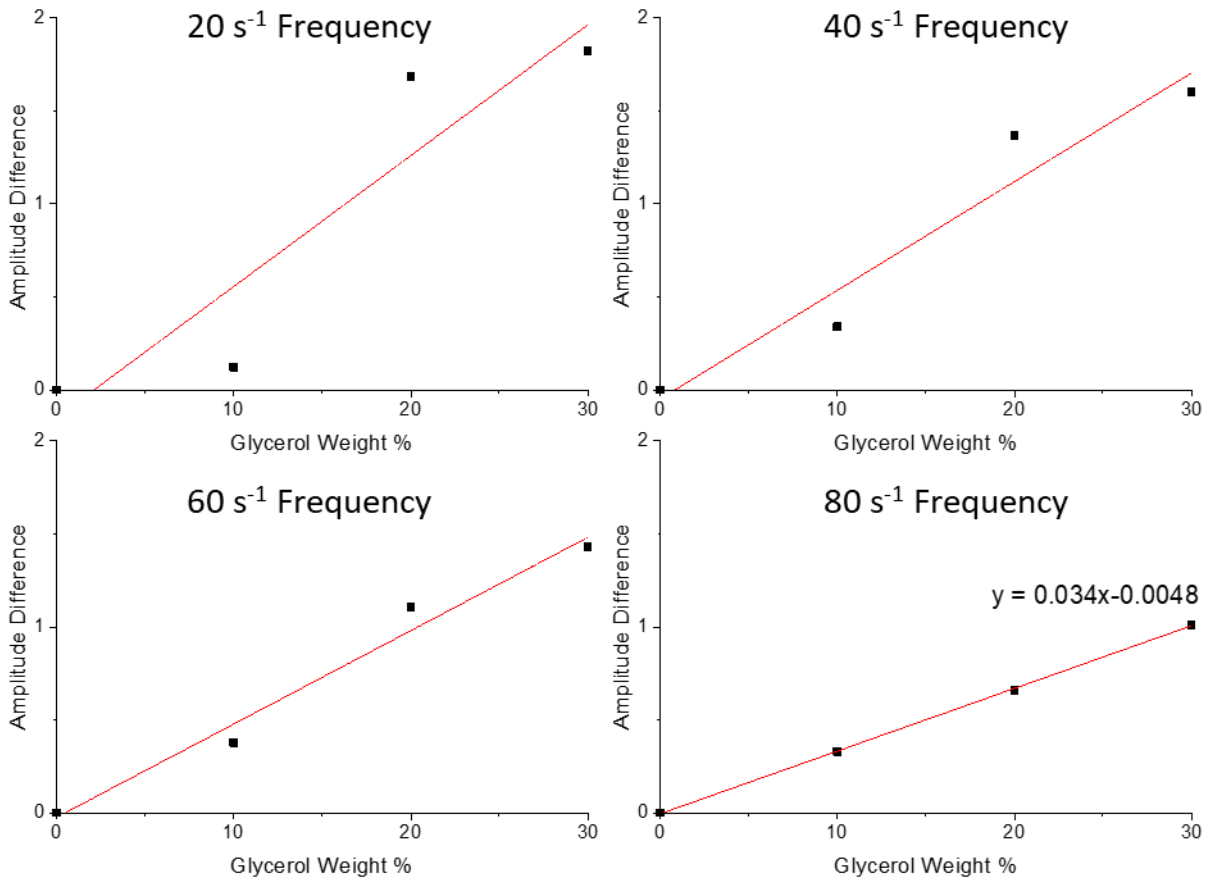

Figure 5-19: Graphs of amplitude difference compared to the amplitude of phosphate directed hematite rods in 0% glycerol at different rotational frequencies of 20, 40, 60 and 80s^{-1}.

As the rotational frequency of phosphate directed hematite rods increases the relationship between the amplitude and the glycerol % becomes increasingly linear. At a frequency of 80 $s^{-1,}$ the relationship is directly proportional. While the overall change in amplitude is considerably less than that obtained for 1,2 propanediamine this linear relationship suggests that at high frequencies the phosphate directed hematite can measure a wide range of viscosities. Since the magneto-optical rig can measure these small changes in amplitude, phosphate hematite particles would be a prospective nanoparticle viscosity sensor over the 1-2.5 cP range.

5.4. Conclusions

Several types of anisotropic nanoparticles have been prepared and their magnetic properties examined. $CePO_4$ nanorods were doped with a range of metal ions including Ni, Co, Mn, W and Fe. Low wt% of between 0.1 – 3.5% of Ni, Co and Mn made small changes in the morphology of $CePO_4$ rods. These resulted in a reduction of nanoparticle length of between 30-100 nm across the doping experiments. XPS did not indicate any Ni, Co or Mn atoms on the surface of the nanoparticles. Raman spectroscopy confirmed the XPS with no introduction of any metal transitions relating to the metal ions. However, the addition of these ions did have a significant effect on the V_3 Raman peak showing an increase in peaks at 1070, 1054, 1024 and 990 cm^{-1} which correspond to the monoclinic phase of $CePO_4$. This suggests that either metal ions have been successfully incorporated into the lattice of $CePO_4$ or the presence of these ions influences the growth of $CePO_4$. Furthermore, in the case of Mn and Ni increases in magnetic susceptibility were found which could be caused by either of the two outcomes suggested above. $CePO_4$ treated with W or Fe had more profound changes in the morphology and magnetic behaviour of the nanoparticles. Raman spectra of the 40.5% W doped $CePO_4$ do not show any characteristic peaks consistent with the presence of WO_3 on the surface. However, XPS indicates the presence of W atoms. This paired with the morphological changes suggests that a small number of W atoms could be doped into the lattice of $CePO_4$. Fe doped $CePO_4$ samples all showed a significant increase in magnetic susceptibility with large changes in the morphology of the product. Raman did not confirm the presence of any Fe vibrations, while XPS indicated an increasing Fe signal as the doping % of Fe was increased with the Fe(2p) binding energy indicating $FePO_4$ and suggesting that $CePO_4$ was successfully doped with Fe ions. To confirm this data, XRD measurements could be used to identify the inclusion of any bulk metal ions.

The magnetic properties and rotational dynamics of hematite and doped-$CePO_4$ nanoparticles were examined. $CePO_4$ rods with lower susceptibilities than the hematite responded to an external magnetic field of 1 T. The 26% Fe doped $CePO_4$ nanorods were the most responsive to an external magnetic field consistent with their relatively high magnetic susceptibility and small aspect ratio compared to the rods with lower wt% doping of Mn, Ni and Co. The 40.5% W doped $CePO_4$ and 26% Fe doped $CePO_4$ were both shown to be capable of monitoring changes in viscosity as a function of their phase shift. The 26% Fe

doped $CePO_4$ samples were more sensitive despite having a lower magnetic susceptibility, this is probably due to the greater size of W doped nanorods causing a greater drag effect.

Hematite nanoparticles were studied for their magneto-optical viscosity sensitivity at different frequencies. It was expected that as the frequency was increased, the transmittance of light would decrease, and the sensitivity would differ across the range. While sensitivity did vary across the 10-80 s^{-1} frequency range, the transmittance of light did not decrease in samples tested using the 1,2 propanediamine directed hematite rods. These particles were very sensitive to changes in glycerol with their sensitivity decreasing as glycerol % was increased. Phosphate directed hematite had a different relationship with very little difference between the signals of particles suspended in different glycerol solutions. However, two areas were of interest: At low frequencies, large differences in amplitude were obtained between 10-20% glycerol, while at higher concentrations the relationship between glycerol and amplitude was linear. The difference in sensitivity between these rods may be a function of their growth as discussed in Chapter 2. Hematite particles grew in the presence of phosphate aggregate together to produce nanorods, while 1,2 propanediamine haematite is a single crystal. The multiple domains formed from the aggregation of hematite subunits could affect the magnetic moment and rotational dynamics of phosphate hematite rendering it less sensitive to changes in drag.

5.5 References

1 D. Lisjak and A. Mertelj, *Prog. Mater. Sci.*, 2018, 95, 286–328.

2 G. Yang, H. Gong, T. Liu, X. Sun, L. Cheng and Z. Liu, *Biomaterials*, 2015, **60**, 62–71.

3 T. R. Kline, M. Tian, J. Wang, A. Sen, M. W. H. Chan and T. E. Mallouk, *Inorg. Chem.*, 2006, **45**, 7555–7565.

4 G. Ferk, P. Krajnc, A. Hamler, A. Mertelj, F. Cebollada, M. Drofenik and D. Lisjak, *Sci. Rep.*, 2015, **5**, 1–8.

5 A. Ramzannezhad, P. Gill and A. Bahari, *BioNanoMaterials*, 2017, 18.

6 P. Aprelev, Y. Gu, R. Burtovyy, I. Luzinov and K. G. Kornev, *J. Appl. Phys.*, 2015, **118**, 074901.

7 H. Li, C. Li, W. Sun, Y. Wang, W. Hua, J. Liu, S. Zhang, Z. Chen, S. Wang, Z. Wu, Q. Zhu, R. Tang, J. Yu, L. He, G. A. Ozin and X. Zhang, *Adv. Mater.*, 2019, **31**, 1900388.

8 Pan, Wang, Dou, Zhao, Xu, Wang, Zhang, Li, Pan and Li, *Crystals*, 2019, **9**, 417.

9 D. W. Wang, X. M. Zhu, S. F. Lee, H. M. Chan, H. W. Li, S. K. Kong, J. C. Yu, C. H. K. Cheng, Y. X. J. Wang and K. C. F. Leung, *J. Mater. Chem. B*, 2013, **1**, 2934–2942.

10 I. Koh and L. Josephson, *Sensors*, 2009, 9, 8130–8145.

11 R. Hong, M. J. Cima, R. Weissleder and L. Josephson, *Magn. Reson. Med.*, 2008, **59**, 515–520.

12 H. Lee, T. J. Yoon, J. L. Figueiredo, F. K. Swirski and R. Weissleder, *Proc. Natl. Acad. Sci. U. S. A.*, 2009, **106**, 12459–12464.

13 X. Wang, J. Feng, H. Yu, Y. Jin, A. Davidson, Z. Li and Y. Yin, *Research*.

14 P. Aprelev, Y. Gu, R. Burtovyy, I. Luzinov and K. G. Kornev, *J. Appl. Phys*, 2015, **118**, 74901.

15 A. Tokarev, B. Rubin, M. Bedford and K. G. Kornev, in *AIP Conference Proceedings*, 2010, vol. 1311, pp. 204–209.

16 I. Zubritskaya, K. Lodewijks, N. Maccaferri, A. Mekonnen, R. K. Dumas, J. Åkerman, P. Vavassori and A. Dmitriev, *Nano Lett.*, 2015, **15**, 3204–3211.

17 S. Schrittwieser, F. Ludwig, J. Dieckhoff, A. Tschoepe, A. Guenther, M. Richter, A. Huetten, H. Brueckl and J. Schotter, *Small*, 2014, **10**, 407–411.

18 R. S. Bejhed, T. Zardán Gómez De La Torre, M. Donolato, M. F. Hansen, P. Svedlindh and M. Strömberg, *Biosens. Bioelectron.*, 2015, **66**, 405–411.

19 S. Schrittwieser, J. Schotter, T. Maier, R. Bruck, P. Muellner, N. Kataeva, K. Soulantika, F.

Ludwig, A. Huetten and H. Brueckl, in *Procedia Engineering*, Elsevier, 2010, vol. 5, pp. 1107–1110.

20 A. Tokarev, B. Rubin, M. Bedford and K. G. Kornev, in *AIP Conference Proceedings*, 2010, vol. 1311, pp. 204–209.

21 F. Ludwig and H. Remmer, *Phys. Sci. Rev.*

22 E. T. Rietschel, T. Kirikae, F. U. Schade, U. Mamat, G. Schmidt, H. Loppnow, A. J. Ulmer, U. Zähringer, U. Seydel, F. Di Padova, M. Schreier and H. Brade, *FASEB J.*, 1994, **8**, 217–225.

23 T. M. Wassenaar and K. Zimmermann, *Lipopolysaccharides in food, food supplements, and probiotics: should we be worried?*, Akademiai Kiado Zrt., 2018, vol. 8.

24 S. M. Opal, *Contrib. Nephrol.*, 2010, **167**, 14–24.

25 J. C. Hurley, P. Nowak, C. Gogos, A. Armaganidis, E. J. Giamarellos-Bourboulis and A. B. Onderdonk, *J. Clin. Microbiol.*, 2015, **53**, 1183–1191.

26 M. A. Dobrovolskaia, B. W. Neun, J. D. Clogston, H. Ding, J. Ljubimova and S. E. McNeil, *Nanomedicine*, 2010, **5**, 555–562.

27 Fairley N, *CasaXPS Manual: 2.3.15 Spectroscopy*, 2009.

28 M. L. Sheely, *Extent of Illness and of Physical and Mental Defects Prevailing in the United States*, Sydenstricker, E., Pub. Health Repts, 1929, vol. 24.

29 M. P. Oliveira, L. S. Silva, S. G. Mercena, A. A. Coelho, C. T. Meneses and J. G. S. Duque, *J. Supercond. Nov. Magn.*, 2017, **30**, 587–591.

30 S. A. I. Nemoshalenko V.V., Didyk V.V., Krivitskii V.P., *Zh. Neorg. Khimii 28, 2182*.

Chapter 6 Conclusion

The distinctive characteristics of anisotropic nanoparticles make them uniquely suited for developing magneto-optical sensors[1–3]. Developing such techniques is a complex problem as the suitability of nanoprobes depends upon a myriad of different properties. However, these can be summarised as a combination of those which contribute to the surface plasmon resonance and those that affect the magnetic behaviour of the nanomaterials. Three examples of important parameters in nanoprobes are[4–8]:

1. The aspect ratio
2. The surface morphology
3. The magnetic susceptibility and rotational dynamics

This thesis investigated how these properties can be optimised across multiple nanoparticle systems and examined how these nanoparticles can act as nano-rheological detectors and hence their suitability for use in diagnostics.

The aspect ratio and general morphology of a nanorod can have profound effects on its optical properties. This stems from the relative amplification of the transverse mode compared to the longitudinal mode in surface plasmon resonance. As the length of a nanorod or spheroid is increased the extinction coefficient of the surface plasmon increases[9]. Therefore, developing synthetic methods which can easily and predictably produce a range of aspect ratios is important in developing optimised magneto-optical sensors[10]. Hydrothermal growth is an ideal preparation method, as nanoparticles can be developed in an easy one-pot synthesis in which the growth of the particles can be influenced through additives that act as directing agents[11,12].

The hydrothermal growth of hematite nanoparticles was studied in the presence of two different directing agents: Potassium phosphate and 1,2 propanediamine. The effect of the two directing agents had a significant impact on the growth mechanism of the nanoparticles forming two distinctly different final products. As suggested by Frandsen et al. and Sugimoto et al. phosphate directed nanoparticles were shown to grow through the nucleation of seeds which facilitated the development of hematite subunits[13,14]. These subunits aggregated together and through Ostwald ripening, form single ellipsoid hematite particles with large crystal domains. However, in contrast to the findings of Frandsen et al,.the

phosphate directed particles indicated that hematite was the dominant phase throughout the growth of the particles. However, PiFM indicated that the sides of the hematite rod had higher concentrations of carbonates, which are linked to the presence of the hydroxides. Akaganéite nuclei may adsorb to the ends and sides of the rod and the phosphate plays a role in aiding this preferential binding on certain crystal planes through capping others. The hematite particles formed in the presence of phosphate are similar in morphology to the works of Ozaki et al. and Rodríguez et al. which showed elongation through the [001] axis forming ellipsoid particles[15,16]. This is probably the case in the hematite particles formed in the presence of phosphate in this study since the XRD shows relative intensities of the [104] and [110] crystal planes which are typical of growth along the [001] axis[16]. By increasing the concentration of the phosphate up to $6x10^{-3}$ M the aspect ratio could be reliably varied to as high as 7. This is possibly caused by the increased amount of phosphate available to absorb onto the [104] and [110] planes, resulting in an increase in preferential binding in the [001] direction. However, increasing the phosphate to $6x10^{-3}$ M phosphate concentration this relationship changes, this perhaps corresponds to the point a full monolayer is formed on the [104] and [110] planes and so it becomes less favourable to the phosphates to bind onto these, and they begin to cap other crystal surfaces resulting in a loss of the rod morphology.

Hematite nanoparticles prepared with the assistance of 1,2 propanediamine are predicted to grow through the nucleation of a goethite sphere where hematite recrystallised into 'arms' on either side of the nanoparticles as described by Li et al. [17]. Samples prepared between 140-180 ^{o}C possessed similar morphologies to those prepared by Li et al. PiFM data supported these predictions, vibrational spectroscopy maps of nanoparticles prepared at 160 ^{o}C indicated that goethite was localised in a central sphere while hematite was present in the 'arms'. These maps also confirmed the molecules of 1,2 propanediamine gathered in the hematite regions, suggesting that the diamine has a role in directing the recrystallization of hematite while stabilising the oxide form in respect to the hydroxide. The temperature of the reaction appears to be profoundly linked to the growth mechanism of the nanoparticles, with particles formed at 180 ^{o}C consisting of only hematite, implying that the higher temperature aids with the goethite-hematite phase transition. The overall growth direction in the nanoparticles formed at 180 ^{o}C is on the [001] axis, suggesting that

the 1,2 propanediamine has very similar behaviour to the phosphate and absorbs to the [104] and [110] crystal faces.

While hematite particles were highly tuneable, their aspect ratio was relatively low, typically <10. This can result in significantly increased extinction coefficients. The growth of cerium based nanorods yielded aspect ratios of up to an average of 25. The morphology of nanoparticles formed through the phosphate assisted hydrothermal growth of cerium nanoparticles relied heavily on the reaction parameters. The method could be tuned to produce both nanocubes and rods depending on a combination of the temperature and phosphate concentration. The dominant morphology of the product is a function of the competitive absorption PO_4^- and NO_3^- ions onto $Ce(OH)_3$[18,19]. Depending on the concentration of PO_4^- ions either $CePO_4$ would form through the reaction of $Ce(OH)_3$ and PO_4^{-2}. n the absence of PO_4^- ions the $Ce(OH)_3$ nuclei forms CeO_2 through dissolution-crystallisation. When CeO_2 is formed, the NO_3^- ions would inhibit growth along the [100] plane and result in a cubic morphology. At low temperatures and high concentrations of PO_4^- ions, the mechanism favours the formation of $CePO_4$ nanorods. A combination of PiFM and Raman spectroscopy indicated that the nanorods were in dual-phase which consisted of both monoclinic and hexagonal $CePO_4$. The proportion of the monoclinic phase is probably linked to the amount of phosphate in the preparation method. The monoclinic V_3 contributions increased with increasing phosphate concentration and decreasing temperature. If PO_4^- ions were in excess on a $CePO_4$ surface they increase the surface energy significantly. To decrease the surface energy the hexagonal $CePO_4$ may undergo a crystallographic rearrangement and form the monoclinic form[20].

While the aspect ratios and morphologies of nanoparticles could be successfully tuned and optimised, they represent only a small factor contributing to the magneto-optical suitability of a nanoparticle. The use of plasmonic metals coatings to enhance the optical properties of anisotropic nanoparticles is the second key factor examined in this thesis. Gold growth on untreated surfaces of silica and hematite was low and resulted in very few gold islands developing. However, the seed-mediated method when combined with surface functionalisation with silanes, such as APTES, provides a method to control the deposition of gold. The morphology of a gold coat grown by the seed-mediated method was found to be based on a combination of two factors:

1. Number and dispersion of seeds particles.
2. The volume of gold growth solution.

When there are too few seeds supported on the surface of a nanoparticle there are insufficient nucleation points for a smooth coat to form. The composition and formation of the shell rely on there being enough seed particles well dispersed across the surface. In this ideal condition, they are equally spaced across the surface and in proximity. When these seed particles grow their diameters increase to such a point that they almost overlap and begin to coalesce. When there are too few seed particles, the diameters of the seeds do not grow to a point where they coalesce. The relationship between gold volume and shell roughness is more straightforward, the gold volume added to the pre-seeded particles is directly proportional to the increase in their diameter. Therefore, the theoretical 'perfect' amount of gold growth solution is the exact amount needed for the seed to grow sufficiently to a point where they coalesce. After this critical point, further growth leads to increasing roughness in the coating. This could be explained with a process of 'overgrowth' like that described by Wang et al. [21] which Kwon et al. described as analogous to the Stranksi-Krastanov growth mechanism by [22]. This type of growth can be visualised as a competition for gold between the substrate and the seeds, growth consists of two steps[23]. As the core surface has been functionalised the gold is attracted to the surface resulting in the formation of a smooth shell. This first layer is probably deposited with its lattice under strain because of its interface with the substrate lattice. When this layer has been formed the 'gold: core' interactions are lower, as the coating increases in thickness these interactions decrease. Eventually, the 'gold: core' interaction is low enough that there is a swap from a 'gold: core' dominated system to a system where 'gold: gold' interactions are preferable. As the next layer is deposited, gold nucleates with its original crystal structure into particles with cubic and spherical morphologies rather than a smooth shell[22]. In the Fe_2O_3/SiO_2/Au samples, the gold adatoms with their original lattice reach such a size that the lattice strain is too high at the Fe_2O_3/Au interface and the gold detaches from the substrate. It appeared possible that this type of growth and detachment could be reduced through a more controlled coat growth method examined on $CePO_4$ nanoparticles using a different functionalisation method. Irrespectively, these particles were difficult to coat, probably because too few seed particles could be supported upon their surface relative to

their volume. This would reduce the overall interfacial area between the gold coat and the surface. These particles required the introduction of a silica intermediate between the $CePO_4$ and Au, forming a sandwich structure. These nanocomposites had aspect ratios of approximately 10 but and some were formed from the combination of two cerium phosphate rods.

The growth of $CePO_4$ nanorods could be controlled with simple changes to reaction temperature and time and using this combination of parameters the aspect ratio of the $CePO_4$ rods could be tuned between 3 – 27. These particles would be ideal as magneto-optical probes because of the tailorable preparation method. However, the particles formed are more than 10× less magnetically susceptible than hematite. We have shown that the presence of Ni and Mn ions in low wt% affected the magnetic susceptibility of the $CePO_4$ nanoparticles, despite XPS and Raman showing no evidence for successful doping. The changes in magnetism could be due to changes in the $CePO_4$ particles size and morphology as there was a net trend for particle length to decrease as additive ion % increased[24] Changes in the V_3 transition were observed when adding dopant metal ions and the changes in magnetic behaviour could be a result of a transition between the hexagonal and monoclinic phases. More pronounced changes were evident in the morphologies of nanoparticles prepared in the presence of Fe and W ions where wt% of between 12-52% were investigated compared to the 0.1-3.5% of the other dopants. Fe doping resulted in a consistent increase in susceptibility across all samples irrespective of the wt% of Fe and the XPS data indicated the presence of $FePO_4$ on the surface of these samples which increased proportionally with the Fe wt%.

The W and Fe doped $CePO_4$ samples were sufficiently magnetically susceptible to be rotated in an aqueous solution and these particles were able to detect changes in viscosity caused by glycerol. However, the sensitivity of the Fe doped particles was greater than that of the W despite the higher magnetic susceptibility of the latter. This could be because of increased lag effects felt in the W doped particles from their longer length.

Phosphate directed and 1,2 propanediamine hematite particles were both successfully rotated in an aqueous solution by an external magnetic field and the particles were analysed at different rotational frequencies. The sensitivity of both types of hematite particles varied with the rotational frequency. Hematite nanorice showed a net increase in phase shift as

the frequency was increased, this was characterised by a decrease in amplitude, while the 1,2 propanediamine directed hematite particles had a more complex behaviour, with a decrease in amplitude from 10-30 s^{-1} and an increase in amplitude at frequencies greater than 40 s^{-1}. The change in amplitude had no overall effect on the particles' sensitivity to changes in viscosity. However, the sensitivity of the 1,2 propanediamine directed hematite decreased as the glycerol wt% increased. This effect was not observed in the phosphate particles at frequencies greater than 70 s^{-1} where the relationship of amplitude was linear to the viscosity of the glycerol solution.

The changes in the rotational dynamics of the hematite and cerium phosphate particles could be used for the sensing of changes in viscosity caused by the agglomeration of proteins in a solution. One such model could be the Limulus Amebocyte Lysate detection (LAL) of bacterial endotoxins (bet) [25]which can be linked to the time-critical disease sepsis. With further research into these particles, they could be used in the development of point of care diagnostics.

6.1 Further Work

Throughout this thesis, the focus was on how particles or coatings grow. Hence, the coating of hematite particles was examined, but the effects on the plasmon peaks were not accurately measured. A study examining how surface roughness and shell thickness affects the plasmonic activity of the particles would be the next logical step. Paring this with an examination of several aspect ratios of hematite particles coated in a consistent gold shell thickness would be ideal to understand the effects of morphology on the plasmonic properties of hematite nanoprobes. Gold is one of several possible shells for these plasmonic particles. Silver and copper have been used as alternatives and a study exploring these as possible shells in comparison to gold would also be of interest in the design of the 'perfect' hematite magento-optical nanoprobe for point of care diagnostics.

This thesis aimed to understand the method by which a shell can grow on a core particle and applied it across multiple systems. However, the relationships were not perfectly transferable across different core: shell interfaces. One solution to this is to study the silica: gold interface further which could act as an intermediate between many different cores and their metal shell. Before undertaking this work an evaluation of the effect of shell thickness on magnetic susceptibility would be needed. Furthermore, the coating of $CePO_4/SiO_2/Au$

was not fully optimised in this thesis. A study using smaller gold seeds and different amounts of PVP could be undertaken to examine if this system can form smooth shells.

The nanoparticles synthesised in this study were able to detect changes in viscosity. however, the actual sensitivities were not found due to restricted time with the COVID-19 pandemic. It would be ideal to develop several more solutions of different viscosities and measure their viscosities in several ways comparing how the magneto-optical system performs for each morphology and type of rod. Furthermore, this is a model system, when fully optimised the logical next step would be examining its effectiveness in the presence of LAL and bacterial endotoxins.

6.2 References

1 M. G. Manera, A. Colombelli, A. Taurino, A. G. Martin and R. Rella, *Scientific RePORTS |*, 2018, **8**, 12640.

2 G. Evtugyn, A. Porfireva, R. Shamagsumova and T. Hianik, *Chemosensors*, 2020, 8, 1–37.

3 S. Szunerits, T. Nait Saada, D. Meziane and R. Boukherroub, *Nanomaterials*, 2020, **10**, 1271.

4 C. Lumdee, B. Yun and P. G. Kik, *Nanoscale*, 2015, **7**, 4250–4255.

5 J. H. Li, S. W. Chen, Y. Chou, M. C. Wu, C. H. Hsueh and W. F. Su, *Journal of Physical Chemistry C*, 2011, **115**, 24045–24053.

6 W. L. Liu, F. C. Lin, Y. C. Yang, C. H. Huang, S. Gwo, M. H. Huang and J. S. Huang, in *2013 Conference on Lasers and Electro-Optics, CLEO 2013*, 2013.

7 S. Schrittwieser, J. Schotter, T. Maier, R. Bruck, P. Muellner, N. Kataeva, K. Soulantika, F. Ludwig, A. Huetten and H. Brueckl, in *Procedia Engineering*, Elsevier, 2010, vol. 5, pp. 1107–1110.

8 F. Ludwig and H. Remmer, *Physical Sciences Reviews*,

9 X. Ye, L. Jin, H. Caglayan, J. Chen, G. Xing, C. Zheng, V. Doan-Nguyen, Y. Kang, N. Engheta, C. R. Kagan and C. B. Murray, *ACS Nano*, 2012, **6**, 2804–2817.

10 A. Tokarev, B. Rubin, M. Bedford and K. G. Kornev, in *AIP Conference Proceedings*, 2010, vol. 1311, pp. 204–209.

11 C. Anastasescu, S. Mihaiu, S. Preda and M. Zaharescu, *1D Oxide Nanostructures Obtained by Sol-Gel and Hydrothermal Methods*, Springer International Publishing, Cham, 2016.

12 P. Basnet and S. Chatterjee, *Nano-Structures and Nano-Objects*, 2020, 22, 100426.

13 H. Itoh and T. Sugimoto, *Journal of Colloid and Interface Science*, 2003, **265**, 283–295.

14 C. Frandsen, B. a Legg, L. R. Comolli, H. Zhang, B. Gilbert, E. Johnson and J. F. Banfield, *Crystengcomm*, 2014, **16**, 1451–1458.

15 M. Ozaki, N. Ookoshi and E. Matijević, *Journal of Colloid And Interface Science*, 1990, **137**, 546–549.

16 N. Gálvez, V. Barrón and J. Torrent, *Clays and Clay Minerals*, 1999, **47**, 304–311.

17 Z. Li, X. Lai, H. Wang, D. Mao, C. Xing and D. Wang, *Nanotechnology*, 2009, **20**, 245603.

18 Q. Wu, F. Zhang, P. Xiao, H. Tao, X. Wang, Z. Hu and Y. Lü, *Journal of Physical Chemistry C*, 2008, **112**, 17076–17080.

19 C. Dong, Y. Zhou, N. Ta and W. Shen, *CrystEngComm*, 2020, **22**, 3033–3041.

20 J. Bao, R. Yu, J. Zhang, X. Yang, D. Wang, J. Deng, J. Chen and X. Xing, *CrystEngComm*, 2009, **11**, 1630–1634.

21 C. Wang, Y. Wei, H. Jiang and S. Sun, *Nano Letters*, 2009, **9**, 4544–4547.

22 S. G. Kwon, G. Krylova, P. J. Phillips, R. F. Klie, S. Chattopadhyay, T. Shibata, E. E. Bunel, Y. Liu, V. B. Prakapenka, B. Lee and E. V. Shevchenko, *Nature Materials*, 2015, **14**, 215–223.

23 J. E. Prieto and I. Markov, *Surface Science*, 2017, **664**, 172–184.

24 B. Issa, I. M. Obaidat, B. A. Albiss and Y. Haik, *International Journal of Molecular Sciences*, 2013, 14, 21266–21305.

25 C. Allender, J. Bowen S. Eppler, R. Matelon and J. Thurlow, *Magneto-optical method and apparatus for detecting analytes in*, 2019, **WO19960095**, 1–43.

Chapter 7 Supporting Information

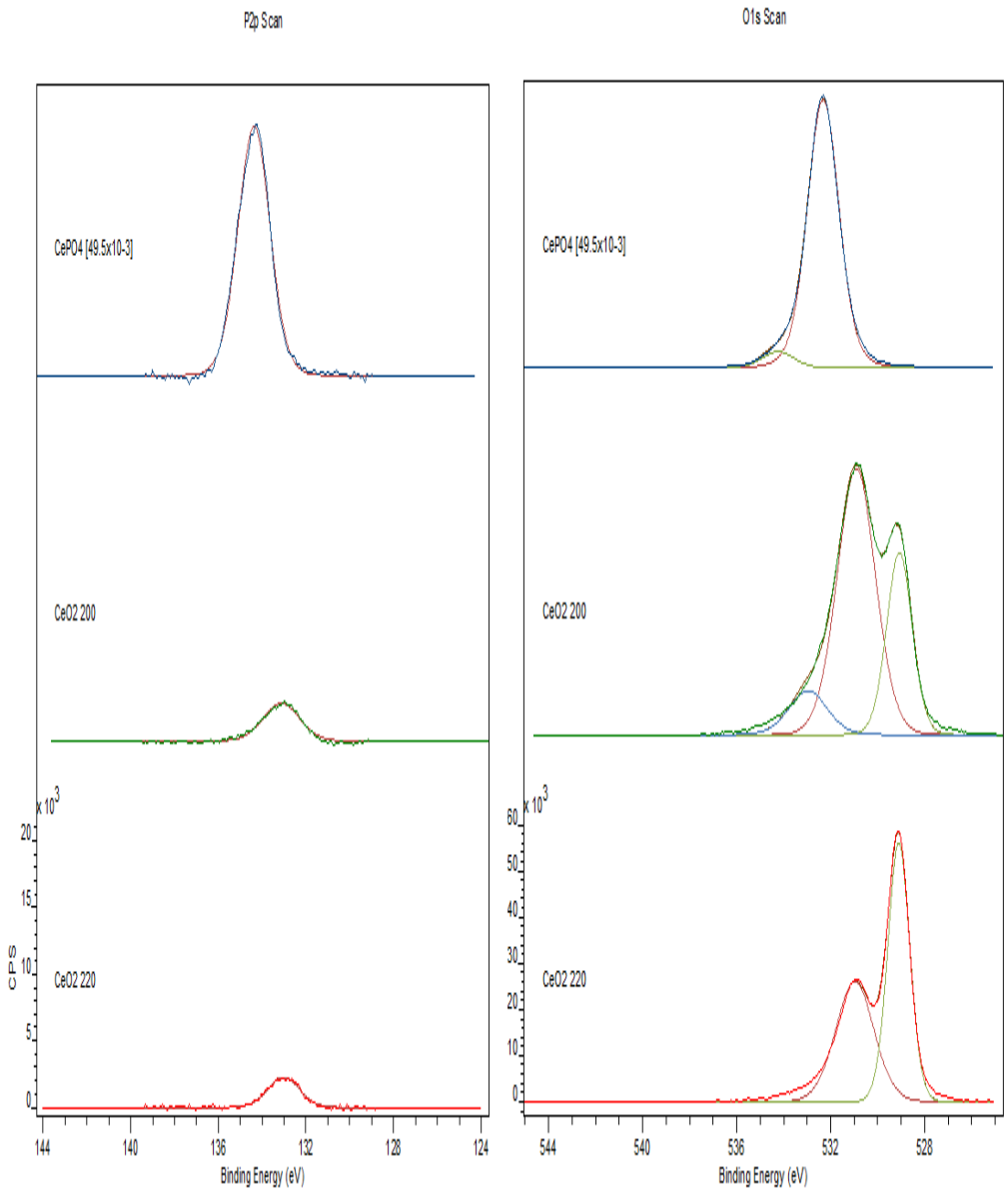

Supporting Information 1: Xp Spectra of the O(1s) and P(2P) scans of cerium nanoparticles formed at

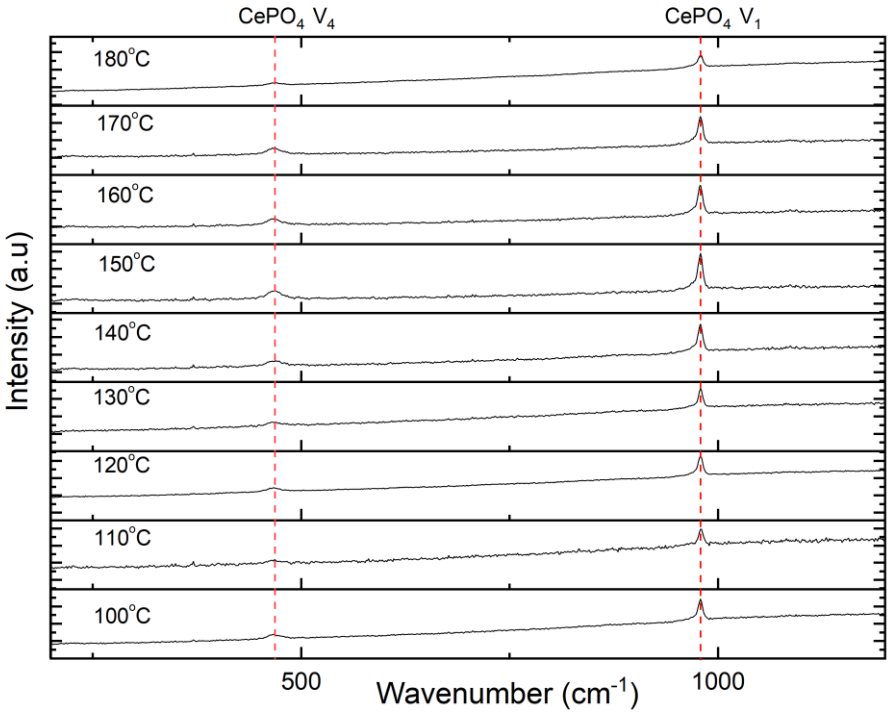

Supporting information 2. Raman spectroscopy of $CePO_4$ samples formed at different temperatures and sampled after each colourless to cloudy colour change.

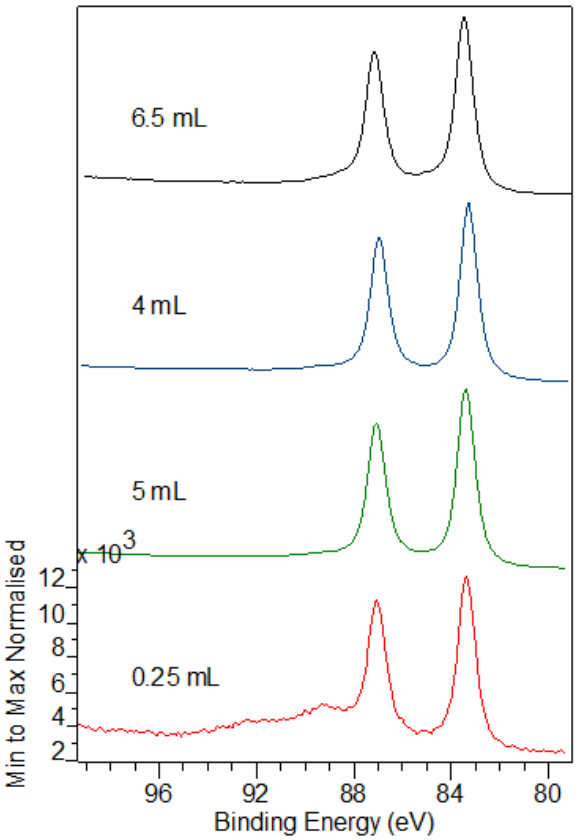

Supporting Information 3. Au XP spectra of phosphate hematite prepared with different amounts of gold growth solution.